HAL
open science

Structure de matériaux à base de polylactide obtenus par extrusion réactive : formation et transformation thermomécaniques

Berit Brüster

To cite this version:

Berit Brüster. Structure de matériaux à base de polylactide obtenus par extrusion réactive : formation et transformation thermomécaniques. Mechanics of materials [physics.class-ph]. Université de Lorraine, 2017. English. NNT : 2017LORR0156 . tel-01661553

HAL Id: tel-01661553

https://theses.hal.science/tel-01661553

Submitted on 12 Dec 2017

HAL is a multi-disciplinary open access archive for the deposit and dissemination of scientific research documents, whether they are published or not. The documents may come from teaching and research institutions in France or abroad, or from public or private research centers.

L'archive ouverte pluridisciplinaire **HAL**, est destinée au dépôt et à la diffusion de documents scientifiques de niveau recherche, publiés ou non, émanant des établissements d'enseignement et de recherche français ou étrangers, des laboratoires publics ou privés.

UNIVERSITÉ DE LORRAINE

AVERTISSEMENT

Ce document est le fruit d'un long travail approuvé par le jury de soutenance et mis à disposition de l'ensemble de la communauté universitaire élargie.

Il est soumis à la propriété intellectuelle de l'auteur. Ceci implique une obligation de citation et de référencement lors de l'utilisation de ce document.

D'autre part, toute contrefaçon, plagiat, reproduction illicite encourt une poursuite pénale.

Contact : ddoc-theses-contact@univ-lorraine.fr

LIENS

Code de la Propriété Intellectuelle. articles L 122. 4
Code de la Propriété Intellectuelle. articles L 335.2- L 335.10
http://www.cfcopies.com/V2/leg/leg_droi.php
http://www.culture.gouv.fr/culture/infos-pratiques/droits/protection.htm

Laboratoire d'Energétique et de Mécanique Théorétique et Appliquée

École doctorale Énergie Mécanique et Matériaux

THÈSE

Pour l'obtention du titre de

DOCTEUR DE L'UNIVERSITE DE LORRAINE

Spécialité : Mécanique - Énergétique

par

Berit BRÜSTER

Structure of Polylactide-Based Materials Obtained by Reactive Extrusion: Formation and Thermomechanical Transformations

---

Thèse soutenue publiquement le 02 octobre 2017 à Nancy devant le jury suivant :

Rapporteurs :	Jannick DUCHET	Professeur à l'INSA Lyon
	Bruno FAYOLLE	Professeur à l'ENSAM Paris
Examinateurs :	Tatiana BUDTOVA	Directrice de Recherche au CEMEF Mines ParisTech
	Grégory STOCLET	Maître de Conférences, UMET, Université de Lille
	Isabelle ROYAUD	Professeur à l'Université Lorraine, Nancy
	Philippe DUBOIS	Professeur à l'Université de Mons, Belgique
Invité :	Jean-Marie RAQUEZ	Docteur, Université de Mons, Belgique
Encadrants :	Stéphane ANDRÉ	Professeur à l'Université de Lorraine, Nancy Directeur de thèse
	Frédéric ADDIEGO	Docteur (HDR), LIST, Luxembourg Co-directeur de thèse

Acknowledgement

The work conducted in this Ph.D. thesis was related to a project of the Fond National de la Recherche Luxembourg (FNR) with the project name DuraPLA (C13/MS/5837188). I would like to thank the FNR for the financial support of this interesting project that allowed me to finalize my Ph.D. manuscript. This project was a cooperation between the Luxembourg Institute of Science and Technology (Hautcharage, Luxembourg), the University of Lorraine (Nancy, France), and the University of Mons (Mons, Belgium). During my work on this project in the time period from April 2014 to September 2017, I got many advice and help and I would like to thank all people who supported me at this time.

Especially, I would like to thank my Ph.D. supervisor, Professor Stéphane André from the University of Lorraine (France). He supported me during the whole time with advice and, even though, he is not a specialist in the field of chemistry of polymers his comments and suggestions always helped me to think more critically about my work.

I also would like to thank my scientific supervisor, Dr. Frédéric Addiego, from the Luxembourg Institute of Science and Technology (LIST) in Luxembourg. He helped me to in all stages of my work at LIST: the processing of the material, the simple and advanced characterizations, and finally with all administrative work in French when it was necessary.

I am also thankful to Professor Philippe Dubois and Dr. Jean-Marie Raquez from the University of Mons, who are specialists in the field of polylactide and its processing. Both supported me a lot and I was always grateful for their support, advice, and the helpful discussions about my work.

Furthermore, I would like to thank all my colleagues from LIST, who helped me to understand and conduct the processing or characterization methods. Special thanks to Dr. Kui Wang and Sébastien Gergen for the explanations for mechanical characterizations. For the thermal characterizations, I would like to thank Benoît Marcolini and Régis Vaudemont, who explained me the machines and were always supportive when I had questions for the analysis of DSC or DMA. The AFM analyses were conducted on different equipment and I am grateful to Dr. Yves Fleming and Patrick Grysan for their help with the analysis. Dr. Yao Koutsawa conducted the modeling of the isothermal crystallization data and I would like to thank him for this and also his support in all questions of modeling. Further thanks to the four trainees who conducted a part of their Master Studies at LIST and I was allowed to work with. Finally, I would like to thank all my colleagues who became friends and made this time a really nice experience.

In addition, I would like to thank my colleagues from the University of Mons and the University of Lorraine. Especially, Dr. Nicolas Delbosc for the conduction of NMR analysis and the support for the analysis and Dr. Laurent Farge for the help with the ARAMIS system, but also all colleagues with whom I spend nice times during the lunch breaks when I work at the two universities.

At last, I would like to thank my family and my friends who were supportive in the whole way that brought me to this point of my life. It was always nice to have a more non-scientific opinion about this topic.

Table of Contents

Acknowledgement i

I. List of Abbreviations viii

II. List of Symbols x

III. List of Figures xi

IV. List of Tables xvii

V. Abstract xix

VI. Resumé xxii

1 General Introduction 1

1.1 Background 1

1.2 Problematic 1

1.3 Research Objectives and Methodology 2

1.4 Manuscript Description 3

2 State of the Art 5

2.1 Plastic Materials – Both a Curse and a Blessing 5

2.2 Polylactide as a Forward-Looking Biopolymer 10

2.2.1 History and Environmental Impact of Polylactide 10

2.2.2 Polylactide's Structure 13

2.2.3 Polylactide's Properties Compared to Two Common Plastics 14

2.3 Modification of Polylactide 18

2.3.1 Plasticization by Reactive Extrusion 21

2.4 Crystallization Mechanisms of Polylactide 26

2.5 Deformation Mechanisms of Polylactide 29

2.6 Polylactide's End-of-Life Scenarios 36

2.7 Research Needs 41

3 Process-Structure Relationship for Plasticized Polylactide 43

3.1 Introduction 43

3.2 Analysis of the Structure 46

3.2.1 Processing of Plasticized Polylactide in a Batch-Compounder 46
3.2.2 Thermal Properties 51
3.2.3 Morphology Analysis 54
3.2.4 Impact Resistance 56
3.3 Isothermal Crystallization Kinetics 57
3.4 Scale-Up Process: From Batch Mode to Continuous Process 64
3.4.1 Processing Parameters for the Continuous Process 64
3.4.2 Processing of Plasticized Polylactide in a Mini-Extruder 65
3.4.3 Characterization of the Mini-Extruder Film Samples 68
3.5 Plasticizer Inclusion's Chemical Structure and Mechanical Behavior 71
3.6 Conclusion 76
4 Structure Evolution with Strain 78
4.1 Introduction 78
4.2 Deformation Mechanisms of Plasticized Polylactide 83
4.2.1 Processing 83
4.2.2 Mechanical Investigation 83
4.2.3 Crystallinity Investigation 87
4.2.4 Morphological Investigation 92
4.3 Deformation Heterogeneities in PLA-Based Materials at Room Temperature 95
4.3.1 Processing 95
4.3.2 Characterization of the As-Processed Materials 95
4.3.3 Multiscale Analysis of the Deformation Heterogeneities in Polylactide 96
4.3.4 Influence of the Initial Crystallinity on Polylactide's Deformation Heterogeneities. 101
4.3.5 Influence of the Plasticization on Polylactides's Deformation Heterogeneities 105
4.3.6 Deformation Heterogeneities Related to the Initial Structure 110
4.4 Impact of Deformation on the Inclusion's Structure 113
4.4.1 Processing 113
4.4.2 Inclusion's Chemical Structure after Deformation 113

4.4.3 Inclusion's Structure Model 116
4.5 Conclusion 117
5 Structure Evolution with Reprocessing 119
5.1 Introduction 119
5.2 Thermomechanical Degradation of Plasticized Polylactide After Reprocessing 122
5.2.1 Processing 122
5.2.2 Influence of the Reprocessing on the Macroscopic Behavior 123
5.2.3 Influence of the Reprocessing on the Microstructure 130
5.2.4 Influence of the Reprocessing on the Molecular Structure 132
5.2.5 Degradation Scheme of Plasticized Polylactide 138
5.3 Comparison between Different Thermomechanical Reprocessing Cycles 140
5.4 Isothermal Crystallization of Reprocessed Plasticized Polylactide 143
5.5 Conclusion 150
6 General Conclusions and Perspectives 153
7 List of References 156
Appendix 167
A Experimental Section 167
A.1 Materials 167
A.2 Processing Equipment 167
A.2.1 Micro-Compounder 167
A.2.2 Mini-Extruder 167
A.2.3 Compression Molding 168
A.2.4 Injection Molding 168
A.3 Characterization Methods for Chapter 3: Process-Structure Relationship 169
A.3.1 Processing in the Micro-Compounder 169
A.3.2 Processing in the Mini-Extruder 169
A.3.3 Soxhlet Extraction 170
A.3.4 Gel Permeation Chromatography 172

A.3.5 Swelling Tests in Chloroform 172
A.3.6 Differential Scanning Calorimetry 172
A.3.7 Atomic Force Microscope 173
A.3.8 Impact testing 174
A.3.9 Isothermal Crystallization Measured by Wide-Angle X-ray Scattering 174
A.3.10 Atomic Force Microscope Analysis of Film samples 177
A.3.11 Scanning Transmission X-ray Microscope 178
A.4 Characterization Methods for Chapter 4: Structure Evolution with Strain 179
A.4.1 Processing of the Materials 179
A.4.2 Tensile Testing 181
A.4.3 Wide-Angle X-ray Scattering 182
A.4.4 Differential Scanning Calorimetry 185
A.4.5 Scanning Electron Microscopy 186
A.4.6 Time-Resolved Small-Angle X-ray Scattering 186
A.4.7 Optical Microscope Analysis 187
A.4.8 Digital Image Correlation 188
A.4.9 Micro-Compounded X-ray Tomography 191
A.5 Characterization Methods for Chapter 5: Structure Evolution with Reprocessing 191
A.5.1 Processing and Reprocessing 191
A.5.2 Dynamic Mechanical Analysis 192
A.5.3 Tensile Testing 193
A.5.4 Impact Testing 193
A.5.5 Differential Scanning Calorimetry 193
A.5.6 Scanning Electron Microscope 194
A.5.7 Atomic Force Microscope 194
A.5.8 Gel Permeation Chromatography 194
A.5.9 Fourier Transform Infrared Spectroscopy 195
A.5.10 Nuclear Magnetic Resonance Spectroscopy 195

A.5.11 Rheology Measurements 196

A.5.12 Soxhlet Extraction 196

A.5.13 Isothermal Crystallization Process 196

B Limonene and Myrcene as New Plasticizers for Polylactide 197

B.1 Introduction 197

B.2 Plasticization by (Reactive) Extrusion 198

B.3 Mechanical Investigation 199

B.4 Thermal Properties 201

B.5 Conclusion & Outlook 203

I. List of Abbreviations

A	**acrylPEG**	poly(ethylene glycol) methyl ether acrylate
	AFM	atomic force microscope
	AP	acidification potential
	APA	Environmental Protection Agency
	aS	after Soxhlet extraction
B	**BPA**	bisphenol A
C	**CI**	crystallinity Index
	CM	compression molding
D	**DCP**	dicumyl peroxide
	DIC	digital image correlation
	DMA	dynamic mechanical analysis
	DSC	differential scanning calorimeter
E	**E**	extrusion
	EFSA	European Food Safety Authority
	EP	eutrophication potential
	EPA	Environmental Protection Agency
	EU	European Union
F	**FDA**	Food and Drug Administration
	FTIR	Fourier transformed infrared
G	**GPC**	gel permeation chromatography
	GWP	global warming potential
H	**HDPE**	high-density poly(ethylene)
I	**IM**	injection molding
	ISO	Organization for Standardization
L	**L101 or Luperox**	2,5-Bis(*tert*-butylperoxy)-2,5-dimethylhexane (initiator)
	LCA	life cycle assessment
	LDPE	low-density poly(ethylene)
	LVDT	linear variable differential transformer
M	**MA**	maleic anhydride
	MAPEG	methyl ether acrylate
	µCT	micro-computed X-ray tomography
N	**NEXAFS**	near edge X-ray absorption fine structure
	NMR	nuclear magnetic resonance
	NREU	nonrenewable energy use
O	**OLA**	oligomeric lactic acid
	OM	optical microscope

P	**PA**	poly(amide)
	PBAT	poly(buthyrate)
	PBS	poly(buthylene succinate)
	PC	poly(carbonate)
	PCL	poly(ε-caprolactone)
	PDLA	poly(D-lactic-acid)
	PE	poly(ethylene)
	PEF	poly(ethylene furanoate)
	PEG	poly(ethylene glycol)
	PET	poly(ethylene terephthalate)
	PHA	poly(hydroxyalkanoates)
	PLA	poly(lactide) or poly(lactic acid)
	PLLA	poly(L-lactic acid)
	poly(acrylPEG)	polymerized acrylPEG
	PP	poly(propylene)
	PPG	poly(propylene glycol)
	pPLA	plasticized PLA composition PLA/acrylPEG/L101 79/20/1 (wt%)
	PS	poly(styrene)
	PUR	poly(urethane)
	PVC	poly(vinyl chloride)
R	**RIC**	resin identification code
	ROP	ring opening polymerization
	RT	room temperature
S	**SAXS**	small-angle X-ray scattering
	SEM	scanning electron microscope
	SPI	Society of the Plastic Industry
	STXM	scanning transmission X-ray microscopy
T	**TBC**	tributyl citrate
	THF	tetrahydrofuran
	TMS	tetramethylsilane
	TPP	triphenyl phosphate
	TPS	thermoplastic starch
W	**WAXS**	wide-angle X-ray scattering
X	**XRD**	X-ray diffraction

II. List of Symbols

$Đ$	polydispersity index
E	tensile modulus
k	Boltzman constant
$\overline{M_n}$	number average molar weight
$\overline{M_w}$	mass average molar weight
ν	Poisson coefficient
$t_{1/2}$	half-time crystallization
T_c	crystallization temperature
T_{cc}	cold crystallization temperature
T_d	drawing temperature
T_g	glass transition temperature
T_m	melting temperature
V_{flow}	plastic flow activation volume
X_c	crystallinity index
X_{meso}	crystallinity index of meso phase
ΔH_{cc}	cold crystallization enthalpy
ΔH_m	melting enthalpy (of the crystalline phase)
$\Delta H_{m,0}$	melting enthalpy of a 100% crystalline polymer
ΔH_{meso}	melting enthalpy of the meso-phase
$\Delta H_{meso,0}$	melting enthalpy of a 100% meso-phase
ε_{11}	axial strain
ε_{22}, ε_{33}	transversal strains
ε_{eng}	engineering strain
ε_{true}	true strain
ε_u	ultimate strain/strain at break
ε_v	volume strain
$\dot{\varepsilon}$	strain rate
σ_{eng}	engineering stress
σ_{true}	true stress
σ_u	ultimate stress/stress at break
σ_y	yield stress

III. List of Figures

Figure 2.1 Beneficial plastic applications in the everyday life (left) and in medicine as an implant (middle), but resulting pollution (right). 6

Figure 2.2 Municipal waste recycling rates of 35 European countries in 2004 and 2014 [5]. 8

Figure 2.3 Global production capacities of bioplastics in 2016 and 2021 [8]. 10

Figure 2.4 Synthesis routes for high molecular weight PLA adapted from Hartmann [12]. 11

Figure 2.5 Chemical structures of the monomers for PLA synthesis. 14

Figure 2.6 Schematic diagram of the plasticization process in a polymer. 19

Figure 2.7 Evolution of the tensile modulus and impact toughness in PLA/PCL blends with different compositions [39]. 20

Figure 2.8 PLA plasticized with different molecular weight PEG: (a) DSC curves and (b) mechanical parameters [43]. 21

Figure 2.9 Mechanisms of acrylPEG grafting onto PLA backbone adapted from Kfoury et al. and Choi et al. [41,51]. 23

Figure 2.10 Tensile behavior of PEG-plasticized PLA by reactive extrusion at (a) different plasticizer concentrations [51] and (b) different initiator concentrations [52]. 24

Figure 2.11 Schematic structure of plasticized PLA by blending with MAPEG or AcrylPEG (left), by reactive extrusion with MAPEG (middle) or acrylPEG (right) [41]. 26

Figure 2.12 Growth rate of crystallization as a function of the temperature for PEG/PLA blends [59]. 27

Figure 2.13 Half-time crystallization as function of the crystallization temperature for a PLA with 96% L-lactide (PLA), a mixture of branched and comb-like PLA with D-sorbitol and PEG (LCB P-D/P1), and PLA plasticized with PEG (P-PEG) plotted with the data from You et al.[66]. 28

Figure 2.14 Schematic diagram of the various deformation mechanisms operative in a semicrystalline polymer: (a) interlamellar separation, (b) lamellar stack rotation, (c) interlamellar shear, (d) intracrystalline shear 'fine chain slip', (e) intracrystalline shear 'coarse chain slip' [71]. Deformation above T_g. 30

Figure 2.15 Schematic diagram for the cavitation in a semicrystalline polymer [71]. Deformation below T_g. 30

Figure 2.16 Schematic evolution of amorphous PLA with increasing strain above the T_g [72]. 31

Figure 2.17 Deformation mechanisms of annealed PLA at temperatures slightly and far above Tg [75]. 32

Figure 2.18 Schematic representation of the chronological occurrence of plastic deformation mechanisms during drawing of PLA below glass transition temperature (tensile axis is assumed equatorial) with: (a) nucleation of the shear bands, (b) shear band propagation and simultaneous opening into shear band crazes, (c) orientation of the "shear band crazes" towards the drawaxis and formation of intersections, (d) Nucleation of "standard crazes" both at "shear band crazes" intersections & into the matrix, (e) "standard craze stabilization" by the shear band and "shear band crazes" [55]. 33

Figure 2.19 SEM micrographs showing the surface of the gauge section of PLA specimen drawn to the strains of (a) 0.05, (b) 0.10, and (c) 0.30 [80]. Strain direction vertical. 34

Figure 2.20 SEM micrographs showing the surface of the gauge section of PLA blended with natural rubber specimen drawn to strains of (a) 0.05, (b) 0.10, and (c) 1.00 [80]. Strain direction vertical. 34
Figure 2.21 SEM micrographs of the gauge region of PLA/natural rubber blend strained to 1.0 and cryo-fractured parallel to the drawing direction (vertical) [80]. 35
Figure 2.22 SEM micrograph of the gauge region of PLA/copolyester blend strained to 3.3 and cryo-fractured parallel to the drawing direction (vertical) [81]. 35
Figure 2.23 SEM images on cryo-fractured surfaces in the direction of tensile drawing of (a) PLA/acrylPEG/L101 and (b) PLA/poly(acrylPEG) [50]. 36
Figure 2.24 Biodegradation process of a bottle made of PLA [84]. 37
Figure 2.25 Summary of possible degradation mechanisms in PLA [92]. 39
Figure 2.26 Evaluation of mechanical properties after up to 10 extrusions: (a) representative tensile testing curves for the neat material and after 10 extrusions and (b) impact strength as function of the extrusion number [87]. 39
Figure 3.1 Recorded forces during the (reactive) blending of the materials for the structural analysis of pPLA. 49
Figure 3.2 DSC curves of the samples for pPLA structural analysis from the (a) cooling stage and (b) first (dashed line) and second (continuous line) heating stage. 54
Figure 3.3 AFM height images and stiffness analysis of (a) pPLA, (b) PLA/acrylPEG, and (c) pPLA aS. 55
Figure 3.4 Stiffness values of the matrix and the inclusions for pPLA, PLA/acrylPEG, and pPLA aS from AFM stiffness analysis. 56
Figure 3.5 Impact resistance and crystallinity from DSC second heating stage of PLA-based materials for the pPLA structural analysis. 57
Figure 3.6 Evolution of crystallinity index as a function of time during isothermal crystallization at different temperatures for (a) PLA and (b) pPLA. 58
Figure 3.7 AFM topography images of (a) pPLA as processes, (b) pPLA and (c) PLA after isothermal crystallization at 55°C and 90°C respectively. 61
Figure 3.8 Evolution of crystallinity index as a function of time during isothermal crystallization testing at (a) 90°C and (b) 55°C for modified PLA materials. 62
Figure 3.9 DSC curves of pPLA from the micro-compounder compared to the mini-extruder. Data from second heating stage. 66
Figure 3.10 DSC curves of film samples from the mini-extruder pPLA-film, PLA/acrylPEG-film, and PLA-film for (a) the first (dashed line) and second (continuous line) heating stage and (b) the cooling stage. 68
Figure 3.11 a) C1s NEXAFS spectrum of pPLA inclusion compared to that of pPLA matrix (with the corresponding chemical structures), and b) C1s NEXAFS spectra of pPLA matrix, PLA/acrylPEG matrix, neat PLA, pPLA inclusion, and neat poly(acrylPEG). All the spectra were extracted and reduced from STXM micrographs. 1: C1s → $\pi^*_{(C=O)}$ of the pPLA matrix, 2: C1s → C-H Rydberg of the of the pPLA matrix, 3: C1s → $\pi^*_{(C-H)}$ of the pPLA inclusion, and 4: C1s → $\sigma^*_{(C-O)}$ of the pPLA inclusion. 72

Figure 3.12 Composition maps obtained from STXM micrographs of pPLA indicating the present amount of PLA (a, c, and e), and poly(acrylPEG) (b, d, and f). Images a) to d) represented the same area at different magnifications, while images e) and f) were taken in another area of interest. 1: PLA-rich domains inside the inclusion, 2: poly(acrylPEG)-rich domains at the inclusion shell, and 3: poly(acrylPEG)-rich domains at the inclusion core. 73

Figure 3.13 AFM investigation of PLA (a and b), pPLA (c and d), and PLA/acrylPEG (e and f) with topographical contrast mode (a, c, and e), and modulus contrast mode (b, d, and f). The circles and squares represented the areas where elastic modulus was calculated. 75

Figure 4.1 Influence of (a) the temperature at 4×10^{-2} s^{-1} and of (b) the strain rate at 20°C on the tensile behavior of pPLA including a zoom-in view of the initial part of the curves (some reference curves of PLA were also plotted for comparison). 84

Figure 4.2 Optical microscope images of pPLA deformed in tension at 20°C showing (a) the effect of strain level at 4×10^{-4} s^{-1}, (b) the effect of strain rate at the strain level of 150%, and (c) the effect of relaxation after one week. The images were recorded at the center of the specimen. 85

Figure 4.3 DSC curves of (a) undeformed PLA and undeformed pPLA, as well as pPLA deformed at 20°C to a strain level of 100% for various strain rates, and (b) pPLA and PLA deformed at 50°C to a strain level of 300°C for various strain rates. 88

Figure 4.4 WAXS diagram deconvolution of a) PLA and b) pPLA at the undeformed state exhibiting in the two cases three amorphous halos at 2θ = 15.0°, 21.2°, and 31.0° and in the case of pPLA four crystalline peaks at 2 θ = 14.6°, 16.5°, 18.8°, and 22.2° engendered by the (010), (110/200), (203) and (210) reflections, respectively. 89

Figure 4.5 WAXS investigation of pPLA showing the evolution of the orientation function of the three amorphous halos (references 1 to 3), and of the two main crystalline peaks (reference (110/200) and (203)) on the LHS axis, and of the crystallinity on the RHS axis, as a function of strain. Tensile testing was conducted at different temperatures (20°C (A to C), 50°C (D to F), and 80°C (G to I)) and different strain rates (4×10^{-4} s^{-1} (A, D, and G), 4×10^{-3} s^{-1} (B, E, and H), and 4×10^{-2} s^{-1} (C, F, and I)). 91

Figure 4.6 WAXS investigation of PLA showing the evolution of the orientation function of the three amorphous halos (references 1 to 3), of the mesophase peak (reference meso, just at 50°C) and of the two main crystalline peaks (reference (110/200) and (203), just at 80°C) on the LHS axis, and of the crystallinity on the RHS axis, as a function of strain. Tensile testing was conducted at different temperatures (50°C (A to C), and 80°C (D to F)) and different strain rates ((4×10^{-4} s^{-1} (A and D), 4×10^{-3} s^{-1} (B and E), and 4×10^{-2} s^{-1} (C and F)). At 50°C, the crystallinity based on the mesophase peak. 92

Figure 4.7 SEM observation with the LFD mode of deformed (a) PLA (strain of 298% obtained at 50°C with a strain rate of 4×10^{-2} s^{-1}) and (b) pPLA (strain of 165% obtained at 20°C with a strain rate of 4×10^{-2} s^{-1}). 1: primary cavities containing a secondary cavity, 2: secondary cavities, and 3: drawn poly(acrylPEG) micron inclusions. 93

Figure 4.8 STEM observation of (a) undeformed pPLA and (b) deformed pPLA (strain of 165% obtained at 20°C with a strain rate of 4×10^{-2} s^{-1}). 1: initial poly(acrylPEG) inclusions with high density, 2: drawn poly(acrylPEG) micron inclusions with decreased density. 94

Figure 4.9 (a) Engineering stress-strain curve of PLA with the corresponding integrated scattering intensities for the meridian and equatorial scattering signal. The letters close to the curve correspond to the scattering images on the right (b-g). The tensile axis was vertical and the beam center was close to the image center. 98

Figure 4.10 (a) The engineering stress-strain curve of PLA related to the optical microscope images at the defined time intervals. The tensile axis was vertical in the images. 99

Figure 4.11 (a) True stress-strain tensile curve of PLA and (b) correlated plots of volume strain (LHA) and transversal strain (RHA) as a function of the axial strain. The dotted line separates the elastic regime (low strains) and the plastic regime (high strains). 100

Figure 4.12 Stress-strain curve of PLA-IC with the corresponding integrated scattering intensities for the meridian and equatorial scattering signal. The letters close to the curve correspond to the scattering images at the defined time intervals. The tensile axis was vertical and the beam center was close to the center. 102

Figure 4.13 (a) Engineering stress-strain curve for a representative PLA-IC sample and PLA as a reference sample. The letters (b to e) mark the stage of the optical microscope images of PLA-IC. The right hand axis shows the area of voids compared for PLA-IC and PLA. The tensile axis was vertical. 104

Figure 4.14 (a) true stress-strain tensile curve of PLA-IC and (b) correlated plots of volume strain and transversal strain vs the axial strain. 104

Figure 4.15 SAXS scattering images for pPLA (a-c) and PLA/acrylPEG (d to f) in the defined time intervals. The tensile axis was meridian and the beam center was close to the image center. The scattering intensities of pPLA (red) and PLA/acrylPEG (blue) for the meridian and equatorial scattering are displayed in graph (g). 106

Figure 4.16 Optical microscope images during tensile deformation of PLA/acrylPEG. Images after defined time intervals. The tensile axis was vertical. 107

Figure 4.17 Optical microscope images during tensile deformation of pPLA. Images after defined time intervals. The tensile axis was vertical. 107

Figure 4.18 (a) true stress-strain tensile curve of pPLA and PLA/acrylPEG, and (b) correlated plots of volume strain and transversal strain vs the axial strain. 109

Figure 4.19 DIC true strain fields for the plasticized materials: (a) pPLA and (b) PLA/acrylPEG at the same true strain value of 0.2 and comparison of the true strain profiles along with the drawing axis at true strain values of 0 and 0.2. 110

Figure 4.20 Tensile specimen of PLA-based materials with a corresponding zoomed view of the deformation section showing the deformation heterogeneities. 112

Figure 4.21 Composition maps obtained from STXM micrographs of pPLA at a strain level of 12% indicating the present amount of a) PLA at 288.5 eV, and b) poly(acrylPEG) at 289.7 eV in a first area, and c) PLA

at 288.5 eV in a second area. Tensile axis is diagonal (about 45° diagonally from the upper left to lower right). 1: submicron crack at the vicinity of inclusions of plasticizer, and 2: submicron crack originated from one inclusion and propagating to a neighboring inclusion. 114
Figure 4.22 a) Picture of a drawn tensile sample of pPLA at a strain of 12% with the two areas marked for the 2D µCT images recorded in b) a undeformed or little deformed area, and c) the most deformed area (both µCT images were recorded with a spatial resolution of about 1 µm and 0.3 µm of voxel size). Tensile axis is vertical. 1: inclusion without density contrast, 2: inclusion with a density contrast indicating the presence of the shell. 115
Figure 4.23 Schematic representation of pPLA inclusion structure a) prior drawing showing the core-shell morphology and b) after drawing characterized by a marked decrease of the density of the inclusion core as well as inclusion shell and by the formation of cracks bridging the inclusions. 116
Figure 5.1 Schematic processing and reprocessing procedures of (p)PLA including images of the extruded rods and the compression molded plates for the (p)PLA materials. 123
Figure 5.2 DMA analysis of PLA and pPLA after 1,3, and 5 processing cycles in the temperature range from -100°C to 120°C at 5Hz with some high temperature close-in views: a) storage modulus E', and b) loss factor tan δ. 124
Figure 5.3 Influence of the recycling on the tensile curves of pPLA and PLA as reference obtained at 50°C - a zoom-in view is made for the initial part of the curves. 127
Figure 5.4 Representative DSC curves of a) PLA and b) pPLA after 1, 3, and 5 processing. 128
Figure 5.5 SEM images of pPLA after a) 1, b) 3, and c) 5 processing cycles. 130
Figure 5.6 AFM phase images of pPLA inclusions: a) initial inclusions in pPLA CM1, b) slightly deformed inclusion with porosity in pPLA CM3, and c) strongly deformed inclusion with fibrillation and high porosity in pPLA CM5 (inclusions were surrounded on each image). 131
Figure 5.7 FTIR spectra of pPLA after 1, 3, and 5 processing cycles. 134
Figure 5.8 Viscosity measurements in dependency on the frequency for PLA and pPLA after 1, 3, and 5 processing cycles. 135
Figure 5.9 GPC of soluble fraction after Soxhlet extraction from methanol. 138
Figure 5.10 Schematic degradation scenario of pPLA after 1, 3, and 5 processing cycles. 139
Figure 5.11 Schematic presentation of the three different reprocessing procedures: (a) extrusion and compression molding (CM), (b) just extrusion (E), and (c) extrusion and injection molding (IM). 140
Figure 5.12 Average molecular weights for the main PLA peak in PLA and pPLA for the three different reprocessing cycles: CM, E, and IM. 142
Figure 5.13 Engineering stress-strain curves of PLA and pPLA after 1,3, and 5 reprocessing cycles at 20°C. . 143
Figure 5.14 Evolution of crystallinity index as a function of time during isothermal crystallization testing a) at 90°C for PLA and b) 55°C for pPLA after 1, 3, and 5 processing cycles. 145
Figure 5.15 Experimental (dots) and Carreau-Yasuada theoretical (lines) plots of the complex viscosity vs. the shear rate in the case of PLA and pPLA. 146

Figure 5.16 DSC curves (from the second heating stage) of PLA and pPLA from the IM-cycle after 1,3, and 5 reprocessing steps. 148

Figure A. 1 Experimental set-up for the Soxhlet extrusion. 170

Figure A. 2 WAXS diagram deconvolution of a) PLA and b) pPLA at the undeformed state exhibiting in the two cases three amorphous halos at 2θ = 15.0°, 21.2°, and 31.0° and in the case of pPLA four crystalline peaks at 2 θ = 14.6°, 16.5°, 18.8°, and 22.2° engendered by the (010), (110/200), (203) and (210) reflections, respectively. 185

Figure A. 3 Equatorial (transverse the tensile axis) and (b) meridian (along the tensile axis) masks on a SAXS pattern for the integration of the scattering intensity. Both masks have an angle of 45°. The tensile axis was vertical. 187

Figure A. 4 Processing and reprocessing procedures of (p)PLA including the main experimental conditions. 192

Figure B. 1 Chemical structures of the two plasticizers a) limonene and b) myrcene. 197

Figure B. 2 Extrusion force curves for the non-reactive and reactive blending with a) limonene and b) myrcene. 199

Figure B. 3 Engineering stress-strain curves for limonene- and myrcene-plasticized materials. 200

Figure B. 4 DSC curves of limonene- and myrcene-plasticized materials for a) the first (dashed line) and second (continuous line) heating and b) the cooling stages. 203

IV. List of Tables

Table 2.1 Resin identification code (RIC) for plastic materials and examples of use. 15

Table 2.2 Properties of PLA compared to PET and PS in packaging applications. 17

Table 2.3 Glass transition temperature and mechanical properties of PLA and plasticized PLA materials: PLA with 10% PEG plasticizer (PLA+10%PEG) and PLA with 10% PLA where MA was grafted and 10%PEG (PLA + 10%MA-g-PLA+10%PEG) [49]. 22

Table 3.1 Comparison of the parameters for the efficiency of plasticization: elongation at break, toughness, glass transition temperature and crystallinity for PLA/acrylPEG/initiator materials after blending and reactive blending. Data from Kfoury et al. [41,50] and Choi et al.[52]. 44

Table 3.2 Sample names, description, and their composition for pPLA structural analysis. 47

Table 3.3 Summary of the swelling test and GPC results of the materials for the structural analysis of pPLA. 50

Table 3.4 Thermal parameters of the samples for pPLA structural analysis determined by DSC measurements from the first heating stage (1), the cooling stage (2) and the second heating stage (3). 53

Table 3.5 Crystallization data extracted from experimental curves and Avrami modelling for PLA and pPLA crystallized at different temperatures. 60

Table 3.6 Final crystallinity and half-time crystallization determined from isothermal crystallization for PLA-based materials at different temperatures and Avrami parameters. 63

Table 3.7 Characterizing parameters for the micro-compounder and the mini-extruder in comparison. 65

Table 3.8 DSC and GPC analysis of pPLA from the micro-compounder compared to the mini-extruder. DSC data from second heating. 67

Table 3.9 Thermal parameters of the film samples from the mini-extruder determined by DSC measurements from the first heating stage (1), the cooling stage (2) and the second heating stage (3). 69

Table 3.10 GPC analysis for the main PLA peak of pPLA-film, PLA/acrylPEG-film and PLA-film samples. 70

Table 3.11 Comparison of the thermal parameters and the molecular weight for pPLA produced with the micro-compounder and pPLA-film produced with the mini-extruder. 70

Table 3.12 Average elastic modulus of the matrix and inclusion calculated by AFM for PLA, PLA/acrylPEG, and pPLA (with standard deviations). 75

Table 4.1 Tensile modulus E, yield stress σy, elongation at break ϵu, and ultimate stress σu of PLA and pPLA as a function of the temperature and strain rate extracted from tensile testing curves and yielding activation volume determined from Eyring equation (n.m. stands for not measurable). 85

Table 4.2 Initial properties of the as-processed materials: the processing treatment, crystallinity (Xc) and glass transition temperature (T_g) determined from DSC measurement, and qualitative information about crosslinking an grafting. 96

Table 5.1 Mechanical parameters with standard deviation obtained from tensile testing at 20°C, 50°C and 80°C, and impact testing for pPLA and PLA as reference (n.t. stands for not tested, n.m. stands for not

measurable, no b.p. stands for no breaking point at the maximum cross-head displacement of the tensile machine). 126
Table 5.2 Data from DSC measurements with standard deviation. 128
Table 5.3 Molecular weight (M_w) and dispersity (Đ) for PLA after 1, 3, and 5 processing from GPC with polystyrene standard. 133
Table 5.4 Chain scission number for PLA calculated with molecular weight from GPC and chain scission values for PLA and pPLA calculated with the viscosity from rheology measurements at 1Hz and an optimized value a = 2.9. 136
Table 5.5 Extracted fraction EF (in wt%) for PLA and pPLA after Soxhlet extraction from methanol. 137
Table 5.6 PLA Recycling of PLA-based samples: molecular weight of the main PLA peak. 141
Table 5.7 Mechanical parameters elongation at yield (εy), stress at yield (σy), elongation at break (εu), and stress at break (σu) with standard deviation obtained from tensile testing at 20°C. 144
Table 5.8 Crystallization data extracted from experimental curves and Avrami modelling for PLA crystallized at 90°C and pPLA crystallized at 55°C after 1, 3, and 5 processing cycles. 145
Table 5.9 Molecular weights determined by GPC and zero shear viscosity by rheology for PLA and pPLA of the IM-cycle after 1,3, and 5 processing steps. 147
Table 5.10 DSC results (from the second heating stage) for the samples of PLA and pPLA from the IM-cycle with standard deviation. 148
Table 5.11 Amount of PEG in the pPLA samples from the IM-cycle (by proton NMR) and non-grafted amount of PEG (by Soxhlet). 149

Table A. 1 Composition of materials for pPLA structural analysis. 169
Table A. 2 Processing parameters of plasticized PLA samples and film samples produced with the mini-extruder. 170
Table A. 3 List of the materials that were used in chapter 4 with the reference to section where the processing was described. 179

Table B. 1 Mechanical parameters for limonene- and myrcene plasticized materials compared to PLA. 200
Table B. 2 DSC parameters for limonene- and myrcene-plasticized materials compared to PLA. 202

V. Abstract

Plastic materials are essential to our current way of life. Since they are cheap, light in weight and easy to produce, they replaced other materials like wood, glass, or ceramic in many application fields. Despite these advantages, plastic materials came under criticism due to an extensive plastic consumption and two main drawbacks became apparent. Plastics are made from petrol, which is considered as a nonrenewable resource and the long lifespan of plastic in the environment causes increasing pollution. Bioplastics were developed to overcome these disadvantages of common plastic materials without losing their practical side. Bioplastics are polymer materials that are either bio-based or biodegradable or even both. Bio-based polymers allow the production of the common plastic materials from renewable sources, and biodegradable polymers aim at the end-of-life problematic of plastics. Materials with these properties afford the production of petrol-independent and more environmental-friendly plastics. Especially for packing applications, where the application time is normally much shorter than the lifetime, biopolymers promise to be a good alternative.

Among these biopolymers, polylactide (PLA) is one of the most attractive materials, since it fulfills both criteria of being a bioplastic: it is bio-based and (bio)degradable. Due to its comparable mechanical performance to poly(ethylene terephthalate) (PET) or poly(styrene) (PS), PLA was considered for short-time applications, such as packaging, but also for long-time applications in the automotive industry or electronics. Despite its (bio)degradability, PLA is investigated for these long-time applications, meaning that it could be stable enough to be recycled by reprocessing and reused as other plastics. Such end-of-life scenarios have not been extensively studied in the case of PLA.

At room temperature, PLA is brittle and requires plasticization to further broaden its application range. Conventional plasticization by blending is suboptimal: Small plasticizer molecules with a high mobility cause leaching with time and bigger molecules offer a lower miscibility and cause phase separation. In addition, on one hand, plasticization increases the ductility, but, on the other hand, the material loses stiffness and often rubber-like materials are formed. The methodology of reactive extrusion was developed as a strong tool to obtain a material with a good ductility-stiffness balance. The structure of PLA plasticized by reactive extrusion has not been investigated in details, resulting in a limited knowledge about the thermomechanical behavior of this material.

This thesis aimed at carefully analyzing the structure of plasticized PLA by a multiscale approach and to study the evolution of the structure during thermomechanical transformations. The latter relied on studying deformation mechanisms of the materials upon drawing, and on studying degradation mechanisms of the materials during simulated thermomechanical recycling procedures. The release

of new knowledge concerning the process – structure – thermomechanical behavior relationships of plasticized PLA may enable to improve its performance and recyclability.

The reactive extrusion of PLA with a radical initiator and the reactive plasticizer poly(ethylene glycol) methyl ether acrylate (acrylPEG) yielded a plasticized PLA (pPLA) with particular structural elements. The plasticizer formed partially grafted and partially free inclusions and the radical recombination reactions or the grafting of plasticizer inclusions onto two PLA chains induced a slight crosslinking of the PLA matrix. The impact of these structural elements on the thermal properties as well as on the mechanical properties was analyzed. It was shown that the formed inclusions exhibit a core-shell structure with a poly(acrylPEG)-rich shell and a less poly(acrylPEG)-rich core. The non-grafted part of plasticizer decreased the glass transition temperature and increased, therefore, the crystallization ability and the impact toughness while the grafted part and the crosslinking conserved the material's stiffness partially. Nevertheless, the radical process of inclusion formation was hard to control and depending on the processing, pPLA offered slightly different properties.

The multiscale analysis of pPLA's deformation mechanisms showed that in pPLA like in PLA, the tensile deformation induced an ordering of the amorphous chains. At the same time, the formation of new crystals was in competition with the breaking of initial crystals resulting from shearing and fragmentation. These transformations were dependent on the temperature and strain rate. When deformed, the inclusions were elongated in the tensile direction with an internal decrease of the density in the core and shell regions. Deformation heterogeneities were observed in PLA and pPLA. Indeed, for PLA, marked crazing was noted at room temperature explaining the low ductility of this material, while in pPLA, shear banding and localized submicron cracks originated by the inclusions were noted. Such deformation heterogeneities in pPLA were induced by the grafting and/or crosslinking but were not detrimental for its ductility.

When simulating thermomechanical recycling of PLA, the main degradation mechanism is based on simple chain breaking reactions proved by a decrease of molecular weight. It was shown that the thermomechanical process during the reprocessing is crucial for pPLA's degradation and was related to the time, which the material remained in the melted state. Depending on the thermomechanical steps, pPLA became brittle after three processing cycles and was not reusable due to the detrimental degradation or pPLA underwent five processing cycles without losing the mechanical performance despite an important decrease of viscosity. The origin of the brittleness was attributed to the damage of the inclusion structure and to the formation of cracks. At the same time, the crosslinking and grafting survived the thermomechanical reprocessing.

This thesis released new characterization methodologies, enabling a better identification of biopolymer structural features. In the case of plasticized PLA, such methodologies show that this material has a promising thermomechanical behavior with limited damage mechanisms, but its reprocessing in a suboptimal end-of-life scenario. The grafting and crosslinking, which are not controllable during the reactive extrusion, affect significantly the thermomechanical behavior of plasticized PLA and should be further investigated.

VI. Resumé

Les matières plastiques sont devenues essentielles à notre mode de vie. Cela s'explique notamment par leur faible coût, leur faible densité et leur facilité de mise en œuvre, leur ayant permis de remplacer certains matériaux traditionnels comme le bois, le verre ou la céramique dans de nombreuses applications de notre quotidien. Malgré ces avantages, les matières plastiques sont de plus en plus décriées, à cause notamment de leur utilisation intensive qui engendre actuellement de nombreux problèmes. En effet, la plupart des matières plastiques sont fabriquées à partir du pétrole qui est une source d'énergie non renouvelable. De ce fait, le prix des matières plastiques est lié à celui du pétrole et par conséquent leur coût de production peut fluctuer. Par ailleurs, la grande durée de vie des matières plastiques conduit à une pollution grandissante lorsqu'en fin de vie elles sont abandonnées dans l'environnement. Ces inconvénients ont alarmé la communauté scientifique afin de trouver des matériaux alternatifs à ces matières plastiques très abondantes.

Les bioplastiques ont ainsi été développés, afin de répondre aux problèmes liés aux matières plastiques conventionnelles, tout en conservant leurs aspects pratiques. Par définition, les bioplastiques sont des polymères pouvant être bio-basés et/ou biodégradables. Les polymères bio-basés sont issus de ressources renouvelables, tandis que les polymères biodégradables permettent un scénario de fin de vie favorable pour l'environnement sans libération de substances nocives. Ces nouvelles matières plastiques rendent possible une indépendance au pétrole et sont plus écologiques que les plastiques conventionnels qu'ils tentent de remplacer. Dans le cas de l'emballage, domaine où la durée de l'application est bien plus courte que la durée de vie des matières plastiques, les bioplastiques sont très prometteuses.

L'un des bioplastiques les plus prometteurs est sans nulle doute le polylactide (PLA) qui présente à la fois un caractère bio-basé et (bio)dégradable. Sa performance mécanique étant comparable à celle du poly(éthylène téréphtalate) (PET) ou du poly(styrène) (PS), le PLA peut être choisi pour des applications à court terme telles que l'emballage et pour des applications à long terme telles que l'automobile ou l'électronique. Malgré sa (bio)biodégradabilité, la stabilité du PLA est telle que ce matériau peut répondre au cahier des charges de ces applications à long terme. Il pourrait être ainsi recyclé thermomécaniquement et réutilisé comme la plupart de matières plastiques conventionnelles. Un tel scénario de fin de vie n'a été que très peu étudié dans la littérature.

A la température ambiante, le PLA est fragile et nécessite d'être plastifié pour optimiser sa performance mécanique. La plastification conventionnelle par mélange physique du PLA avec un plastifiant n'est pas une solution optimale. Plus précisément, dans le cas de plastifiants de faible masse moléculaire et de grande miscibilité avec le PLA, un phénomène de migration du plastifiant à la surface

du PLA a lieu avec le temps et s'explique par la grande mobilité du plastifiant. Quant aux plastifiants ayant une grande masse moléculaire, leur manque de miscibilité avec le PLA donne lieu localement à un phénomène de séparation de phase. Par ailleurs, si la plastification permet d'augmenter la ductilité du PLA, sa rigidité se retrouve fortement diminuée. Un comportement de type caoutchoutique est ainsi obtenu. Une nouvelle méthode de plastification a été récemment développée. Il s'agit de la plastification par extrusion réactive conduisant à un bon équilibre entre ductilité et rigidité. La structure du PLA plastifié par cette méthode n'a été que peu étudiée et par conséquent, son comportement thermomécanique n'est pas identifié de manière satisfaisante.

Cette thèse a pour objectifs d'analyser finement la structure du PLA plastifié par extrusion réactive selon une approche multi-échelles et d'étudier comment cette structure évolue au cours de transformations thermomécaniques. Le manuscrit est organisé suivant six parties. La première partie est l'introduction générale décrivant la problématique générale de ce travail. La deuxième partie est un état de l'art regroupant les informations les plus pertinentes au sujet des bioplastiques, du PLA en tant qu'alternative aux matières plastiques conventionnelles et les problématiques qui en découlent, de la plastification par extrusion réactive, et de la structure complexe du PLA plastifié comme préalablement établie. Puisque cette structure n'a été que partiellement élucidée, la troisième partie de ce manuscrit vise à étudier finement les relations élaboration – structure du PLA plastifié. La cinquième partie intitulée évolution de la structure au cours de la déformation, et la sixième partie intitulée évolution de la structure au cours du recyclage, se focalisent respectivement sur l'impact de l'étirage et du recyclage thermomécanique sur la structure du matériau. La sixième partie nommée conclusions générales et perspectives résume les résultats de ces travaux de recherche et identifie de nouvelles thématiques de recherche permettant d'accroître les chances d'utilisation du PLA en tant qu'alternative aux matières plastiques conventionnelles. Dans l'appendice A, une description détaillée des matériaux utilisés et des méthode d'analyse est exposée. Enfin, l'appendice B résume les résultats préliminaires obtenus lors de la plastification du PLA avec les plastifiants bio-basés limonène et myrcène, en termes de propriétés thermiques et mécaniques.

L'analyse de la structure du PLA plastifié a été réalisée dans le chapitre 3. Le mélange réactif du PLA avec l'acryPEG en tant que plastifiant et un initiateur radicalaire conduit à un PLA plastifié appelé pPLA possédant une structure unique. Afin de comprendre les différentes réactions induites par la plastification réactive et leur influence sur les propriétés du pPLA, différents systèmes ont été élaborés. En particulier, l'influence du plastifiant à l'état libre non-greffé (cas PLA/acrylPEG), du plastifiant polymérisé (cas PLA/poly(acrylPEG)), du plastifiant greffé (cas pPLA aS), et de l'initiateur

(cas PLA/L101) a été étudiée sur la structure finale. Cette dernière a été caractérisée par des tests de gonflage et par des analyses morphologiques. Les essais de gonflage ont mis en évidence la formation d'un gel dans le cas du pPLA et du PLA/L101 prouvant une faible réticulation dans ces matériaux. Par ailleurs, les analyses morphologiques ont indiqué la formation d'inclusions avec une grande rigidité dans le cas du pPLA et avec une rigidité plus faible dans le cas du PLA/acrylPEG. Dans le cas du pPLA, le plastifiant polymérise au cours de l'extrusion et il a été montré que la présence de poly(acrylPEG) augmente légèrement la résistance à l'impact du PLA, tandis que la présence d'acrylPEG libre ou l'ajout d'acrylPEG lors de l'extrusion réactive augmente fortement la résistance à l'impact du PLA. Quant au matériau PLA/L101, caractérisé par des mécanismes de greffage et de réticulation, sa résistance à l'impact est inférieure à celle du PLA de référence. En comparant les matériaux pPLA et PLA/acrylPEG, la présence de réticulations et greffages dans le pPLA conduit à une diminution de la résistance à l'impact par rapport au PLA/acrylPEG. Dans le pPLA, la présence de plastifiant libre augmentant la résistance à l'impact est en compétition avec la présence de réticulations/greffages/plastifiant polymérisé diminuant la résistance à l'impact. Comme autres propriétés structurales, les cinétiques de cristallisation des matériaux ont été mesurées. Le pPLA présente des vitesses de cristallisation supérieures à celles du PLA, ce résultat étant expliqué par une plus grande mobilité de chaîne après plastification. Toutefois, la présence de réticulations et de greffages dans la structure moléculaire du pPLA limite la croissance cristalline et limite ainsi le taux de cristallinité final par rapport au PLA. La structure originale du pPLA a pour effet une augmentation de la résistance à l'impact et accélère la cristallisation du PLA. L'application d'un matériau dépend non seulement des propriétés mécaniques mais aussi de la capacité de production. Dans ce contexte, une procédure de montée en échelle a été réalisée du procédé discontinu par batch à l'échelle laboratoire à un procédé continu avec une mini-extrudeuse à l'échelle pilote. A noter qu'à l'échelle pilote, l'injection des liquides n'a pas été possible en continu due à une limitation technique. L'utilisation de la mini-extrudeuse a conduit à une dégradation plus importante de la matrice PLA par rapport à la micro-extrudeuse, d'après des mesures de masses moléculaires. Cette dégradation est plus marquée lorsque la température et la vitesse de rotation des vis augmentent. Des films de pPLA, PLA/acrylPEG et PLA ont été produits avec la mini-extrudeuse équipée d'une filière spécifique. Si les films de PLA et de PLA/acrylPEG ont été fabriqués facilement, les films de pPLA ont nécessité plus de développements. En particulier, deux étapes ont été nécessaires : i) une première extrusion du pPLA en granulés a été réalisée (matériau pPLA-ME), et ii) une seconde extrusion du pPLA-ME pour donner des films de pPLA (matériau pPLA-film). Ces derniers ont un aspect proche du pPLA produit avec la micro-extrudeuse, mais présentent une rugosité indiquant une plus grande hétérogénéité par comparaison avec le pPLA. La formation d'inclusions de plastifiant polymérisé a été une nouvelle fois prouvée par une augmentation de la

rigidité locale par AFM. Ces inclusions présentent les mêmes caractéristiques que les inclusions se formant dans le pPLA. Enfin, la structure chimique des inclusions a été identifiée. Elle est semblable à celle du plastifiant polymérisé. Par ailleurs, les inclusions présentent une structure de peau différente de la structure du cœur. En particulier, la peau des inclusions est plus riche en poly(acrylPEG) que la structure chimique du cœur. L'origine précise de cet effet cœur/peau n'a pas été clarifiée, mais il a été supposé qu'après formation d'agglomérations de plastifiant, une forte réactivité est présente à l'interface matrice – inclusions. Ainsi, la polymérisation du plastifiant débute au niveau de la peau des inclusions, de même que le greffage et la réticulation. Ces mécanismes de greffage et de réticulation conduisent à une limitation de la polymérisation des inclusions laissant place à la structure cœur/peau. Ces résultats confirment que la structure du pPLA-film est similaire à celle du pPLA basée sur une matrice PLA contenant des inclusions de plastifiant polymérisé et partiellement greffé.

Le quatrième chapitre porte sur l'étude des mécanismes de déformation du pPLA et du PLA en traction. Il a été montré que ces mécanismes sont dépendant des conditions de déformation (température et vitesse de déformation). A une température élevée, les mécanismes de transformation de phase de la phase amorphe et cristalline sont prépondérants, tandis qu'à la température ambiante, l'endommagement est prépondérant. Il est important de mentionner qu'à la température ambiante le PLA est fragile, alors que le pPLA est ductile suite à la plastification ayant diminué la température de transition vitreuse. La comparaison entre les mécanismes de changement de phase aux différentes températures a montré que dans le cas du pPLA les mécanismes de formation de cristaux dus à l'orientation des chaînes amorphes et la destruction des cristaux initiaux due au cisaillement sont en compétition. Une compétition similaire a été notée dans le PLA pour une température proche de sa température de transition vitreuse. En général, lorsque la température augmente, la déformation conduit à une cristallinité de plus en plus importante, la mobilité moléculaire étant accentuée. Lorsque la vitesse de déformation diminue, la cristallisation induite par l'orientation des chaînes augmente, tandis qu'une augmentation de la vitesse de déformation ne favorise pas cette cristallisation, les molécules nécessitant un certain temps pour s'ordonner et former un nouveau cristal. L'étude morphologique a montré que les inclusions de poly(acrylPEG) se déforment dans la matrice polymère formant des ellipsoïdes dont le grand axe est orienté dans la direction de traction. Un phénomène de blanchiment est également noté dans le cas du PLA et du pPLA, ce phénomène étant relié à différents facteurs. Dans le PLA, ce blanchiment est permanent et s'explique par la formation de craquelures, leur extension conduisant ensuite à des cavités. Le blanchiment est alors dû à un phénomène de diffusion de la lumière par ces défauts. Quant aux films de PLA (PLA-film) et pPLA (pPLA-film), leur déformation à température ambiante est engendrée par différentes hétérogénéités de déformation. Ces dernières sont influencées par la cristallinité initiale

du PLA et le type de plastification. En particulier, des craquelures se forment également dans les films de PLA, donnant ensuite lieu à des cavités. Dans le cas des films de PLA ayant subi un recuit pour augmenter la cristallinité (PLA-IC), des cavités semblent se former directement, sans la phase de craquelures. Si dans le PLA les craquelures puis les cavités se propagent perpendiculairement à la direction de traction, un comportement différent est noté dans le cas du PLA-IC. En effet, les cavités dans ce matériau ont une forme de vague et se forment presque toutes en même temps et enfin grossissent. La fraction surfacique des cavités du PLA-IC est 1,5 fois plus importante que celle mesurée pour le PLA, et peut être reliée à la une plus grande densité de points de faiblesse après recuit. Dans le cas du PLA-film et du PLA-IC la déformation s'accompagne par une variation de volume très importante. Le matériau pPLA-film est beaucoup plus ductile que le PLA-film et PLA-IC, comme attendu avec la plastification. La détermination du coefficient D, en tant qu'indicateur de déformation à volume constant, confirme que le PLA/acrylPEG-film à un comportement caoutchoutique, tandis que le pPLA-film présente un comportement plus rigide que le PLA/acrylPEG-film, mais plus caoutchoutique que le PLA-film. Dans le cas du PLA/acrylPEG-film, aucune hétérogénéité de déformation n'a été observée, tandis que des cavités très localisées ont été notées dans le cas du pPLA-film. La présence de ces cavités est supposée être due aux greffages et aux réticulations dans le matériau. Le comportement en traction du pPLA-film et du PLA/acrylPEG-film à température ambiante est similaire à celui du PLA-film à une température proche ou au-dessus de sa transition vitreuse. En effet, la plastification conduit à une diminution de la température de transition vitreuse du PLA. Toutefois, la présence de réticulations et de greffages induit la formation d'un réseau moléculaire hétérogène, donnant lieu à une localisation de la déformation plus importante dans le pPLA-film par comparaison au PLA/acrylPEG-film. En conclusion, la cristallisation par recuit et la plastification par extrusion réactive empêchent la formation de craquelure, les hétérogénéités de déformation mettant principalement en jeu des cavités. Les inclusions de plastifiant dans le pPLA-film ont un impact sur la déformation du matériau. Ces inclusions ont une densité qui diminue avec la déformation comme l'a montré une analyse par tomographie aux rayons X. Par ailleurs, aucune décohésion inclusion-matrice n'a été constatée. Ainsi, les inclusions facilitent la plasticité du matériau et ce, sans donner lieu à de l'endommagement généralisé. Toutefois, à une échelle très locale, des fissures submicroniques ont été observées entre ces inclusions. Ces défauts ne semblent pas se propager dans tout le matériau mais restent localisées, ce qui permet de conclure que ces défauts ne sont pas préjudiciables pour la plasticité du pPLA-film.

Dans le cinquième chapitre, le recyclage thermomécanique du PLA et du pPLA a été étudié avec l'identification des mécanismes de dégradation sous-jacents. Il a été montré que la dégradation au cours des procédures de réélaboration dépend fortement du type de procédé utilisé. Dans la première

partie de cette étude, le procédé de compression à chaud a été utilisé dans les procédures de recyclage conduisant à une diminution drastique des propriétés mécaniques du pPLA. A noter qu'au cours de cette étude, les matériaux PLA et pPLA ont été analysés aux échelles macroscopique, microstructurale et moléculaire après 1, 3 et 5 cycles d'élaboration successifs. Dans le cas du PLA, où aucun greffage ni réticulation ne sont présents, le mécanisme de dégradation principal est un simple mécanisme de coupure aléatoire de chaînes. Ce mécanisme a été prouvé par une diminution de la masse moléculaire de 69% et 53% après respectivement le troisième et de cinquième cycle d'élaboration. La cristallisation froide est facilitée lorsque le nombre de cycle d'élaboration augmente, reflétant la diminution de la masse moléculaire et donc une mobilité moléculaire plus importante. Toutefois, le PLA reste amorphe quel que soit le nombre de cycle d'élaboration. L'analyse de la structure chimique indique aucun changement de fonction chimique (groupe de fin de chaîne) comparé au PLA non recyclé. En conclusion, dans le cas du PLA seul un mécanisme de coupure de chaîne est actif au cours de la réélaboration et est responsable de la diminution des propriétés mécanique de ce matériau. Dans le cas du pPLA, l'identification des mécanismes de dégradation nécessite une approche différente en se focalisant sur tous les composants structuraux de ce matériau qui peuvent interagir les uns avec les autres. D'un côté, les propriétés mécaniques chutent fortement entre le premier et le troisième cycle d'élaboration. En effet, le matériau devient fragile avec une forte diminution de la ductilité en traction et de la résistance à l'impact. D'un autre côté, les propriétés viscoélastiques telles que le module de conservation et le module de traction du pPLA ne varient pas avec le recyclage. La microstructure du matériau pPLA évolue fortement avec la réélaboration. Les inclusions de poly(acrylPEG) s'endommagent suite à une déformation de leur forme, donnant lieu à une diminution de leur taille, de la porosité et une fibrillation. Des fissures liées au recyclage ont été constatées dans le pPLA après le cinquième cycle d'élaboration, expliquant la perte de ductilité. Toutefois, l'origine de ces défauts n'a pas été clairement établie. Il a été supposé que l'endommagement des inclusions a pour conséquence une diminution des interactions physiques entre la matrice et les inclusions donnant lieu aux fissures. Une seconde hypothèse repose sur un mécanisme de rupture de chaîne engendrant des contraintes de rétraction localisées qui créent ainsi des fissures. Comme pour le PLA, aucun changement de fonction chimique de fin de chaîne n'a été constaté, mais la forte diminution de la viscosité du matériau pPLA fait penser que les mêmes mécanismes de rupture de chaînes sont actifs dans les deux matériaux, malgré des comportements thermiques différents. En particulier, dans le cas du pPLA, la cristallinité augmente avec le recyclage, mais dans le même temps aucune cristallisation froide n'est observée. Les résultats ont également permis de conclure que la réticulation et le greffage ne sont pas influencés par la réélaboration. Le nombre de coupures de chaîne après 5 procédures d'élaboration, calculé à partir de tests de rhéologie, est deux fois plus important pour le pPLA que

pour le PLA, signifiant que la matrice PLA dans le pPLA est plus dégradée que le PLA de référence. Des tests d'extractions Soxhlet ont permis de séparer la phase de plastifiant non liée à la matrice de la phase matrice dans le cas du pPLA. Les résultats de ces tests ont montré qu'une certaine quantité de matrice est tout de même extraite par Soxhlet en même temps que le plastifiant libre, mettant en évidence une dégradation importante de cette matrice dans le pPLA. En résumé, la procédure de recyclage développée dans ce travail n'est pas désirable dans le cas du pPLA, puisqu'elle conduit à un matériau très fragile. De plus, les mécanismes de dégradation sont beaucoup plus importants pour le pPLA que pour le PLA.

L'influence de trois procédures de recyclage thermomécanique sur les propriétés du PLA et du pPLA a été étudiée brièvement. Il s'agit de procédures i) d'extrusion et de compression à chaud (CM), ii) d'extrusion (E), et iii) d'extrusion et de moulage par injection (IM). Ces différentes procédures de recyclage ont mis en évidence différents niveaux de dégradation. En effet, l'extrusion suivie de la compression à chaud, procédure de recyclage étudiée principalement dans ce chapitre, conduit à la plus grande diminution de masse moléculaire par comparaison avec les deux autres procédures. Cette importante dégradation est liée à l'étape de compression à chaud où le matériau fondu subi le plus long temps de maintien à haute température par rapport aux autre étapes de réélaboration.

Les différentes études sur les mécanismes de dégradation du pPLA ont mis en évidence des différences notables par rapport au PLA de référence, de même que l'importance du type d'étape de réélaboration. Le pPLA ne peut être utilisé que pour des applications où un nombre limité d'étapes de réélaboration est requis ou pour des étapes de réélaboration moins sévères que la compression à chaud. Néanmoins, les greffages et les réticulations ne sont pas détruits par le recyclage, ce qui permet de conclure que notre méthode de plastification réactive pourrait être pertinente pour d'autres polymères ayant une plus grande résistance aux dégradations thermomécaniques du recyclage que le PLA.

Cette thèse a permis de développer de nouvelles méthodologies de caractérisations permettant une meilleure identification structurale des polymères bio-basés. Dans le cas du PLA plastifié par extrusion réactive, ces méthodologies ont montré que ce matériau présente un comportement thermomécanique prometteur avec des mécanismes d'endommagement limités, mais son recyclage n'est pas encore un scénario de fin de vie optimal. Le greffage et la réticulation, qui ne sont pas contrôlables au cours de l'extrusion réactive, influencent de manière significative le comportement thermomécanique du PLA plastifié. Une étude plus quantitative de ces greffages et ces réticulations permettrait une meilleure compréhension du matériau et donc une optimisation du procédé d'extrusion réactive.

1 General Introduction

1.1 Background

Plastic materials surround us in everyday life. Despite many advantages like lower density and weight, as well as a higher freedom of design compared to glass and metal, plastic materials exhibit many drawbacks, such as the generation of increasing pollution at their end-of-life. Hence, current research focused on the replacement of conventional plastics by more environmental-friendly materials. As one forward-looking possibility, the development of biopolymers started out. Biopolymers were defined as polymers that are either bio-based or biodegradable or even both. Among these biopolymers, polylactide (PLA) excelled and began to replace common packaging plastics, such as poly(ethylene terephthalate) (PET) or poly(styrene) (PS) in the field of packaging applications. PLA fulfills both requirements of biopolymers and the environmental impact of this bio-based and (bio)degradable polyester is to be considered lower than for common plastic materials. In addition, PLA promises to be enough stable for long term applications as electronics and automotive, and therefore, biodegradation is probably not the most relevant end-of-life scenario. Compared to common plastic materials, PLA exhibits a higher stiffness and brittleness at room temperature, where the field of packaging requires on the contrary higher flexibility. Therefore, research is aiming to modify PLA by plasticization with suboptimal achievements until now. An increase of the flexibility was obtained by plasticization, but this technique decreased the glass transition temperature and, hence, the thermal stability. On one hand, the flexibility and toughness were improved, but, on the other hand, important plasticization creates very soft, sometimes rubber-like materials, which misfit with the packaging specifications. Furthermore, in plasticized materials phase separation and/or migration of the plasticizing agents with time was observed. Reactive plasticization was developed as a possibility to tune the properties of the plasticized material in a more suitable direction. Reactive processing has shown to graft a plasticizer onto the PLA backbone and avoids phase separation and migration of the plasticizer. In addition, the flexibility was increased, but at the same time, a high tensile strength was retained. For packaging, this technique allowed the processing of a durable plasticized PLA with a good flexibility and toughness properties.

1.2 Problematic

Until now, the structure of plasticized PLA, resulting from reactive extrusion, has not been identified in details. Hence, the thermomechanical transformations of this promising material in terms of deformation mechanisms upon drawing and degradation mechanisms during reprocessing procedures

are not well elucidated. Yet, this information is suitable to further improve plasticized PLA processing and performance during its use and end-of-life treatment.

1.3 Research Objectives and Methodology

Polylactide was recently plasticized by reactive extrusion with a poly(ethylene glycol) methyl ether acrylate (acrylPEG) in the presence of a free radical initiator, namely Luperox L101. This reactive extrusion formed a PLA-based material with plasticized PLA matrix and partially grafted and partially free inclusions of acrylPEG plasticizer. In addition, crosslinking of PLA occurred. This work aims at (i) further analyzing the as-processed structure of plasticized PLA by a multiscale approach to understand the processing structure relationship, (ii) investigating how the structure evolves upon drawing to identify deformation mechanisms, and (iii) investigating how the structure evolves when submitted to thermomechanical recycling procedures to identify the degradation mechanisms.

First, the structure of plasticized PLA was carefully characterized at different scales ranging from the molecular level to the macroscopic level. Molecular structure was characterized by combining gel permeation chromatography (GPC), swelling testing, and differential scanning calorimeter (DSC). Complementary information about the microstructure was obtained by scanning transmission X-ray microscopy (STXM) coupled with near edge X-ray absorption fine structure (NEXAFS) performed at the synchrotron. Crystalline structure and isothermal crystallization kinetics of plasticized PLA were studied by DSC and X-ray diffraction (XRD). The microstructure of plasticized PLA was investigated by means of a conventional atomic force microscope (AFM) and an advanced AFM with nanomechanical measurements. To understand processing-structure relationships of plasticized PLA, different formulations were processed (neat PLA, reactive and nonreactive PLA/AcrylPEG blends), and extrusion was conducted on a batch extruder (micro-compounder producing rods) as well as on a continuous extruder (mini-extruder producing films). Note that the scale-up from laboratory to pilot line scales was briefly addressed by the use of these two extruders.

The evolution of the plasticized PLA's structure upon drawing was studied by tensile testing at different tensile speeds and different temperatures. The deformation mechanisms in terms of chain orientation and phase transformation were first monitored by ex-situ DSC and wide-angle X-ray scattering (WAXS) for samples produced with the micro-compounder. For film samples (produced with the mini-extruder), the deformation mechanisms were studied in-situ with time-resolved small-angle X-ray scattering (SAXS) at the synchrotron. Attention was focused on the deformation heterogeneities that were investigated in real-time by SAXS and optical microscope observations. The true stress-strain behavior was addressed by means of Digital Image Correlation (DIC) and allowed classifying the

deformation behavior. Last, the macroscopic structure of plasticized PLA was studied in terms of mechanical performance by tensile and impact testing. Micro-computed X-ray tomography (µCT) testing was performed to get complementary structural information about plasticized PLA prior and after drawing.

The impact of reprocessing on the structure of plasticized PLA was conducted to simulate recycling procedures. Again, a multi-scale analysis of the plasticized PLA's structure was conducted after one, three, and five processing steps, which included extrusion and shaping by compression or injection molding. In particular, the thermomechanical performance of the materials was investigated by dynamic mechanical analysis (DMA) and tensile and impact testing. The samples rheological and thermal characteristics were determined by rheological measurements and DSC, respectively. The material's microstructure was analyzed with a scanning electron microscope (SEM) and an atomic force microscope (AFM). Last, the molecular and chemical structures were characterized by combining GPC, Soxhlet extraction, nuclear magnetic resonance spectroscopy (NMR), and Fourier-transformed infrared spectroscopy (FTIR). In the end, based on all the multiscale data, the degradation mechanisms were summarized.

1.4 Manuscript Description

This **General Introduction** is followed by **The State of the Art**, which analyzes the problematic of nowadays used plastic materials and the development of PLA. Information about PLA's structure, modification, mechanical behavior, and end-of-life scenarios are provided. In the end, the State of the Art leads to a description of the aims of this work by highlighting the research gaps in the field of PLA that will be addressed by this thesis.

The third chapter, **Process-Structure Relationship for Plasticized Polylactide**, analyzes the structure resulting from the reactive extrusion plasticized PLA at different scales.

The fourth chapter, **Structure Evolution with Strain**, focuses on the evolution of plasticized PLA structure upon drawing with the identification of deformation mechanisms and damages.

The fifth chapter, **Structure Evolution with Reprocessing**, deals with the thermomechanical recycling of the plasticized PLA material. A multiscale analysis of the plasticized PLA's structure is conducted to access the degradation mechanisms of plasticized PLA.

Chapter six, **Conclusion and Outlook**, summarizes all results and depicts questions, which were not solved until now, regarding the structural properties of plasticized PLA.

In **Appendix A,** all used materials and the analysis methods are described in detail. The processing, as well as analysis conditions, are defined for all materials and analysis techniques. **Appendix B** gives some preliminary results for the mechanical and thermal characterization of materials plasticized with two new natural plasticizers, limonene and myrcene.

2 State of the Art

Nowadays used plastic materials create problems, but are essential for our way of life. Hence, this State of the Art will describe the advantages and drawbacks of plastic materials and introduce biopolymers as possible alternative materials. Among the bioplastics, poly(lactic acid) or poly(lactide) (PLA) is a forward-looking material regarding the replacement of petrol-based plastics since it is bio-based and (bio)degradable. This State of the Art will briefly summarize the general properties of PLA including its production history, its environmental impact, and its structural properties compared to two common plastic materials with similar mechanical properties, namely poly(ethylene terephthalate) (PET) and poly(styrene) (PS). Since the properties of neat PLA are not always suitable for applications, the modification and adaptation of PLA's properties will be discussed in terms of two mechanisms that are essential for applications: crystallization and deformation. Despite its (bio)degradability PLA offers also other end-of-life scenarios, whereas the thermal degradation during thermomechanical recycling will be amplified and compared to the (bio)degradation. **This State of the Art will tackle the academic research needs concerning PLA that were the starting point of this thesis.**

2.1 Plastic Materials – Both a Curse and a Blessing

The Oxford University press defined a plastic as "a synthetic material made from a wide range of organic polymers (…), that can be molded into shape while soft, and then set into a rigid or slightly elastic form"[1]. The wide range of organic polymers leads to a broad field of applications that can be separated into two main categories: short-term and long-term application. For short-term applications, like packaging, plastic materials have to be flexible and ductile, while for long-term applications, like in automotive industry, very robust materials are required. Plastic materials accompany our everyday life - but could you imagine a life without plastic? A question that is often asked in connection with the increasing pollution for which plastics are responsible for. The discussion about plastic materials polarizes the society: Some people try to avoid and ban plastic, while others just see the advantages.

On one hand, pollution by plastic materials is problematic, but, on the other hand, plastics are essential to our way of life. In addition to the plastic packaging – that is often avoidable – plastics are applied in electronic and automotive industry, as well as in medicine. The wide range of organic polymers allows to produce plastics for a broad field of applications and compared to other raw materials like wood, glass or ceramic, plastic materials are often cheaper and lighter. The different organic polymers offer several properties that other materials cannot fulfill. For example, plastic

bottles replaced glass bottles, with the advantage that their lighter weight decreases the transport costs. In the automotive industry, car pieces like the bumper bars are made of plastic to get lighter cars that consume less fuel. In the medicine, parts of the metal tools used by the doctors were substituted by plastic materials due to light weight and the better feel during handling for doctors and patients. In addition, the resistance of plastic against different solvents and acids or bases facilitates their sterilization. Despite an already broad field of plastic materials with different properties, a physical and/or chemical treatment could adapt the plastic's properties even better to the needs. A famous example for the different properties of materials based on the same polymer is poly(ethylene) (PE). Depending on the processing, it exists in two grades: low-density PE (LDPE) and high-density PE (HDPE). While LDPE is more flexible and used for plastic bags, HDPE offers a higher stiffness and is used as water and gas pipes. Another method for the modification of plastic materials is the blending with other polymers or smaller molecules. Blending often aims at a plasticization effect to allow obtaining a higher flexibility of the material at lower operating temperatures.

Figure 2.1 Beneficial plastic applications in the everyday life (left) and in medicine as an implant (middle), but resulting pollution (right).

Plastic materials bear many advantages, but also caused negative headlines, unfortunately. Especially, plasticization with bisphenol A (BPA) arose criticism since BPA and also other commonly used plasticizers are under the cloud to be cancer-causing. In 2015, the European Food Safety Authority (EFSA) concluded their comprehensive scientific study about the safety of BPA with the sentence: "Exposure from all sources is very low and well below the new safe limit for all age groups – products made from BPA-based materials can therefore be regarded as safe for consumers."[2], but the fears remained resulting in a partial prohibition of BPA. Furthermore, plasticization is often nondurable; the plasticizer is leached out, the material loses its flexibility and, finally, becomes brittle. Another problem is the production of conventional plastics based on petrol because their price also depends on the petrol price that increased continuously within the last decades. Even though, only about 4% of the

global oil production is used for plastic [3]. New studies focus on the toxicity for consumers and blame plastics to be complicit for the global warming [4]. In addition, plastics are of high durability. Despite an often short-time application especially in the sector of packaging, the plastic materials show a long lifetime that challenges degradability and/or recycling. The wrong disposal of plastic waste leads to pollution of the environment even though recycling of most plastic materials is possible nowadays. Since the development and daily use of plastics, the so-called throwaway society litters objects of daily use without thinking about the consequences. Large amounts of plastic garbage end up in the environment, but a decomposing is very slow or nonexistent. Deformed turtles caught in a plastic suit, putrescent birds with a stomach full of plastic waste, or swimming plastic islands in the ocean - images that dismay, but cannot change all people's mind to a responsible handling of plastic materials. However, the society decries plastic materials more and more. Recent dialogues and decisions, like the prohibition of free plastic bags of the European Union (EU) or warnings about higher concentrations of microplastic in seawater than plankton, show the importance of this topic. Furthermore, the increasing number of books and blogs that describe how to avoid plastic in the daily life, or packaging-free supermarkets indicates the public's interest.

Despite their drawbacks, plastic materials offer sustainable factors. Sustainability is divided into three pillars – social, economic, and environmental – and describes the impact on the people, the profit, and the planet [3]. While the advantages for the social and economic sectors are obvious, the impact on the environmental sector is a controversy. The use of plastic materials simplifies the everyday life e.g. by improvements in the safe food packaging or the medical sector, and, as already mentioned, plastic materials are often cheaper regarding their production and their transport due to their lighter weight. The environmental pillar is often defined by the CO_2 footprint, which describes the balance between produced, saved and consumed CO_2 during the life cycle of a material. For example, the use of light plastic materials for cars, airplanes, and packaging reduces the fuel consumption for transportation and consequently the CO_2 emission. Furthermore, it was described that the incineration of plastic waste regains energy, but contrariwise incineration creates a high amount of CO_2. Therefore, other end-of-life scenarios should be considered and, especially the environmental aspects demand a responsible handling of plastic materials to reduce the environmental impact.

In order to decrease the negative environmental impact of plastic materials, recycling has become a more and more interesting topic for academic and industrial research as well as for the policy during the last decades. Recycling describes the possibility to treat or process used or waste materials so as to make them suitable for reuse. The municipal waste recycling rates of 35 European countries in 2004 and 2014 are compared in Figure 2.2 [5]. The data include material recycling as well as composting and digestion of biowaste. It was noted, that most of the countries increased their recycling rate from

2004 to 2014. For instance, the United Kingdom, Italy, and Portugal doubled their recycling rates in these ten years. Czech Republic, Poland, and Lithuania made strong progress and reached the average of all European countries in 2014, while they were far below the average in 2004. Latvia, Greece, Cyprus, Croatia, and Romania progressed strongly, but are still below the average. In the ten years, the average of the countries for the recycled and composted municipal waste increased from 21.4% to 31.1%.

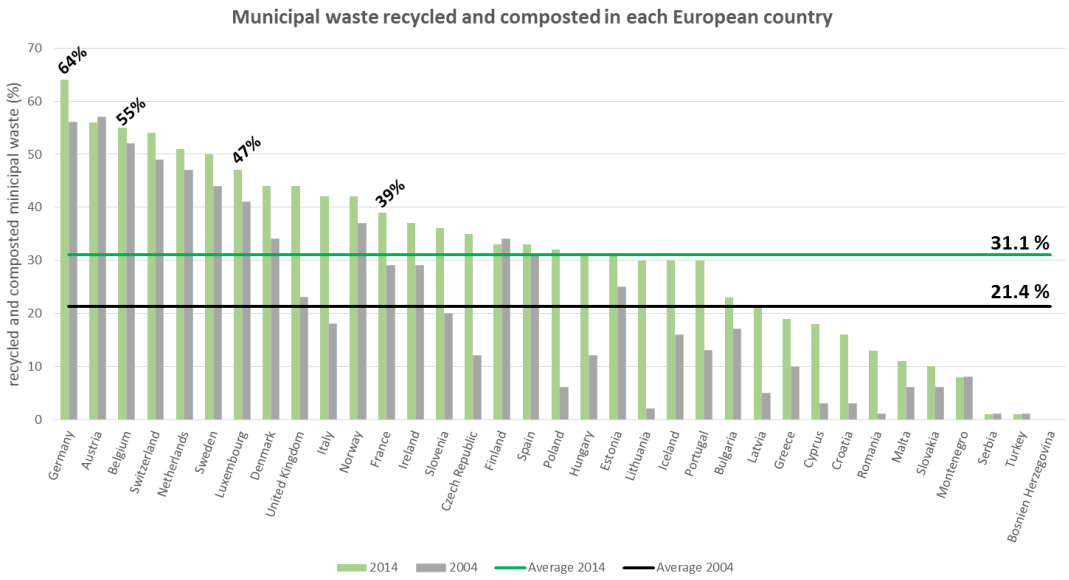

Figure 2.2 Municipal waste recycling rates of 35 European countries in 2004 and 2014 [5].

In this period, Luxembourg increased the recycling and composting rate from 41% to 47%. All nations of the Greater Region, Luxemburg, Belgium, France and Germany implemented a higher recycling rate than the European average and increased it in the considered time frame. While France has a slightly lower recycling rate of 39%, Belgium and Germany are with 55% and 64%, respectively, in the top three for the recycling and composting rate of the European countries. The statistic clearly indicates that recycling and composting of waste is a forward-looking topic in Europe and in particular in the Greater Region. The increasing recycling rates indicate that recycling became more and more important in Europe during the last years (Figure 2.2). However, energy and time investment for recycling exceed the application time, especially for packaging waste. Therefore, the handling of waste, especially plastic waste, should follow the waste management hierarchy: source reduction, recycling, composting, incineration with energy recovery, and landfill [6]. The best choice is always to avoid waste, reduction of consumption reduces also the waste. The second option is to recycle the

materials as often as possible. For the reuse or recycling materials have to be resistant to damage and should not underlie aging or degradation. The third option, composting materials, needs time, but the material can be completely decomposed and reused as compost. For the incineration with energy recovery, it is important that during the burning no toxic product is released. Nevertheless, incineration creates a high amount of CO_2. The last option for all kind of waste is landfill, but this normally causes high pollution.

Since it is impossible to avoid plastic everywhere, research focused on the development of new environmental-friendly materials with the principle of so-called green chemistry. In 1990, the US Environmental Protection Agency (EPA) defined the concept of green chemistry: "To promote innovative technologies that reduce or eliminate the use or generation of hazardous substances in the design, manufacturing, and use of chemical products" [7]. Currently, the field of plastics offers a big potential for reducing and replacing nowadays used petrochemicals and focuses on finding more environmental-friendly and nontoxic alternatives. Common plastic materials are petrol-based and not degradable, therefore so-called bioplastics were developed to overcome these drawbacks. However, European Bioplastics defined a bioplastic as a material, that is either bio-based or biodegradable or both [8]. On one hand, bioplastics can replace petrol-based materials in well-known processes of plastic industry. For example, bio-based materials were already processed on PET and PE industrial platforms. On the other hand, new bio-based and biodegradable materials can be found and improved, such as starch-based materials or poly(lactide).

According to European Bioplastics [8], the production capacity of bioplastics is expected to increase from 4.16 million tons to 6.11 million tons in the next five years (Figure 2.3). The percentage of bio-based, but not biodegradable plastics will slightly increase from 76.8% to 79.4%. This trend could be due to the fact that it is easier to implement bio-based materials in well-known processes to replace the petrol-based grade than to develop completely new processes with new materials. For example, the percentage of bio-based PET will increase from 22.8% in 2016 to 28.2% in 2021. Among the biodegradable plastics, only one production capacity will increase: In 2016 polylactide (PLA) made 5.1% of the bioplastics and in 2021 it is expected to gain 5.3%. Considering the global increase, 212,160 tons were produced in 2016 and 323,830 tons are expected in 2021, which means an increase of PLA production capacity by a factor of 1.5 within five years. PLA is a (bio)degradable and bio-based polymer with promising properties to replace common petrol-based plastics. Since PLA is also biocompatible, it was mainly used in medical applications, but within the last decades, the production capacity of PLA increased, therefore the price decreased and the material became interesting for plastic industry (packaging, automotive) as well. Since a few years, PLA is applied in the packaging sector in Europe [6]. In Sweden, shopping bags were produced from PLA already since 2003. In France, the hypermarket

chain Auchan used PLA for salad boxes and a drug store chain in Germany sells bottled beauty, energy and memory drinks in PLA-made bottles. Furthermore, the company Danone serves their Activia® Yoghurt in PLA cups. All these applications used neat PLA without improved functions, but, of course, PLA lacks perfection to replace all common plastic materials. For example, Sunchips® in the USA were sold in PLA-based bags, but the noise of the material was disturbing and the production was stopped after four years [6]. Recently, PLA was considered for durable long-term applications in automotive (prototype of an air filter [9]) and electronics (housing [10]), implying that its stability is comparable to conventional polymers, which were used for these applications.

PLA, as a bio-based and (bio)degradable polymer, promises to be an environmental-friendly alternative for common petrol-based plastic materials. To broaden PLA's application range, especially in the packaging sector, academic and industrial research like this thesis on hand focus on the improvement of this trendsetting material. For this purpose, detailed studies about the modification possibilities have to be made to adapt PLA's properties in the desired field of application and to overcome the known drawbacks.

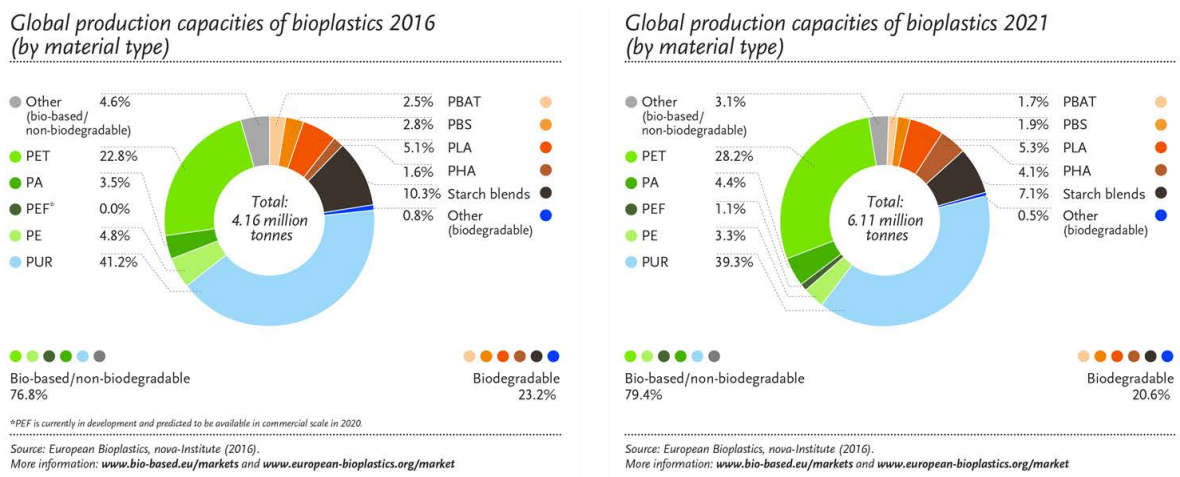

Figure 2.3 Global production capacities of bioplastics in 2016 and 2021 [8].

2.2 Polylactide as a Forward-Looking Biopolymer

2.2.1 History and Environmental Impact of Polylactide

Despite many drawbacks, plastic materials are partially inevitable or at least favored in the everyday life, but the increasing pollution and health problems become more and more problematic. The development of bioplastics could manage these drawbacks and keeps the advantages of plastic materials at the same time. Within the last years, polylactide or poly(lactic acid) (PLA) aroused high

interest since it fulfills both criteria for being considered as a bioplastic: It is bio-based and (bio)degradable.

The synthesis of its monomer lactic acid was already described in 1912 and the polymerization process was described 20 years later by Carothers et al. [11] and further developed by DuPont. The main challenge during the polymerization was to obtain polymers with a high molecular weight since the polycondensation reaction of lactic acid leads to low molecular weight products. Therefore, three different routes were developed to obtain high molecular weight PLA (Figure 2.4). The first method gains a low molecular weight PLA-prepolymer by polycondensation of the lactic acid monomer. After the addition of chain coupling agents (route (I)), a high molecular weight PLA polymer is formed. The second route contains two steps: After the formation of the low molecular weight PLA, lactide, the dimer of lactic acid, is produced (II-a), and lactide is polymerized by ring opening polymerization (ROP) to a high molecular weight PLA (II-b). The last route for the synthesis of high molecular weight PLA is the direct azeotropic dehydration condensation (III) [12]. Figure 2.4 shows the reaction schemes of the three different routes. In the industry, normally the second route is applied since it is the easiest to control.

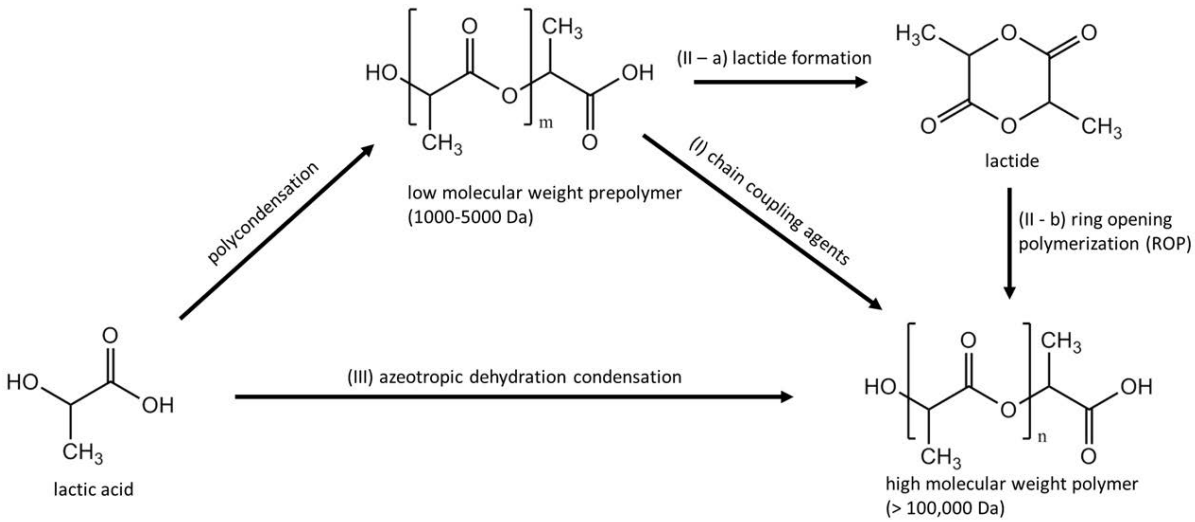

Figure 2.4 Synthesis routes for high molecular weight PLA adapted from Hartmann [12].

PLA is the shortcut for poly(lactic acid) as well as for poly(lactide) since PLA can be obtained from both monomers, lactic acid and lactide. In the past, the production of PLA was inadequately developed which made its synthesis costly. The main sources for the monomer synthesis competed against the food industry so that the production capacities, as well as the applications, were strongly limited. Since

PLA is biocompatible and nontoxic [4], it was mainly used for biomedical applications [13]. Nowadays, the monomer lactic acid can be synthesized by bacterial fermentation of various carbon sources like corn starch, sugar or even paper sludge or kitchen and agricultural waste [4]. With increasing production capacities, the price decreased, which opened a market for other PLA applications. Likewise other bioplastics, PLA can be designed for packaging, disposal nonwoven, consumer goods or agricultural products [14]. Furthermore, PLA established itself in the textile industry and as one of the main materials for 3D printing. Materials used for packing applications have to fulfill special requirements like transparency, low crystallinity, and high flexibility, as well as good barrier properties and resistance to solvents and water to protect the inside against outside influences [15,16]. Since PLA satisfies these requirements it could replace common plastic materials like poly(ethylene terephthalate) (PET), poly(ethylene) (PE), or poly(styrene) (PS) in the packaging sector and reduce the environmental impact of packaging. Furthermore, compared to these ordinary packaging materials PLA shows a good balance in the life cycle assessment (LCA). LCA determines the environmental impact of a material by defined criteria like their nonrenewable energy use (NREU) or their global warming potential (GWP). Despite the International Organization for Standardization (ISO) defined criteria for the LCA, the evaluation remains subjective and complicates a comparison between different studies [17]. Normally, LCA includes parameters of the whole production process from the starting material to the final product and use so that fossil-based polymers obtain high NREU values. In contrast, biopolymers increase the land and water consumption and also the needs for fertilization, harvesting, and transportation. Moreover, the milling and production of the starting material (monomers) and the final products (polymers) are crucial factors. Although LCA leaks a scientific basis, a comparison between different materials can be made and sheds light on their impact in specific fields. In 2013, Yates et al. [17] reviewed studies on LCA of PLA compared to PET, PS, HDPE, and poly(propylene) (PP) focusing on the categories GWP, NREU, acidification potential (AP), and eutrophication potential (EP). While PLA had normally lower values for GWP and NREU, the values for AP and EP were often higher. Another important point for the LCA is the end-of-life option for materials. Among disposal options such as landfill, incineration, home and industrial compost, recycling was considered as the most favorable solution for environmental interest. Recycling allows the recovery of either the monomer material by chemical recycling or the polymer material by mechanical recycling. Despite the (bio)degradability of PLA, other end-of-life options such as (chemical and mechanical) recycling showed lower environmental impact. For common plastics like PET and PE chemical and mechanical recycling cycles are well developed, but for new materials such as PLA, they are still missing. Therefore, the environmental impact of these new materials is often considered to be lower but is still higher than for commonly used plastics. After all, the authors agreed that PLA

could be favorable compared to common plastics considering the environmental impact, but its production process and recycling require further improvements. Castro-Aguirre et al. [6] recently showed that PLA has grown from a supporting actor in the field of biopolymers to one of the main alternatives for fossil-based polymers. By developing and improving the production methodologies, the environmental footprint improved further and PLA became a real bio-based solution for the plastic problematic.

2.2.2 Polylactide's Structure

Plastic materials, such as PLA, consist of chain-like macromolecules with monomer repeating units. The plastic's properties strongly depend on the structure of the macromolecules. Hereby, the structure is ruled by primary, secondary, tertiary, and quaternary structure elements, whereas the quaternary structure is mainly important for protein structures and less for bulk polymers [18,19]. The primary structure depends on the chemical nature of the repeating unit and defines the chemical and electrical properties of the macromolecule. The PLA repeating unit consists of an ester function as backbone chain and a methyl side group so that PLA is among the polyesters. The secondary structure focuses on the properties of one single macromolecule, whereas the molecular weight and the linking between the repeating units define the size and the shape of this macromolecule, respectively. Due to the different macromolecular chains, plastic materials own no defined molecular weight but rather a weight average molar mass ($\bar{M}_w$) or number average molar mass ($\bar{M}_n$). The polydispersity index (Đ) is defined as the quotient of these two: $Đ = \bar{M}_w/\bar{M}_n$. PLA, as used in applications, offers molecular weights higher than 100,000 Da and polydispersity indices between 1 and 3 depending on its grade. The shape of the macromolecule is impacted by the chemical structure of the repeating units. In the case of PLA, the monomer lactic acid has two stereoisomers, namely L-lactic acid and D-lactic acid, and, therefore, the dimer of lactic acid, which is the intermediate for the production of high molecular weight PLA by ring opening polymerization, offers three stereoisomers: R,R-lactide, meso-lactide, and S,S-lactide (Figure 2.5).

Furthermore, the backbone bonds in the macromolecule lead to a defined rigidity of the macromolecules. The secondary structure determines the ternary structure since the size and the shape of macromolecules allow or avoid an ordering so that amorphous or semicrystalline polymers are obtained, respectively. The tertiary structure explains the interactions between different macromolecules. While a homopolymer of L-lactic acid (PLLA) or D-lactic acid (PDLA) crystallizes easily, an increase of the stereoisomer content leads to polymers with reduced ability to crystallize [16]. Furthermore, the thermal properties are related to the structure. Semicrystalline polymers, like PLA,

exhibit a glass transition temperature (T_g) due to the amorphous phase and a melting temperature (T_m) where the crystalline phase melts. All thermal properties depend on the thermal history and since T_g is always lower than T_m, in semicrystalline polymers a cold-crystallization is possible [20]. PLA is a thermoplastic material and the neat L- or D- isomer of PLA has a T_g at around 60°C and a T_m at around 180°C [21]. With increasing stereoisomer content both temperatures decrease slightly and the crystallization ability is reduced. The overall ordering of the ternary structures defines the quaternary structure, but in polymer materials, the ternary structures are often not homogeneous so that a further ordering of these phases is insignificant. However, the materials properties, especially the physical properties, are impacted by the structure and the resulting ordering of the macromolecular chains.

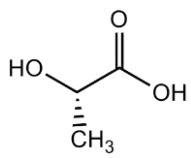

(a) (*S*)-lactic acid / L-lactic acid

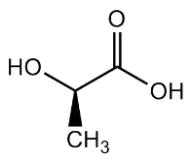

(b) (R)-lactic acid / D-lactic acid

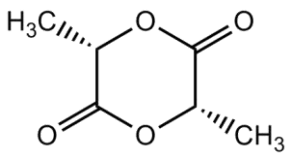

(c) (S,*S*)-lactide / L-lactide

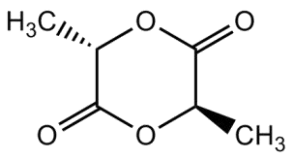

(d) *meso*-lactide

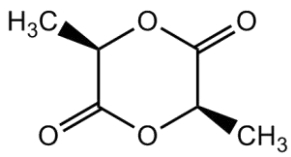

(e) (*R,R*)-lactide / L-lactide

Figure 2.5 Chemical structures of the monomers for PLA synthesis.

2.2.3 Polylactide's Properties Compared to Two Common Plastics

PLA's environmental footprint was reported to have less environmental impact than common plastic materials, but PLA has also to be applicable in the same way as known plastics to be a real alternative for petrol-based plastics. Depending on the monomer molecules that are used for synthesis, plastic materials offer different properties and therefore different fields of application. In 1988, the Society of the Plastic Industry (SPI) developed the resin identification code (RIC) that classifies plastics by their constituent monomer. The symbol associated with the different plastic materials consists of a triangle with three arrows, and a number from 1 to 7. The RIC provides no information about the recyclability of the material, even if the cycled arrows may lead to this assumption. Table 2.1 shows the symbols, the materials' names and gives some examples for applications of the materials. In category 7 all other plastics are summarized, for example newly developed bioplastics like polylactide [22]. All applications

of plastics fit the specific properties of the materials, and research and industry already managed to adapt and optimize the properties of these materials to the application by different chemical, physical or thermal treatments. For example, polyethylene offers two forms for applications: high- (HDPE, RIC category 2) and low-density polyethylene (LDPE, RIC category 4). While HDPE offers a high stiffness, LDPE excels in flexibility. Furthermore, plasticizers can be used to adapt the plastic's properties to the fields of application, which complicates the apparent simple classification of the RIC.

Table 2.1 Resin identification code (RIC) for plastic materials and examples of use.

RIC	plastic's name	examples for applications in packaging and other fields [23]
01 PET	poly(ethylene terephthalate)	beverage bottles, insulation for wires
02 PE-HD	high-density poly(ethylene)	bags, food containers, insulation, piping
03 PVC	poly(vinyl chloride)	squeeze bottles (shampoo), pipes, electric isolation, construction materials
04 PE-LD	low-density poly(ethylene)	bags, film wrap, food containers, wire and cable covering
05 PP	poly(propylene)	food containers, bottle caps, chairs, car parts (bumpers, carpets)
06 PS	poly(styrene)	disposal cups and food containers, disc and DVD cases, medicine bottles
07 O	others: poly(carbonate) (PC), poly(lactide) (PLA), …	water bottles, food containers, car parts, eye glass lenses

Regarding the field of applications, PLA offers promising properties for the packaging industry. It has a good transparent appearance and low toxicity [4], but mainly the mechanical performance rules the application fields. The mechanical properties of PLA are comparable to poly(ethylene terephthalate) (PET) and poly(styrene) (PS) and therefore PLA was desired to replace these materials in common applications like the packaging. PET is mostly known as beverage bottles, since it offers good barrier properties for gasses such as CO_2, which occurs in many drinks due to the added carbon acid [24], while PS is often used for food service disposals, due to its protection again spoilage. As PE, PS exists in different grades, but in the case of PS, it is not the degree of branching and therefore the density, which impacts the properties, but rather the tacticity. Depending on the synthesis route, the formation of atactic, isotactic or syndiotactic PS is preferred. While the glass transition temperature

of nearly 100°C is barely influenced by the tacticity, the crystallization kinetics and the melting temperature alter strongly. Syndiotactic PS crystallizes fast and has a high melting temperature of 270°C and isotactic PS crystallizes slowly and has a lower melting point around 240°C. The atactic PS offers no melting point since it is completely amorphous and the random tacticity prevents crystallization [25]. Compared to PET with a melting temperature of about 250°C, PLA's thermal stability is limited, so that the glass transition temperature about 60°C and the relatively low melting temperature of 153°C exhibit PLA's drawbacks. Depending on the application, PET and PS have different molecular weights. For example, PET bottles are obtained from PET with a molecular weight between 24,000 g/mol and 26,000 g/mol [26] and PS containers have molecular weights between 1,000 g/mol and 1,000,000 g/mol [27]. For PLA, grades with a molecular weight higher than 100,000 g/mol were most suitable for applications. In packaging applications, the mechanical properties such as the tensile strength, elongation at break, modulus of elasticity, and the impact strength are of paramount importance. All these mechanical properties are ruled by the structure of the macromolecules. Depending on the grade influenced by the D-lactide content, the molecular weight, and the thermal history the reported mechanical parameters for PLA can vary. PLA's tensile yield strength is about 53 MPa, and its tensile modulus is about 3.9 GPa [16]. In comparison to PET and PS, these values are slightly higher and indicate a high stiffness of PLA. While PET has a high elongation at break between 50% and 300% [28], PLA offers normally a low elongation at break of around 5% [16], which is comparable to PS. In the same way, PLA's impact strength with 18 J/m is much lower compared to PET's with 79 J/m. These values highlight PLA's drawbacks in flexibility and toughness. The elongation at break and toughness are impacted by the chain rigidity and the mass between entanglements. PLA offers for the chain rigidity a similar value as PS but has a lower molecular weight between entanglements [29–31]. Compared to PET, PLA and PS have much higher chain rigidity values and higher mass between entanglements [29–31]. These two parameters explain the higher elongation at break and higher toughness values for PET compared to the other two materials.

Since the thermal history strongly impacts the properties of plastic materials, the processing gains an important role [32]. PLA can be used for different applications like films or bottles, and different industrial processing techniques such as extrusion, injection molding, injection stretch blow molding, casting, blown film, thermoforming, foaming, blending, fiber spinning, and also compounding can be applied. The main processes are based on a melting process: The polymer material is melted and shaped in the desired form [33]. The choice of the processing technique depends on both the application and the characteristics of the material. While for injection molding PLA with a D-lactide content of less than 1% was used, for thermoforming and extrusion higher D-lactide (4% to 8%) contents were more suitable. While heating up, PLA could also undergo a thermal degradation which

complicates the processing steps and needs special attention. Nevertheless, PLA offers comparable mechanical performance as PET and PS and could be applied in the same field, but its low thermal stability, flexibility, and toughness demonstrate PLA's limits in applications at room temperature.

Table 2.2 Properties of PLA compared to PET and PS in packaging applications.

	PLA	PET	PS (atactic)
name	poly(lactide) or poly(lactic acid)	poly(ethylene terephthalate)	poly(styrene)
chemical structure of the repeating unit	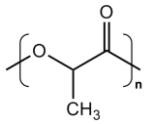	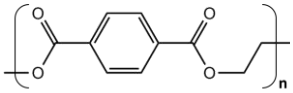	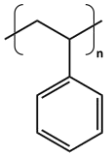
main applications in packaging	bottles, plastic bags, cups, food service disposals [6]	beverage bottles	food service disposals
relative permeability for CO_2 (no-dimensional value)	-	17.8 [24]	10.4 [24]
average molecular weight (g/mol)	> 100,000	24,000 - 36,000*[26]	1,000 - 1,000,000**[27]
Chain rigidity (-)	11.8 [29]	4.1 [31]	10.8 [31]
Mass between entanglements (g/mol)	8900-10500 [30]	1450 [31]	18700 [31]
tensile yield strength (MPa)	53 [16]	47 [28]	34-46 [28]
tensile modulus (GPa)	3.9 [16]	3.1 [28]	2.9-3.5 [28]
tensile elongation (%)	5.4 [16]	50-300 [28]	3-4 [28]
Notched Izod Impact (J/m)	18 [16]	79 [28]	-
glass transition temperature T_g (°C)	60 [28]	75 [28]	95 [28]
melting temperature T_m (°C)	153 [28]	250 [28]	-

* for PET bottles, ** for food packaging containers

Until now, none of existing grades of PLA satisfies the requirements for the packaging industry like PET and PS do. Therefore, research focuses on imitating the properties of PET and PS by changing PLA's structural properties. After all, it is important to improve PLA's weak points, e.g. the elongation at break, without losing the advantages over common plastics, e.g. the stiffness to boost PLA's chances to replace common plastics.

2.3 Modification of Polylactide

As discussed previously, PLA offers promising mechanical properties to replace common plastic materials, but its brittleness limits the applications. Different research studies dealt with the modification of PLA to obtain materials with a better mechanical performance for specific applications since it is not possible to obtain the perfect material from PLA that fits for all applications. Therefore, it is important to focus on one application field and optimize PLA's properties in a special direction. For example, in the automotive industry with normally long-term applications, the toughness and thermal stability should be more important than the biocompatibility, while in the food packaging, it is inevitable to have nontoxic materials. Materials for packaging applications require flexibility at room temperature, high transparency, low crystallinity as well as good barrier properties [15]. The modification has always to be adapted to the field of application. The modifications are realizable by different methods, for instance, copolymerization or blending. However, especially for packing applications in the food industry or medical sector, there are essential requirements for added substances like being nontoxic, biodegradable and biocompatible [34].

A simple physical treatment of the PLA material, like drawing, can already change the structural properties and improves the mechanical performance, such as tensile and fracture properties [4]. Increased crystallinity had a positive effect on the impact strength, but the tensile strength decreased [35]. Since PLA is a copolymer from L- and D-lactide, their ratio impacts the mechanical properties. With increasing D-lactide content (from 0% to 15%), the crystallinity decreased continuously up to a completely amorphous sample for 15% D-lactide content, but the highest values for tensile strength and impact strength were obtained for 0.5% D-lactide content [35]. A further possibility for the improvement of PLA's properties is the copolymerization of PLA with other polymers, e.g. lactones or cyclic carbonates [35]. The copolymerization was recognized as a method to improve PLA's properties, but this process has to be implemented in the synthesis route of PLA and is not a modification of an existing PLA grade. However, blending PLA with other molecules can have a plasticization effect and the flexibility of PLA can be improved by increasing the free volume [15,36–39]. These molecules are called plasticizers or plasticizing agents and were classified into two various groups [40,41]. The first

group contains monomers and small molecules, whereas oligomer and polymer plasticizer form the second group. Small plasticizing molecules offer a better miscibility and, therefore, less phase separation than big molecules, but have the disadvantage of low boiling points and often evaporate during the processing. In addition, small molecules show the tendency to migrate towards the surface and reduce the flexibility of the plastic material. Bigger molecules, such as oligomers and polymers, do not evaporate during the processing and exhibit a lower mobility within the polymer matrix, but for these additives, a worse miscibility often causes phase separation. The plasticizer molecules are mixed with the polymer matrix and increase the free volume and therefore the flexibility, as schematically illustrated in Figure 2.6. Ljungberg et al. described a kind of "saturation concentration" for plasticizers in PLA, which indicates that PLA can uptake just a certain amount of plasticizer: The lower the molecular weight of the plasticizer the more can be taken up without phase separation [42]. The two groups of plasticizer show completely opposed advantages and disadvantages, so that a compromise for the synthesis based on the application of the material must be found. Furthermore, depending on the application, the additive should be nontoxic and (bio)degradable [34,42] to keep PLA's main advantages.

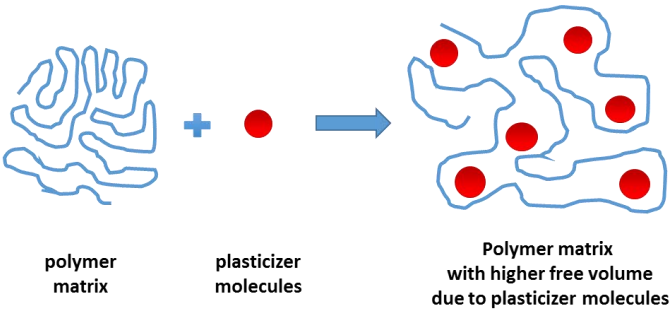

Figure 2.6 Schematic diagram of the plasticization process in a polymer.

Normally, plasticizing lowers the T_g of PLA and makes the material more flexible at room temperature. Various plasticizers have already been studied for PLA with different success. The modification with small molecules like citrate lowered the T_g and improved the elongation at break resulting in a more flexible PLA material. In the case of tributyl citrate (TBC) derivate, the plasticizing was effective, but the bigger the TBC derivate the earlier phase separation occurred [42]. The use of TBC oligomers or lactide oligomers promised a sufficient flexibility [42] without losing the transparency of the material [43]. Beside plasticizing PLA with small molecules like the monomer lactic acid, promising results were obtained by blending PLA with other biopolymers such as poly(ε-caprolactone) (PCL) [39], poly(ethylene glycol) (PEG), thermoplastic starch (TPS), or oligomeric lactic acid (OLA) [36,39,43].

While the plasticizing with PEG and OLA was quite effective, the use of glycerol as plasticizer had a rather negative effect [36]. TPS and PCL are also biodegradable and obtainable from renewable sources, which makes the applications more interesting for the biomedical sector and the food packaging industry. When blended with PCL, the impact toughness of PLA increased from less than 20 J/m for neat PLA to over 120 J/m for neat PCL, but its tensile modulus decreased from over 3000 MPa to less than 600 MPa with increasing PCL content, as shown in Figure 2.7 [39].

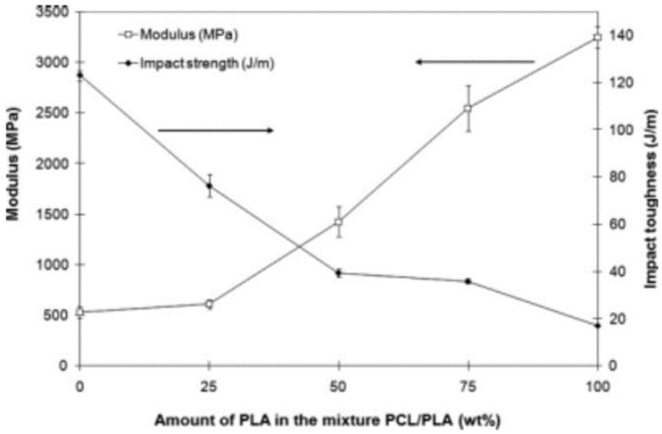

Figure 2.7 Evolution of the tensile modulus and impact toughness in PLA/PCL blends with different compositions [39].

On one hand, plasticization with PEG or OLA decreased the T_g by more than 20°C and increased the elongation at break, and on the other hand, blending with starch led easily to phase separation and formation of PLA inclusions in the starch matrix for a high content of starch [36]. The plasticization with poly(propylene glycol) (PGG) had a slightly better effect on the improvement of the elongation at break, but at the same time, the yield stress and the stress at break were decreased; with 10% of PEG or PPG plasticizer, the elongation at break was 25% and 90%, but the stress at break was 17.1 MPa and 15.8 MPa, respectively [44]. PPG's monomer unit has a slightly higher molecular weight than PEG and leads to earlier phase separation, especially during crystallization. Many studies focused on PEG as a plasticizer for PLA since it is biocompatible and can be bio-sourced produced. Baiardo et al. [45] studied the influence of PEG's molecular weight (400, 1500, and 10,000 g/mol) and its added amount (5 wt% to 20 wt%) to a PLA matrix on the plasticizing effect. The thermal and mechanical properties are summarized in Figure 2.8. The plasticizing efficiency decreased with increasing molecular weight of PEG, but the T_g was decreased in all cases. The highest reduction of T_g to 19°C was reached with 20 wt% of the lowest molecular weight PEG, while the highest elongation at break (230%) was reached with 20 wt% of PEG with a molecular weight of 1500 g/mol, but in these cases

the lowest tensile moduli were obtained with values of 0.5 MPa and 0.6 MPa, respectively. Other studies with PEG as plasticizer showed similar results: While the elongation at break and the impact resistance can be strongly improved, the tensile strength and the yield stress suffer from the plasticization [46]. In conclusion, PEG is one of the most effective plasticizers for PLA to improve the mechanical properties, but the plasticization bore problems, such as migration or leaching of the plasticizer during storage [42], which are just hard to handle and limit the applicability.

a)

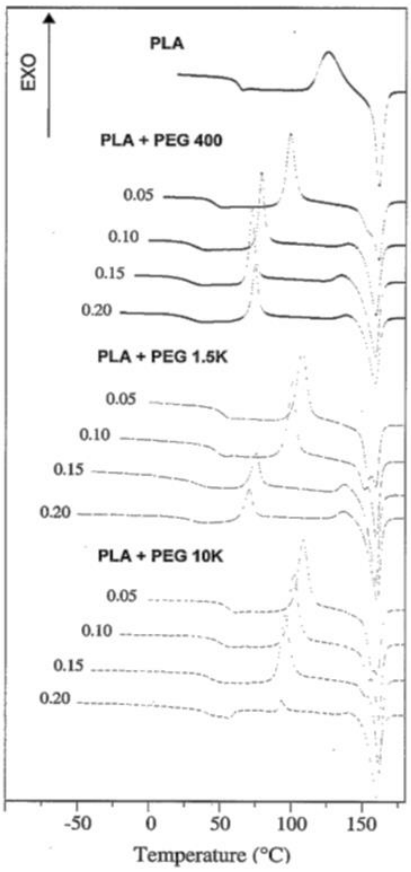

b)

Mechanical Properties of Plasticized PLA

Material	σ_b (MPa)	E (GPa)	ε_b (%)	T_a^{onset} (°C)
Pure PLA	66	3.3	1.8	60
PEG 400 (wt %)				
5	41.6	2.5	1.6	40
10	32.5	1.2	140	23
12.5	18.7	0.5	115	22
15	19.1	0.6	88	20
20	15.6	0.5	71	19
PEG 1.5K (wt %)				
5	52.3	2.9	3.5	46
10	46.6	2.8	5	42
12.5	18.5	0.7	194	30
15	23.6	0.8	216	27
20	21.8	0.6	235	20
PEG 10K (wt %)				
5	53.9	2.8	2.4	49
10	48.5	2.8	2.8	42
15	42.3	2.5	3.5	36
20	22.1	0.7	130	34
ATBC (wt %)				
5	53.4	3.2	5.1	49
10	50.1	2.9	7	41
12.5	17.7	0.1	218	26
15	21.3	0.1	299	27
20	23.1	0.1	298	24

Figure 2.8 PLA plasticized with different molecular weight PEG: (a) DSC curves and (b) mechanical parameters [43].

2.3.1 Plasticization by Reactive Extrusion

As described above, plasticizers – no matter if big or small molecules – create different problems. While small plasticizer molecules easily migrate towards the material's surface, bigger molecules offer a lower mobility in the matrix material, but also lower the miscibility and the plasticizing effect. A solution to overcome these issues was found in the method of reactive extrusion. This approach allows polymerization, grafting, branching or functionalization reactions during the processing in a cost-effective and one-stage way [14]. In the case of PLA modification, a radical initiator was used to create

reactive sites on the PLA backbone. These PLA radicals can further react with molecules for the modification. Different studies on the functionalization of PLA with a maleic anhydride (MA) aimed at the creation of materials with reactive groups for further modification [47,48] and application in the medical sector. The chemical modification with the MA was also the first step for different studies to plasticize PLA with citrate derivatives [34] or poly(ethylene glycol) [49]. Hassouna et al. [49] showed that, on one hand, the reactive blending between PLA, PLA with grafted MA (PLA-g-MA) and 10%PEG decreased the glass transition temperature and increased the elongation at break in the same range as the blending of PLA with 10%PEG, but, on the other hand, the reactive blending kept a higher storage modulus and yield stress (Table 2.3). It was highlighted that the reactive processing allows the production of plasticized materials with a high flexibility, but still an appropriate strength.

Table 2.3 Glass transition temperature and mechanical properties of PLA and plasticized PLA materials: PLA with 10% PEG plasticizer (PLA+10%PEG) and PLA with 10% PLA where MA was grafted and 10%PEG (PLA + 10%MA-g-PLA+10%PEG) [49].

	T_g (°C)	storage modulus (MPa)	yield stress (MPa)	elongation at break (%)
PLA	60.0	2190	67.8	7
PLA + 10% PEG	34.3	1750	15.1	112
PLA + 10% MA-g-PLA + 10% PEG	33.3	1870	29.1	116

Despite advantages in plasticization of PLA, these approaches still need a two-step processing. Therefore, different research groups focused on a one-step reactive extrusion to obtain plasticized PLA with functionalized plasticizers. The used plasticizers contained reactive groups that allowed a grafting of the plasticizer directly onto the PLA matrix. Kfoury et al. [41] compared the plasticizing effect of PEG methyl ether methacrylate (MAPEG) and poly(ethylene glycol) methyl ether acrylate (acrylPEG) and proved that radical extrusion with both materials decreases the T_g, limits the migration of PEG, and improves material stiffness and impact resistance. AcrylPEG was proved to be the better plasticizer with this technique and further studies highlighted that reactive extrusion between PLA, acrylPEG, and the free radical initiator 2,5-Bis(*tert*-butylperoxy)-2,5-dimethylhexane (Luperox, L101) improves the impact resistance nearly three times better compared to the physical blending of PLA with acrylPEG [50]. Choi et al. [51,52] studied a similar acrylPEG plasticized PLA, but they used dicumyl peroxide (DCP) as a radical initiator, while Kfoury et al. used L101 [41,50].

The grafting mechanism of acrylPEG onto the PLA matrix was described by both groups [41,51] and contained several steps: (I) the peroxide bond of the initiator is split thermally, so that two radicals are formed, (II) the initiator radicals abstract a hydrogen from the PLA backbone and a PLA radical is formed, and (III) the PLA radical reacts with the double bond of the acrylPEG. In this way, acrylPEG can polymerize on the PLA backbone, but it was also considered, that (IV) acrylPEG can form polymerized acrylPEG (poly(acrylPEG)) directly by the radical initiator without grafting onto the PLA backbone.

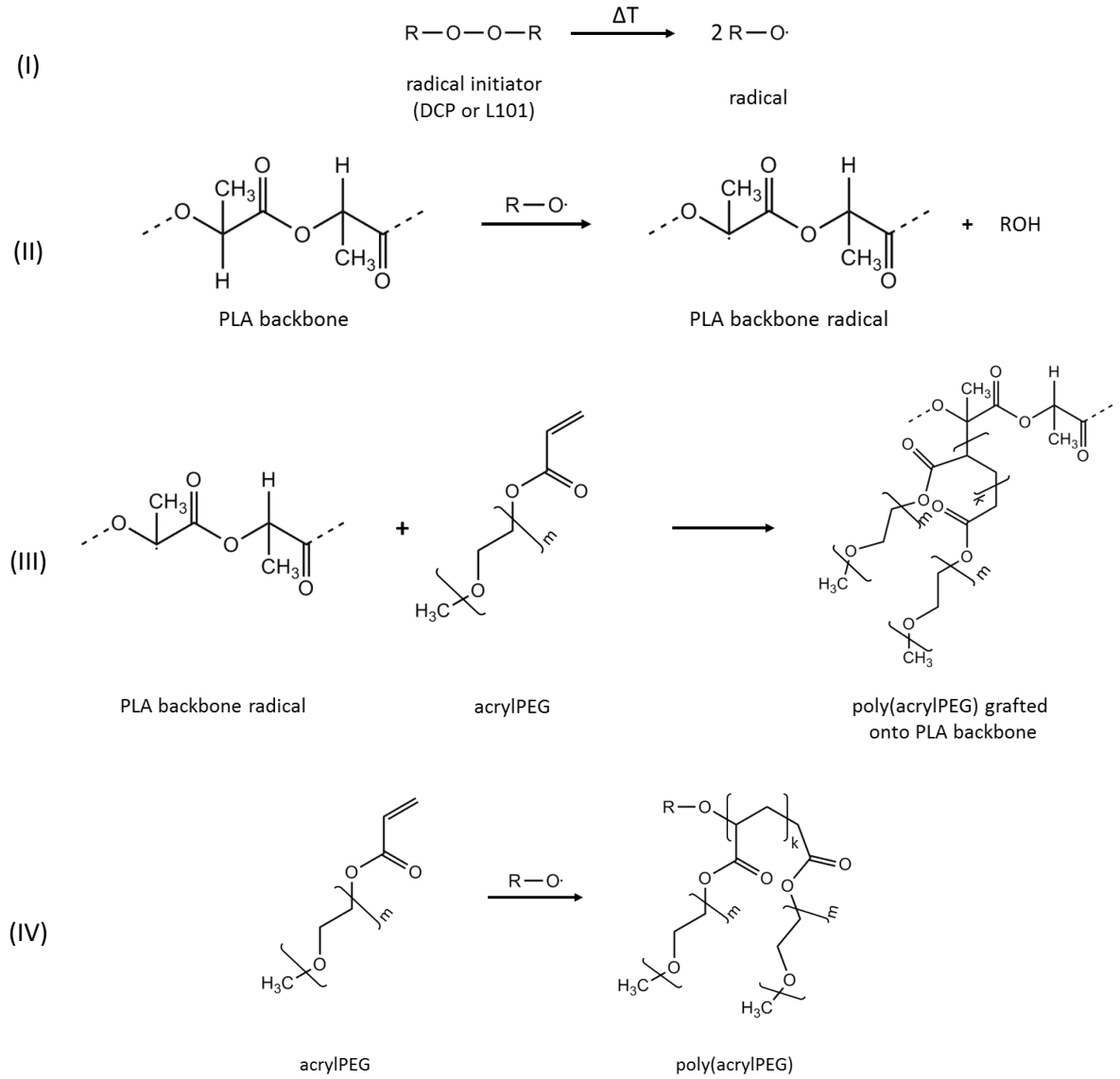

Figure 2.9 Mechanisms of acrylPEG grafting onto PLA backbone adapted from Kfoury et al. and Choi et al. [41,51].

Recent studies aimed at the optimization of the plasticizer and initiator content [41,50–52]. Unmodified PLA was brittle at room temperature and had a low elongation at break of less than 5%,

but a good tensile modulus higher than 2.2 GPa. PLA had a low toughness with an impact energy below 3 kJ/m^2. The simple blending of acrylPEG with PLA increased the overall ductility with values over 200% for the elongation at break and over 80 kJ/m^2 for the impact energy, but decreased at the same time the storage modulus strongly from 1.8 GPa to 0.6 GPa [41]. In general, it was observed that at the same initiator concentration, an increase of the plasticizer content increased the elongation at break, but lowered the tensile modulus [51]. The stress-strain curves for a PEG-plasticized PLA with different amounts of plasticizer and different amounts of initiator are reprinted in Figure 2.10. Furthermore, an increase of the initiator concentration (up to 1%) had a contrary effect; the tensile modulus increased up to 1.2 GPa (even higher compared to PLA with 1.1 GPa). At the same time, the elongation at break as well as the impact energy decreased with increasing initiator concentration, but even at high concentration, both values were higher for the modified samples than for PLA [52]. It is obvious, that Kfoury et al. [50] reported a much higher tensile modulus for neat PLA of 2.2 GPa than Choi et al. [52] with 1.1 GPa. This difference and other differences in the mechanical properties can be reasoned by the differences in the preparation methods and final tensile characterization. Especially the thickness of the samples differed: While Choi et al. [52] used nearly film samples with a thickness of 0.5 mm, Kfoury et al. [50] produced samples with a thickness of 3 mm.

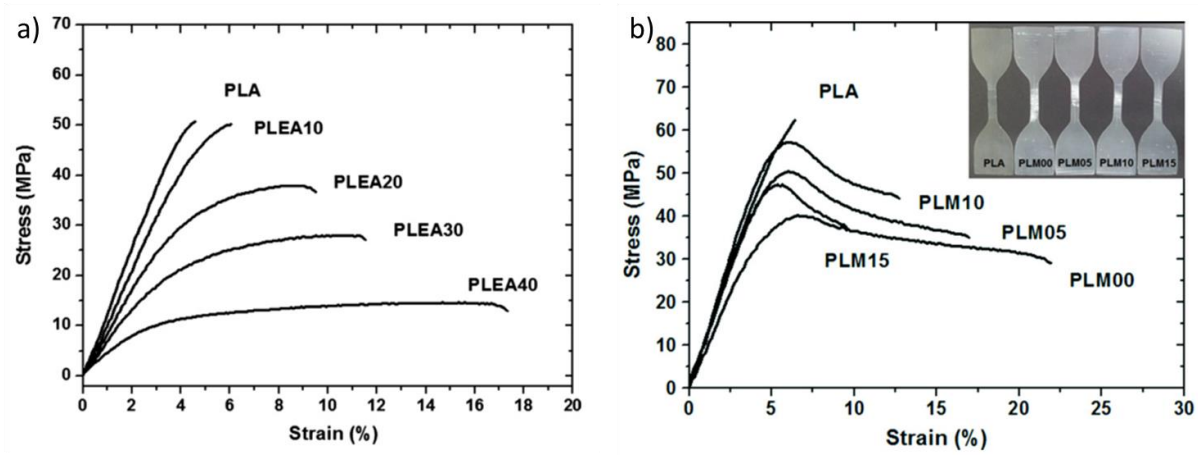

Figure 2.10 Tensile behavior of PEG-plasticized PLA by reactive extrusion at (a) different plasticizer concentrations [51] *and (b) different initiator concentrations* [52].

In their studies, Kfoury et al. compared the reactive blending to the blending without initiator [41] and to the blending with a previously polymerized acrylPEG, poly(acrylPEG) [50]. While the blending with the simple plasticizer led to a very high elongation at break over 200% the blending with poly(acrylPEG) increased the elongation at break just to 37%. The reactive blending with grafting of

the plasticizer showed a value between 150% and 200% depending on the initiator concentration. At the same time, the tensile modulus was similar for the samples with and without initiator (about 650 MPa), but the blend with poly(acrylPEG) showed a much higher value (about 1.5 GPa). Nevertheless, the impact energy of this sample was the lowest (about 36 kJ/m^2) compared to the other samples with initiator (about 102 kJ/m^2) and even without initiator (about 86 kJ/m^2), but still much higher than the impact energy of neat PLA (about 3 kJ/m^2). In addition to the mechanical properties, the thermal properties of the materials were changed by the modification with the plasticizer. In general, the glass transition temperature was lowered by about 15°C compared to PLA with a T_g around 60°C. The simple blending with the plasticizer and the polymerized plasticizer decreased the T_g as well to 29°C and 42°C, respectively. However, the glass transition became less visible after reactive blending with higher initiator concentrations (about 1%) and could not be observed for all samples [41,50]. Interestingly, all plasticization methods increased the crystallinity of the samples. While PLA was nearly amorphous, the blending with the plasticizer or the polymerized plasticizer increased the crystallinity to 2% and 6%, respectively. Higher degrees of crystallinity with up to 30% were obtained by the reactive grafting of the plasticizer [41,50].

In two different studies, Choi et al. investigated the impact of the plasticizer and initiator content [51,52]. With increasing plasticizer content, the glass transition temperature decreased strongly, but the material became more rubber like and lost stiffness while the elongation at break increased [51]. With increasing initiator concentration, it was proved that the radical reactions decreased the plasticizing effect. While the tensile modulus and the tensile strength increased, the elongation at break and the impact toughness decreased [52]. These studies underlined the main problem of plasticization: Improvement of elongation at break is normally just possible at the expense of stiffness. Therefore, the modification has to be adapted to the needs of the material and it is hardly possible to improve all materials properties at the same time. One key point for the variation of the properties is the structure of this PLA modified by reactive extrusion. The reaction mechanisms (Figure 2.9) showed that different reactions are in competition during the reactive modification: Poly(acrylPEG) can polymerize separately or grafted onto the PLA backbone and polymerize. Additionally, since radicals are formed, any kind of radical combination as termination reaction is possible. The structure of this plasticized PLA, as shown in Figure 2.11, was described by Kfoury et al. [41] as a PLA matrix with partially grafted and partially free inclusions of poly(acrylPEG). Furthermore, the occurrence of crosslinking between the PLA chains with the help of the poly(acrylPEG) inclusions was described [41,52]. However, this plasticized PLA had a complex structure and, until now, detailed studies of inclusion structure and crystallization ability are missing.

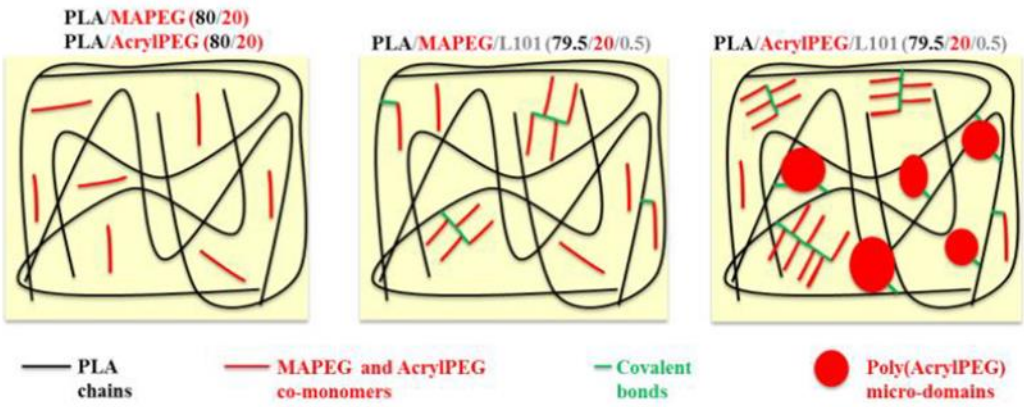

Figure 2.11 Schematic structure of plasticized PLA by blending with MAPEG or AcrylPEG (left), by reactive extrusion with MAPEG (middle) or acrylPEG (right) [41].

2.4 Crystallization Mechanisms of Polylactide

While modification allows adapting plastic materials to their applications and needs, it is important to understand the underlying mechanisms, which govern the microstructure setting and its evolution during in-use application. For PLA, two main mechanisms are of interest: the crystallization and the deformation mechanisms. Since crystallization also occurs during deformation, both mechanisms are linked. As already described earlier, the ratio of the two incorporated isomers L- and D-lactide strongly impacts PLA's crystallization behavior. While more than 93% L-lactide leads to a semicrystalline polymer, an amount of L-lactide between 50% and 93% within PLA forms amorphous polymers [16]. The homopolymer PLLA crystallizes, depending on the processing conditions, in three kinds of orthorhombic crystal configurations: α-, β-, and γ-crystals [16]. The α-form occurs with a T_m at around 185°C in a conventional melt or solution crystallization, while the thermal less stable β-form (T_m = 175°C) exists after stretching at high draw ratio and high temperature. Epitaxial crystallization creates the γ-form. Since β- and γ-crystals just occurred under certain conditions, the α-form is the main crystallization form for semicrystalline PLA. Furthermore, depending on the crystallization temperature, the formation of a disordered α-form, named α' was described [53]. The α' crystallized at temperatures (T_c) below 100°C (T_c < 100°C) while above 120°C the neat α-form was formed. In the temperature range between 100°C and 120°C, both forms were observed and a first-order phase transition (α'-to-α) occurred with increasing crystallization temperature. For some PLA materials, a melting peak around the glass transition temperature was reported in differential scanning calorimetry (DSC), which was related to a transition from a mesophase to the α-phase [54] or aging of the PLA material [55].

Generally, the crystallization kinetics are controlled by the nucleation of spherulites and the spherulite growth rate, whereas the latter has the higher impact [56,57]. With increasing molecular weight of

PLA, the spherulite growth rate decreased due to more restricted chain segment motions. Both, the nucleation and the growth rate are influenced by different factors like the crystallization temperature, the addition of nucleating agents, and/or other modifications such as plasticization [58]. Normally, plasticization increases the chain mobility and causes a decrease of the T_g and T_{cc} that leads to an increase of the crystallization ability. In the case of plasticization with PEG, PLA's ability of crystallization is favored by the increase of spherulite growth rate, but it was shown that PEG did not co-crystallize with PLA [45,56,59]. An increased segmental mobility and a decreased surface energy of the lamellae yield a decreased required energy for the chain folding during crystallization [59,60]. As presented in Figure 2.12, the growth rate of PLA was increased by blending with PEG: The higher the PEG content, the higher was the growth rate for PLA crystals. However, for crosslinked and branched polymers crystallization is restricted due to the steric hindrance that results in poor folding properties of the branched architecture. The formed crystals exhibit imperfections caused by chain ends and branching points. It is worth to mention, that increasing the crystallinity significantly worsened the drawability of PLA plasticized with PEG [56].

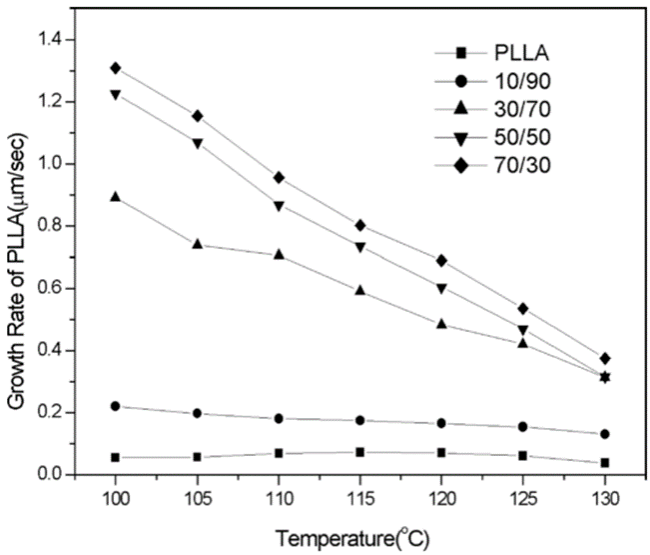

Figure 2.12 Growth rate of crystallization as a function of the temperature for PEG/PLA blends [59].

Despite the slow crystallization kinetics of PLA [61], a further crystallization appears by thermal- or strain-treatment, whereas the latter will be discussed more in detail in the next section (2.5 Deformation Mechanisms of Polylactide). When a plastic material is exposed to a temperature higher than the glass transition temperature the chain motion increases and an ordering of the chains results in a gain of the crystallinity if allowed by the structural properties. This, so called thermal

crystallization, can occur in isothermal or non-isothermal conditions. The kinetics of the crystallization process can be defined by the Avrami model [62], which allows describing the dimensionality of the crystals and concentration of nuclei by the Avrami exponent n and the factor k, respectively [63]. The parameter n is between 0 and 4 and describes the shape of crystallization. In general, the shape varies from rods, over disks to spheres with increasing parameter n [63,64]. Zhou et al. split the Avrami exponent in $n = n_d + n_n$, whereas n_d describes the dimensionality of the growing crystals as one- ($n_d = 1$), two- ($n_d = 2$), or three-dimensional ($n_d = 3$) growing. The time dependence of the nucleation is described by the parameter n_n, which is ideally equal to 0 for instantaneous (heterogeneous) nucleation or equal to 1 for sporadic (homogeneous) nucleation. In reality, n_n is normally in between 0 and 1 [65]. The Avrami parameter k is correlated to the shape of growing crystallites and the type of nucleation. It controls the temperature-dependent growing rate [63,64]. Since PLA crystallizes in general slowly, You et al. [66] investigated the effect of nucleating agents and plasticizers on the crystallization behavior. The PLA with 96% L-lactide content was found to crystallize slowly with a half-time crystallization of over 13 min at 125°C, but after adding a nucleating agent this time was reduced to less than 1 min. Furthermore, the half-time crystallization, which is inversely proportional to the Avrami parameter k, decreased with decreasing crystallization temperature for PLA from more than 13 min at 125°C to less than 6 at 110°C.

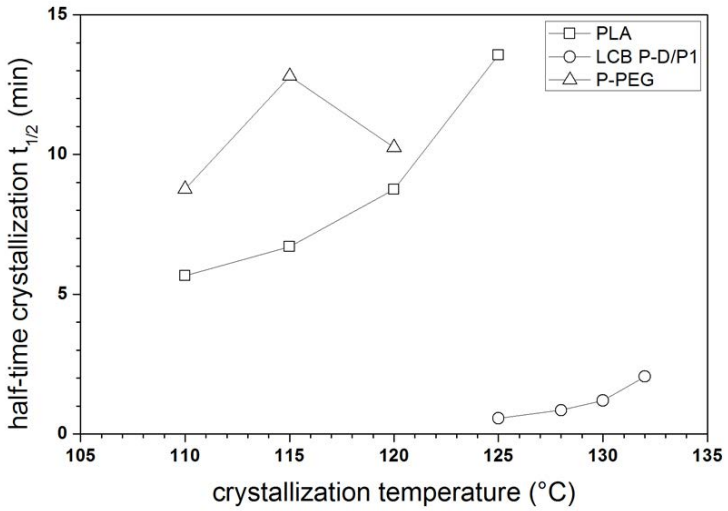

Figure 2.13 Half-time crystallization as function of the crystallization temperature for a PLA with 96% L-lactide (PLA), a mixture of branched and comb-like PLA with D-sorbitol and PEG (LCB P-D/P1), and PLA plasticized with PEG (P-PEG) plotted with the data from You et al.[66].

As clarified in Figure 2.13, the addition of 8.5% of PEG-plasticizer increased the half-time crystallization for PLA at all tested crystallization temperatures. In another study [67], it was shown that the

plasticization with triphenyl phosphate (TPP) had a negative impact on the primary nucleation of PLA. The crystallization rate constant decreased with increasing amount of TPP, but at the same time the crystallization mechanisms were not affected; it just occurred slower. Lai et al. [59] studied the impact of the end groups of a PEG plasticizer (OH or CH_3) on the crystallization of PLLA. For a 50/50 blend (PLA/PEG), the half-time crystallization increased with decreasing the hydrophilicity of PEG end groups: from 501 s (for two OH end groups) to 596 s (for one OH and one CH_3 end group), finally to 929 s (for two CH_3 end groups). The isothermal crystallization at 124°C showed that the plasticization led to two competitive effects. The dilution of PEG caused a decrease of the T_m and therefore reduced the driving force of crystallization, but PEG also lowered the T_g and increased the segmental mobility. Therefore the half-time crystallization first decreased up to a PEG content of 30% and afterward increased again for 50/50 PLLA/PEG [59].

The crystallization kinetics of PLA materials are controlled by many factors, like the temperature, the L-lactide content, and modifications as nucleating agent or plasticizers. Nevertheless, the half-time crystallization ($t_{1/2}$) and the Avrami factor k give an overall evaluation of the crystallization speed and are influenced by the nucleation density and the growth rate [66], while the Avrami exponent n gives the dimensionality of the crystal growth. Hence, the determination of Avrami parameters and the half-time crystallization allows an estimation of crystallization kinetics and their comparison for different PLA-based materials to highlight the impact of plasticizers or nucleating agents. While the impact of plasticizers on the crystallization behavior of PLA were widely reported, studies about the impact of grafted plasticizers or recycling on the crystallization mechanisms are missing up till now.

2.5 Deformation Mechanisms of Polylactide

During their solid state processing and their applications, thermoplastic polymers are exposed to different kind of mechanical constraints. The identification of the underlying deformation mechanisms is crucial to optimize the processing and the durability of these materials. Indeed, PLA can be processed by thermoforming [68,69] and biaxial stretching [70] for packaging applications (cups, films), requiring resistance to impact and high rigidity/strength. Basically, it is desirable that the material accommodates the mechanical constraints by molecular relaxation and orientation, while deformation heterogeneities as crazing should be avoided.

Depending on the temperature at which deformation occurs different molecular deformation mechanisms are active, whereas a clear difference was observed above and below the glass transition temperature of a polymer. Zhang et al. [71] identified the general deformation mechanisms of semicrystalline polymer on the example of isotactic poly(propylene) and separated them depending

on the drawing temperature. Above the T_g, five general deformation mechanisms were active as illustrated in a schematic diagram (reprinted in Figure 2.14). The interlamellar separation increased the space between the crystalline lamellar by stretching of the intermediate amorphous phase and the lamellar stack rotation described the turning of semicrystalline blocks towards an inclined position. Furthermore, three shear mechanisms were defined. The oppositional displacement of crystalline lamella perpendicular to the drawing direction was called interlamellar shear and the intracrystalline shear was separated into the fine chain slip and coarse chain slip. While in the fine chain slip the semicrystalline blocks were sheared, in the coarse chain slip also shearing within the crystals occurred. Below the T_g, deformation mainly involved heterogeneities as voiding or cavitation by crazing while molecular deformation mechanisms were less involved (reprinted in Figure 2.15). When the crystalline layers were oriented perpendicular to the deformation direction, cavitation occurred between these lamellae stacks and propagated perpendicular to the tensile direction. This mechanism is responsible for the rapid failure of the material without or with limited shear mechanisms.

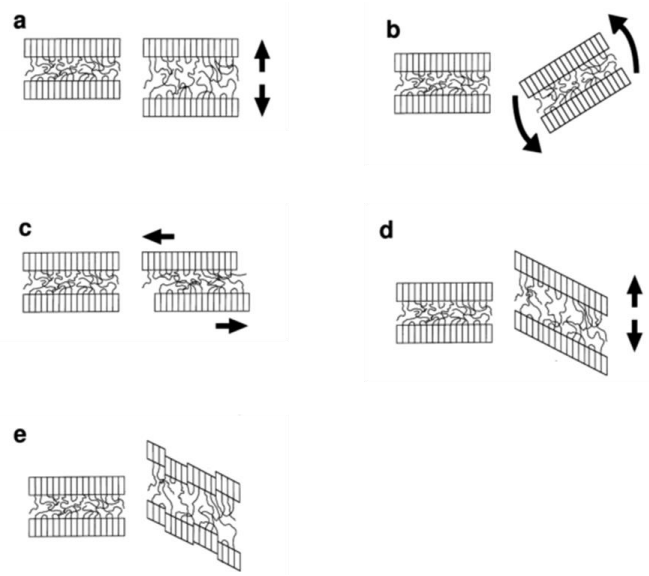

Figure 2.14 Schematic diagram of the various deformation mechanisms operative in a semicrystalline polymer: (a) interlamellar separation, (b) lamellar stack rotation, (c) interlamellar shear, (d) intracrystalline shear 'fine chain slip', (e) intracrystalline shear 'coarse chain slip' [71]. *Deformation above T_g.*

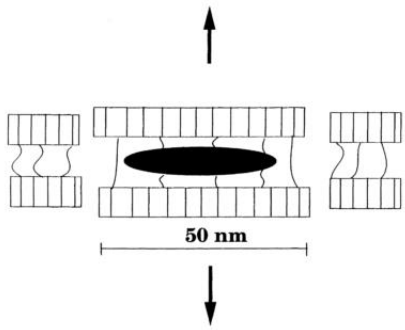

Figure 2.15 Schematic diagram for the cavitation in a semicrystalline polymer [71]. *Deformation below T_g.*

In the case of semicrystalline PLA, the previously identified molecular deformation mechanisms and deformation heterogeneities during drawing were observed, but additional features depending on the initial crystallinity, the drawing temperature, and the presence of plasticizers occurred and were further investigated.

The stress-strain behavior of PLA drawn at room temperature shows the typical curve of a brittle material. The stress increases strongly and the material breaks before the yielding point. PLA offers a deformation of less than 5% and a tensile modulus of about 4 GPa [16]. By increasing the temperature above the T_g the chain mobility could be increased and the typical plastic deformation occurs. First, the stress increases strongly up to a yield point and drops suddenly before increasing slightly again. Depending on the drawing conditions, for PLA, two types of deformation mechanisms were defined, which include (I) ordering of the amorphous phase, and (II) transformation of initial crystalline phases. Additionally, occurring voiding was noted as a deformation heterogeneity. These mechanisms occurred separately, in parallel, or after each other depending on the conditions like the drawing rate and temperature [72–75]. Zhang et al. [72] described the importance of the strain rate for the molecular orientation and crystallinity. During the stretching of amorphous PLA at 75°C, the two mechanisms of crystal formation and crystal damage competed. At low strain, orientation-induced crystallinity occurred, but with increasing strain, these crystals broke and voiding and cavitation appeared. At high strains, both mechanisms were active, but the crystallinity increased proving that more orientation of amorphous phase occurred than crystal damage. The ratio between the formation of new crystals and breaking of existing crystals depended on the strain rate, and higher strain rates led to a stronger increase of crystallinity and orientation.

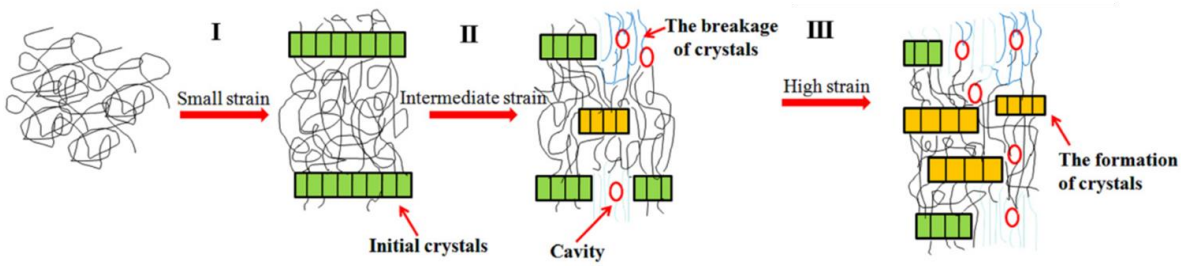

Figure 2.16 Schematic evolution of amorphous PLA with increasing strain above the T_g [72].

For amorphous PLA, Zhang et al. [72] highlighted the formation of crystalline already at low strains as the first mechanism. Hence, the initial crystallinity was studied by Zhang et al. [75] as a crucial factor for the deformation mechanisms and more attention was paid on cavitation, which led to a damage of the material. To this end, the PLA samples were annealed at 120°C for 5h to promote the formation of stable α crystals and tested at temperatures above the glass transition of PLA. While the strain induced crystallization formed the α' phase [72], annealing led to the formation of more stable α crystals [75]. The structure evolution was subdivided into three parts: first, the pre-yielding region at

low strain, second, plastic deformation region including the development of necking and third, the strain hardening stage till fracture. At temperatures slightly above the glass transition, the scenario regarding the development of cavitation consisted of the following three steps. First, cavitation initiated and developed perpendicular to the strain direction, while the amorphous phase started to orientate in the strain direction. Second, the cavitation progressively orientated in the strain direction and, at the same time, the crystalline lamellae fractured providing additional cavitation between the lamellae residues. In the last step, crystals further fractured and cavitation further developed. In contrast, for higher temperatures, the mechanism was found to be different. In the first two steps, there was neither fracture of the initial crystals nor formation of cavitation. Just the orientation of amorphous chains increased. In the last step, cavitation was parallel to the strain direction and fracture of the crystals occurred. In summary, higher temperatures reduce the formation of cavitation and the further fracture of lamellae with increasing the strain. The above-described deformation mechanisms of annealed PLA at a temperature slightly above the T_g and far above the T_g are illustrated in Figure 2.17.

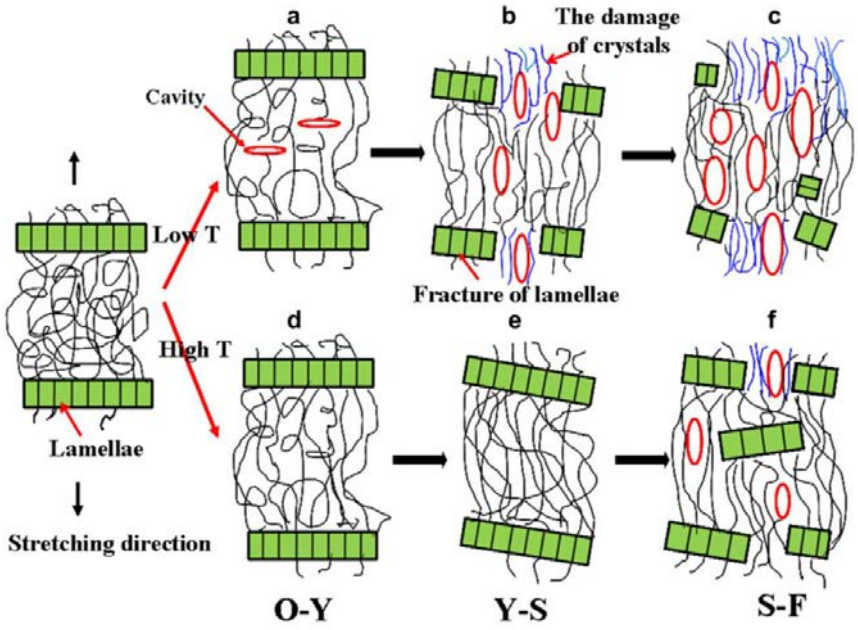

Figure 2.17 Deformation mechanisms of annealed PLA at temperatures slightly and far above Tg [75].

The above-shown mechanisms point at the importance of the initial crystallinity, but also at the importance of the drawing temperature. Stoclet et al. [73,74] studied the different disorder to order transitions at different temperatures for a PLA with 4.3% D-lactide. At higher strains (> 130%) ordering occurred and depending on the temperature, mesophase or α' phase was formed. While lower

drawing temperatures (≤ 70°C) created the mesomorphic phase and higher temperatures created α' phase, at the intermediate temperature (80°C) both phases occurred. In a further study, Stoclet et al. [76] investigated the impact of the stereoisomers of PLA on the formation of the mesophase. It was shown, that a D-lactide content of more than 8% inhibited the thermal- as well as strain-induced crystallization. While the maximum crystallinity strongly decreased with increasing D-isomer content, the strain induced crystallization kinetics were independent of the D-isomer content, but an increase of D-content decelerated the isothermal crystallization. Nevertheless, the samples that crystallized formed at drawing temperatures (T_d) close to the T_g ($T_d = T_g + 5$°C) the mesophase, and far above the T_g (T_d = 90°C) the α' phase.

Since PLA is mainly applied at room temperature, special attention was paid on the craze formation which is the main mechanisms occurring during cold drawing. A craze was defined as a cavitation with fibrils that are perpendicular to the drawing direction of the craze [77,78]. For PLA as a glassy amorphous polymer, Stoclet et al. [55] described two main deformation heterogeneity mechanisms during cold drawing, which are reprinted in Figure 2.18. The first one, shear banding, occurred in the amorphous phase with an angle of about 45° to the direction of the applied stress. These shear bands were localized or diffuse but did not induce volume changes in the samples. The second one, crazing, caused sample dilatation and the crazes grew perpendicular to the strain direction. Note that crazes also are generated along shear bands and both conventional crazes and shear band-induced crazes can interact. As already seen for the other deformation mechanisms, such as the transformation of amorphous or crystalline phases, the lamellae fracture, shear banding and crazing, also depend on the conditions of deformation. It was shown that for polymers, where crazing was dominant, higher temperature or preorientation could lead to a preferred shear banding instead of crazing [55]. Crazing occurred all the time even when an increase of initial crystallinity favored the brittle behavior [79].

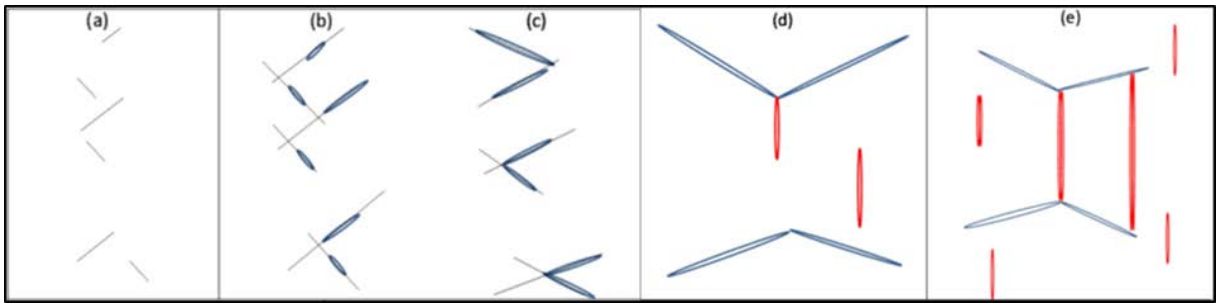

Figure 2.18 Schematic representation of the chronological occurrence of plastic deformation mechanisms during drawing of PLA below glass transition temperature (tensile axis is assumed equatorial) with: (a) nucleation of the shear bands, (b) shear band propagation and simultaneous opening into shear band crazes, (c) orientation of the "shear band crazes" towards the drawaxis and formation of intersections, (d) Nucleation of "standard crazes" both at "shear band crazes" intersections & into the matrix, (e) "standard craze stabilization" by the shear band and "shear band crazes" [55].

Different ways to improve PLA's drawability even at temperatures below the glass transition temperature of PLA were discussed in section 2.3 Modification of Polylactide. Effective plasticization increased the free volume, decreased the glass transition temperature and improved the flexibility of the material. Kowalczyk et al. described the deformation mechanisms in PLA blended with a natural rubber [80] or with an aliphatic-aromatic copolyester [81] and in both case, a two-phase system was observed. The initial deformation of PLA was described by the formation of cavitation, which was possibly due to imperfections and impurities (Figure 2.19). Already at low strains (Figure 2.19 a), small shear bands were observed at the tips of the crazes. With increasing strain (Figure 2.19 b and c), further shear banding was observed and at the highest strain, the crazes obtained a curved shape without sharp edges. The deformation of the blend of PLA with natural rubber is represented in Figure 2.20, the initial deformation was dominated by crazing (Figure 2.20 a) and Kowalczyk et al. [80] described with increasing strain the appearance of islands, which were surrounded by shear bands (Figure 2.20 b). For the highest deformation, the crazes nearly disappeared and just further shear banding occurred (Figure 2.20 c). The blending improved the flexibility and therefore, the deformation mechanisms were impacted. However, for all deformations of PLA and blended PLA, the shear banding was determined to dominate the deformation mechanisms.

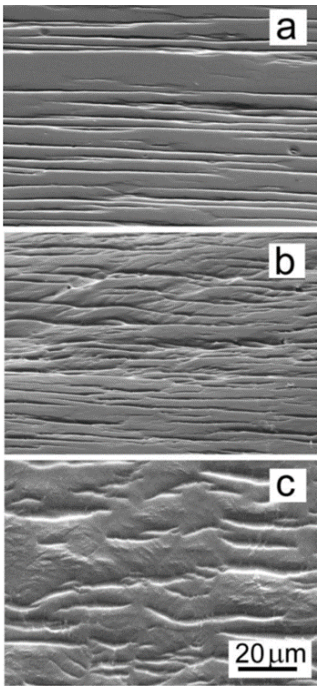

Figure 2.19 SEM micrographs showing the surface of the gauge section of PLA specimen drawn to the strains of (a) 0.05, (b) 0.10, and (c) 0.30 [80]*. Strain direction vertical.*

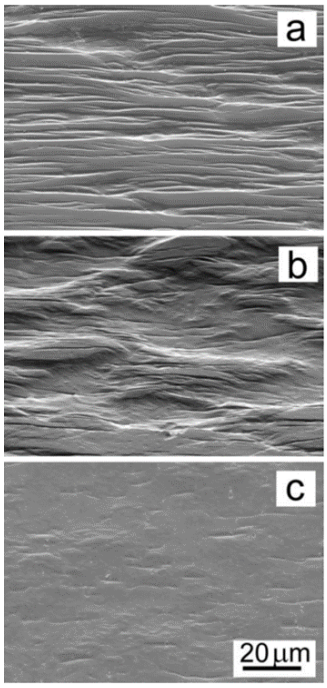

Figure 2.20 SEM micrographs showing the surface of the gauge section of PLA blended with natural rubber specimen drawn to strains of (a) 0.05, (b) 0.10, and (c) 1.00 [80]*. Strain direction vertical.*

In addition to the deformation of the PLA matrix, which was mainly dominated by shear banding, the blending with natural rubber or a copolyester formed particles of a second phase surrounded by the PLA matrix. It was shown that, in the case of natural rubber, the crazes started from the rubbery particles resulting in a lower yield stress [80]. Furthermore, cavities were observed in the rubbery particles. In almost the same manner, cavitation occurred in the copolyester particles, whereas the copolyester hindered a crazing and the cavitation inside the particles enabled shear yielding and boosted the toughness [81]. In both cases, the particles were deformed with the matrix and obtained an elongated shape as seen in Figure 2.21 and Figure 2.22.

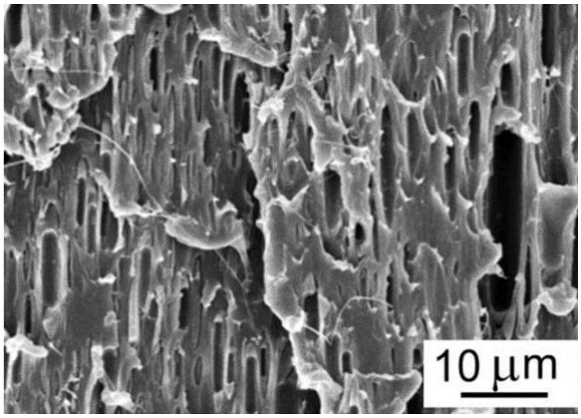

Figure 2.21 SEM micrographs of the gauge region of PLA/natural rubber blend strained to 1.0 and cryo-fractured parallel to the drawing direction (vertical) [80].

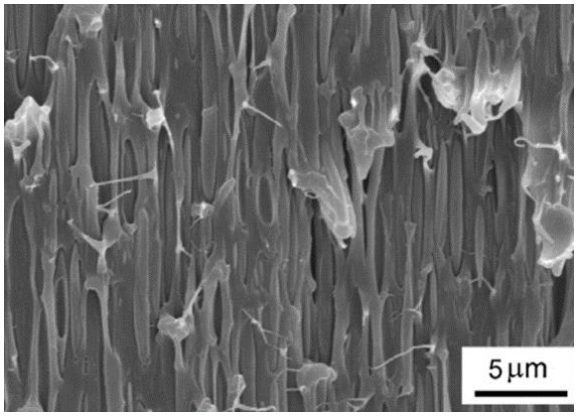

Figure 2.22 SEM micrograph of the gauge region of PLA/copolyester blend strained to 3.3 and cryo-fractured parallel to the drawing direction (vertical) [81].

Just as blending, the plasticization by reactive extrusion affected the mechanical properties and increased the flexibility. Consequently, a difference between the deformation mechanisms of plasticized PLA and neat PLA can be observed. Kfoury et al. [50] compared the deformation of PLA plasticized by reactive extrusion with acrylPEG and L101 to PLA blended with poly(acrylPEG). The SEM images after deformation in Figure 2.23 indicate a similar trend as observed for the blends with the natural rubber or the copolyester. It was assumed that the formation of voids inside the rubbery inclusions of poly(acrylPEG) led to a lower yield stress, but increased the toughness. As already seen for the blended samples with the natural rubber or the copolyester, the matrix, as well as the inclusions, deformed and no debonding between acrylPEG-domains and the matrix were observed.

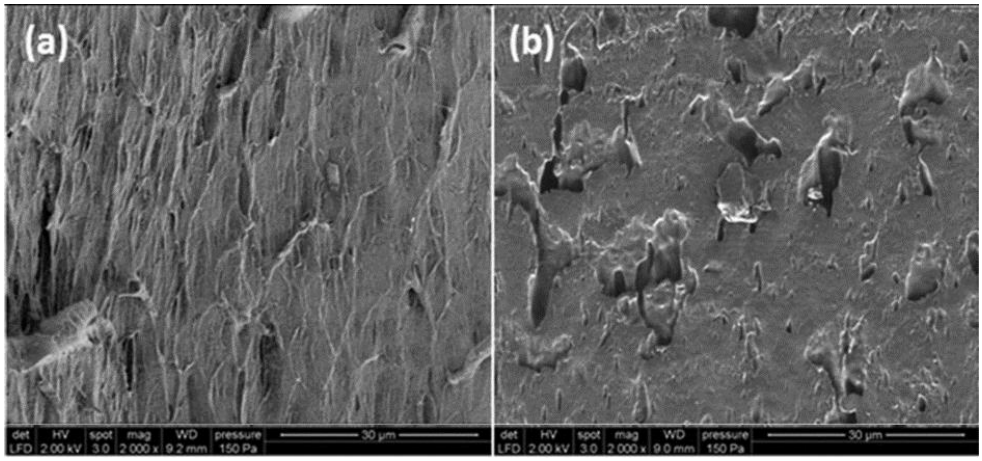

Figure 2.23 SEM images on cryo-fractured surfaces in the direction of tensile drawing of (a) PLA/acrylPEG/L101 and (b) PLA/poly(acrylPEG) [50].

Since the plasticization improves the drawability at room temperature, the deformation mechanisms are also affected and should be investigated. The plasticization with acrylPEG increased also the initial crystallinity and recent studies [75], as mentioned above, proved the impact of initial crystallization on the deformation mechanisms, but detailed studies concerning the crystallization and phase transformation in plasticized PLA during drawing are missing.

2.6 Polylactide's End-of-Life Scenarios

Due to pollution caused by plastic, the end-of-life for these kinds of materials became more and more important within the last years. Therefore, the development of new materials also focused on their end-of-life options. PLA is promoted as a bio-based and (bio)degradable polymer, but beside the biodegradation, it offers also hydrolytic, thermal, and photodegradation [6,82]. In addition, PLA is suitable for incineration with energy recovery since no poisonous or corrosive gases are released [16]. For the first applications of PLA in the biomedical field, studies focused on the biodegradation for implants or drug delivery systems under the physiological conditions of the human body. First, PLA is hydrolyzed and afterward, the remaining oligomers are metabolized by the cells. The first step of hydrolysis is important since, under the conditions in the human body, biodegradation of PLA is just possible for low molecular weight PLA [4,16]. Hence, it is obvious that biodegradation just occurs at certain conditions. Packaging applications require PLA with a high molecular weight to obtain high mechanical performance. Along with the molecular weight, the efficiency of biodegradability is impacted by crystallinity, impurities, and the surrounding conditions such as temperature and moisture [16]. During the biodegradation, high molecular weight PLA is first hydrolyzed and degrades

to lower molecular weight products (monomers and low molecular weight oligomers). Subsequent, microorganisms split these products and finally, carbon dioxide and water are obtained [4,16]. Figure 2.24 illustrates the biodegradation of a PLA plastic bottle produced by Nature Works and used in the United States by Biota® [6]. PLA is promoted as a (bio)degradable polymer, but as already seen, the biodegradation requires specific conditions. A degradation as shown in Figure 2.24 requires high temperatures (> 60°C) and high humidity (> 90%) and therefore, PLA, as used in packaging applications, is not degraded in the backyard or a home composter in the same time frame [16]. The conditions in a home compost lead to a hydrolytic degradation that takes a long time for high molecular weight PLA. Due to this fact, PLA offers no advantages compared to common plastic material concerning the end-of-life and can be considered as degradable, but just under special conditions as biodegradable [17,83]. Therefore, the notation of "(bio)degradation" was chosen for PLA.

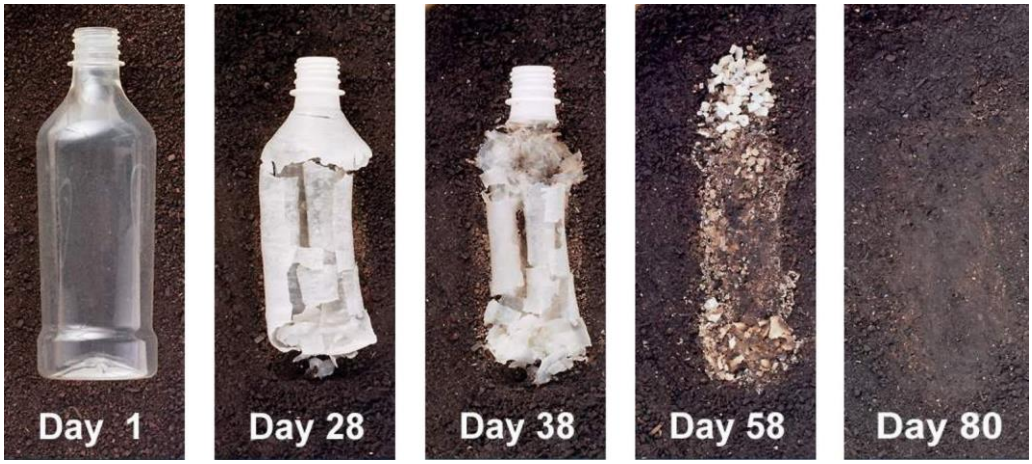

Figure 2.24 Biodegradation process of a bottle made of PLA [84].

The (bio)degradation as an end-of-life option for PLA bears problems since it is cost and energy consuming to obtain the conditions for biodegradation and hence, recycling provides an end-of-life alternative. Recycling describes the procedure to treat or process used or waste materials to make them suitable for reuse. The recycling extends the life cycle of materials, lowers the environmental pollution and the consumption of raw materials. One possibility is the chemical recycling upon the LOOPLA® process [85,86], which starts in the same way like the biodegradation by hydrolysis of the high molecular weight PLA, but afterward, the monomer lactic acid is recovered and can be used further [16]. After the chemical recycling, the monomer can be used again, but it would be more efficient to reuse the already existing material. Since for other plastic materials, such as PET or PE,

well-developed mechanical recycling cycles with rates up to one-third are existing, the introduction of new bio-based materials on the market is challenging. On one side, the recycling of these new materials should be as good developed as for the existing materials and on the other side, the new materials should not disturb the existing recycling cycles since it was shown that PLA traces in PET recycling worsen the properties of PET strongly after recycling [4,86]. Therefore, the separation of the new materials from the old materials plays an important role in the development of recycling. However, before applying a recycling cycle in industrial scale, enough material that can be recycled, has to exist and the possibilities of recycling have to be known. Different studies dealt with the mechanical recycling of PLA at the laboratory scale and proved a thermal degradation effect during the reprocessing [82,86–89], which was attributed to various phenomena: hydrolysis by small amounts of water, zipper-like depolymerization, main-chain decomposition by oxidation, intermolecular transesterification to monomer and oligomeric esters as well as intermolecular transesterification to PLA with lower molecular weight or monomers [33]. Thermal degradation of polyesters like PLA was governed by the internal elimination of monomer molecules and non-radical backbiting creating intramolecular transesterifications. The remaining polymerization catalyst from the PLA production could catalyze, but also humidity promoted the degradation [82,90,91].

Badia et al. [92] summarized five routes for the degradation of PLA as reprinted in Figure 2.25. The first route, hydrolysis route, occurs in the presence of water or humidity and forms two oligomers from the PLA chain, each with a hydroxyl and a carboxyl function as chain ends. The second route is an esterification, where an ester function is created from the hydroxyl group of a PLA chain end by an addition of e.g. methanol. The third route describes the intramolecular transesterification that starts either from a chains end and creates a backbiting reaction or starts from the middle of a chain creating cycling oligomers and shorter linear PLA chains. The fourth route contains intermolecular transesterification reactions. The ester units of different chains are switched with a resulting increase of heterogeneity. The last, fifth route summarizes all chain scission reactions that especially occur above the melting temperature. Furthermore, oxygen can force radical reactions, which lead to degradative chain scission. For the recent durable applications of PLA, thermomechanical recycling is currently under development as an alternative end-of-life scenario. This procedure was often simulated in laboratory scale by the reprocessing of the material, where degradation mainly occurred by chain scission upon the thermal and mechanical constraints. The degradation during recycling of PLA materials leads normally to a worsening of the mechanical performance.

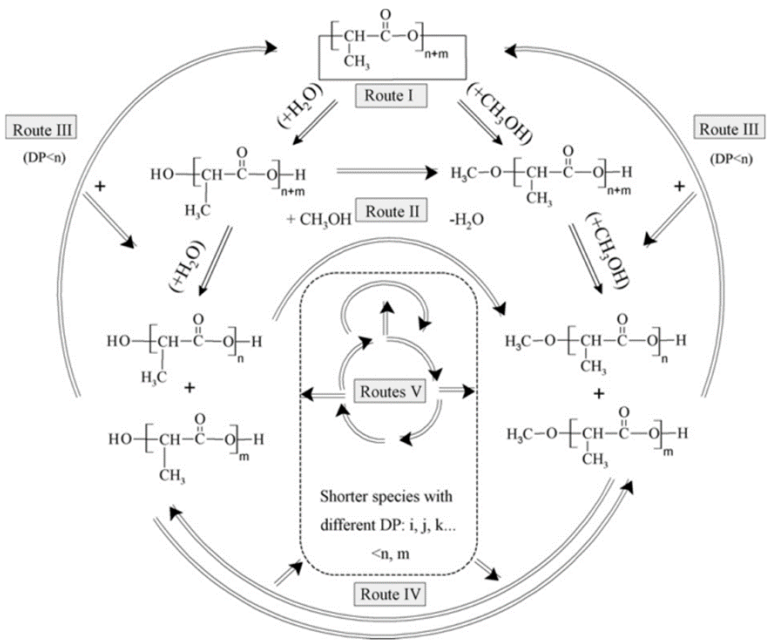

Figure 2.25 Summary of possible degradation mechanisms in PLA [92].

Żenkiewicz et al. [87] analyzed the mechanical and thermal properties of up to 10 times extruded PLA. While the tensile strain at break was independent of the extrusion number, the tensile strength decreased by 5.2% and the impact strength decreased by 20.2% (Figure 2.26). Furthermore, the cold crystallization temperature decreased from 125.1°C to 115.8°C and the crystallinity of the amorphous PLA without extrusion increased to 34%. Even if no analysis of the molecular weight was conducted in this study, Pillin et al. [89] proved the decrease of molecular weight after multiple injections of PLA as a reason for the increased crystallinity and the decrease of mechanical performance. The molecular weight decreased continuously with each injection so that after four injections 56% and after seven injections 36% of the initial molecular weight were gained. However, chain scission mechanisms were the main reason for the worsening of PLA's properties after recycling [87–89].

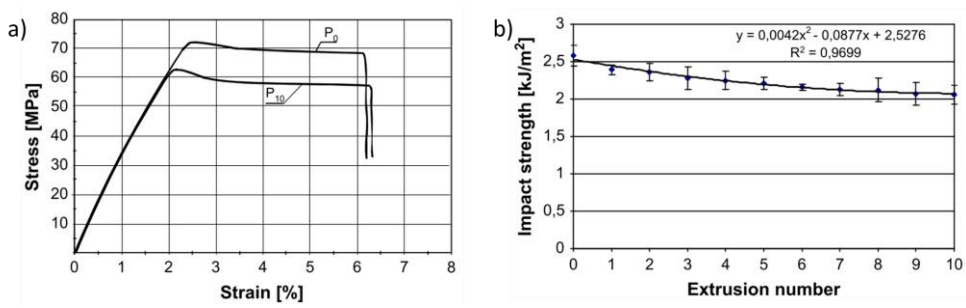

Figure 2.26 Evaluation of mechanical properties after up to 10 extrusions: (a) representative tensile testing curves for the neat material and after 10 extrusions and (b) impact strength as function of the extrusion number [87].

Nevertheless, the results proved that PLA after reprocessing was no more suitable for the initial applications, but the recycled material could be used as an additive to virgin PLA pellets with an optimized proportion [87]. Furthermore, it was shown that the addition of stabilizers, such as quinone, could diminish the degradation [89].

Due to the brittle behavior of PLA at room temperature, PLA was modified in different ways to improve the properties and make it more suitable for applications. The end-of-life scenarios for these materials shall also be investigated. Nevertheless, the modifications cause often a loss or decrease of initial advantages of PLA. Depending on the copolymer or plasticizer, the resulting material is not (bio)degradable or the degradation products are harmful to the environment. Therefore, especially for modified PLA materials, the mechanical recycling should be studied in detail and adapted to the applications to obtain competitive materials that could replace petrol-based plastics. Till now, a few studies focused on the recycling of blended or plasticized PLA materials by analyzing the materials after multiple extrusions to simulate recycling in the laboratory. The recycling of PLA/PS blends, reported by Hamed et al. [93], led to a decrease of the transparency of the materials as well as a debasement of the mechanical properties, like the Young's modulus, the strain at break and the stress at break. This deterioration of mechanical performance was reasoned by the decrease of PLA's molecular weight due to thermal degradation. Scaffaro et al. [94] studied the preparation and recycling of plasticized PLA with Polyone and Sukano as plasticizers. While the dispersion of the plasticizer improved after the first recycling, the same disadvantages as for the recycling of PS/PLA blends were observed. With an increasing number of reprocessing the molecular weight decreased and the crystallinity increased. The higher crystallinity caused higher stiffness but worsened all other mechanical "plastic" properties. In summary, the recycling of PS/PLA and plasticized PLA with Polyone or Sukano bore the same problems as reported for neat PLA, since the degradation of PLA ruled the reprocessing.

Despite efforts to avoid the degradation of PLA during recycling, the reuse of PLA or plasticized PLA in the same applications as before seems to be complicated due to the thermal degradation and alternative applications after recycling gained interest. For example, recycled PLA was degraded with polyols and blended with starch for further applications [95]. Nevertheless, the recycling of PLA and especially of plasticized PLA is challenging and needs further research to obtain competitive bio-based materials.

2.7 Research Needs

Poly(lactide) (PLA) as a bio-based and (bio)degradable polyester offers the possibility to replace common, petrol-based plastic materials in an environmental-friendly way, but as all bioplastic materials, it bears drawbacks. Due to its brittle behavior at room temperature PLA cannot be used in various applications, and plasticization methods, especially by reactive extrusion, were developed to overcome the disadvantages of current plasticization methods. In previous works, the reactive plasticization of PLA with poly(ethylene glycol) methyl ether acrylate (acrylPEG) as a plasticizer and Luperox 101 (L101) as a free radical initiator, yielded a PLA-based material with a complex structure: PLA was partially crosslinked and plasticizer inclusions – partially grafted and partially free – were created. This material exhibited promising mechanical properties but its structure was not fully investigated. For example, no analysis has been performed on the inclusion structure and on the inclusion-matrix interface that are expected to influence material mechanical properties. It is to be noted that grafting reactions can occur at this interface. A complementary treatment of plasticized PLA enabling to increase mechanical properties may be isothermal crystallization that again has never been studied. An in-depth study of plasticized PLA structure is consequently needed to understand if this structure can be further optimized by modifying processing conditions. Last, the evolution of plasticized PLA structure from the lab-scale to the pilot-scale has never been done to verify if lab material properties are retained or not during the scale-up.

Since the mechanical performance of a polymer material determines its solid-state processing ability and application areas, it is of primary importance to identify its deformation mechanisms in terms of molecular and heterogeneity aspects. For PLA-based materials, deformation mechanisms were previously identified and analyzed as a function of the drawing temperature, the initial crystallinity, and the plasticization. However, the impact of a grafted plasticizer on the deformation mechanisms has not been tackled and needs a detailed study focused on a multiscale characterization approach.

A last critical point for bioplastics are the end-of-life scenarios. Since common plastics offer already well-developed recycling cycles the introduction of new bio-based materials should be associated with their recycling possibilities. Detailed studies of thermomechanical recycling of PLA were conducted, but lack for plasticized PLA. Especially the impact of reprocessing on the structure requests a further analysis.

The figure below summarizes the three main research needs related to the formation of a PLA-based material with grafted plasticizer inclusions. While the processing of this grade of plasticized PLA was already developed, the structural properties of this material will be further investigated. The structure takes also the center for the investigation of the deformation mechanisms and the reprocessing possibilities of this plasticized PLA.

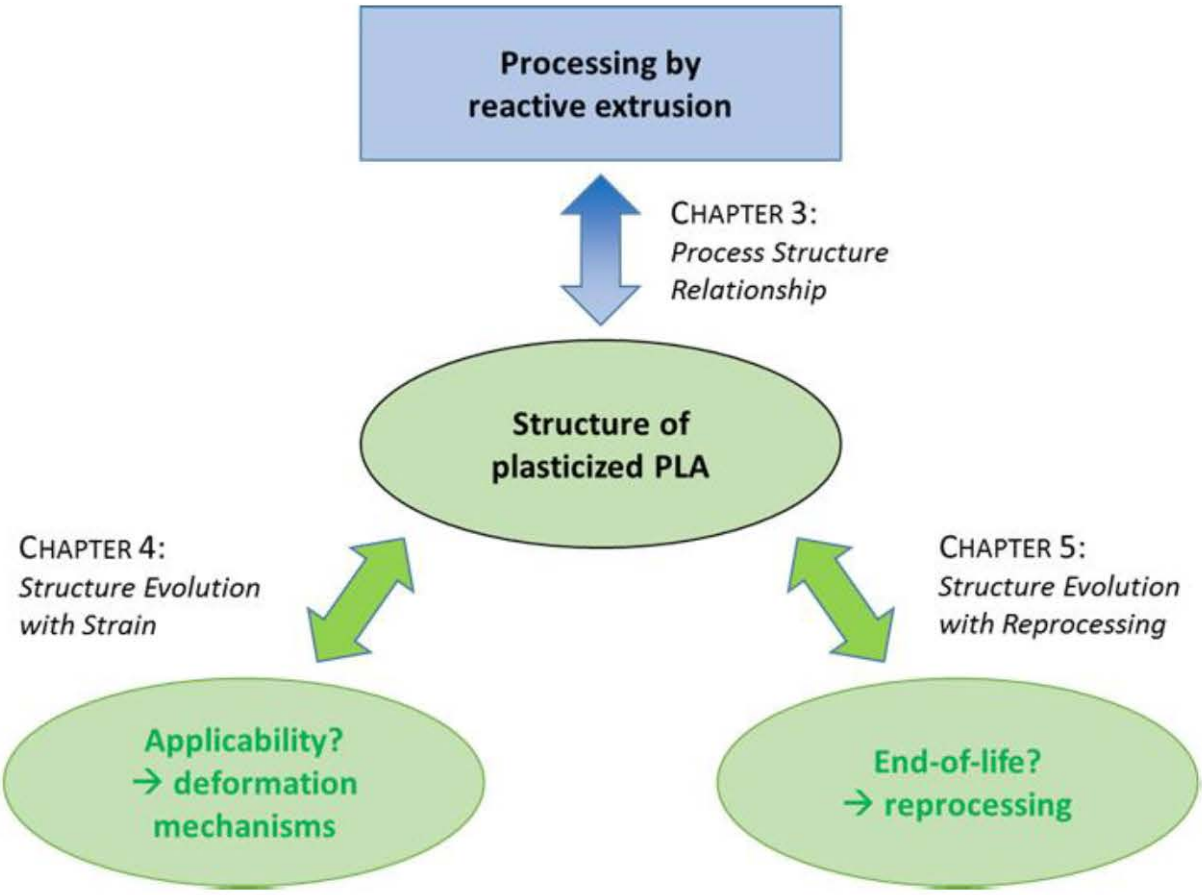

3 Process-Structure Relationship for Plasticized Polylactide

3.1 Introduction

Polylactide (PLA) is one of the most promising biomaterials for packaging, but its low toughness and high brittleness limit the applications at room temperature. Plasticization, as a strong tool to adapt the properties of PLA to the needs of the applications, improved, on one side, the toughness and the ductility, but, on the other side, often caused a loss of strength. Furthermore, in the case of a simple mixing between the plasticizer and the matrix material, the plasticizer often migrates and phase separation occurs. Therefore, reactive extrusion was developed to graft a plasticizer chemically on the matrix and to avoid this migration and to obtain materials with a good flexibility-strength balance.

In the case of PLA, two research groups worked on PLA's plasticization by reactive blending and grafted poly(ethylene glycol) methyl ether acrylate (acrylPEG) onto the PLA matrix [41,50–52]. Both research groups proposed the same mechanism for the grafting initiated by thermal decomposition of either DCP [51,52] or Luperox L101 [41,50]. During the reactive blending, the radicals initiated competitive reactions. On one side, these radicals abstracted a hydrogen from the PLA backbone and created PLA radicals that reacted with the acryl function of PEG and grafted rubbery poly(acrylPEG) inclusions by polymerization. On the other side, a homopolymerization of the plasticizer by the acryl function without grafting occurred and formed PEG oligomers. This new methodology for the plasticization of PLA led to an original structure of plasticized PLA with partially free and partially grafted poly(acrylPEG) inclusions, which could also graft onto two PLA backbone chains and enforce crosslinking by recombination of radicals [41,51]. The method of reactive blending managed to improve ductility and toughness compared to neat PLA. The properties of the materials, which were produced by the two research groups, are compared in Table 3.1. Kfoury et al. [41,50] compared neat PLA with the PLA/acrylPEG blend and the PLA/acrylPEG/101 reactive blend. Furthermore, they polymerized the plasticizer separately (poly(acrylPEG)) and blended it with PLA (PLA/poly(acrylPEG). It was noticed, that the reactive blending increased the elongation at break and the impact energy strongly, and the reactive blending increased the toughness even higher to a value of 101.6 kJ/m^2, but the elongation at break was slightly lower compared to the simple blending but still higher than for neat PLA. The blending of PLA with the polymerized plasticizer improved both, the elongation at break and the impact energy, but both parameters were much lower compared to the other two plasticized materials. The study of Choi et al. [52] proved the enhancement of ductility and toughness by both blending and reactive plasticization, but in their case, the reactive plasticization lowered both, the elongation at break and the also the impact energy compared to the simple blending. The mechanical parameters are influenced by the thermal and morphological properties, which are strongly impacted

by the plasticization. For example, a decrease of the glass transition temperature assists normally the ductile behavior, while an increase of the crystallinity increases toughness. Both research groups proved the decrease of the glass transition temperature by plasticization, no matter if blending or reactive plasticization, and indicated an increase of the crystallinity, especially for the samples after reactive plasticization. Anyhow, the existing studies about the reactive blending of PLA with acrylPEG as a plasticizer and a free radical initiator proved that it is possible to design a material based on PLA with a good balance between the mechanical parameters, but until now these studies missed evaluating the detailed structure of the by reactive extrusion plasticized PLA.

Table 3.1 Comparison of the parameters for the efficiency of plasticization: elongation at break, toughness, glass transition temperature and crystallinity for PLA/acrylPEG/initiator materials after blending and reactive blending. Data from Kfoury et al. [41,50] *and Choi et al.*[52].

	elongation at break ε_u (%)	impact energy I.E. (kJ/m^2)	glass transition temperature T_g (°C)	crystallinity X_c (%)	
PLA	4	2.8	61	0	[41]
PLA/acrylPEG (80/20)	230	86.0	29	2	[50]
PLA/acrylPEG/L101 (79/20/1)	155	101.6	n.d.	33	[41]
PLA/poly(acrylPEG) (80/20)	37	35.5	42	6	[41]
PLA	5.9	2.5	59.3	0.8	[52]
PLA/acrylPEG (80/20)	22.8	13.7	46.9	17.6	[52]
PLA/acrylPEG/DCP (79/20/1)	13.0	9.7	45.9	21.3	[52]

n.d. not detected

Since the thermal properties often limit the application range a detailed analysis of the thermal properties via differential scanning calorimetry (DSC) is favored for new materials. PLA's high glass transition temperature around 60°C explains its brittle behavior at room temperature. Plasticization increased the chain mobility and decreased, therefore, the glass transition temperature, and a more ductile material arose as proved in different studies [41,50–52]. In addition to the glass transition temperature (T_g), a thermal characterization by DSC gives also information about the melting (T_m) and cold crystallization temperature (T_{cc}) as well as the crystallinity index (X_c) of the material. The cold crystallization enthalpy ΔH_{cc} and the melting enthalpy ΔH_m allow the calculation of the crystallinity index with the equilibrium melting enthalpy ($\Delta H_{m,0}$) of the 100% crystalline polymer. In blended materials, it is important to consider the part of the material that crystallizes. In the case of PLA/PEG blends, it was shown that no cocrystallization occurred and just PLA crystallized [45,56,59], which is

expressed by the amount of PLA x_{PLA}. In 1973, Fischer et al. [96] determined a value for $\Delta H_{m,0}$ of 1600 cal/mol corresponding to 93 J/g for a 100% crystalline PLA. The crystallinity was calculated with the DSC determined parameters according to Equation (3.1).

$$X_c = \frac{\Delta H_m - \Delta H_{cc}}{x_{PLA} \cdot \Delta H_{m,0}} \cdot 100\% \tag{3.1}$$

The thermal properties of polymer materials depend strongly on their thermal history. Therefore, in DSC always two heating stages are conducted. The first heating stage is associated with the materials properties as-processed and the second heating stage allows a comparison between differently processed materials since they have after the first heating and cooling stage the same thermal history.

It was shown that plasticization by reactive blending increased the crystallinity (Table 3.1), and hence, the crystallization behavior is an important characteristic to study. The Avrami model allows specifying the parameters of crystallization kinetics that are addicted to the crystal nucleation and growth rate. The Avrami Equation (3.2) describes the typical S-shaped curve of the crystallinity index X_c as a function of the crystallization time with the Avrami exponent n and the Avrami factor k, whereas n provides information about the nature of the crystal nucleation and crystal growth geometry, and k reflected the overall rate constant associated with both nucleation and growth contributions [97]. The determination of the Avrami parameters enables the calculation of the half-time crystallization $t_{1/2}$ by Equation (3.3). The half-time crystallization defines the time when the crystallization is half finished.

$$X_c(t) = 1 - \exp(-k\, t^n) \tag{3.2}$$

$$t_{1/2} = \left(\frac{\ln(2)}{k}\right)^{\frac{1}{n}} \tag{3.3}$$

The Avrami parameters, as well as the half-time crystallization, allow the comparison of the crystallization kinetics of different material, even though the Avrami parameters were interpreted differently depending on the study [59,62–67].

This chapter aims at the structural analysis of plasticized PLA obtained by reactive blending. PLA was plasticized with poly(ethylene glycol) methyl ether acrylate (acrylPEG) and the radical initiator

Luperox (L101) in the weight composition 79/20/1 to obtain a ductile material with improved impact toughness. Previous research showed the formation of a weakly crosslinked PLA matrix with partially grafted and partially free plasticizer inclusions [41,51]. To better understand the structure formation of PLA, it is worth to study the impact of the formulations on the properties of PLA-based materials, including pPLA, PLA/L101, PLA/acrylPEG, and neat PLA. Special attention is paid to the thermal properties, the morphology, and the crystallization behavior. The second part focuses on a possible scale-up from a batch to a continuous process to check the industrial practicability of this plasticization method of PLA. An analysis of the chemical structure of the inclusions is conducted and the thermal and morphology behavior allows a comparison to the batch-wise produced samples.

3.2 Analysis of the Structure

3.2.1 Processing of Plasticized Polylactide in a Batch-Compounder

The details about the processing equipment are given in Appendix A.2 Processing Equipment and the description of the characterization methods can be found in Appendix A.3 Characterization Methods for Chapter 3: Process-Structure Relationship.

In the previous research studies, PLA was plasticized with different plasticizers and initiators in different compositions [41,50–52]. For the structural analysis of plasticized PLA, poly(ethylene glycol) methyl ether acrylate and 2,5-Bis(*tert*-butylperoxy)-2,5-dimethylhexane (Luperox101 or L101) were chosen as the plasticizer and the free radical initiator, respectively. The plasticizer showed a good compatibility with PLA and restricted leaching after reactive grafting [41]. The initiator Luperox L101 was selected for several reasons: L101 is known as a food additive by the Food and Drug Administration (FDA) (Code of Regulation; Title 21 “Food and Drugs” in “Food Additives”) [98] and it offers a half life time of 1 min at 180°C that was suitable for the reaction conditions [99]. In a previous study, the selected composition of PLA/acrylPEG/L101 79/20/1 wt% improved the impact toughness strongly to over 100 kJ/m^2 as well as the elongation at break to over 150% [50]. Nevertheless, depending on the processing conditions and the composition the properties of plasticized PLA varied. For this reason, the roles of the different components (matrix material, plasticizer, and initiator) were analyzed. All samples were processed batch-wise in a micro-compounder at 180°C under nitrogen purge with a screw speed of 50 rpm to have comparable processing conditions for all the materials. The samples are listed in Table 3.2 with their composition and a description. For the plasticized PLA, the PLA was first melted in the micro-compounder and then the mixture of liquid plasticizer and liquid initiator was introduced. In the following, this grade of plasticized PLA is called pPLA. To analyze the influence of the different components, PLA was just blended with the plasticizer PLA/acrylPEG (80/20),

or the initiator PLA/L101 (99/1). The physical mixing of PLA/acrylPEG was already analyzed [41,51]. The mixing between PLA and the initiator L101 led to branching, crosslinking and/or chain scission [100]. Furthermore, acrylPEG was first polymerized with the initiator acrylPEG/L101 (95/5) and the resulting poly(acrylPEG) was mixed with PLA in a ratio 79/21 PLA/poly(acrylPEG), to obtain a material with the same content of PLA/acrylPEG/L101 as the pPLA. However, Kfoury et al. [41] described the structure of pPLA with a plasticized PLA matrix, containing inclusions of polymerized plasticizer, that partially grafted on the matrix or formed crosslinks. Therefore, a pPLA sample after removing the non-grafted amount of the plasticizer by Soxhlet extraction from methanol was analyzed as well, called pPLA aS. The amount of extracted, non-grafted acrylPEG was about 7 wt%, which was in good agreement with the literature [41]. Finally, neat PLA was extruded under the same conditions as a comparison sample.

Table 3.2 Sample names, description, and their composition for pPLA structural analysis.

sample name	composition (theoretically, wt%)	description
pPLA	79/20/1 PLA/acrylPEG/L101	plasticized PLA produced in the micro-compounder; plasticized PLA with the weight composition of 79/20/1 will be always abbreviated with **pPLA**
PLA/L101	99/1 PLA/L101	PLA mixed with the initiator
PLA/acrylPEG	80/20 PLA/acrylPEG	physical mixing between PLA and the plasticizer
poly(acrylPEG)	95/5 acrylPEG/L101	polymerization of acrylPEG with the free radical initiator
PLA/poly(acrylPEG)	79/21 PLA/poly(acrylPEG)	PLA mixed with the polymerized plasticizer poly(acrylPEG)
pPLA aS	not determined	sample after Soxhlet extraction; the acrylPEG content is lower than in the produced pPLA
PLA	100/0/0 PLA/acrylPEG/L101	extruded PLA without any plasticizer or additives; for comparison

During the reactive blending, the force indicates ongoing reactions. After the injection of liquid components (plasticizer, initiator) to the melted PLA the force decreased due to the lowered viscosity

and after the starting of reaction, the force increased due to grafting and/or crosslinking reaction [41]. Figure 3.1 illustrates the recorded forces for the different materials and shows the already described behavior for the reactive plasticization of pPLA. After the injection of the mixture of acrylPEG and L101 the force dropped, but in less than one minute, the initial force was recovered and exceeded. With some small variations, the force reached a plateau after the 5 min compounding time. This confirms the previously described reactions: The drop of force is due to the decreased viscosity caused by the injection of the liquids, and after the initiator started the reactions, the force increased due to polymerization and grafting reactions. The second sample, PLA just with the initiator (PLA/L101), showed a small decrease of force after the injection of the initiator, maybe due to a small decrease of viscosity. Afterward, a strong increase of the force was observed for the first 1.5 min, followed by a decrease up to 2 min. Until the end of the extrusion time, the force increased again slightly. The first strong increase could be due to spontaneous crosslinking that occurred directly after the initiation of the plasticizer, then a mixing occurred and the radicals are dispersed in the melt. The following decrease could be due to degradation reactions since radicals can provoke chain breaking of PLA. With increasing extrusion time, further crosslinking and/or branching occurred, so that the force increased again, but slowly [100]. In the case of simple blending of PLA with the plasticizer (PLA/acrylPEG), the force decreased as well after the injection and swung into a stable state that was lower than the initial force of just PLA. The addition of the plasticizer caused a lower viscosity, and because of the lack of initiator, no grafting and crosslinking reaction occurred that would have increased the force. For the polymerization of the plasticizer with the free radical initiator (poly(acrylPEG)), the force increased within the first minute strongly and reached a stable plateau. This leads to the assumption, that a fast polymerization reaction of acrylPEG with the free radical initiator to poly(acrylPEG) occurred. The blend between the polymerized plasticizer and PLA (PLA/poly(acrylPEG)) showed the same behavior like PLA. After the introduction and melting of the material in the extruder, the force stayed stable over the whole extrusion time. This leads to the assumption that there is just a simple blending without further chemical reactions between the polymerized plasticizer and the PLA matrix since all the initiator already reacted in the preparatory step of the acrylPEG polymerization.

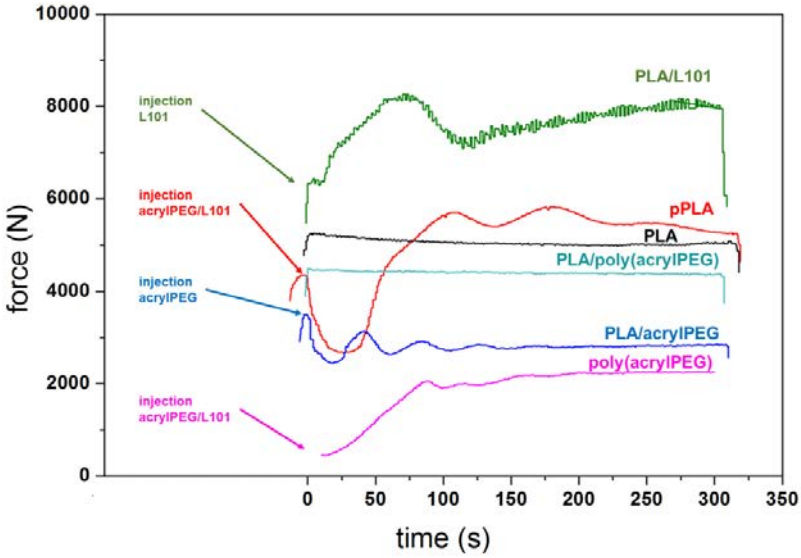

Figure 3.1 Recorded forces during the (reactive) blending of the materials for the structural analysis of pPLA.

The grafting and crosslinking were qualitatively proved by swelling tests in chloroform and gel permeations chromatography (GPC) in tetrahydrofuran (THF). The pPLA formed a gel in chloroform, but due to instability, a separation and quantification of the gel content were not possible. The same behavior was observed for pPLA aS. The swelling behavior underlined the assumption of the formation of a crosslinked material during the reactive plasticization. The PLA/L101 sample formed no stable gel, but small pieces of insoluble gel were observed. The reaction of PLA with high concentrations of L101 as a free radical initiator led to the formation of highly branched and possibly crosslinked PLA structures [100]. The samples of poly(acrylPEG) formed a stable gel that was insoluble in chloroform and PLA/poly(acrylPEG) created a turbid solution. The poly(acrylPEG) in the PLA/poly(acrylPEG) blend seemed to be well distributed and the presumption that no grafting onto the PLA matrix occurred was assisted since no gel of PLA was formed. The PLA/acrylPEG blend showed no formation of gel and created transparent solutions just as the PLA sample. While chloroform and THF are suitable solvents for unmodified PLA, the plasticized samples were no more soluble except for the blend PLA/acrylPEG. Therefore, an analysis of the molecular weight was imprecise since just the soluble part could be analyzed, while the insoluble part was removed by filtration. The PLA and PLA/acrylPEG samples were completely soluble in THF and easily filterable. For all samples, at least two peaks were observed, but only the first peak associated with the main fraction of PLA was analyzed. The samples based on PLA without reaction during blending (PLA, PLA/acrylPEG, PLA/poly(acrylPEG)) had all a weight average molecular weight around 200 kDa assuming that plasticization with acrylPEG or poly(acrylPEG) did not change the structure of PLA matrix. The PLA/L101 was not completely soluble and hard to filter when a higher molecular weight about 250 kDa was reached. As shown in previous studies, the free radical

initiator induced a branching and/or crosslinking of the material, so that the material's solubility was decreased and the molecular weight was increased [100]. Due to the filtration, the polydispersity was in the same range for all samples (between 1.6 and 2.5) since the highly branched structures were filtered out. The reactive processing lowered the molecular weight of the main PLA peak. While pPLA offered an average molecular weight around 160 kDa, the Soxhlet extraction decreased the molecular weight to less than 100 kDa. For both samples, no visible parts of the samples were remaining after dissolving in THF, but a resistance to the filtration was obvious. This leads to the assumption that acrylPEG polymerized and reached molecular weights that overlap with the main peaks of PLA. Furthermore, a degradation of the PLA matrix was considered. Especially for the pPLA aS sample, the molecular weight decreased strongly. During the Soxhlet extraction from hot methanol, PLA could undergo methanolysis and degraded to PLA with lower molecular weight [92].

Table 3.3 Summary of the swelling test and GPC results of the materials for the structural analysis of pPLA.

	swelling in chloroform	GPC in THF	molecular weight PLA peak		polydispersity
			$\bar{M}_w$ (kDa)	$\bar{M}_n$ (kDa)	Đ = $\bar{M}_w/\bar{M}_n$
pPLA	stable gel; no separation possible	resistance to filtration	160.3 ± 9.7	64.1 ± 3.4	2.5
PLA/L101	formation of small gel pieces	resistance to filtration; not completely dissolved	241.3 ± 19.6	118.9 ± 5.5	2.0
PLA/acrylPEG	no gel; transparent solution	filterable; completely dissolved	194.6 ± 4.3	124.1 ± 3.9	1.6
PLA/poly(acrylPEG)	no gel; turbid solution	not completely dissolved	216.5 ± 1.0	122.0 ± 3.6	1.8
pPLA aS	stable gel; no separation possible	resistance to filtration	97.2 ± 0.1	43.2 ± 1.3	2.2
poly(acrylPEG)	stable gel; no separation possible	not completely dissolved	-	-	-
PLA	no gel; transparent solution	completely dissolved	203.2 ± 2.1	96.5 ± 2.1	2.1

Nevertheless, the results of the recorded force, as well as the swelling tests and GPC analysis, indicate the roles of the different compositions in the plasticized PLA. The initiator led, on one side, to grafting

and crosslinking in PLA, and, on the other side, enabled a polymerization of acrylPEG, which could start from the PLA backbone to form grafted poly(acrylPEG). When blended with the initiator, the acrylPEG itself neither polymerized nor showed grafting and crosslinking reaction with PLA. The non-grafted part of plasticizer in pPLA could be removed by Soxhlet extraction. While the PLA matrix degraded due to methanolysis, the crosslinked structure remained and gel formation was observed.

3.2.2 Thermal Properties

The thermal properties of the materials were characterized by DSC and support the analysis of the structure of the different materials. Figure 3.2 shows representative DSC curves for (a) the first (dashed lines) and second (straight lines) heating as well as for (b) the cooling of the materials and Table 3.4 summarizes the thermal parameters and the crystallinity values. The first heating is related to the material's parameters as processed, while the second heating allows a comparison between different materials with a similar thermal history. However, for the plasticized samples the glass transition was hardly visible in all curves. Previous publications proved that the T_g was decreased by plasticization with acrylPEG but at the same time, the T_g localization was difficult to get observed with increasing initiator concentration, due to possible crosslinking [52]. For pPLA (red line), the two heating stages presented nearly identical curves, except a small increase of crystallinity from 29.4% in the first heating to 31.7% in the second heating. Previous research on this plasticized PLA indicated that crystallinity increased with increasing initiator concentration (up to 1%) and decreased when plasticizer concentration was increased over 20 wt% [51,52]. The dispersed phase of plasticizer in the PLA matrix led to nucleation sites, which could improve the crystallization [101]. For pPLA aS (orange line), which is the sample after the extraction of the non-grafted share of the plasticizer, the crystallinity decreased from the first to the second heating stage from 33.3% to 26.5%. The slightly higher crystallinity of pPLA aS compared to pPLA in the first heating stage can be justified by the extraction process. The extraction from hot methanol for 24 h could induce an annealing process, which increased crystallinity. In the second stage, a lower crystallinity was detected due to the lower amount of free plasticizer in the material. The plasticization increased the free volume and facilitated orientation of the PLA chains. When the free part of the plasticizer was removed, the crystallinity decreased, which means that the free part of plasticizer enhanced the crystallization. The PLA/acrylPEG (blue line, without grafting of plasticizer) and PLA/poly(acrylPEG) (light blue line, with the previously polymerized plasticizer) showed crystallinities of 11.8% and 7.2%, respectively, in the first heating. For both materials, the crystallinity increased strongly in the second heating stage to 28.4% and 26.2%, respectively. It is worth to mention, that for both samples, cold crystallization occurred in the first heating stage, but no more in the second heating stage. The cold crystallization

peak for PLA/acrylPEG was found at a lower temperature 74.1°C, than for PLA/poly(acrylPEG) with 94.7°C. Baiardo et al. [45] showed, that a PEG with a higher molecular weight decreased the cold crystallization temperature weaker than lower molecular weight PEG, and, therefore, the polymerized plasticizer could induce a less strong decrease of the cold crystallization temperature since its mobility in the PLA matrix is limited. Nevertheless, compared to PLA (black line) with a cold crystallization at 126.9°C, the polymerized plasticizer also increased the cold crystallization ability: The cold crystallization temperature was lowered and the crystallization enthalpy increased. Furthermore, PLA/poly(acrylPEG) exhibited two melting peaks, while the PLA/acrylPEG had a single quite narrow melting peak. The two melting peaks are related to two families of crystals with different thermodynamic stability and perfection [102]. The single melting peak of PLA/acrylPEG could indicate a higher homogeneity than in PLA/poly(acrylPEG). This assumption was supported by the appearance of a second melting peak at -5.6°C for PLA/poly(acrylPEG), which was related to the melting of the poly(acrylPEG) phase. The DSC curve of poly(acrylPEG) (pink line) exhibited a cold crystallization peak at -34.7°C and subsequent melting peak at -1.9°C. The poly(acrylPEG) samples had an obvious glass transition at -60.4°C, but this glass transition was not observed for PLA/poly(acrylPEG) (light blue line), which only had one glass transition at 52.2°C. Therefore, the miscibility of PLA with poly(acrylPEG) is probably lower than with acrylPEG, but still present. PLA/poly(acrylPEG) (light blue line) was the only plasticized sample with a visible glass transition in the first heating stage. Compared to PLA (black line) the T_g was lowered from 60.8°C to 52.2°C, even though, previous research reported an even stronger decrease of the T_g to 42°C for this composition [50]. Like for PLA (black line) and PLA/L101 (green line), for PLA/poly(acrylPEG), an endotherm meso-transition peak around the glass transition temperature was observed, which could indicate that the PLA matrix was less plasticized in the case of polymerized plasticizer probably due to less miscibility. The PLA/L101 (green line) sample differed not strongly from unmodified PLA. Mainly, the decrease of the cold crystallization temperature from 126.9°C to 104.0°C and the increase to 7.6% of the crystallinity in the first heating stage and 16.0% in the second heating stage were observed. The addition of the free radical initiator led to branching, crosslinking and chain scission in the material [100] and, therefore, the cold crystallization temperature was lower than for PLA but higher than for plasticized samples.

All modifications increased the crystallinity compared to amorphous PLA and enabled the crystallization during the cooling stage, due to an increased mobility in the material that enhanced the orientation. The simple blending with plasticizer PLA/acrylPEG led to a material with a very low crystallization temperature at 72.8°C during the cooling stage. Due to lower miscibility with the polymerized plasticizer, PLA/poly(acrylPEG) crystallized at a higher temperature 88.5°C. Surprisingly, the crystallization temperature of pPLA (109.0°C) was a bit higher compared to pPLA aS (104.9°C).

Normally, it was expected that pPLA aS had the higher crystallization temperature due to a higher crosslinking content and less amount of free plasticizer that could reduce the crystallization temperature. As already stated, methanolysis could occur during the extraction and forced chain scission, which could explain the higher crystallinity as well as the lower crystallization temperature since the shorter PLA chains enabled easier orientation. For the same reason, PLA/L101 had a similar crystallization temperature like pPLA. The higher the degree of branching and crosslinking, the higher was the crystallization temperature, but the initiator could also lead to chain scission [100].

Table 3.4 Thermal parameters of the samples for pPLA structural analysis determined by DSC measurements from the first heating stage (1), the cooling stage (2) and the second heating stage (3).

		T_g (°C)	T_{cc} (°C)	T_m (°C)	ΔH_{cc} (J/g)	ΔH_m (J/g)	X_c (%)
pPLA	1	n.d.	-	156.6 ± 0.1	-	21.6 ± 0.1	29.4 ± 0.2
	2	n.d.	109.0 ± 1.2	-	20.0 ± 0.2	-	-
	3	n.d.	-	146.7 ± 1.2	-	23.3 ± 0.2	31.7 ± 0.2
PLA/L101	1	59.3 ± 0.2	104.0 ± 1.4	153.1 ± 2.5	10.1 ± 2.6	17.1 ± 1.3	7.6 ± 1.4
	2	53.1 ± 0.1	104.6 ± 0.7	-	10.3 ± 1.3	-	-
	3	61.1 ± 0.4	105.4 ± 0.1	151.8 ± 0.8	2.1 ± 0.8	16.8 ±2.3	16.0 ± 1.5
PLA/acrylPEG	1	n.d.	74.1 ± 0.1	151.8 ± 0.3	15.3 ± 1.2	24.1 ± 1.2	11.8 ± 0.8
	2	n.d.	72.8 ± 0.0	-	9.1 ± 0.4	-	-
	3	n.d.	67.6 ± 0.1	151.3 ± 0.0	3.6 ± 0.2	24.7 ± 0.8	28.4 ± 0.9
poly(acrylPEG)	1	-60.4 ± 0.5	-34.7 ± 0.2	-1.9 ± 0.6	26.3 ± 0.7	28.7 ± 0.9	-
	2	-67.7 ± 0.5	-	-	-	-	-
	3	-60.0 ± 0.4	-35.6 ± 0.4	-0.6 ± 0.6	27.5 ± 0.1	29.6 ± 0.3	-
PLA/poly(acrylPEG)	1	52.2 ± 0.8	94.7 ± 0.4	143.8 ± 0.1 & 153.7 ± 1.1	15.1 ± 0.6	20.4 ± 0.3	7.2 ± 0.4
	2	n.d.	88.5 ± 0.1	-	12.7 ± 0.4	-	-
	3	49.7 ± 0.2	81.5 ± 0.1	144.3 ± 0.3 & 152.7 ± 0.4	1.4 ± 0.1	20.9 ± 1.0	26.2 ± 0.9
pPLA aS	1	n.d.	-	149.6 ± 0.4	-	26.3 ± 3.5	33.3 ± 4.4*
	2	n.d.	104.5 ± 2.1	-	17.3 ± 1.9	-	-
	3	n.d.	-	147.0 ± 0.2		21.0 ± 0.7	26.5 ± 0.9*
PLA	1	60.8 ± 0.6	126.9 ± 0.0	155.4 ± 0.5	4.7 ± 0.1	8.3 ± 1.4	3.9 ± 1.4
	2	54.4 ± 0.4	-	-	-	-	-
	3	60.9 ±0.1	127.9 ± 0.1	154.5 ± 0.1	2.1 ± 0.8	2.8 ± 0.5	0.8 ± 0.3

n.d.: not detected; * for the calculation a PLA fraction of 0.85 was assumed.

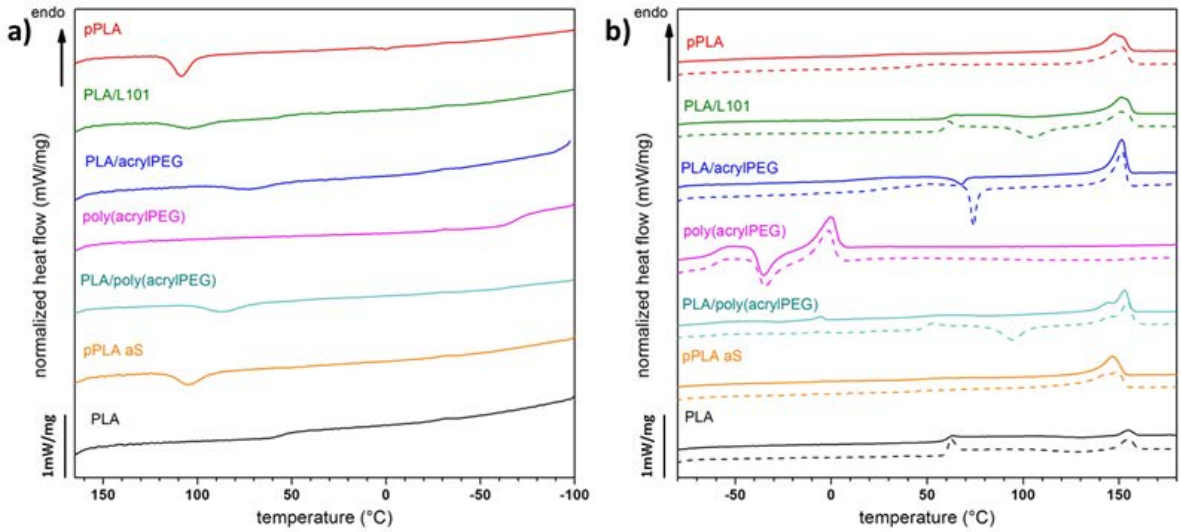

Figure 3.2 DSC curves of the samples for pPLA structural analysis from the (a) cooling stage and (b) first (dashed line) and second (continuous line) heating stage.

3.2.3 Morphology Analysis

AFM measurements provide an insight into the analysis of the morphology of the samples in combination with an analysis of the mechanical properties. As previously shown, the plasticized PLA consists of the plasticized PLA matrix and partially grafted inclusions of plasticizer. Therefore, an AFM analysis was conducted to determine the stiffness of the matrix and the inclusions separately on pPLA, PLA/acrylPEG and pPLA aS (Figure 3.3 d, e, and f). The height images (Figure 3.3 a, b, and c) show deeper regions for all materials, which were by stiffness analysis identified as inclusions of softer material parts. In the pPLA, inclusions with a quite broad size distribution appeared and were well dispersed in the matrix. For PLA/acrylPEG, the plasticizer phase formed bigger inclusions, which could be reasoned by a kind of phase separation between plasticizer and matrix phase. The sample after the extraction of the free part of plasticizer pPLA aS showed small inclusions, which were dispersed in the sample and just a few big inclusions remained. It seemed that the free plasticizer formed aggregations and big inclusions, as seen in pPLA and PLA/acrylPEG, but the grafted inclusions seem to be small and well distributed in the matrix.

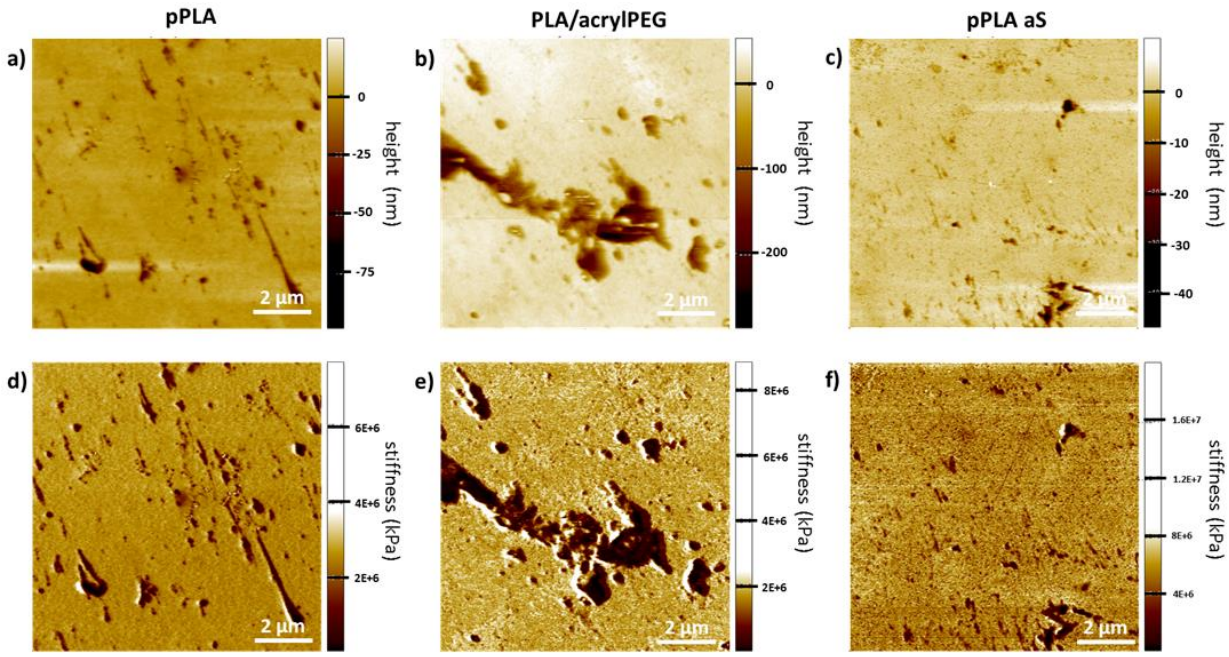

Figure 3.3 AFM height images and stiffness analysis of (a) pPLA, (b) PLA/acrylPEG, and (c) pPLA aS.

The stiffness was determined for different matrix areas and for different inclusion areas on the samples and average values were calculated (Figure 3.4). Obviously, the inclusions showed always a much lower stiffness than the matrix. For pPLA, the matrix stiffness was 2.77 GPa whereas the inclusions had a stiffness of 0.20 GPa. While the blend PLA/acrylPEG showed a lower stiffness for matrix and inclusions of 1.87 GPa and 0.05 GPa, respectively, the sample after extraction showed in both higher values (5.54 GPa and 0.48 GPa). The nonreactive blending of PLA and acrylPEG leads to a good plasticization which normally causes a lower stiffness of the matrix. Although the plasticizer molecules are very small, it seems that a phase separation or at least migration of the plasticizer molecules toward each other occurred. Since the plasticizer molecules were not polymerized, the plasticizer phase also had a very low stiffness. For pPLA aS the matrix stiffness increase can be due to the lower amount of free plasticizer and higher crystallinity of the sample. The increase in inclusion stiffness could be explained by the fact, that the plasticizer was polymerized and grafted onto the matrix. In pPLA, both, the polymerized plasticizer and unpolymerized plasticizer, exist. Therefore the values are between those for the other two samples. However, the inclusions' stiffness could just be measured with high errors, since it was hard to distinguish between the neat inclusions and the neat matrix. Especially for pPLA, a mixture of both seemed to exist due to the grafting of the plasticizer onto the PLA backbone.

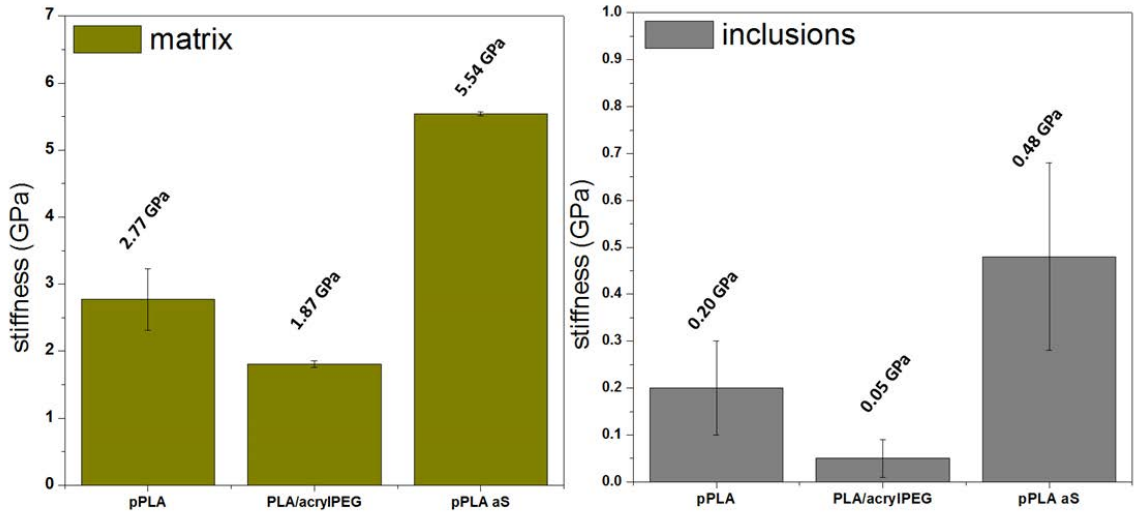

Figure 3.4 Stiffness values of the matrix and the inclusions for pPLA, PLA/acrylPEG, and pPLA aS from AFM stiffness analysis.

3.2.4 Impact Resistance

Along with increasing the ductility by reducing the T_g, plasticization by reactive blending can also improve the toughness of PLA-based materials [41,50,52]. Compared to PLA with an impact energy of 4.1 kJ/m^2, the plasticization by reactive blending increased the impact toughness strongly to 38.4 kJ/m^2 for pPLA. The highest impact energy of 84.2 kJ/m^2 is reached for the PLA/acrylPEG sample, while the pPLA aS sample lost toughness compared to pPLA and reached just 6.7 kJ/m^2. The part of free plasticizer seems to have an important influence on the impact resistance. However, the sample with the polymerized plasticizer PLA/poly(acrylPEG) reached a value of 4.7 kJ/m^2. This leads to the assumption, that the smaller plasticizer molecules, which are well dispersed in the material, leading to a better energy dissipation than the polymerized plasticizer molecules. Furthermore, the in-situ polymerization of the plasticizer in pPLA seemed to lead to better dispersion of the molecules and a better plasticization than with the polymerized plasticizer. The PLA/L101 sample had the lowest impact energy with 2.6 kJ/m^2, which was even lower than for PLA. Different factors like crystallinity, the entanglement density, and the plasticization influence the impact toughness. However, Kfoury et al. [50] produced a similar plasticized PLA in a ratio of PLA/acrylPEG/L101 79/20/1 that offered a Notched Izod impact energy of 101.6 kJ/m^2. As seen already in DSC measurements, the thermal history impacts the properties and especially the crystallinity. Therefore, a comparison of materials with different thermal histories, which also included the processing, is complicated. While the samples of Kfoury et al. were produced by compression molding [50], the actual study used injection molding as shaping procedure for the impact testing specimen. Nevertheless, it was proved that plasticization by reactive blending increased the impact toughness strongly compared to the neat PLA. While the

grafting and crosslinking, induced by the radical initiator, negatively affected the impact toughness, the free, less polymerized plasticizer increased the impact toughness. This underlines the assumptions that the polymerized plasticizer was less able to dissipate the impact energy than the free plasticizer and that crystallinity just led to a higher impact resistance if the higher crystallinity was not combined with grafting/crosslinking.

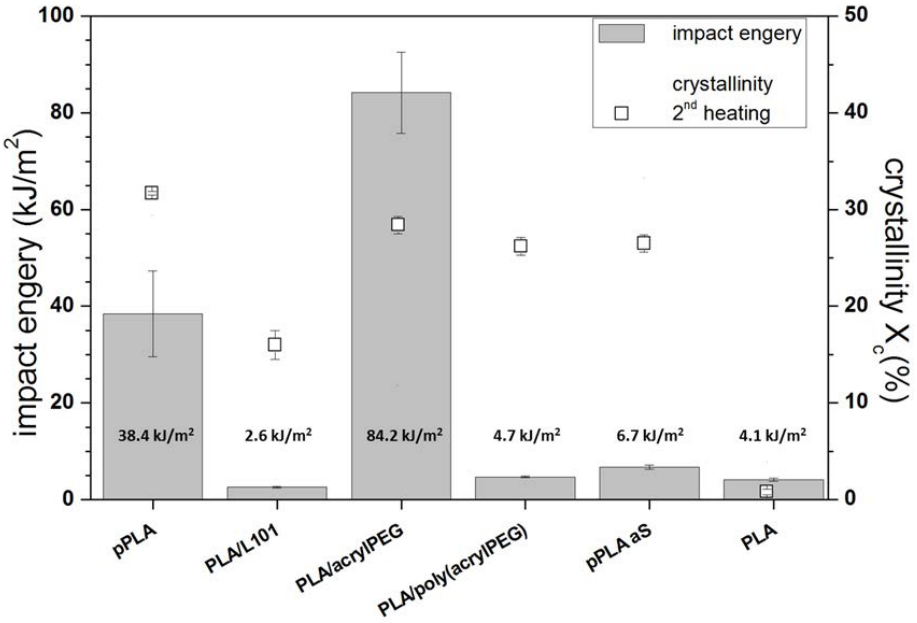

Figure 3.5 Impact resistance and crystallinity from DSC second heating stage of PLA-based materials for the pPLA structural analysis.

3.3 Isothermal Crystallization Kinetics

Just as for the mechanical properties, the structure influences the crystallization behavior, which is an important key point for the final bulk microstructure and in turn for the range of applications. Despite PLA materials with a low D-lactide content are semicrystalline, their ability of crystallization is normally low, but increased after plasticization with PEG [58]. While the DSC allowed the determination of crystallization temperatures and gave information about the ability of cold crystallization, isothermal crystallization was used to understand the crystallization kinetics. The samples were melted and quenched in liquid nitrogen to obtain completely amorphous materials and afterward heated to the isothermal crystallization temperature. Recording WAXS diagrams allowed the determination of the crystallinity index as a function of the time. Figure 3.6 compares the isothermal crystallization of (a) PLA and (b) pPLA at different crystallization temperatures. It is obvious, that PLA crystallized at 80°C

very slowly and the crystallization was not completed even after 10h (600 min). With increasing temperature, the S-shaped curves shifted to the left side indicating that the velocity of crystallization increased. While the maximum crystallinity for the curves at 85°C and 90°C was reached at the same time (around 400 min), a measurable crystallinity occurred after less time for the higher temperature. For example, a crystallinity index of 0.1 was reached after 77 min, 88 min, and 241 min at 90°C, 85°C, and 80°C, respectively. At higher temperatures, 100°C and 110°C, the crystallization was much faster; the crystallization half-times were 34 min and 22 min for 100°C and 110°C, respectively. In comparison to PLA, the pPLA crystallized at lower temperatures (Figure 3.6 b). While at 80°C PLA's crystallization was not completed after 600 min, for pPLA crystallization a tenth of this time was needed at the same temperature and the crystallization was completed in less than 1h. It is worth to mention, that the crystallization of pPLA at 80°C and 90°C was too fast, that no exact crystallization half-time could be determined (first measuring points had already a normalized crystallization index higher than 0.5); the crystallization half-times were lower than 10 min. Even at lower temperatures, the crystallization was faster compared to PLA, isothermal crystallization at 70°C, 65°C, and 60°C led to crystallization half-times of less than 20 min. Even for low crystallization temperatures such as 55°C and 50°C, the typical S-like shaped curves were observed and the maximum crystallization was reached after less than 6 h.

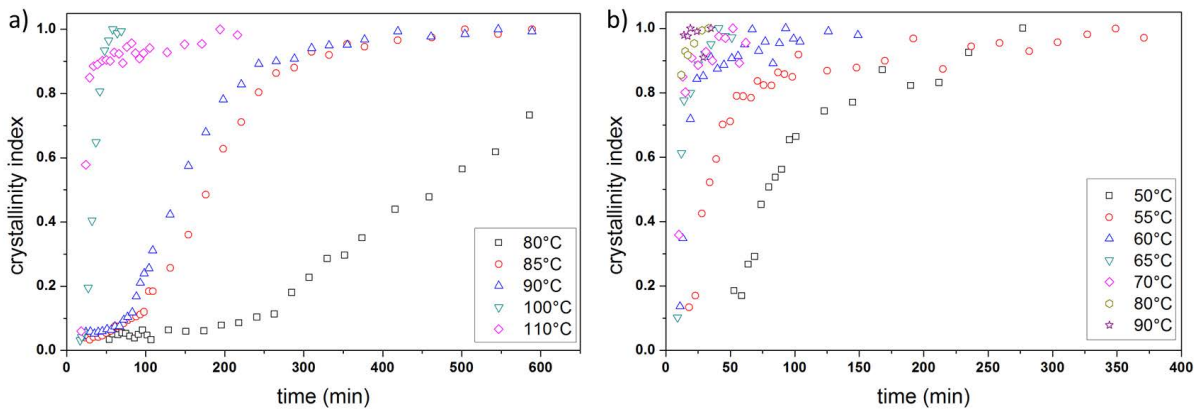

Figure 3.6 Evolution of crystallinity index as a function of time during isothermal crystallization at different temperatures for (a) PLA and (b) pPLA.

The Avrami model describes the typical S-shaped curves and allows a determination of the crystallization kinetics (Equation (3.2)). The Avrami exponent n provides information about the nature of the crystal nucleation and crystal growth geometry, and k reflects the overall rate constant associated with both nucleation and growth contributions [97]. Furthermore, the crystallization half-time can be calculated from these parameters (Equation (3.3)). The model parameters are reported

in Table 3.5 with the final crystallinity and the experimental crystallization half-time. The Avrami model determined crystallization half-times matched with the half crystallization times determined from the graphical plot (crystallinity index of 0.5). Therefore, it was assumed that the Avrami model provided reliable values for a comparison between the isothermal crystallization temperatures. For PLA crystallized at lower temperatures (80°C to 90°C), the parameter n is in the range around 2.4 and increased to 4.3 and 4.8 for the higher temperatures (100°C and 110°C). Whatever the type of nucleation (homogeneous or heterogeneous), n values comprised between 2 and 3 demonstrated a 2D growing geometry (disc-like geometry) between 80°C and 90°C for PLA. At higher temperatures, n values comprised between 4 and 5 indicate an intermediate geometry between a 3D growing (sphere-like geometry) and a sheaf-like geometry [103]. The increase of n can be interpreted as an increase of crystal growth homogeneity with temperature. While the crystallization half-time progressively decreased with increasing temperature, the parameter k first increased between 80°C and 90°C, and then it decreased. Such a final decrease of k may be linked to the final change of crystal geometry growing. The analysis of the Avrami parameters hints also on different crystallization kinetics for pPLA compared to PLA. At low temperatures (50°C and 55°C) the values for n were quite small (< 1.5), while at the same time the parameter k increased. Values for n comprised between 1 and 2, that were also observed at the highest temperatures (80°C and 90°C) imply a 1D growing (rod-like geometry) [103] representing an imperfect crystal growing [104]. It was observed, that the n values decreased with increasing degree of chain branching [105], and for pPLA, the chain branching was increased because of the grafting of plasticizer on the backbone. At the same time, the strong increase of k together with the decrease of the crystallization half-time showed a strong increase of the crystallization rate. However, the samples at 60°C, 65°C, and 70°C obtained much higher n values and lower k values. The n value of pPLA at 60°C is quite close to those of PLA between 80°C and 90°C, but with a higher crystallization rate, indicated by the higher parameter k and the lower crystallization half-time. The increase of n in the case of pPLA between 50°C and 65°C may reflect an evolution from a 1D crystal growing geometry to a sheaf-like crystal growing geometry, and inversely from 65°C to 90°C [103]. All these observations show that the parameters of the Avrami model can be considered as indicators of the crystal growth and the growth rate, though absolute values do not correspond to univocal structural situations.

Table 3.5 Crystallization data extracted from experimental curves and Avrami modelling for PLA and pPLA crystallized at different temperatures.

				Avrami parameters		
T_{ic} (°C)	sample	X_c (%)	$t_{1/2}$[1] (min)	n	k (min^{-n})	$t_{1/2}$ (min)
80	PLA T80	15.3*	470	2.4	2.9 E-07	465
85	PLA T85	23.4	178	2.4	2.5 E-06	178
90	PLA T90	25.3	143	2.3	5.9 E-06	147
100	PLA T100	19.7	34	4.3	1.6 E-07	34
110	PLA T110	23.2	22	4.8	1.4 E-07	22
50	pPLA T50	11.3*	79	1.5	9.8 E-04	81
55	pPLA T55	15.2	33	1.1	1.7 E-02	32
60	pPLA T60	15.5	16	2.4	9.4 E-04	16
65	pPLA T65	16.1	11	5.2	1.9 E-06	12
70	pPLA T70	15.0	11	3.2	2.9 E-04	11
80	pPLA T80	15.2	< 10	1.0	1.9 E-01	4
90	pPLA T90	16.8	< 10	0.4	1.5 E+00	<1

* The crystallization was maybe not completely finished; [1] the half-time crystallization was determined graphically at CI=0.5.

The plasticization drastically increased the crystallization rate of PLA when comparing crystallization half-times of pPLA and PLA at the same temperature, and tended to decrease the final crystallinity X_c. Indeed, whatever the temperature, X_c was in the ranges 15.3% to 25.3% for PLA and 11.3% to 16.8% for pPLA. The isothermal crystallization results showed that: (i) crystallization rate markedly increased with the plasticization of PLA at a given temperature, (ii) plasticization decreased the final crystallinity, and (iii) pPLA crystal growing geometry varied with the crystallization temperature. It was found that for PLA 90°C and for pPLA 55°C are good crystallization temperatures because a well-defined crystallization curve was observed at these temperatures.

Since PLA and pPLA crystallized in different ways, a special attention was paid to the morphology of the crystalline structures for the two cases. PLA as-processed was nearly amorphous, while pPLA offered a crystallinity around 30%. After the isothermal annealing at 90°C, PLA reached a crystallinity of 25.3% and pPLA 15.3% for an isothermal annealing at 55°C. Figure 3.7 illustrates the morphology of (a) the as processed pPLA, (b) pPLA and (c) PLA after isothermal crystallization at 55°C and 90°C respectively. As previously described, the as-processed pPLA consisted of a plasticized PLA matrix, with grafted inclusions and partial crosslinking. The morphology of pPLA (Figure 3.7 a) exhibited

impinged sheaf-like spherulites [106] and dispersed inclusions of different sizes. While the big inclusions arose as single inclusions, the smaller inclusions often formed aggregates. After the isothermal crystallization of pPLA at 55°C (Figure 3.7 b), some spherulites nuclei of a few lamellae were also noted as in the as-processed sample, but were less developed and appeared smaller. In contrast, PLA formed crystalline domains containing lamellae with an average thickness of around 30 nm. These domains may have a 2D geometry as highlighted by the Avrami modeling of crystallization kinetics (Table 3.5). Nevertheless, after the isothermal crystallization, crystals of pPLA are less developed as in the as-processed sample, while PLA crystallized in spherulitic structures. The growing of crystalline areas in pPLA seemed to be restricted by the inclusions. It was already shown that crystallization favored phase separation [44] so that the small crystalline areas could be limited by acrylPEG rich phases. It is believed that the grafting and/or crosslinking points of the inclusions played an important role in pPLA crystallization since these points reduced locally the chain mobility even if they acted as nucleating agents. Similar results were obtained in previous studies where a special nucleating agent was added to PLA [107]. Based on Avrami modeling, the crystalline morphology of pPLA may vary with the imposed temperature (Table 3.5). An optimal nucleation should result in a homogeneous crystal growing not in only one direction. Thus, the temperature range between 60°C and 70°C may represent the optimal nucleation temperature range for pPLA.

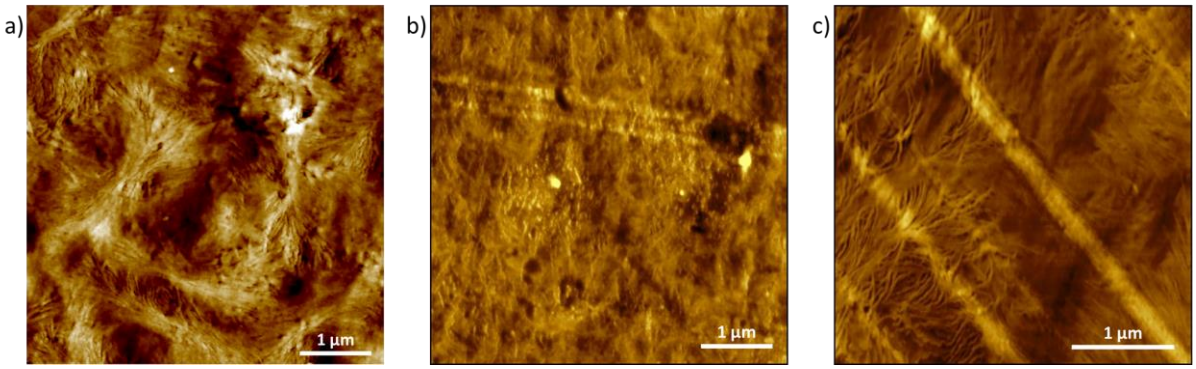

Figure 3.7 AFM topography images of (a) pPLA as processes, (b) pPLA and (c) PLA after isothermal crystallization at 55°C and 90°C respectively.

As already mentioned, pPLA crystallized in a different way than PLA due to the complex structure that was formed during the reactive blending. To evaluate the different structures that can arise, PLA/L101, PLA/acrylPEG, and pPLA aS were also isothermally crystallized and compared to the crystallization kinetics of PLA and pPLA at 90°C and 55°C. Figure 3.8 a illustrates that the slowest crystallization was observed for unmodified PLA. The addition of the initiator reduced the half-time crystallization from

143 min to 31 min. As already seen the crystallization of pPLA was too fast at 90°C, that the graphical determination of the half-time crystallization was not possible since the first crystallinity index at 14 min was already over 0.5. After the extraction (pPLA aS), the crystallization appeared a bit slower, but still, the first crystallinity index was higher than 0.5 and observed after 15 min. For the isothermal crystallization at 55°C, the same behavior was observed. While pPLA offered a half-time crystallization of 33 min, pPLA aS crystallized much slower with a half-time crystallization of 122 min. Nevertheless, PLA/acrylPEG crystallized fast as well with a half-time crystallization below 39 min, but just low crystallinity values of less than 10% were observed when pPLA and pPLA aS reached 13.5% and 15.2%, respectively. Furthermore, PLA/acrylPEG showed less clear crystallization peaks so that an exact determination of the crystallinity index and final crystallinity is precluded.

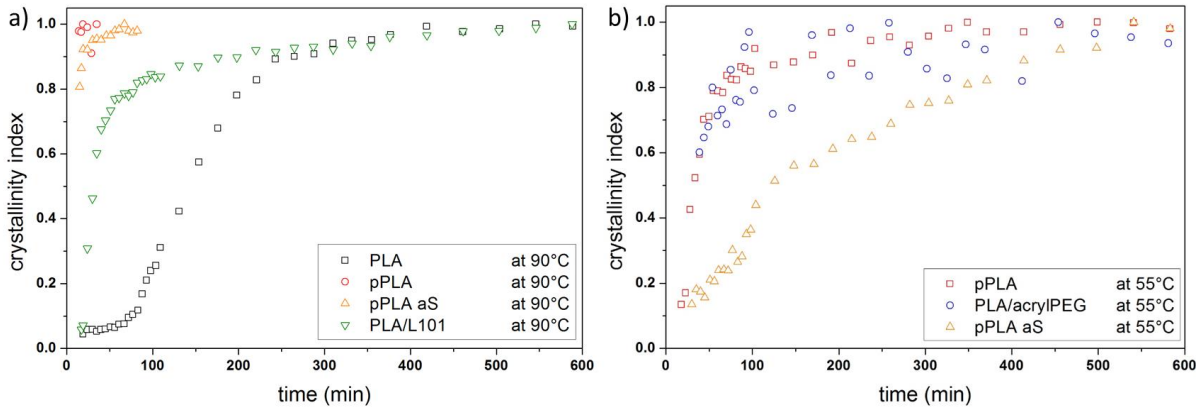

Figure 3.8 Evolution of crystallinity index as a function of time during isothermal crystallization testing at (a) 90°C and (b) 55°C for modified PLA materials.

These results, as well as the Avrami modeling parameters, are summarized in Table 3.6 and point at the importance of the structure variation by the initiator and the plasticizer. The addition of initiator created grafting points, which can act as nucleating agents and provided for fast crystallization. Even tough, the increase of the Avrami parameter k by more than 4 decades supports this assumption. The plasticized samples pPLA and pPLA aS offered the same crystallization sides and therefore a fast crystallization. The proposed structure of pPLA contained grafting and crosslinking points that functioned as nucleating agents and increased the crystallization velocity, but also the free and grafted part of plasticizer affected the crystallization kinetics. The impact of the plasticizer was more obvious in the comparison at 55°C. Again, the half-time crystallization was lower in the pPLA sample compared to the pPLA aS sample, assuming that the free part of plasticizer increased the velocity of crystallization. In addition, the blend PLA/acrylPEG showed an accelerated crystallization even if the

sample lacked grafting and crosslinking. Even though the $t_{1/2}$ values which were calculated from the Avrami parameters are in good accordance with the experimental ones, the Avrami parameters n and k did not obtain reliable values, since n should be between 1 and 4 [63,64].

Table 3.6 Final crystallinity and half-time crystallization determined from isothermal crystallization for PLA-based materials at different temperatures and Avrami parameters.

				Avrami parameters		
T_{ic} (°C)	sample	X_c (%)	$t_{1/2}$[1] (min)	n	k (min^{-n})	$t_{1/2}$ (min)
			T 90°C			
90	PLA T90	25.3	143	2.3	5.9 E-06	148
90	pPLA T90	16.8	< 14	0.4	1.5 E+00	< 1
90	pPLA aS T90	24.1	< 15	0.6	4.0 E-01	3
90	PLA/L101 T90	18.7	31	4.0	6.8 E-07	31
			T 55°C			
55	pPLA T55	15.2	33	1.1	1.7 E-02	32
55	PLA/acrylPEG T55	9.3	< 39	0.4	2.3 E-01	14
55	pPLA aS T55	13.5	122	1.1	3.7 E-03	147

[1] the half-time crystallization was determined graphically at CI=0.5.

In summary, the reactions during the reactive blending that are in competition impact the crystallization kinetics strongly. On one hand, the crystallization velocity was increased by the free plasticizer since the mobility was increased. On the other hand, the grafting and crosslinking points improved the nucleation and crystal growth and therefore accelerated the crystallization as well. The comparison of pPLA with pPLA aS indicates that the free part of plasticizer increases the crystallization velocity stronger. The final crystallinity indices were impacted by the plasticization and the free part of plasticizer seemed to decrease the final crystallinity as seen for PLA/acrylPEG. The crystallization induces a reduction of the amorphous phase where the grafting/crosslinking occurs and leads to zones with high crosslink/grafting densities, which limit the crystal growth. The inclusions of plasticizer gave a further limitation of crystal growth since no cocrystallization was observed.

3.4 Scale-Up Process: From Batch Mode to Continuous Process

3.4.1 Processing Parameters for the Continuous Process

The first experiments of reactive plasticization of PLA with acrylPEG were conducted in small batches of 6 g per compounding with a micro-compounder and the same procedure as described in the literature [41,50]. However, industrial applications, e.g. packaging, require higher production capacities. Therefore, a scale-up from this batch process to a continuous process gained importance, and a pre-industrial study with a mini-extruder was conducted. It was already shown, that the controllability of the structure of the pPLA was limited due to the competitive reactions during the reactive blending so that the processing parameters governed the product's properties in both the batch and continuous processes. The batch process was characterized by a defined compounding volume, compounding time, the screw speed, and the barrel temperature. All experiments in the batch extruder were conducted under nitrogen purging. The scale-up process needed a transposition of these parameters to the continuous process to obtain a similar material like in the batch process. The characterizing parameters for the micro-compounder and the mini-extruder are compared in Table 3.7. In the mini-extruder, the continuously feeding rate determined the output volume, and a maximum output volume of 1.6 kg/h was determined with a feeding rate of 25% at a screw speed between 50 and 400 rpm. The feeding rate of 25% was also related to 1.6 kg/h input volume, so that the in- and output rate correlated well. In contrast to the batch process, where the reaction time can be easily adapted, in the continuous process, the retention time mainly depends on the dimensions of the extruder. For a screw speed of 150 rpm and a feeding rate of Q = 10% (about 0.75 kg/h), a retention time between 4 and 6 min was determined and was, therefore, comparable with the reaction time in the batch process. Both, the micro-compounder and the mini-extruder, work in co-rotating mode. While the batch extruder operates with fixed screw geometry, the screws of the mini-extruder are composed of different pieces and the screw geometry can be adapted to the needs. Depending on the screw geometry the mini-extruder has zones with higher shearing or higher mixing rates, but their influence was not studied in this work and the screws were used with the same set-up for all extrusions. Compared to the micro-compounder, the mini-extruder offers a bigger range for the screw speed (10 - 400 rpm), so that higher shearing forces can be reached. The mini-extruder has ten separate, controllable temperature zones, while in the micro-compounder the use of different temperature zones is of no importance due to the circulation of the material. In the mini-extruder, the different temperature zones can influence the melting, mixing and shearing of the material.

Table 3.7 Characterizing parameters for the micro-compounder and the mini-extruder in comparison.

	micro-compounder	mini-extruder
volume	6 g per batch	continuous (max. 1.6 kg/h)
rotation mode	co-rotation	co-rotation
residence time	variable (set to 5 min)	4-6 min (at 150 rpm)
temperature	1 barrel temperature	10 temperature zones
screw speed	25 - 100 rpm	10 - 400 rpm

3.4.2 Processing of Plasticized Polylactide in a Mini-Extruder

In the early stages, the processing parameters to produce pPLA were chosen as close as possible to the parameters of the micro-compounder: screw speed of 50 rpm, all temperature zones at 180°C and a weight composition of the material of 79/20/1 PLA/acrylPEG/L101. Due to the slower screw speed, it was possible that the retention time was higher compared to the micro-compounder. The main problem of the scale-up process was the feeding of the liquids (plasticizer and initiator) since the available pump system was suitable for amounts higher than 10 ml/min and the feeding rates of the plasticizer and the initiator were less than 3 ml/min for a feeding of PLA with 0.7 kg/h. Therefore, PLA, acrylPEG, and L101 were mixed in a beaker and manually fed to the extruder with a constant rate. In the following, the pPLA from the micro-compounder process are simply labeled with pPLA, whereas the samples obtained from the mini-extruder are marked with ME in the name (e.g. pPLA-ME for all pPLA samples with a weight composition of 79/20/1 produced in the mini-extruder). While the micro-compounder process formed rods of pPLA with a smooth surface, the surface of the pPLA-ME samples was rough and it seemed that the samples contained air bubbles and were not as flexible as the pPLA samples. The naked-eye observation of the pPLA-ME versus pPLA showed huge differences and it was tried to analyze the impact of the processing parameters on pPLA-ME by variation of the screw speed and the temperature. The thermal properties of the different pPLA-ME were compared to the pPLA (Figure 3.9 and Table 3.8). The second heating stage allowed the comparison of the samples with different processing conditions. It is obvious, that DSC of all pPLA-ME differed from the one of pPLA. All four pPLA-ME showed the melting peak of the plasticizer inclusions poly(acrylPEG) which appeared also in the DSC curve of the PLA/poly(acrylPEG) (Figure 3.2 light blue line). For both, pPLA and pPLA-ME samples, a melting peak with a shoulder was observed, which indicated different perfections of the formed crystalline structures. While for pPLA the shoulder of the melting peak occurred on the side of higher temperatures, all materials from the mini-extruder showed a shoulder on the side of lower temperatures. The main melting peak was for all materials around 146°C. This behavior indicated a higher crystal perfection in pPLA compared to the samples from the mini-extruder, since the melting peak, in general, occurred at higher temperatures. The appearance of the poly(acrylPEG)

plasticizer phase and the lower perfection of the crystals could indicate a poor mixing of both phases. It could be assumed that the reaction preferences in the mini-extruder differed from those in micro-compounder. While the grafting on the PLA matrix could be privileged in the micro-compounder, the polymerization of the plasticizer phase seemed to be dominant in the mini-extruder. In addition, the miscibility of the polymerized plasticizer in the PLA matrix seemed to be stronger limited in the mini-extruder, since a separate melting peak of the poly(acylPEG) phase was observed.

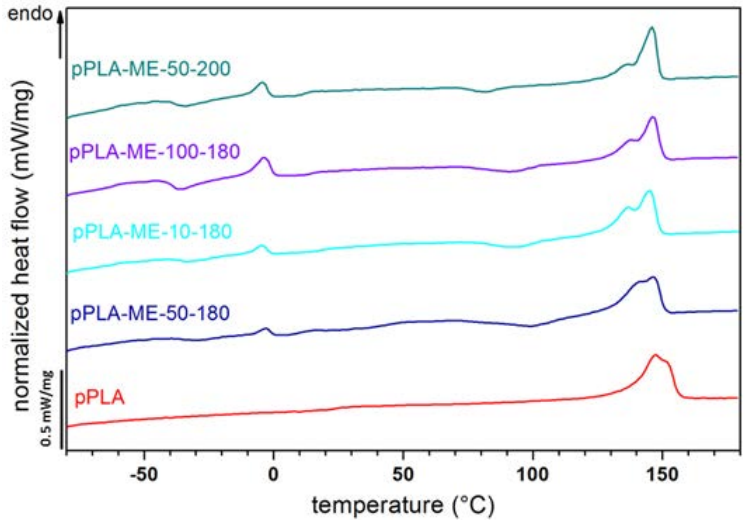

Figure 3.9 DSC curves of pPLA from the micro-compounder compared to the mini-extruder. Data from second heating stage.

For none of the samples, the determination of an exact glass transition temperature was possible, therefore a conclusion about the impact of processing conditions on the reduction of the glass transition by plasticization was not possible. For all pPLA-ME samples, a cold crystallization was observed. Even if the cold crystallization enthalpies were quite low, lower crystallinity values were obtained compared to pPLA. While for pPLA a crystallinity above 30% was measured, the pPLA-ME samples had crystallinities below 20%. Regarding the different processing conditions in the mini-extruder, the main difference concerned the cold crystallization temperature. The sample produced at 200°C showed the lowest T_{cc} at 81.4°C and the samples produced at 180°C showed higher cold crystallization temperatures. Since the cold crystallization temperature also depends on the molecular weight of the PLA, a GPC analysis was used to determine the degradation of the material (Table 3.8). While pPLA had an average molecular weight about 64 kDa, all samples from the mini-extruder had lower molecular weights (between 69% and 94% of pPLA's molecular weight). The degradation of PLA was higher in the mini-extruder and increased with increasing screw speed and increasing processing temperature. The molecular weights of the samples with the highest screw speed (100 rpm) and the

highest processing temperature (200°C) were 44 kDa and 47 kDa, respectively. However, the molecular weight was not the only factor affecting the crystallization temperature. The sample produced at 200°C had indeed the lowest crystallization temperature, but pPLA-ME-100-180 with a comparable molecular weight had a cold crystallization temperature of 90.8°C, which was close to the sample pPLA-ME-50-180 with 87.8°C and 55kDa. In conclusion, the reactive processing of PLA in the mini-extruder led to pPLA-ME with a slightly different structure. On one side, the phase of polymerized plasticizer was observed separately (in DSC) and, on the other side, higher degradation occurred during the reactive processing.

Table 3.8 DSC and GPC analysis of pPLA from the micro-compounder compared to the mini-extruder. DSC data from second heating.

	pPLA micro-compounder, 50 rpm, 180°C, 5min	pPLA-ME-50-180 mini-extruder, 50 rpm, 180°C	pPLA-ME-10-180 mini-extruder, 10 rpm, 180°C	pPLA-ME-100-180 mini-extruder, 100 rpm, 180°C	pPLA-ME-50-200 mini-extruder, 50 rpm, 200°C
T_g (°C)	n.d.	n.d.	n.d.	n.d.	n.d.
T_{cc} (°C)	-	87.8 ± 4.8	97.9 ± 1.3	90.8 ± 0.4	81.4
T_m (°C)	146.7 ± 1.2	139.3 ± 2.1 & 146.4 ± 0.2	140.4 ± 0.8 & 146.0 ± 0.6	137.2 ± 0.4 & 145.6 ± 0.8	134.9 ± 1.7 & 145.7 ± 0.2
ΔH_{cc} (J/g)	-	1.6 ± 0.8	4.9 ± 0.1	3.5 ± 0.3	1.3 ± 0.5
ΔH_m (J/g)	23.3 ± 0.2	18.4 ± 2.5	19.2 ± 0.3	19.3 ± 1.0	15.6 ± 1.9
X_c (%)	31.7 ± 0.2	22.9 ± 4.4	19.4 ± 0.6	21.6 ± 1.8	20.3 ± 1.3
$\bar{M}_w$ (kDa)	64	55	60	44	47
$\bar{M}_n$ (kDa)	160	127	167	102	97
Đ = $\bar{M}_w/\bar{M}_n$	2.5	2.3	2.8	2.3	2.1

n.d. stands for not detected.

3.4.3 Characterization of the Mini-Extruder Film Samples

A further advantage of the mini-extruder is the direct production of films with a sheet die. Films are often used in packaging applications and therefore films of pPLA, PLA/acrylPEG and PLA were produced and analyzed. For all film samples produced with the mini-extruder, the ending "-film" was attached when labeling the specimen data. The materials PLA-film and PLA/acrylPEG-film were obtained directly in one extrusion step at 180°C and 150 rpm. The films of pPLA were obtained in two steps: First, the reactive extrusion was conducted and pellets of pPLA-ME were obtained with a screw speed of 100 rpm and at a temperature of 200°C by the cylindrical die. Second, these pellets were reshaped to films at 190°C and 200 rpm by extrusion with the sheet die. Notwithstanding that after the first extrusion step, pPLA-ME samples showed a different structure as when produced with the micro-compounder, the film samples exhibited no separated melting of the plasticizer inclusions. A clear glass transition occurred at 36.4°C and 38.3°C for the first and second heating, respectively, but cold crystallization was observed as in the pPLA-ME samples. While pPLA-ME and pPLA reached high crystallinity levels (around 20% and above 30%, respectively), pPLA-film shows lower levels of 13.5% for the first and 4.1% for the second heating stage. The PLA/acrylPEG sample exhibited just slight differences from the material produced in the batch process. PLA/acrylPEG-film and PLA-film had melting temperatures around 150°C, which were slightly higher than the melting temperature of pPLA-film (about 147°C). Furthermore, for the second heating stage, a double melting peak was observed so that pPLA seemed to bear crystals with different perfections.

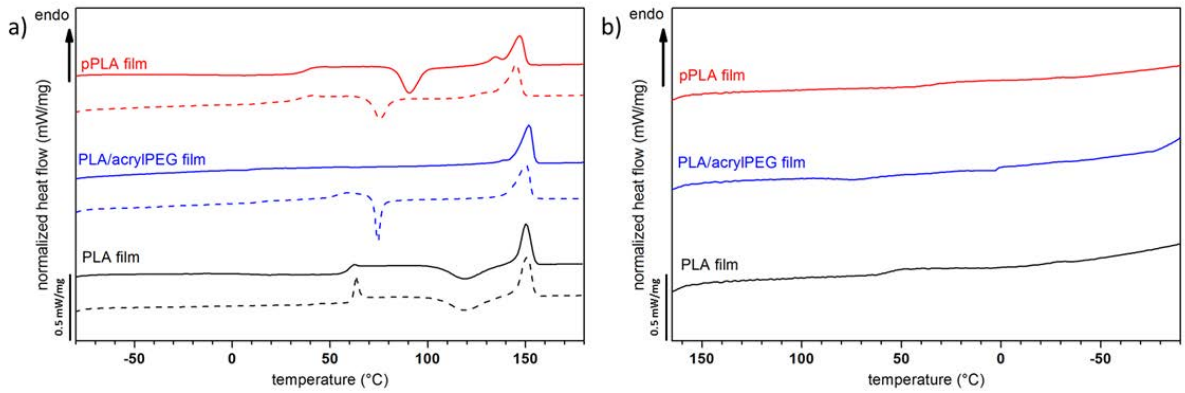

Figure 3.10 DSC curves of film samples from the mini-extruder pPLA-film, PLA/acrylPEG-film, and PLA-film for (a) the first (dashed line) and second (continuous line) heating stage and (b) the cooling stage.

While for PLA/acrylPEG just a very weak glass transition was visible, the crystallinity increased from the first to the second heating stage to the double and reached 34.3%. The cold crystallization occurred in the first heating but disappeared in the second heating stage. PLA-film exhibited the same

glass transition temperature as the PLA samples from the batch process, but the cold crystallization temperature and the melting temperature were visibly lower in the continuous process with the mini-extruder. Furthermore, PLA film showed higher values for crystallization and melting enthalpy, while the crystallinity was still below 5%. The increased cold crystallization and melting enthalpy with the decrease of both temperatures led to the assumption that PLA degraded slightly during the extrusion.

Table 3.9 Thermal parameters of the film samples from the mini-extruder determined by DSC measurements from the first heating stage (1), the cooling stage (2) and the second heating stage (3).

		T_g (°C)	T_{cc} (°C)	T_m (°C)	ΔH_{cc} (J/g)	ΔH_m (J/g)	X_c (%)
pPLA-film (79/20/1) PLA/acrylPEG/L101	1	36.4 ± 0.6	76.4 ± 1.1	146.1 ± 1.3	15.4 ± 0.0	25.3 ± 0.3	13.5 ± 0.5
	2	34.4 ± 2.1					
	3	38.3 ± 0.4	91.2 ± 0.8	135.1 ± 0.6 & 147.2 ± 0.1	21.7 ± 1.2	24.7 ± 0.0	4.1 ± 1.6
PLA/acrylPEG-film (80/20)	1	11.4 ± 1.6	75.6 ± 1.6	150.6 ± 0.4	14.3 ± 1.1	25.0 ± 0.2	14.5 ± 1.3
	2	n.d.					
	3	n.d.		152.0 ± 0.1		25.5 ± 0.1	34.3 ± 0.1
PLA-film	1	62.5 ± 0.2	118.6 ± 0.0	150.4 ± 0.3	18.9 ± 0.3	23.2 ± 0.9	4.6 ± 1.2
	2	57.1 ± 0.7					
	3	59.7 ± 0.1	119.0 ± 0.1	150.5 ± 0.2	19.3 ± 1.8	23.4 ± 0.7	4.4 ± 1.2

n.d. stands for not detected.

Again the degradation in the mini-extruder seemed to play an important role, which impacts the thermal properties (Table 3.10). For all three samples, the molecular weight is much lower compared to the samples from the micro-compounder. This could be due to the higher shearing forces or somewhat higher residence time in the mini-extruder. While PLA-film and PLA/acrylPEG-film still had high average molecular weights of 193 kDa and 181 kDa, respectively, pPLA-film's average molecular weight was halved. As described earlier, during the filtration of pPLA samples the crosslinked and probably grafted part remains in the filter and just the PLA peak could be analyzed. Nevertheless, the conditions in the mini-extruder seemed to increase the degradation compared to the micro-compounder. The double processing of pPLA seemed not to induce further degradation, but a more homogeneous material was obtained since no separate melting of the plasticizer phase occurred. Compared to the micro-compounder samples, pPLA offered not the same homogeneity since very rough samples were obtained.

Table 3.10 GPC analysis for the main PLA peak of pPLA-film, PLA/acrylPEG-film and PLA-film samples.

	$\bar{M}_n$ (kDa)	$\bar{M}_w$ (kDa)	polydispersity Đ = $\bar{M}_w$ / $\bar{M}_n$
pPLA-film	40	102	2.6
PLA/acrylPEG-film	80	181	2.3
PLA-film	73	193	2.6

The comparison of the pPLA-film sample from the mini-extruder with the pPLA from the micro-compounder shows that the two techniques lead to pPLA with different properties (Table 3.11). The evaluation of the thermal properties after the second heating (to compare materials with a similar thermal history) highlighted the differences: pPLA-film offered cold crystallization and a significantly lower crystallinity of 4.1%, while pPLA had a high crystallinity index of 31.7%. In addition, the molecular weight of the soluble PLA fraction was for pPLA-film clearly lower by nearly one third. These different parameters could indicate differences in the structure formation, which are due to the uncontrollable radical reactions. Both samples formed gels and were not completely filterable for the GPC analysis. Therefore it was assumed, that crosslinking and grafting are in both materials present, but the exact density of crosslinking and/or grafting could be proved reliable. In addition, the surface of the samples indicated further differences: The surface of pPLA was smooth, but pPLA-films were rough and uneven.

Table 3.11 Comparison of the thermal parameters and the molecular weight for pPLA produced with the micro-compounder and pPLA-film produced with the mini-extruder.

	T_g (°C)	T_{cc} (°C)	T_m (°C)	X_c (%)	$\bar{M}_n$ (kDa)	$\bar{M}_w$ (kDa)	Đ = $\bar{M}_w$ / $\bar{M}_n$
pPLA	n.d.	-	146.7 ± 1.2	31.7 ± 0.2	64	160	2.5
pPLA-film	38.3 ± 0.4	91.2 ± 0.8	135.1 ± 0.6 & 147.2 ± 0.1	4.1 ± 1.6	40	102	2.6

n.d. stands for not detected.

3.5 Plasticizer Inclusion's Chemical Structure and Mechanical Behavior

This subchapter is partially adapted from the publication: Resolving inclusion structure and deformation mechanisms in polylactide plasticized by reactive extrusion by B. Brüster, C. Amozoqueño, P. Grysan, I. Peral, B. Watts, J.-M. Raquez, P. Dubois, and F. Addiego. Submitted to Macromolecular Materials and Engineering in July 2017.

The samples were produced from the film samples from the mini-extruder. The film shape was not important for the characterization, so the samples were simply called: pPLA, PLA/acrylPEG, and PLA.

The inclusion's chemical structure in pPLA was examined by scanning transmission X-ray microscopy coupled with near-edge X-ray absorption fine structure nano-spectroscopy (STXM/NEXAFS) and compared to that of the pPLA matrix, the PLA/acrylPEG matrix, neat PLA, and poly(acrylPEG) (Figure 3.11). First, C1s NEXAFS spectra of pPLA inclusion and pPLA matrix were compared in order to identify a photon energy displaying differences in the X-ray absorption that could be utilized to differentiate these materials (Figure 3.11 a). In the case of the pPLA matrix, a strong resonance peak was noted at 288.5 eV. It was assigned to the C1s → $\pi^*_{(C=O)}$ [108,109] and was obviously one of the most representative chemical functions in PLA monomer unit (peak labeled 1). Another resonance peak appeared at 289.9 eV and is commonly attributed to the C1s → C-H Rydberg states (peak labeled 2) [108,110]. Last, some resonance peaks observed in the range 292 eV - 300 eV were probably associated with C1s →$\sigma^*_{(C-C)}$ transitions [108,111]. In the case of pPLA inclusions, two main resonance peaks centered at 288.8 eV and 289.7 eV were noted. Based on NEXAFS testing done on oligo(ethylene glycol) and PEG-based plasma polymer, the resonance at 288.8 eV can be attributed to C1s → $\pi^*_{(C-H)}$ transition (peak labeled 3), while the resonance at 289.7 eV can be attributed to the C1s → $\sigma^*_{(C-O)}$ transition (peak labeled 4) [112,113]. Additional resonance peaks were observed for the inclusion in pPLA in the range 292 eV - 300 eV and assigned probably to C1s →$\sigma^*_{(C-C)}$ transition [108,111]. Note that the weak resonance at 285.2 eV was attributed to some carbon contamination [114].

When comparing the pPLA inclusion spectrum with the pPLA matrix spectrum, it can be clearly seen that the energy of peak labelled 1 (C1s → $\pi^*_{(C=O)}$ of the matrix) can be used to highlight PLA-rich domains, while the energy of peak labelled 4 (C1s → $s^*_{(C-O)}$ of the inclusion) can be used to highlight plasticizer-rich domains. By comparing the pPLA matrix spectrum with that of PLA/acrylPEG matrix and neat PLA, no significant difference was noted (Figure 3.11 b), indicating that the chemical modifications of PLA matrix (grafting and crosslinking with the plasticizer) were not detected by STXM/NEXAFS. More interestingly, the spectrum of poly(acrylPEG) was similar to that of pPLA's inclusions (Figure 3.11 b), which the previously suggested reaction mechanism that acrylPEG polymerizes to form inclusions [41,51].

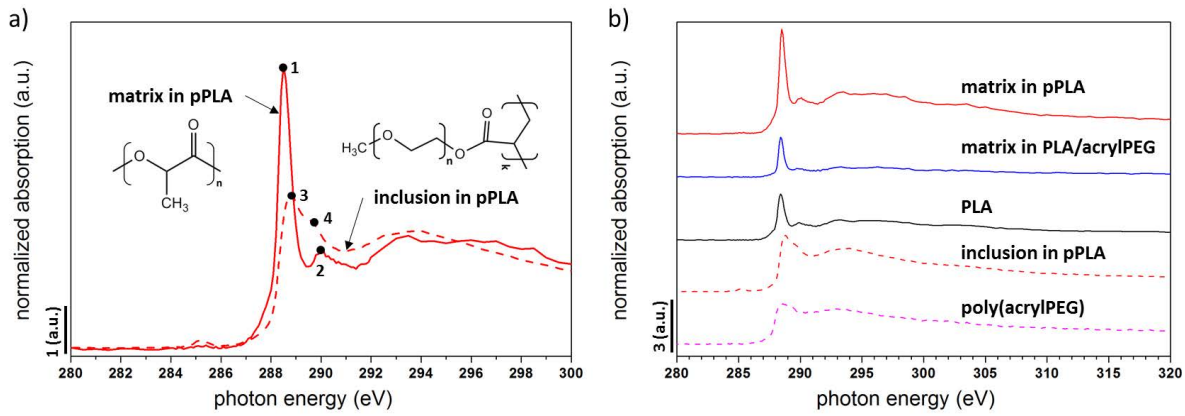

Figure 3.11 a) C1s NEXAFS spectrum of pPLA inclusion compared to that of pPLA matrix (with the corresponding chemical structures), and b) C1s NEXAFS spectra of pPLA matrix, PLA/acrylPEG matrix, neat PLA, pPLA inclusion, and neat poly(acrylPEG). All the spectra were extracted and reduced from STXM micrographs. 1: C1s → $\pi^*_{(C=O)}$ of the pPLA matrix, 2: C1s → C-H Rydberg of the of the pPLA matrix, 3: C1s → $\pi^*_{(C-H)}$ of the pPLA inclusion, and 4: C1s → $\sigma^*_{(C-O)}$ of the pPLA inclusion.

STXM images recorded at 288.5 eV (PLA-rich domains) and at 289.7 eV (poly(acrylPEG)-rich domains) in the case of pPLA were shown in Figure 3.12. PLA-rich domains were obviously observed in the matrix (Figure 3.12 a, c, and e), while inside the inclusions, only some small areas of these PLA-rich domains were noted (Figure 3.12 c). Concerning the poly(acrylPEG)-rich domains, they were localized within the inclusions (Figure 3.12 b, d, and f). One important result was that inside the inclusions, the distribution of these poly(acrylPEG)-rich domains was heterogeneous. In particular, these domains appeared to be localized at the inclusion shell (Figure 3.12 b and f), or were randomly distributed in the rest of the inclusion, especially for the large inclusions (Figure 3.12 d). To understand the inclusion structure obtained by STXM/NEXAFS, it is important to consider the sample preparation methodology of slicing 100 nm-thick specimens. It was hypothesized that a core-shell structure exists in pPLA inclusions. When the specimen cutting passed through the equatorial region of an inclusion, then a perfect core-shell effect may be visible as in Figure 3.12 f. The inclusion shell would be in this case from poly(acrylPEG)-rich domains, while the inclusion core would be less rich in poly(acrylPEG). In the case where the specimen cutting would pass near a border region of the inclusion, the resulting structure would mainly consist of the poly(acrylPEG)-rich domains. However, the cutting procedure could lead to a damage of the inclusions structure, resulting in a heterogeneous structure as shown in Figure 3.12 b. Note that the presence of PLA-rich domains in the inclusion (Figure 3.12 c) was expected to be due to the cutting procedure that may extract some PLA from the matrix.

To understand the core-shell structure of pPLA inclusions, the processes involved in producing the material have to be examined. It can be hypothesized that during the first seconds of the plasticizer and free radical initiator injection into the extruder, the liquids were heated and distributed/dispersed

within the melted PLA matrix under shear and elongational flows. When the radical initiator attained its decomposition temperature, free radicals were formed and radical reactions occurred in all of the material. As described in by Kfoury et al. [41], the free radical initiator can create radicals in the PLA backbone chain or can polymerize the acrylPEG to poly(acrylPEG). Furthermore, the formed PLA radicals can also start the polymerization of acrylPEG so that poly(acrylPEG) gets grafted onto the PLA backbone and the recombination of radicals or grafting of poly(acrylPEG) twice to the PLA matrix induced crosslinking. The localization of poly(acrylPEG) at the shell of the inclusions is hard to explain by a mechanism, because the radical reactions are uncontrollable and, in addition, the material underlay shear forces in the extruder. It was assumed, that the plasticizer forms agglomerates in the viscous PLA matrix so that reactions at the interface between the agglomerates and the PLA matrix were preferred. Indeed, in this area free radicals engendered from the radical initiator, acrylPEG, and PLA are present, which enhance reactivity. It is to be noted that the grafting and crosslinking bonds between the plasticizer and the matrix can at a given point of the reactive extrusion decrease the mobility and could hinder the formation of more dense inclusions (Figure 3.12 f).

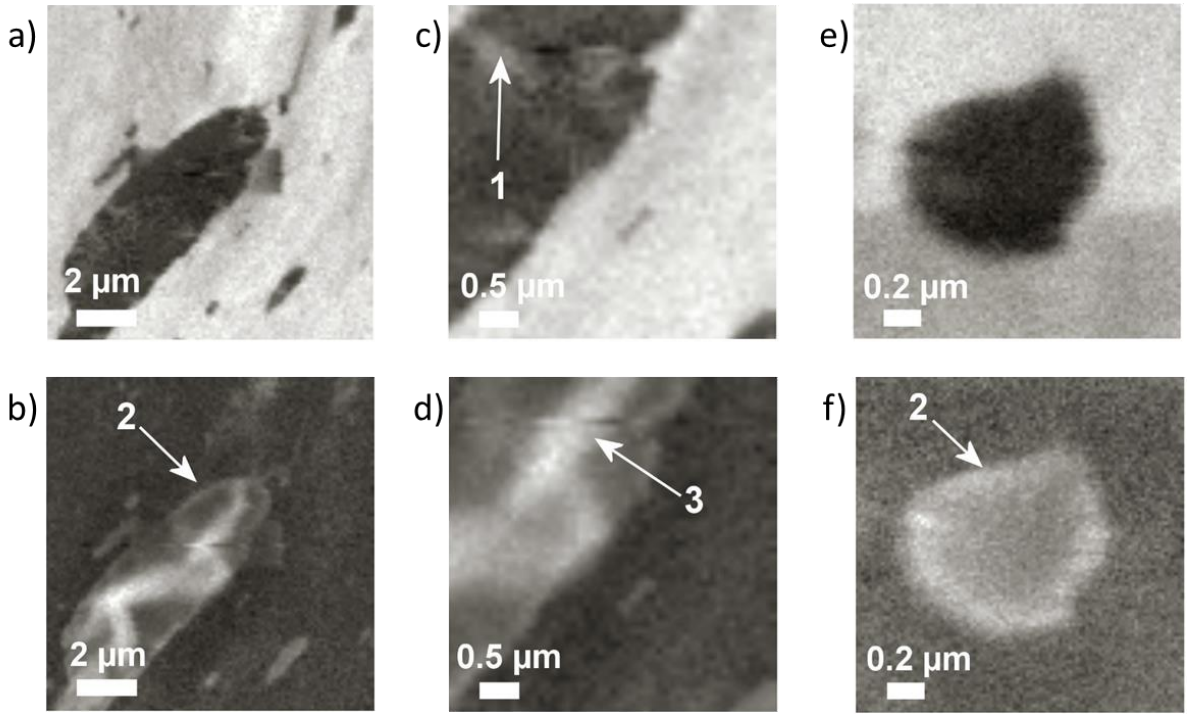

Figure 3.12 Composition maps obtained from STXM micrographs of pPLA indicating the present amount of PLA (a, c, and e), and poly(acrylPEG) (b, d, and f). Images a) to d) represented the same area at different magnifications, while images e) and f) were taken in another area of interest. 1: PLA-rich domains inside the inclusion, 2: poly(acrylPEG)-rich domains at the inclusion shell, and 3: poly(acrylPEG)-rich domains at the inclusion core.

As for the samples produced by the micro-compounder, the mechanical behavior of PLA-based films was investigated by AFM imaging. In this context, the coupling between topographical contrast imaging and elastic modulus contrast imaging of PLA, PLA/acrylPEG, and pPLA was represented in Figure 3.13. The average elastic modulus of the matrix and inclusions were reported in Table 3.12. Concerning PLA, an average matrix elastic modulus of 2.40 ± 0.26 GPa was obtained (Figure 3.13 b). In the case of pPLA, the presence of holes and nanometric inclusions was observed (Figure 3.13 c). The average elastic modulus of the pPLA matrix was 2.60 ± 0.26 GPa, while that of the inclusions was 0.23 ± 0.04 GPa. The presence of holes may be due to the destruction of plasticizer inclusion shells during sample preparation, highlighting again the possible core-shell effect. The stiffness values are in good accordance with the previously determined values for the stiffness of inclusions and matrix of PLA, pPLA, and PLA/acrylPEG (Figure 3.4). The AFM investigation of PLA/acrylPEG was much more complicated due to the leaching of plasticizer at the sample surface. As shown by DSC, PLA/acrylPEG has a T_g below room temperature and behaves hence rubber-like at room temperature. The migration of the plasticizer to the surface was observed since the simple blending of PLA and acrylPEG formed no inclusions of grafted plasticizer. The observed areas of plasticizer were agglomerations of leached plasticizer, which complicated the separate analysis of matrix and plasticizer phase only done on a limited number of areas (Figure 3.13 e and f). The average elastic modulus of PLA/acrylPEG matrix was 1.79 ± 0.10 GPa, while that of its plasticizer phase was 0.04 ± 0.01 GPa. This nanomechanical study of PLA-based materials revealed that the plasticizer's elastic modulus increased by a factor of 475% from PLA/acrylPEG to pPLA that is clearly a further evidence for the acrylPEG polymerization, in addition to the STXM/NEXAFS results (Figure 3.11 b). Note that here only poly(acrylPEG) inclusions with a faultless shell could be analyzed, which were difficult to find. Indeed, most of the supposed inclusions were holes in the case of pPLA (Figure 3.13 c), which did not permit the determination of the inclusion elastic modulus. The weak increase of elastic modulus of the matrix from PLA to pPLA may be due to the local grafting/crosslinking points of PLA with poly(acrylPEG) and to the increased crystallinity (Table 3.12). On the contrary, the decrease of matrix elastic modulus from PLA to PLA/acrylPEG may be due to the local dispersion of acrylPEG plasticizer within the PLA matrix that overcame the gain in rigidity due to the increase of matrix crystallinity.

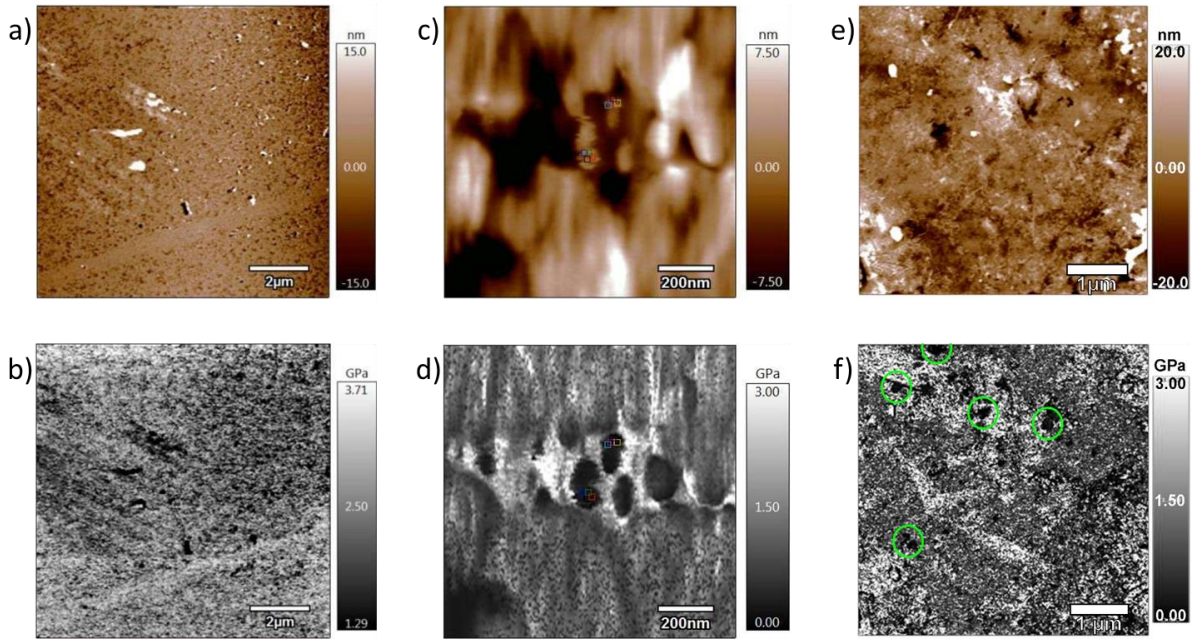

Figure 3.13 AFM investigation of PLA (a and b), pPLA (c and d), and PLA/acrylPEG (e and f) with topographical contrast mode (a, c, and e), and modulus contrast mode (b, d, and f). The circles and squares represented the areas where elastic modulus was calculated.

Table 3.12 Average elastic modulus of the matrix and inclusion calculated by AFM for PLA, PLA/acrylPEG, and pPLA (with standard deviations).

Material	Averaged elastic modulus (GPa)	
	Matrix	Inclusion
PLA	2.40 ± 0.26	-
PLA/acrylPEG	1.79 ± 0.10	0.04 ± 0.01
pPLA	2.60 ± 0.26	0.23 ± 0.04

In conclusion, the scale-up from the batch micro-compounder to the continuous mini-extruder was possible, but the material's properties depend strongly on the processing conditions. The mini-extruder induced a higher degradation and the production of pPLA-ME showed a less homogeneous material with a separated melting of the plasticizer phase. The production of pPLA-films directly in one extrusion step was not possible. Therefore, pPLA-film had to be produced in two extrusion steps. The second processing step did not favor degradation but homogenized the material and pPLA-film's thermal properties were comparable to pPLA produced with the micro-compounder, but still a higher roughness of the surface was observed. The chemical analysis of the plasticizer phase proved the polymerization of the plasticizer to form inclusions and the morphology analysis of the film samples indicated a similar trend of stiffness evolution as observed for the micro-compounder samples.

3.6 Conclusion

The reactive blending of PLA with acrylPEG as a plasticizer and a free radical initiator led to a plasticized PLA with a quite unique structure, which was called pPLA. To understand the different ongoing reaction during the reactive extrusion and their impact on pPLA's properties, the impacts of the free non-grafted plasticizer (PLA/acrylPEG), the polymerized plasticizer (PLA/poly(acrylPEG)), the grafted plasticizer (pPLA aS), and of the initiator (PLA/L101) were analyzed and compared to the need PLA matrix and the structure of pPLA. The occurring structural elements of grafted and free inclusions as well as crosslinking were further analyzed by the swelling behavior of the materials and the morphology of the materials. While the gel formation in swellings tests proved the slight crosslinking in pPLA and PLA/L101, the morphology analysis indicated the formation of inclusions with a higher stiffness in PLA and agglomeration of the plasticizer in PLA/acrylPEG with a lower stiffness. In pPLA, the plasticizer could polymerize and it was shown, that the poly(acrylPEG) just slightly improved the impact toughness when blended with PLA while blending with acrylPEG or the formation of pPLA increased the impact toughness obviously. Furthermore, the initiator induced grafting and crosslinking, and, reasonably, PLA/L101 had a reduced impact toughness even lower than PLA, so that the crosslinking also decreased the impact toughness of pPLA compared to PLA/acrylPEG. In sum, the positive effect of free plasticizer in pPLA on the impact toughness competed with the negative effect of crosslinking, grafting and polymerization of the plasticizer. In addition, the impact toughness was influenced by the crystallinity. The faster crystallization during isothermal crystallization of pPLA compared to unmodified PLA was attributed to the higher PLA chain mobility induced by the plasticization. Regarding the crystallization ability, crosslinking and grafting acted as crystallization hindering points explaining the lower final crystallinity values. The particular structure of pPLA had a high impact on the impact resistance and the crystallization behavior and improved both.

The applicability of a material depends also on the production capacities. For this purpose, a scale-up from the batch process to a semi-continuous process in a mini-extruder was realized. The comparison to a completely continuous process was not possible due to the missing of a suitable pump for liquid feeding. The mini-extruder caused a higher degradation of the PLA matrix, which was proved by the molecular weight analysis of the PLA fraction. With increasing screw speed and temperature, the degradation increased as well. The mixing in the micro-compounder and the mini-extruder differed since the pPLA-ME samples showed a separated melting peak of the plasticizer slightly below 0°C, which did not occur in pPLA. In a further step, films of pPLA, PLA/acrylPEG, and PLA were produced. PLA-film and PLA/acrylPEG-film were obtained easily by extrusion and shaping with a sheet die. The production of pPLA needed two steps: First, pPLA-ME was produced in pellets and afterward pPLA was extruded again and shaped to pPLA-film. After the second processing step to obtain films, the melting

peak of plasticizer phase disappeared and the pPLA-film material was more alike pPLA. This could lead to the assumption, that the second processing step produced a more homogeneous material, but the samples had still a rough surface which indicated a higher heterogeneity compared to the batch process. Again, the formation of plasticizer inclusions was proved by AFM stiffness analysis and showed the same trends as observed for the materials from the micro-compounder. Finally, the inclusion's chemical structure was identified as the polymerized plasticizer and the formation of core-shell like structures. It was shown that the inclusions exhibit a poly(acrylPEG)-rich shell, while the core was less rich in poly(acrylPEG). The exact origin of this structures was not clarified, but it was assumed that formation of plasticizer agglomerations started the polymerization in the shell region and the grafting and crosslinking limited a more dense inclusion formation in the core. These results confirmed the assumed structure of a PLA matrix with polymerized partially grafted plasticizer inclusions.

All these results indicate that the final structure is impacted by the processing, but an exact control of the structure is hardly realizable due to the free radical reactions. It was not possible to control or quantify the grafting and crosslinking reactions, but it was proved that these reactions have a positive impact on the impact toughness and the crystallization ability. Nevertheless, the detailed structure analysis proved the formation of poly(acrylPEG) inclusions and can help to identify and understand ongoing mechanisms during deformation or thermomechanical recycling, which will be discussed in the next chapters.

4 Structure Evolution with Strain

4.1 Introduction

PLA, as a bio-based and (bio)degradable polymer, offers many possibilities to replace common plastic materials but its drawbacks demand further investigations. One main drawback is its brittleness at room temperature which suggests to consider a plasticization principle to improve its drawability at room temperature. In neat PLA, the deformation mechanisms depend on the deformation rate and the temperature. PLA is brittle below its glass transition temperature and becomes rubber-like with increasing temperature. In the literature [72–75], three main mechanisms were considered during PLA deformation: (i) the ordering of the amorphous phase, (ii) transformation of initial crystalline phases, and (iii) damage by cavitation. The first mechanism describes the ordering of the amorphous phase to crystalline phases. Normally, PLA crystallizes in the α-form, but also the formation of the metastable meso-form and crystallization in α'-form can take place. The second mechanism contains the transformation of initial crystalline phases, normally α-form, into the meso-form or the α'-form. The third mechanism is not counted as a deformation mechanism, but as a damage mechanism and clarifies the damage of the material by cavitation. Depending on the drawing conditions, the mechanisms occur separately, after each other or in parallel. The tensile deformation allows the determination of characteristic parameters such as the tensile modulus E, the yield stress σ_y, the strain at break (also called ultimate strain) ε_u, and the ultimate stress σ_u. With the help of the yield stress σ_y at different strain rates $\dot{\varepsilon}$, the plastic flow activation volume V_{flow} was determined by the Eyring equation

$$\sigma_y = \frac{E_0}{V_{flow}} + \frac{kT}{V_{flow}} \cdot \ln \frac{2\dot{\varepsilon}}{\dot{\varepsilon}_0} \tag{4.1}$$

where E_0 is the activation energy barrier for plastic deformation, k is the Boltzmann constant, T is the temperature and $\dot{\varepsilon}_0$ is a pre-exponential factor. A plot of σ_y versus ln($\dot{\varepsilon}$) allowed the determination of V_{flow} via the resulting slope, which is equal to kT/V_{flow} [115,116].

The crystalline phase transformations can be analyzed by DSC and WAXS measurements. In addition, DSC allows the measurement of the thermal properties like the glass transition temperature (T_g), the cold crystallization temperature (T_{cc}), the melting temperature (T_m) and the melting temperature of PLA's mesophase (T_{meso}). As described in the previous chapter, the crystallinity is calculated by Equation (4.2) with the enthalpy of a 100% crystalline PLA, which is $\Delta H_{m,0}$ = 93 J/g [96]. For pPLA

samples, the mass fraction of PLA in the samples has to be considered with a factor x_{PLA} = 0.79, whereas the factor for neat PLA is considered to be 1. Since the transformation of the mesophase is related to the deformation mechanisms, the mesophase content in neat PLA was determined by using the mesophase enthalpy ΔH_{meso} based on the Equation (4.3), where $\Delta H_{meso,0}$ corresponds to the heat associated to the fusion of a 100% mesophase PLA, which is $\Delta H_{meso,0}$ = 70 J/g [74].

$$X_c = \frac{\Delta H_m - \Delta H_{cc}}{x_{PLA} \cdot \Delta H_{m,0}} \cdot 100\% \tag{4.2}$$

$$X_{meso} = \frac{\Delta H_{meso}}{\Delta H_{meso,0}} \cdot 100\% \tag{4.3}$$

While DSC allows calculating the crystalline and mesophase amount of the material, WAXS analysis enables the determination of the different ordered phases in PLA. In the WAXS diagram, three amorphous halos are located at 2θ angles of approximately 15.0°, 21.2°, and 31.0°. The first two scattering halos were attributed to interchain periodicities, while the last scattering halo was attributed to an intrachain periodicity (distance between methyl groups) [21]. Concerning crystalline phases, the peaks centered at 2θ angles of 14.6°, 16.5°, 18.8°, and 22.2° were attributed to the (010), (110/200), (203) and (210) reflections, respectively [51,73]. Since it is generally not possible to unambiguously distinguish between the crystalline phases α and α′, only one crystalline phase was considered for the WAXS analyses [21]. In the case of PLA, an amorphous to mesomorphic phase transformation can occur when drawing the material, resulting in the formation of a broad peak centered at 16.5° [76]. For a given azimuthal Φ direction, the weight fraction of crystallinity X_c was calculated as the ratio between the total crystalline peak area to the overall peak area. The average crystallinity $< X_c >$ was calculated using the Equation (4.4) [117,118],

$$< X_c > = \frac{\int_0^{\pi/2} X_c(\Phi) \cdot \sum A(\Phi) \cdot \sin(\Phi) \cdot d(\Phi)}{\int_0^{\pi/2} \sum A(\Phi) \cdot \sin(\Phi) \cdot d(\Phi)} \tag{4.4}$$

where X_c (Φ) is the crystallinity obtained for a given azimuthal angle Φ, while $\sum A(\Phi)$ is the sum of the area of all the peaks (amorphous, crystalline and mesomorphic phases) for a given azimuthal angle Φ. The same methodology is used to calculate the weight fraction of the mesophase $<X_{meso}>$.

The transformations in the amorphous and crystalline phases is quantified thanks to the ordering inside the different phases. The calculation of Herman's orientation function allows estimating the ordering in the different phases for different phases at different deformation states. The Herman orientation function is calculated for the three amorphous halos, the two main crystalline peaks (110/200) and (203) and the mesomorphic peak based on the following equation:

$$f_{i,z} = \frac{3 < \cos^2 \Phi_{i,z} > -1}{2} \tag{4.5}$$

where *i* is the considered case and $< \cos^2 \Phi_{i,z} >$ is the average of the cosine squared angle between the drawing direction *z* and the normal of the considered scattering planes *i* (evolved by the crystalline diffractions or by the amorphous molecular scatterings). For PLA, the following notation was used: $f_{1,z}$ corresponds to the amorphous halo positioned at 15.0°, $f_{2,z}$ corresponds to the amorphous halo positioned at 21.2°, $f_{3,z}$ corresponds to the amorphous halo positioned at 31.0°, $f_{(110/200),z}$ corresponds to the crystalline peak (110/200), $f_{(203),z}$ corresponds to the crystalline peak (203) and $f_{meso,z}$ corresponds to the mesophase. The value $< \cos^2 \Phi_{i,z} >$ was calculated from

$$< \cos^2 \Phi_{i,z} > = \frac{\int_0^{\pi/2} I_i(\Phi) \cdot \sin(\Phi) \cdot \cos^2(\Phi) \cdot d(\Phi)}{\int_0^{\pi/2} I_i(\Phi) \cdot \sin(\Phi) \cdot d(\Phi)} \tag{4.6}$$

where $I_i(\Phi)$ corresponds to the scattering intensity of the *i* objects considered (crystalline peaks or amorphous halos) for a given azimuthal Φ direction.

While at temperatures close to or above the glass transition temperature of PLA, the ordering or transformation mechanisms dominate, the damage mechanisms are more important at room temperature. The main damage mechanisms in PLA was determined to be the crazing mechanisms. Crazes are damage structures, which are not completely voided, but consist in voids alternating with fibrils perpendicular to the growing direction of the craze [77]. Small angle X-ray scattering (SAXS) testing allows a detailed analysis of these craze structures since the voids and fibrils as well as the craze walls give a different scattering due to their different electron densities [21,55,73,74,79]. With increasing strain, these craze structures develop to cracks when the fibrils cannot suffer the strain anymore and break. The brittle behavior of PLA is reasoned by the breakdown of the fibrils, which means that the crazing is unstable below the ductile-brittle transition [71]. Stoclet et al. [55] proved

recently, that the drawing below the glass transition temperature can involve both crazing and shear bands. The crazing mechanisms for PLA at room temperature results in the limited plasticity at room temperature. As described in the previous chapter (3 Process-Structure Relationship for Plasticized Polylactide), the plasticized PLA from reactive extrusion has a unique structure with partially grafted inclusions of the plasticizer. Since the plasticization improves the drawability of PLA-based materials at room temperature, it also impacts the deformation and especially the damage mechanisms.

To analyze the true tensile behavior of materials, it is important to follow the evolution of the axial (ε_{11}) and two transversal strains (ε_{22} and ε_{33}) during the tensile deformation. In the case where only one transversal strain can be measured, one is let to assume that the two transversal strains are equal $\varepsilon_{22} \approx \varepsilon_{33}$. The flow behavior of the samples can be characterized by the volume strain, which is the sum of the axial and transversal strains resulting in Equation (4.7).

$$\begin{aligned} \varepsilon_v &= \varepsilon_{11} + \varepsilon_{22} + \varepsilon_{33} \\ &= \varepsilon_{11} + 2 \cdot \varepsilon_{22} \end{aligned} \tag{4.7}$$

The literature describes the definition of a coefficient relating the transversal and axial strain to obtain a parameter that indicates the anisotropy of a material [119]. The ratio of the axial deformation (ε_{11}) to the average absolute value of the transversal deformation ($|\varepsilon_t|$) was defined as the coefficient $D = \varepsilon_{11}/|\varepsilon_t|$, whereas $\varepsilon_t = (\varepsilon_{22} + \varepsilon_{33})/2$. With the assumption $\varepsilon_{33} \approx \varepsilon_{22}$, D can be determined as $D = \varepsilon_{11}/|\varepsilon_{22}|$ or from the volume strain measurement as described by Equation (4.8). In the elastic regime, the factor D can be related to the Poisson coefficient ν ($D^{-1} = \nu$), which classifies materials in rigid (ν = 0.33) and rubber-like (ν = 0.5) materials [120].

$$\varepsilon_v = (1 - 2D^{-1}) \cdot \varepsilon_{11} \tag{4.8}$$

This chapter aims at the identification of deformation mechanisms of pPLA compared to PLA, in terms of molecular aspects and deformation heterogeneities. The first part deals with the impact of different strain rates and temperatures on the deformation mechanisms of pPLA compared to PLA. For this purpose, the crystallinity and the orientations of the chains in the amorphous and crystalline phases are determined by DSC and WAXS analysis ex-situ. The objective of the first part is mainly to identify molecular aspects, including the strain-induced chain orientation and phase transformation of pPLA during drawing. The second part concentrates on the drawing-induced heterogeneities in PLA-based materials at room temperature. The impact of initial crystallization and plasticization on these

heterogeneities is studied by a multiscale approach. A time-resolved SAXS analysis identifies the cavitation mechanisms at the nanometer scale and an optical microscope analysis at the micrometer scale. In addition, the volume strain at millimeter scale is determined by means of Digital Image Correlation (DIC). The third part is related to a more detailed analysis of the structure of pPLA's inclusions and its impact on the deformation. The pPLA sample is analyzed by scanning transmission X-ray microscopy (STXM) equipped with near-edge X-ray absorption fine structure nano-spectroscopy (NEXAFS) to analyze the representative bonds of the plasticizer and to determine its spatial distribution in the matrix. Micro-computed X-ray tomography (µCT) is used to visualize the inclusion after the deformation and analyze the damaging mechanisms in pPLA.

4.2 Deformation Mechanisms of Plasticized Polylactide

This subchapter is adapted from the publication: Strain-induced deformation mechanisms of polylactide plasticized with acrylated poly(ethylene glycol) obtained by reactive extrusion by K. Wang, B. Brüster, F. Addiego, G. Kfoury, F. Hassouna, D. Ruch, J.-M. Raquez and P. Dubois in Polymer International 64 (2015), 1544-1554. [121]

4.2.1 Processing

The experimental details of this section are explained in the Appendix A.4.1 to A.4.5.

Two materials, namely PLA and pPLA, with a weight composition of 100/0/0 and 79/20/1 PLA/acrylPEG/L101 were produced in the micro-compounder with a residence time of 5 min at 180°C and 100 rpm as screw speed. After the extrusion, the samples were pelletized and shaped to tensile specimens by hot-pressing. The specimen shape was based on the ASTM D638-10 type V and had an overall length of 63.5 mm, a thickness of 3 mm and a gauge section of 25 mm x 3 mm. The represented stress-strain curves are engineering stress vs engineering strain curves.

4.2.2 Mechanical Investigation

The influence of the temperature (20°C, 50°C, and 80°C) and of the strain rate (4×10^{-2} s^{-1}, 4×10^{-3} s^{-1}, and 4×10^{-4} s^{-1}) on the tensile behavior of pPLA is shown in Figure 4.1, while the extracted mechanical parameters are reported in Table 4.1. As a reference, the same mechanical investigation was conducted on the untreated PLA grade. At 20°C and 4×10^{-2} s^{-1} (Figure 4.1), the tensile behavior of pPLA exhibited three stages: (i) an initial viscoelastic stage where the stress increased drastically with the strain up to a maximum point related to the yield point σ_y = 25 MPa characterized by a tensile modulus of 865 MPa, (ii) the onset of the viscoplastic stage characterized by a drop of the stress, and (iii) a final increase of the stress until the breakpoint at the ultimate strain ε_u = 16%. Under the same conditions, PLA exhibited a brittle tensile behavior without any viscoplastic stage characterized by a tensile modulus E = 3123 MPa and an ultimate strain of ε_u = 2%. In the case of pPLA, with increasing temperature or decreasing strain rate, a decrease of the tensile modulus, yield stress, and ultimate stress was noted. At the same time, an increase of the ultimate strain was observed (Table 4.1). For example, at 80°C and 4×10^{-4} s^{-1}, E = 63.5 MPa, σ_y = 4 MPa, and ε_u = 470% for pPLA. It must also be mentioned that the intensity of the stress drop at the beginning of the viscoplastic stage decreased when decreasing strain rate from 4×10^{-2} s^{-1} to 4×10^{-4} s^{-1} and when increasing temperature from 20°C to 80°C. For PLA, when increasing the temperature from 20°C to 50°C, a viscoplastic stage appeared with an ultimate strain of 298% (Figure 4.1 a and b). The yield activation volume of the materials was calculated using the Eyring equation (Equation (4.1)) from the yield stress (Table 4.1). As at room temperature PLA was brittle and exhibited no plasticity, no activation volume was determined for this

condition. It was found that the activation volume of pPLA at 50°C equal to 9.2 nm^3 was higher compared to that of PLA equal to 0.2 nm^3. At 80°C, the activation volume of PLA was higher than that of pPLA (27.6 nm^3 vs. 19.7 nm^3). For both materials, the activation volume increased with the temperature.

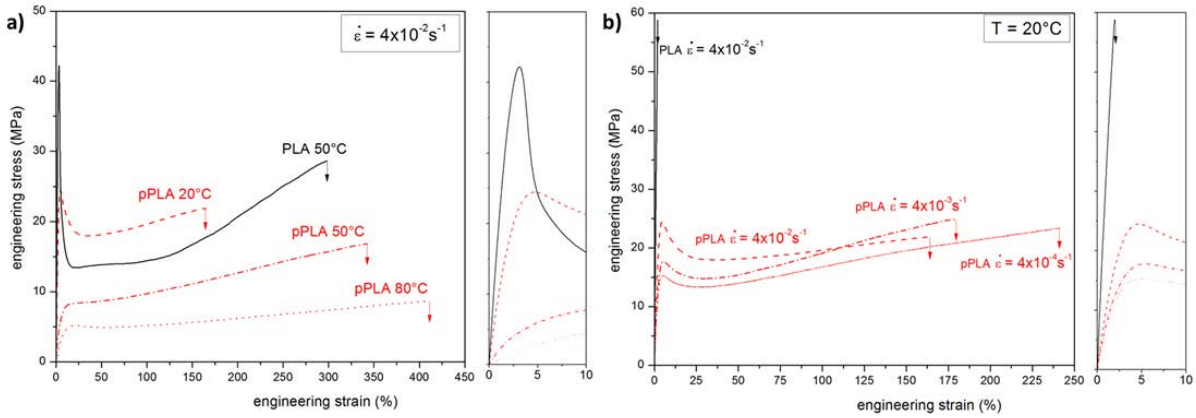

Figure 4.1 Influence of (a) the temperature at 4×10^{-2} s^{-1} and of (b) the strain rate at 20°C on the tensile behavior of pPLA including a zoom-in view of the initial part of the curves (some reference curves of PLA were also plotted for comparison).

Optical microscope images of pPLA recorded for different strain levels and strain rates are represented in Figure 4.2. For the characterization of the whitening intensity, the average gray level of the optical image was calculated by means of the software ImageJ from a 1.5 mm × 1.5 mm squared area taken at the center of the specimen. The average gray level ranged from 0 (black) to 255 (white). At the undeformed state (Figure 4.2 a), pPLA was quite transparent (but less transparent than untreated PLA) with a gray level of 102.5. With increasing strain level at 20°C and 4×10^{-4} s^{-1}, a progressive whitening of the samples was observed (Figure 4.2 a). Indeed, the gray level increased from 102.5 at the undeformed state to 254 for the strain of 240%. Note that at a strain of 150%, the gray level was equal to 191.8 for the same strain rate. Increasing the strain rate to 4×10^{-2} s^{-1} led to a weak increase of the whitening at a strain of 150% as the gray level increased from 191.8 at 4×10^{-4} s^{-1} to 208.8 at 4×10^{-2} s^{-1} (Figure 4.2 b). After a recovery period of one week at an initial strain of 150% obtained at 4×10^{-2} s^{-1}, a partial disappearance of the whitening-related to a gray level of 123.8 was observed (Figure 4.2 c). When decreasing strain rate to 4×10^{-4} s^{-1}, the whitening was more permanent than for 4×10^{-2} s^{-1}. Concerning PLA, some whitening phenomena were also noted at the highest strain rate of 4×10^{-2} s^{-1} and 50°C, and in this case, it was permanent even after several weeks.

Table 4.1 Tensile modulus E, yield stress σ_y, elongation at break ϵ_u, and ultimate stress σ_u of PLA and pPLA as a function of the temperature and strain rate extracted from tensile testing curves and yielding activation volume determined from Eyring equation (n.m. stands for not measurable).

	Temperature T (°C)	strain rate $\dot{\epsilon}$ (s^{-1})	tensile modulus E (MPa)	Yield stress σ_y (MPa)	Yielding activation volume V (mm^3)	elongation at break ϵ_u (%)	ultimate stress σ_u (MPa)
PLA		4×10^{-2}	3123	brittle	n.m.	2.0	58.8
	20	4×10^{-3}	2839	brittle		1.7	47.3
		4×10^{-4}	2766	brittle		1.6	45.8
		4×10^{-2}	1748	42.2	0.9	298.2	28.6
	50	4×10^{-3}	1297	29.2		327.0	26.3
		4×10^{-4}	922	18.2		366.1	24.9
		4×10^{-2}	2.0	0.9	27.6	845.4	7.7
	80	4×10^{-3}	1.2	0.4		1114.1	1.6
		4×10^{-4}	n.m.	0.1		n.m.	n.m.
pPLA		4×10^{-2}	865	24.5	2.0	165.1	21.9
	20	4×10^{-3}	626	17.7		179.6	24.8
		4×10^{-4}	567	15.2		239.8	23.3
		4×10^{-2}	174	8.4	9.2	342.3	16.8
	50	4×10^{-3}	134	6.9		372.8	16.9
		4×10^{-4}	123	6.1		419.5	16.4
		4×10^{-2}	67.0	5.1	19.7	409.9	8.6
	80	4×10^{-3}	64.9	4.4		452.5	9.0
		4×10^{-4}	63.5	4.0		469.7	8.3

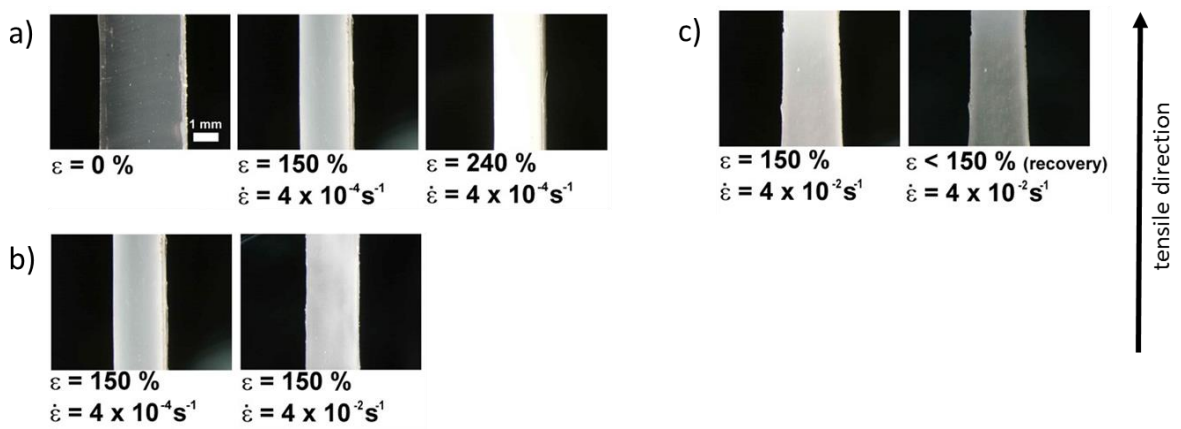

Figure 4.2 Optical microscope images of pPLA deformed in tension at 20°C showing (a) the effect of strain level at 4×10^{-4} s^{-1}, (b) the effect of strain rate at the strain level of 150%, and (c) the effect of relaxation after one week. The images were recorded at the center of the specimen.

To understand the macroscopic behavior of pPLA, its initial glass transition temperature T_g and crystallinity X_c were first determined. By DSC analysis, a T_g of 32.6°C for pPLA and of 59.8°C for PLA was found (Figure 4.3). Note that the T_g of poly(acrylPEG) was previously found to be around -60°C by DSC (Table 3.4) and hence, the inclusions were considered as having a rubbery behavior between 20°C and 80°C. Based on WAXS measurements, X_c was equal to 0% for PLA and 15.4% for pPLA. The tensile behavior of pPLA is therefore influenced by the glassy/rubbery state, the presence of the rigid crystalline phase and the presence of the rubbery poly(acrylPEG) inclusions. At 20°C, the tensile curve of pPLA is similar to that of rubber-toughened amorphous polymers as high-impact polystyrene (HIPS) drawn below their T_g [122,123]. In this case, the tensile curve is characterized by an initial viscoelastic stage where the stress drastically increases with the strain until the yield point. At the onset of the viscoplastic stage, the stress drops resulting in a strain softening stage, and then finally increases resulting in a strain hardening stage. Despite the glassy state of the molecular network, these materials exhibit ductility due to the vicinity of the testing temperature with their glass transition temperature and to the presence of the rubbery poly(acrylPEG) inclusions. In other words, pPLA has enough mobility to withstand the imposed strain, exhibiting plasticity. The presence of the crystalline phase in pPLA is expected to increase the Young's modulus, to increase the yield stress and to decrease the ductility compared to neat PLA [79]. In contrast, the presence of rubbery poly(acrylPEG) inclusions is expected to get the opposite effect. The yield in pPLA may be induced by the activation of shearing mechanisms in crystalline lamellae (crystal plasticity), as commonly considered for semicrystalline polymers [124]. To prove the effective role of crystalline lamellae on the mechanical behavior of PLA-bases materials, stress transfers have to be active between the amorphous phase and crystalline lamellae. This point was further investigated by WAXS. In parallel, the presence of rubbery poly(acrylPEG) inclusions in pPLA may also play a role in the activation of the material plasticity by yielding internal cavitation [125]. It is important to note that in the case of neat PLA stretched below its T_g, the onset of the viscoplastic stage can be associated with cavitation mechanisms within the polymer matrix [126]. The measurement of the yielding activation volume of the materials may provide information about the molecular mechanisms involved in the plastic flow (Table 4.1). At 50°C, the higher activation volume of pPLA compared to PLA may be explained by a lower chain mobility in PLA compared to pPLA as neat PLA is in its glassy state. It can be also explained in pPLA by the presence of crystalline lamellae and the inclusions that are expected to contribute to the plastic flow, increasing the number of molecular segments involved in the yielding process of pPLA compared to PLA. Increasing temperature generally increases the molecular mobility, which may be at the origin of the increased activation volume for PLA and pPLA. Note that this increase in mobility appears more marked for PLA than for pPLA resulting in a higher activation volume for PLA than for pPLA at 80°C.

The possible cavity formation during the viscoplastic stage in neat or rubber-toughened amorphous polymers may induce marked variation in the refractive index compared to the matrix, and consequently, visible light can be scattered off. If cavities have a micrometric size, as visible light wavelengths, they can induce a whitening phenomenon as they approximately scatter the same amount of light for all the visible spectrum wavelengths [127–129]. For pPLA and PLA, whitening was observed upon drawing (Figure 4.2). Whitening was nonreversible for PLA and reversible for pPLA, indicating different underlying mechanisms. The presence of cavitation in PLA and pPLA will be verified by SEM investigation.

For pPLA, the yield stress and the strain-softening intensity decreased with increasing temperature or decreasing strain rate (Figure 4.1 and Table 4.1). These results can be explained by enhanced molecular relaxation and orientation of the amorphous chains, and at the same time enhanced shearing mechanisms of the crystalline lamellae. As a result, the material may exhibit less resistance to the imposed strain. The influence of rubbery poly(acrylPEG) inclusions on the yield of pPLA is also expected to decrease with increasing temperature, yielding less cavitation. From 50°C, the tensile curve of pPLA is similar to that observed for semicrystalline polymers drawn above their glass transition temperature characterized by a rubbery amorphous phase [117,118]. At 80°C, the yield stress of pPLA was higher than that of PLA due to the presence of the crystalline phase in pPLA, which may significantly increase the tensile strength above T_g.

4.2.3 Crystallinity Investigation

DSC thermograms of undeformed PLA and pPLA exhibited a crystallinity index for pPLA of X_c = 25.4%, while PLA was totally amorphous (Figure 4.3). The glass transition and cold crystallization temperature decreased when comparing PLA (T_g = 59.8°C and T_{cc} = 128.5°C) with pPLA (T_g = 32.6°C and T_{cc} = 73.2°C), indicating that the plastification of PLA by the reactive extrusion effectively increased the molecular mobility for the matrix. The drawing process significantly modified the thermograms of both materials. In the case of pPLA, the melting temperature decreased when comparing the undeformed one with the deformed pPLA for all the experimental conditions, showing that deformation induced smaller crystalline lamellae. At 50°C and 4×10^{-2} s^{-1}, pPLA had an increased crystallinity at a strain state of 300% compared to the undeformed state reaching maximum X_c = 30.5%. At 20°C and 4×10^{-3} s^{-1}, pPLA had a decreased crystallinity with a strain of 100% compared to the undeformed state reaching minimum X_c = 14.1%. Therefore, strain significantly changes the crystallinity of pPLA, and hence, crystalline lamellae participate to the overall deformation mechanisms of the material. The deformation mechanisms of the crystalline phase are investigated in-depths in the following WAXS section. The

glass transition temperature increased from 32.6°C to a maximum of 45.6% (T = 50°C, ε = 300%, $\dot{\varepsilon}$ = 4×10^{-2} s-1) when comparing undeformed pPLA with deformed pPLA, and at the same time, the cold crystallization temperature decreased from 73.2°C to a minimum of 59.6°C (T = 50°C, ε = 300%, $\dot{\varepsilon}$ = 4×10-3 s^{-1}). It is generally admitted that the glass transition involves cooperative motions in one chain that is influenced by intramolecular and intermolecular interactions. A certain dynamic free volume is required enabling conformational change of the considered chain [130]. In the case of pPLA, the grafting of the plasticizer is expected to room out the chains and hence, may increase the free-volume and decrease T_g. The increase in T_g with the imposed tensile strain may be explained by a chain ordering process that globally reduces the free volume, and hence, hinders the glass transition process. It was however found that the free volume at the vicinity of the chain ends increased with the stretching, indicating more mobility in these regions for the glass transition [131]. The strain-induced ordering of the chains may facilitate the cold-crystallization of pPLA, which can explain the decrease in T_{cc} when comparing undeformed pPLA with deformed pPLA. No significant effect of the strain rate was noted on the thermal properties of pPLA when stretched at 20°C and 50°C. Concerning PLA, the imposed strain also caused an increase in T_g and a decrease in T_{cc} compared to the undeformed state, that can be explained by the same reasons. An original aspect of stretched PLA is the occurrence of an endothermic peak positioned at about 70°C that is attributed to the melting of the mesomorphic phase [74]. For the same strain level of 300% at 50°C, a fraction of mesophase that increased from 9.5% to 12.0% was found when increasing the strain rate from 4×10^{-4} s^{-1} to 4×10^{-2} s^{-1}. The formation of the mesophase in the case of neat PLA induced by the drawing at 50°C may be due to its low chain mobility that does not enable to create the more ordered α or α' crystalline phase.

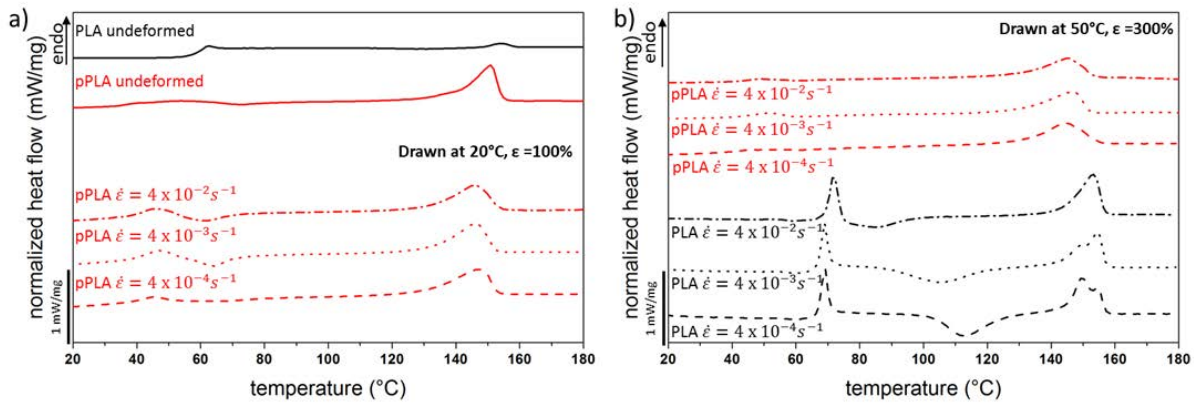

Figure 4.3 DSC curves of (a) undeformed PLA and undeformed pPLA, as well as pPLA deformed at 20°C to a strain level of 100% for various strain rates, and (b) pPLA and PLA deformed at 50°C to a strain level of 300°C for various strain rates.

A detailed study of the orientation of the chains in the crystalline and amorphous phases was conducted by WAXS analysis according to the information given in the introduction section 4.1 Introduction. Figure 4.4 a and Figure 4.4 b show the deconvolution obtained on PLA and pPLA, respectively, with the specific amorphous halos and the crystalline peaks.

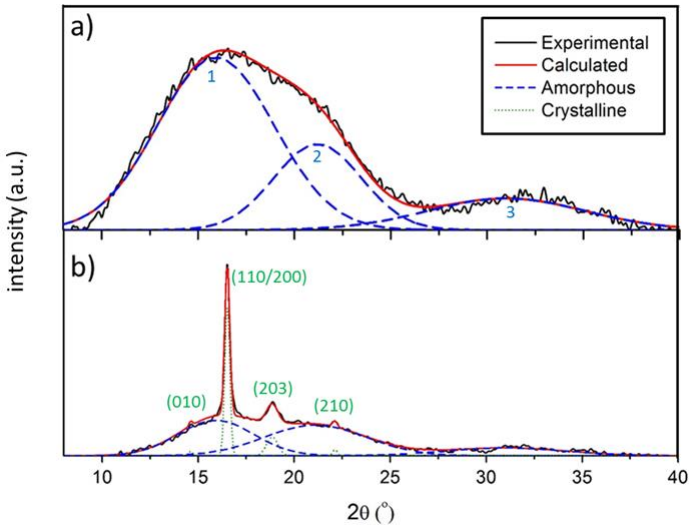

Figure 4.4 WAXS diagram deconvolution of a) PLA and b) pPLA at the undeformed state exhibiting in the two cases three amorphous halos at 2θ = 15.0°, 21.2°, and 31.0° and in the case of pPLA four crystalline peaks at 2 θ = 14.6°, 16.5°, 18.8°, and 22.2° engendered by the (010), (110/200), (203) and (210) reflections, respectively.

The evolution of the crystallinity and of the orientation functions with the strain level of pPLA and PLA subjected to the tension are represented in Figure 4.5 and Figure 4.6, respectively. The crystallinity found by DSC analyses was higher compared to WAXS results. This variation is due to the fact that these two techniques rely on different methods and in addition each of them has inherent uncertainties. It must be noted that by DSC analyses, drawing did not yield the formation of mesophase in the case of pPLA for all investigated temperatures and strain rates investigated. In the case of PLA, drawing-induced the formation of mesophase only at 50°C. At 20°C, pPLA had a decreased crystallinity with increasing strain level whatever the strain rate was. In particular, X_c evolved from 15.4% at the undeformed state to 6.6% at the strain level of 240% obtained at a strain rate of 4×10^{-4} s^{-1}. At 50°C, the crystallinity of pPLA was stable or slightly decreased with strain level and then increased with the high strain levels. At 80°C, the crystallinity of pPLA increased with the strain level. In particular, X_c reached at maximum 37% for a strain of 400% at a strain rate of 4×10^{-4} s^{-1}. These results demonstrate that during the drawing of pPLA a competition between crystal destruction and crystal formation is present. Crystal destruction may be due to the shearing and subsequent fragmentation of the initial crystalline lamellae [117], while crystal formation may be due to the

ordering of the amorphous chains. The deformation of the crystalline phase by shearing is shown in pPLA by the decrease of the orientation functions $f_{(110/200),z}$ and $f_{(203),z}$ with the strain for all the temperatures and strain rates. At the same time, the ordering of the amorphous chains is proved by the evolution of the orientation functions $f_{1,z}$, $f_{2,z}$ and $f_{3,z}$ from 0 to values above 0.5 for $f_{3,z}$, from 0 to values below -0.125 for $f_{2,z}$, and from 0 to values below -0.25 for $f_{1,z}$. With increasing temperature from 20°C to 80°C, it appears that the intensity of the orientation of the crystalline chains increased when considering the orientation function of the main crystalline peak (110/200) at a strain of 100%. For example, $f_{(110/200),z}$ decreased from 0.00 to -0.33 when increasing the temperature from 20°C to 80°C at 4×10^{-4} s^{-1}. This result shows that the crystal shearing is facilitated when increasing the temperature and that fragmentation may be hence restricted, resulting in no or limited crystalline destruction. At the same time, the intensity of the orientation of the amorphous chains increased as shown by the values of the orientation function of the main amorphous halo 1 positioned at 15.0°. For example, at a strain of 100%, $f_{1,z}$ evolved from -0.12 to -0.23 when increasing the temperature from 20°C to 80°C at 4×10^{-4} s^{-1}. Therefore, the crystal formation in pPLA is enhanced when increasing the tensile testing temperature. This WAXS investigation proves that in pPLA both amorphous and crystalline phases exhibit chain orientation during the drawing, demonstrating that deformation mechanisms involve these two phases and stress transfers are effective between them. Concerning PLA, the formation of the mesomorphic phase was observed at 50°C whichever the investigated strain rate, confirming the DSC results. The fraction of the mesomorphic phase reached 5.2% at a strain of 300% and at a strain rate of 4×10^{-4} s^{-1}. At 80°C, PLA exhibited the formation of the α or α' crystalline phase for all the strain rates. When increasing temperature, the ordering of the amorphous chains upon drawing increased in the case of PLA as an amorphous to mesophase transformation evolves to an amorphous to crystalline transformation. At 50°C and 80°C, PLA was characterized by an increase of the orientation of its amorphous and non-amorphous chains (crystalline or mesomorphic phases) with the strain. It must be noted that for pPLA and PLA, no significant effect of the strain rate was observed in the evolution of crystallinity/mesophase fraction and on the orientation functions with the strain level.

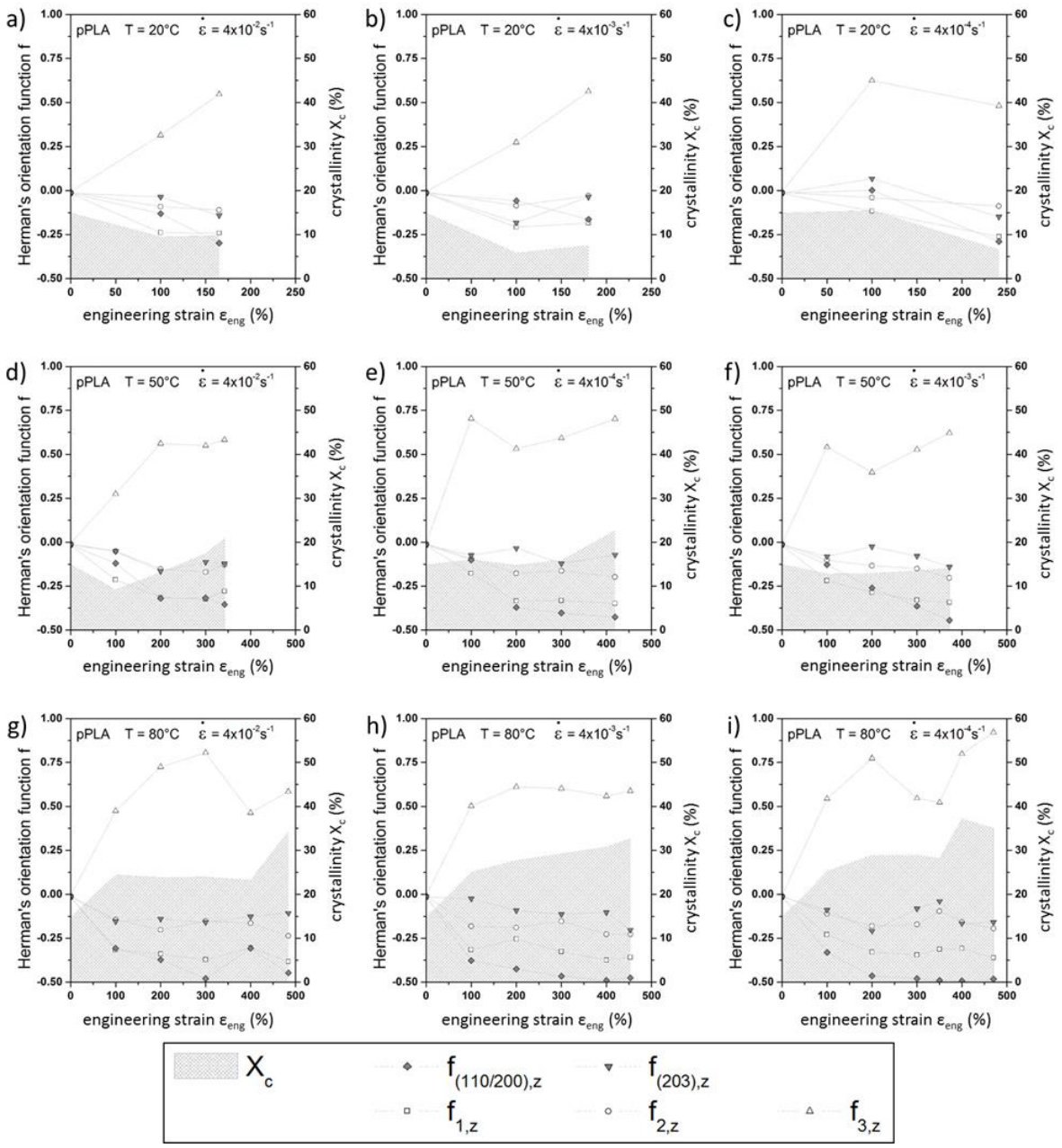

Figure 4.5 WAXS investigation of pPLA showing the evolution of the orientation function of the three amorphous halos (references 1 to 3), and of the two main crystalline peaks (reference (110/200) and (203)) on the LHS axis, and of the crystallinity on the RHS axis, as a function of strain. Tensile testing was conducted at different temperatures (20°C (A to C), 50°C (D to F), and 80°C (G to I)) and different strain rates (4×10^{-4} s^{-1} (A, D, and G), 4×10^{-3} s^{-1} (B, E, and H), and 4×10^{-2} s^{-1} (C, F, and I)).

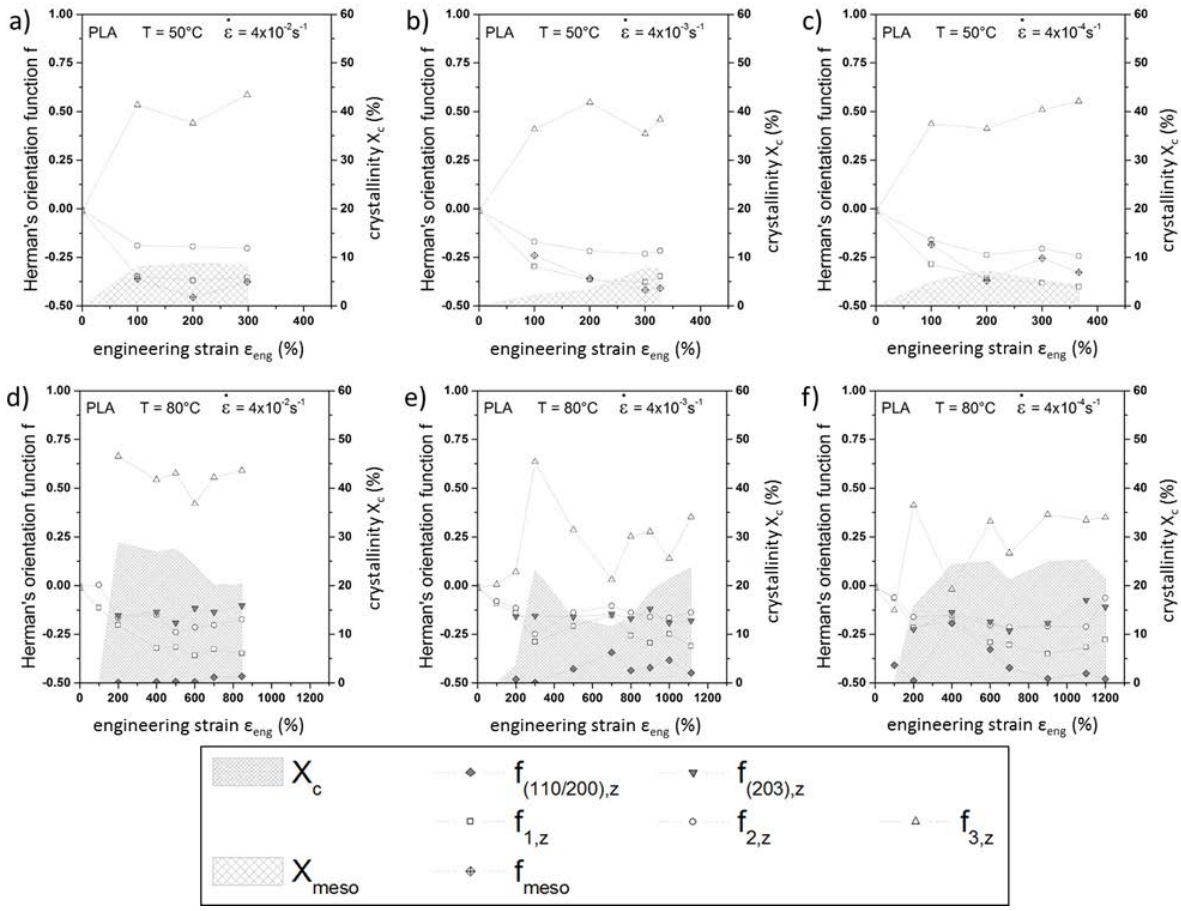

Figure 4.6 WAXS investigation of PLA showing the evolution of the orientation function of the three amorphous halos (references 1 to 3), of the mesophase peak (reference meso, just at 50°C) and of the two main crystalline peaks (reference (110/200) and (203), just at 80°C) on the LHS axis, and of the crystallinity on the RHS axis, as a function of strain. Tensile testing was conducted at different temperatures (50°C (A to C), and 80°C (D to F)) and different strain rates ((4×10^{-4} s^{-1} (A and D), 4×10^{-3} s^{-1} (B and E), and 4×10^{-2} s^{-1} (C and F)). At 50°C, the crystallinity based on the mesophase peak.

4.2.4 Morphological Investigation

The morphology of deformed PLA and pPLA observed by SEM is represented in Figure 4.7. PLA exhibited some micro-sized primary cavities having an ellipsoid shape with the major axis oriented in the tensile direction (Figure 4.7 a). Based on image analysis of SEM images with the software ImageJ, the average ellipsoid height and width were found to be 2.2 µm and 0.6 µm, respectively, corresponding to a shape factor of 3.7. In addition, an original damage aspect was noted that was the presence of secondary cavities oriented in the tensile direction that seemed to interact with the primary cavities. Indeed, some primary cavities clearly contained a secondary cavity passing through their center. In the work of Rezgui et al. [126], the presence of primary cavities in drawn semicrystalline PLA was also noted but no secondary cavity was observed. The micrometric cavities in PLA may induce variation in the refractive index compared to the matrix, and hence, visible light can be scattered, yielding the whitening. In contrast, pPLA did not exhibit any cavity at the scale of the

observations, but elongated poly(acrylPEG) inclusions forming ellipsoids with the major axis oriented in the tensile direction (Figure 4.7 b). Moreover, with the LFD mode that provided topographical contrast, inclusions appeared in dark gray, which can indicate the presence of voids that emitted little or no electron. The average ellipsoid height and width were 2.8 µm and 0.65 µm, respectively. Therefore, their shape factor was of about 4.3. At the undeformed state, poly(acrylPEG) inclusions had a spherical shape with an average diameter of about 0.7 µm.

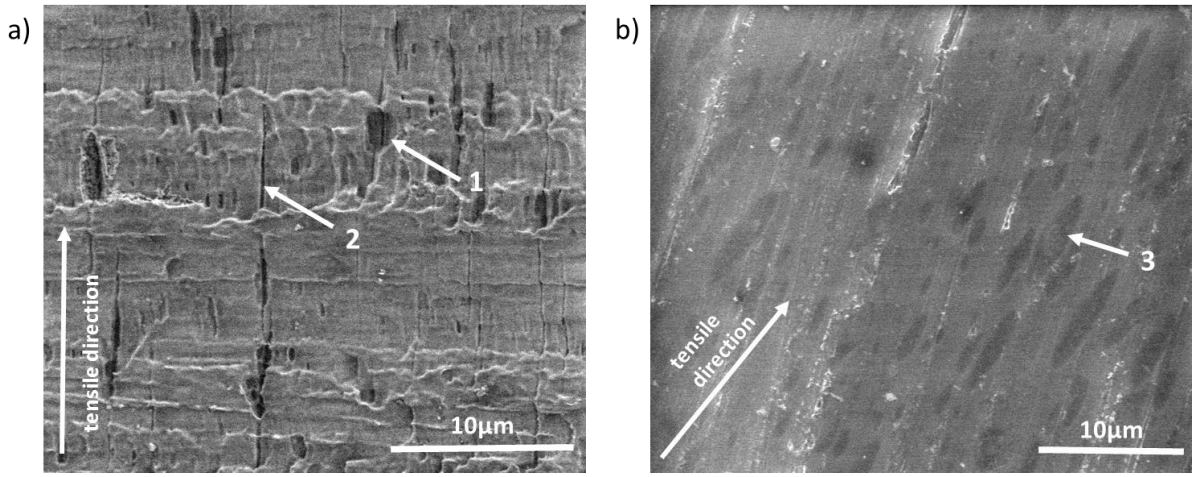

Figure 4.7 SEM observation with the LFD mode of deformed (a) PLA (strain of 298% obtained at 50°C with a strain rate of 4×10^{-2} s^{-1}) and (b) pPLA (strain of 165% obtained at 20°C with a strain rate of 4×10^{-2} s^{-1}). 1: primary cavities containing a secondary cavity, 2: secondary cavities, and 3: drawn poly(acrylPEG) micron inclusions.

To get complementary information about the deformation mechanism of poly(acrylPEG) inclusions in pPLA, some micrographs were recorded with the STEM configuration of the microscope (Figure 4.8). The contrast observed here is a phase contrast linked to the difference in electron scattering by the specimen areas. On STEM images, areas appearing in dark gray correspond to areas having a high density, and inversely. Based on Figure 4.8, the density of the poly(acrylPEG) may significantly decrease with the deformation as the gray level of the inclusions evolved from dark gray to light gray. This result indicates that the volume of these inclusions increased with the strain level by assuming that they have a constant mass, confirming their increased size on SEM images (Figure 4.7 b). Some of the bigger inclusions show a darker zone around the light core, which could indicate the presence of the previously observed core-shell structure of the inclusions (section 3.5 Plasticizer Inclusion's Chemical Structure and Mechanical Behavior). It is thought that the deformation of poly(acrylPEG) involved the formation of nanovoids that are not visible by SEM and STEM, explaining their increased volume. These voids may be generated by the separation of poly(acrylPEG) chains from each other in molecular regions characterized by a high free volume [132]. However, to scatter visible light, voids

must have a micrometric size as visible light wavelengths. It is hence thought that whitening is rather due to scattering by each micron inclusion containing the nanovoids [128,129]. After strain recovery, the whitening partially disappeared demonstrating that it is not permanent (Figure 4.2 c). In particular, the rubbery inclusions may shrink during the recovery stage resulting in a partial disappearance of the nanovoids.

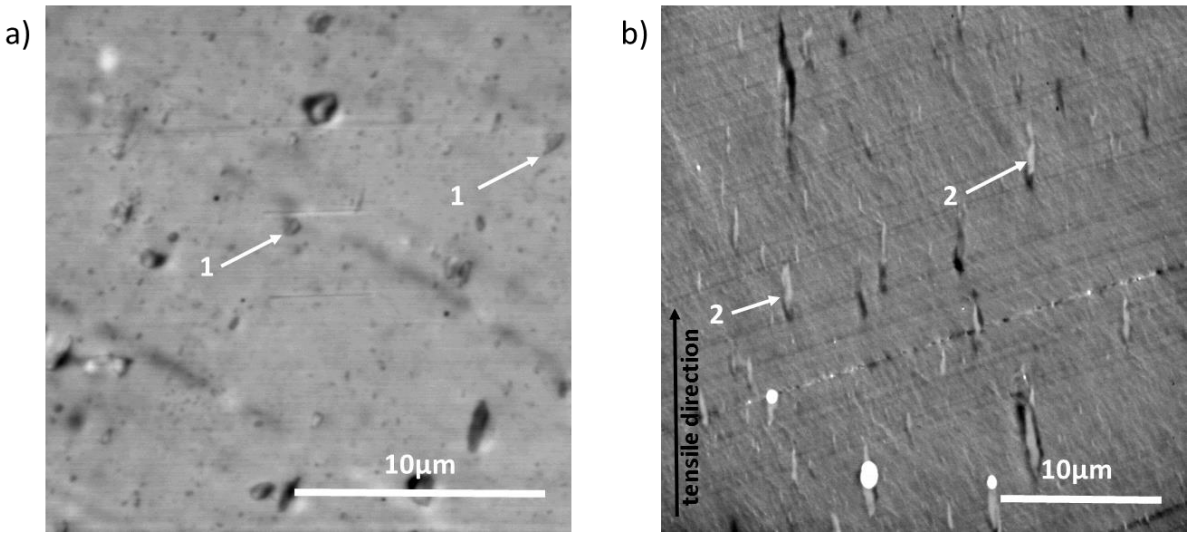

Figure 4.8 STEM observation of (a) undeformed pPLA and (b) deformed pPLA (strain of 165% obtained at 20°C with a strain rate of 4×10^{-2} s^{-1}). 1: initial poly(acrylPEG) inclusions with high density, 2: drawn poly(acrylPEG) micron inclusions with decreased density.

In this section, it was shown that the deformation mechanisms depend on the temperature and strain rate and are different for PLA and pPLA. At room temperature, PLA showed a brittle behavior and pPLA was ductile owing to the plasticization. In both cases, a competition between the crystal destruction due to shearing followed by fragmentation and crystal formation due to the ordering of the amorphous chains was observed. The intensity of both mechanisms depended on the temperature and drawing rate. In pPLA, a reversible whitening was observed, which was related to the scattering of the inclusions of poly(acrylPEG). After deformation, the inclusions obtained an ellipsoidal shape orientated along the tensile axis. Therefore, the further investigation of the cavitation, which are essential at room temperature, will be studied in the next section (4.3 Deformation Heterogeneities in PLA-Based Materials at Room Temperature). In addition, the deformation of the inclusions seems to play an important role in the ductile behavior and will be investigated further (4.4 Impact of Deformation on the Inclusion's Structure). Both following studies were conducted with film samples since they allow a better investigation of deformation heterogeneities compared to bulk samples [133].

4.3 Deformation Heterogeneities in PLA-Based Materials at Room Temperature

This subchapter is adapted from the publication: Multiscale investigation of deformation heterogeneities in polylactide-based materials upon cold-drawing: Influence of annealing and plasticizing by B. Brüster, C. Amozoqueño, A. Martin, S. Bernstroff, J.-M. Raquez, S. André, P. Dubois, and F. Addiego. Paper in preparation.

4.3.1 Processing

The experimental details of this section are explained in the Appendix (A.4.1 to A.4.4, and A.4.6 to A.4.8).

The film samples of the three materials PLA, pPLA, and PLA/acrylPEG were processed in a twin-screw mini-extruder with the respective weight compositions of 100/0/0, 79/20/1, and 80/20/0 of PLA/acrylPEG/L101. The section A.4.1 gives the details about the processing. The dumbbell tensile specimens were carefully cut from the extruded films with the drawing axis parallel to the extrusion direction. The initial gauge length was about 37 mm and the width of the gauge section was 5 mm. The exact values were measured for each sample. To obtain a PLA with a higher initial crystallinity, some PLA specimens were isothermally crystallized in a vacuum oven at 105°C and cooled down slowly to room temperature. These samples were called PLA-IC (PLA isothermal crystallization). All tensile testing experiments were conducted at room temperature and at a low strain rate (2.7×10^{-4} s^{-1}), which allows studying the formation and deformation of heterogeneities in-situ with a multiscale analysis.

4.3.2 Characterization of the As-Processed Materials

Prior to the analysis of the deformation heterogeneities, the materials were characterized by DSC to highlight the main characteristics of the four materials: PLA, PLA-IC, pPLA, and PLA/acrylPEG. The samples' properties are summarized in Table 4.2. PLA refers to the unmodified reference samples of PLA films. To obtain the samples with higher initial crystallinity PLA-IC, the films of PLA were isothermally crystallized. The initial crystallinity increased from 4.6% for PLA to 28.1% for PLA-IC, while the glass transition temperature (T_g) was just slightly increased from 62.5°C to 63.9°C. The plasticization of PLA was conducted by both methodologies described in the materials section. The reactive extrusion with acrylPEG and L101 as a reactive plasticizer and a free radical initiator, respectively, leads to the formation of partially grafted inclusions of polymerized acrylPEG (poly(acrylPEG)) onto the PLA matrix. In addition, the PLA matrix was slightly crosslinked through recombination of radicals or grafting of poly(acrylPEG) onto two PLA reactive sites. The samples from this reactive extrusion process were called pPLA. As a comparison to the reactive extrusion, the blending of PLA with acrylPEG was conducted. These samples refer to PLA/acrylPEG. In this case, neither grafting nor crosslinking was observed. Both plasticization methods increased the crystallinity

in comparison with PLA to 13.5% and 14.5% for pPLA and PLA/acrylPEG, respectively. As described in previous works [41], the plasticization decreased the glass transition temperature for pPLA to 36.4°C, while both PLA samples had a T_g over 60°C. For PLA/acrylPEG, just a frail glass transition was visible at 11.4°C.

Table 4.2 Initial properties of the as-processed materials: the processing treatment, crystallinity (X_c) and glass transition temperature (T_g) determined from DSC measurement, and qualitative information about crosslinking an grafting.

	processing treatment	X_c (%)	T_g (°C)	grafting & crosslinking
PLA	none	4.6 ± 1.2	62.5 ± 0.2	no
PLA-IC	isothermal crystallization	28.1 ± 0.9	63.9 ± 0.4	no
pPLA	chemical plasticization	13.5 ± 0.5	36.4 ± 0.6	yes
PLA/acrylPEG	physical plasticization	14.5 ± 1.3	11.4 ± 1.6	no

4.3.3 Multiscale Analysis of the Deformation Heterogeneities in Polylactide

The impact of the deformation conditions (drawing temperature and strain rate) and of the initial properties of the PLA (initial crystallinity and D-lactide content) on PLA's deformation mechanisms was widely studied [72,75,76,79]. PLA is known as a brittle polymer and shows brittle failure at room temperature due to its glass transition temperature above room temperature. Despite this brittleness, a ductile-like behavior at room temperature was observed for PLLA (PLA without D-lactide content) at low strain rates and with a low initial crystallinity. In the present study, film samples of amorphous PLA with a D-lactide content of 4.2 mol% exhibited a ductile failure for the drawing at room temperature with a strain rate of 2.7×10^{-4} s^{-1} as visible from the tensile curve in Figure 4.9 a.

Indeed, PLA reached a yield point corresponding to a stress level of 34.2 MPa and the failure occurred at a stress value of 31.8 MPa. Despite the failure at an ultimate strain of 4.3% after the yield point (ε_{eng} = 1.7%) in the plastic region, PLA was still considered as a brittle material. Other authors reported a failure before the yielding point at room temperature, but at a higher initial stretching speed (0.01 s^{-1} vs. 2.7×10^{-4} s^{-1}) [55]. As mentioned above, the tensile properties of PLA strongly depend on the drawing conditions and the initial properties of the specimen. Anyway, the reported engineering stress-strain curve matches those reported in the literature [79].

In PLA, crazing is one of the main mechanism for PLA deformation at room temperature [55]. The craze formation can be detected by small-angle X-ray scattering (SAXS), which was described as a powerful method to analyze the early cavitation mechanisms in PLA at a high resolution since new objects with high-density contrast are recognized in nanometer scale [75]. SAXS measurements allow the detection of different electron densities, and hence cavities and/or microvoids exhibit a more

intense scattering than the lamellar structure between the crystalline and amorphous phase [75]. The initial scattering was related to initial cavities or inhomogeneities in the material [75]. Therefore, the first intensity value was subtracted from the following ones to study the net impact of the drawing on the scattering. The scattering images, as presented in Figure 4.9 (b-g), showed the evolution of two scattering signals, one parallel (meridian zone) and one transversal (equatorial zone) to the vertical drawing axis.

The scattering image after 20 s (Figure 4.9 b) shows a slight scattering in the diagonal direction with an angle of about 45° to the drawing direction. In previous studies, these diagonal scatterings were observed as more intense streaks and were related to the scattering between the polymer matrix and the voids [55]. With increasing strain, a scattering developed first in the meridian direction and second in the equatorial zone. Both signals showed two streak-like SAXS pattern with the middle at the beam center. It has to be mentioned that the beam stop covered the signals partially and that the intensity signals were quite weak (Figure 4.9 b-g). The integrated scattering intensities (Figure 4.9 a) indicated that the meridian scattering intensity increased slightly before the yield point of PLA (up to 60 s) and increased stronger after the yield point (from 70 s). The equatorial signal increased just slightly at the end (after 120 s). Previous studies attributed the evolution of these meridian and equatorial scattering intensities to the formation of crazes. The structure of a craze was already described in 1979 by Krenz et al. [77]: Crazes contain fibrils, which are perpendicular to the growing direction of the craze and alternate with voids. During the tensile deformation crazes appear perpendicular to the drawing direction and in the case where the tensile direction is vertical, the meridian scattering is associated with the scattering of the craze walls and the equatorial scattering is associated with the scattering from craze fibrils [55,79,134]. The evolution of the scattering intensities (Figure 4.9 a) leads to the assumption that crazes were formed during the tensile deformation. The strong increase of the meridian scattering signal shows the formation of crazes, while the fibrils in the crazes offer just a weak scattering intensity. Despite one craze contains many fibrils, the scattering intensity of the crazes was stronger than that of the fibrils. This could be due to the fact, that the fibrils were formed less regularly or that the fibrils break down early. Regarding the fibril breakdown, it was observed that at a temperature below the glass transition of PLA (25°C) and a strain rate of 0.01 s^{-1}, the yield stress was lower than the critical stress for the fibril breakdown [55], which results in a fibril breakdown before the yield point and the formation of cracks. The brittle behavior of PLA is reasoned by the breakdown of the fibrils, which means that the fibrillated shear was unstable below the ductile-brittle transition [71]. In the present study, the drawing at room temperature was conducted at a low strain rate (2.7×10^{-4} s^{-1}) and the failure was observed after the yield in the plastic region (Figure 4.9 a). The scattering signals in the meridian and equatorial direction, as well as the ductile failure, support the

assumption of crazes' formation at room temperature and it seems that low strain rate prohibits the breakdown of the fibrils in the elastic region and leads to a ductile-like failure of the material.

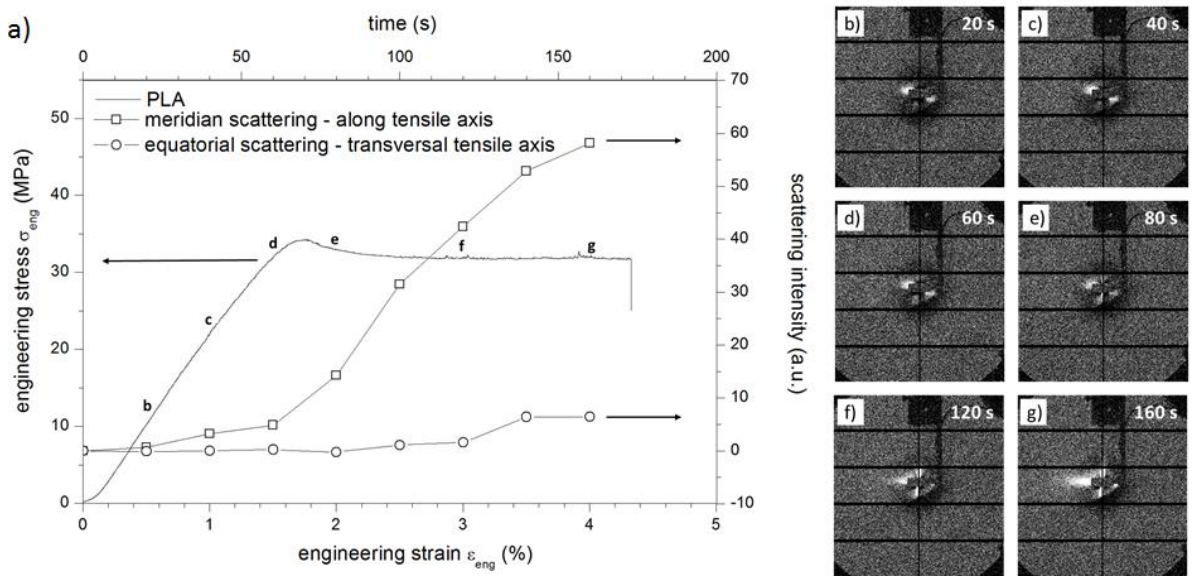

Figure 4.9 (a) Engineering stress-strain curve of PLA with the corresponding integrated scattering intensities for the meridian and equatorial scattering signal. The letters close to the curve correspond to the scattering images on the right (b-g). The tensile axis was vertical and the beam center was close to the image center.

While in previous studies the cracks were observed after the deformation by scanning electron microscope (SEM) or atomic force microscope (AFM) analysis [55,126], the present study used an optical microscope to evaluate the in-situ crack formation on the surface of the material. In Figure 4.10 a, the representative images for the crack formation in PLA (Figure 4.10 b-f) are related to the stage in the engineering stress-strain curve. In the elastic region of PLA, nearly up to the yield, no cracks were observed (Figure 4.10 b) and the crack formation started at about 45 s at a strain of 1.3% (Figure 4.10 c). The optical microscope analysis showed crazes with lengths between 20 µm and 400 µm (Figure 4.10 c) and the crazes grow in the perpendicular direction so that their final, exact size was not detectable due to the image limits. The detected crazes were inhomogeneous in size. With increasing strain, the micrometer-sized cracks grow in the transverse direction (Figure 4.10 c and d), and finally seem to bend themselves (Figure 4.10 e) with the occurrence of shear bands. The crazes opened just before the fracture of the material and gained an elliptical shape (Figure 4.10 f). The engineering stress-strain curves of PLA (Figure 4.10 a and Figure 4.9 a) exhibit clear differences although the overall behavior was similar. At the yield point, the first samples of PLA reached a stress value of 34.2 MPa with a slight stress release after the yield point. The second sample of PLA had no stress release after the yield and a higher flow stress of 38.6 MPa. The failure occurred for both

samples at about 4% (4.1% and 4.3%, respectively). These differences in the tensile behavior can be related to the brittle behavior of PLA induced by an inhomogeneous crack formation.

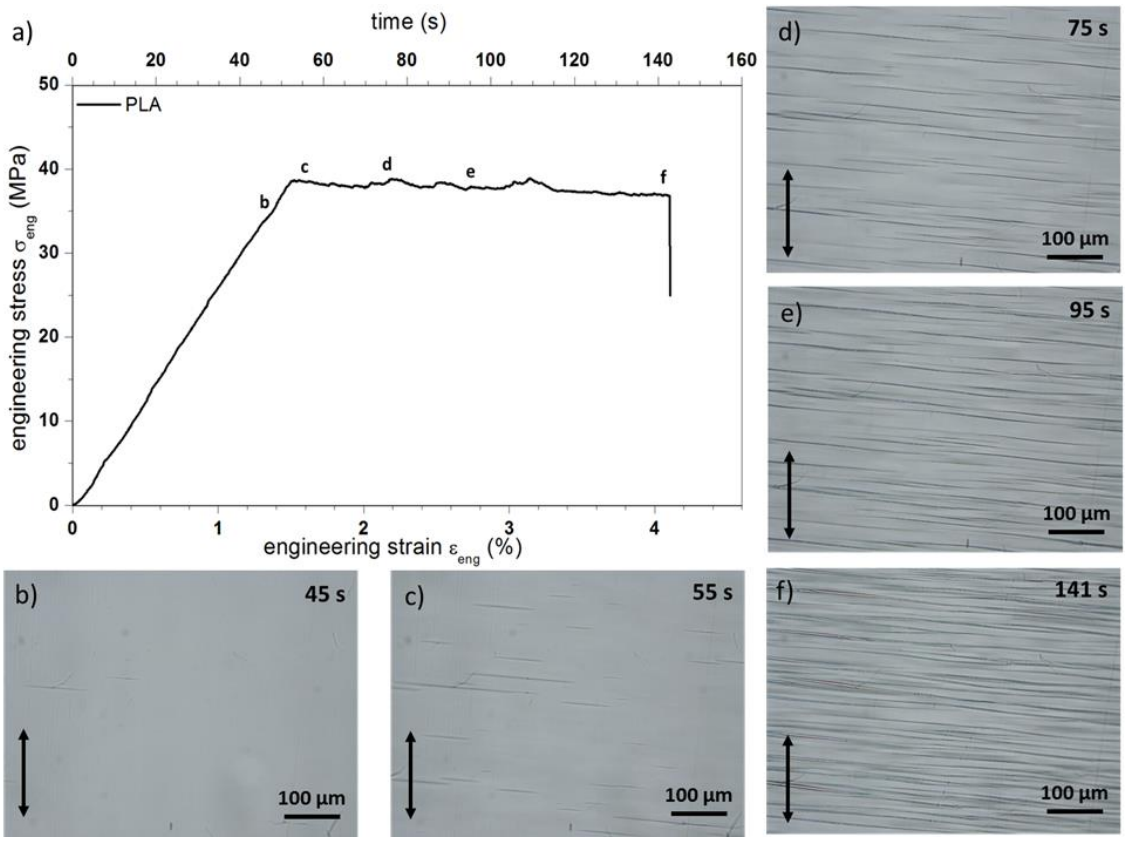

Figure 4.10 (a) The engineering stress-strain curve of PLA related to the optical microscope images at the defined time intervals. The tensile axis was vertical in the images.

By means of Digital Image Correlation (DIC), the true stress-strain behavior of PLA was determined and is represented in Figure 4.11 a. PLA has a Young's modulus of 2.9 GPa, which is in good accordance with the literature [135]. The yield point is reached at 0.02 and PLA breaks under the chosen experimental conditions in the ductile region at a true strain of 0.18. The true stress value of 36.0 MPa before the breaking was slightly lower than the yield stress (38.8 MPa). In comparison with the previous measurements of PLA (Figure 4.9 and Figure 4.10), the true strain at break is found 4 times higher than the engineering strain as a result of the local measurement of the strain produced by DIC.

The plots of the estimated volume strain (ε_v) and the transversal strain (ε_{22}) as a function of the axial strain (ε_{11}) are shown in Figure 4.11 b on the left- (LHA) and right-hand axis (RHA), respectively. The plots are separated into two regions: the elastic region up to the yield ($0 < \varepsilon_{11} < 0.02$) and the region beyond the yield ($\varepsilon_{11} > 0.02$). In the elastic region, the linear dependency of the transversal (ε_{22}) and axial (ε_{11}) strains gives a coefficient (absolute value of the slope obtained by linear regression) of 0.29.

Since the volume strain was calculated by addition of the axial and transversal strains (Equation (4.7)), the volume strain is also linearly dependent on the axial strain and the relation $\varepsilon_v = (1 - 2D^{-1}) \cdot \varepsilon_{11}$ (Equation (4.8)) with a slope of 0.42, produced the same coefficient (D^{-1} = 0.29). In the elastic region, this coefficient can be related to the Poisson coefficient. The classical Poisson coefficient given for plastic rigid materials is 0.33 - 0.35, while rubber-like materials obtain Poisson coefficients of 0.5 [120]. Hence, PLA behaved like a rigid material in the elastic region.

Beyond the elastic behavior, after the yield (ε_{11} > 0.02), the transversal strain remains constant at a very low value of about ε_{22} ≈ -0.005. As ε_{11} increases up to 0.18, the volume strain (Equation (4.7)) increases linearly with ε_{11} (slope about 1) and the intercept of the linear regression of ε_v vs. ε_{11} (value of -0.010) corresponds to $2\varepsilon_{22}$. The apparent volume strain is then governed by the behavior along the tensile direction and is directly linked to the opening of the cracks observed and reported in Figure 4.10 c-f. The stress-strain curve (Figure 4.11 a) shows a constant flow stress in this regime, which was associated with the steady formation of cracks.

The determined coefficient for PLA in the elastic region proves that the deformation process in PLA at room temperature is far from being an isovolumetric process. Rezgui et al. [126] determined at 50°C a Poisson coefficient in the elastic regime of ν = 0.42, which was much closer to a value of 0.5 corresponding to a rubber-like (isovolumetric) behavior expected from the amorphous phase. In addition to the independent measurements of the axial and transversal strain, the manual measurements of the cross-section showed the nonuniform deformation of PLA at room temperature. While the thickness of the samples nearly stayed stable, the width was reduced to 97% of the original size and, hence, the cross-section was also 97% of the original size. From these results, it can be concluded that PLA offers no uniform necking during the deformation at room temperature.

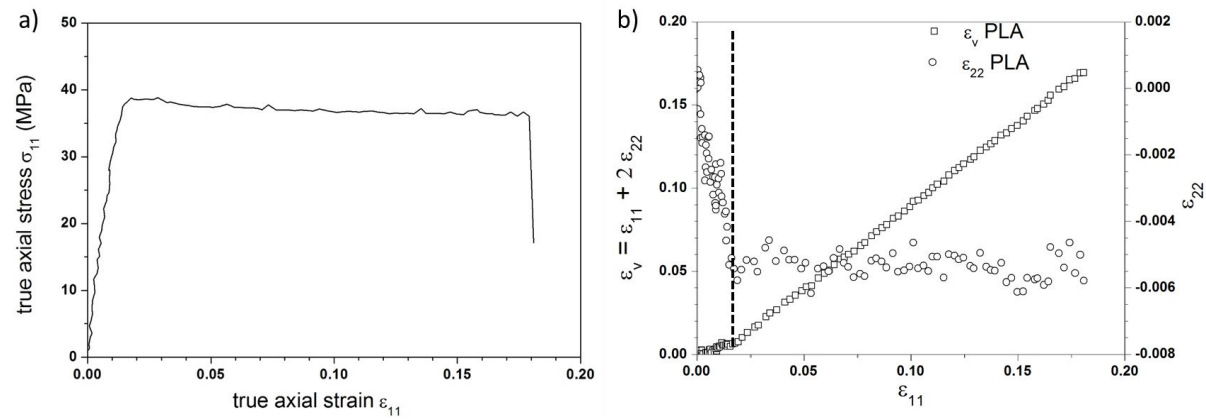

Figure 4.11 (a) True stress-strain tensile curve of PLA and (b) correlated plots of volume strain (LHA) and transversal strain (RHA) as a function of the axial strain. The dotted line separates the elastic regime (low strains) and the plastic regime (high strains).

4.3.4 Influence of the Initial Crystallinity on Polylactide's Deformation Heterogeneities

Despite the low ability of PLA to crystallize, the impact of initial crystallization on PLA's deformation mechanisms falls under a general interest to understand the behavior of semicrystalline polymers. The isothermal crystallization of the film samples for 2h at 100°C created turbid samples with a crystallinity of about 28.1%, called PLA-IC. As a comparison, Stoclet et al. [73] reported an optimal isothermal crystallization temperature of 105°C to obtain nearly 40% of crystallinity after 2 h and showed that at higher or lower temperatures than the optimal crystallization temperature, the obtained crystallinity was lower. The engineering stress-strain curve of PLA-IC, which was recorded during the SAXS measurements, is presented in Figure 4.12. The letters correspond to the recorded SAXS images (Figure 4.12 b-d), from which the meridian and equatorial intensity integrations (plotted in Figure 4.12 on the RHA) were obtained. The tensile behavior of PLA-IC is similar to PLA. The yield and the failure occurred as for PLA at about 1.8% and 4.7%, respectively. In contrast, the yield stress, as well as the stress at break were higher compared to PLA and reached levels of 60.6 MPa and 55.6 MPa, respectively. In the literature, it was reported that annealing PLA increases the tensile modulus and the maximum stress, while the elongation at break decreases [21,79]. The deformation mechanisms in semicrystalline PLA include the breaking of initial crystals and the formation of new crystals in competition [21,75], whereby it should be noted that drawing temperatures below the glass transition temperature avoided the formation of new crystals. Therefore, the initial crystallinity index has an influence on the deformation mechanisms.

As to be seen in Figure 4.12 b-f, the scattering intensities of PLA-IC differed from PLA and are less strong so nearly no scattering was observed by naked eye. The intensities of the meridian and equatorial scattering (Figure 4.12 a RHA) were close to zero up to the yield (at about 80 s) and at 100 s, the meridian scattering signal increased suddenly and kept this value to the end of the measurement (140 s), while the equatorial scattering signal just slightly increased after the yield. As explained before, the scattering intensities are generated by different electron densities. While in PLA the crazes induced the scattering, in PLA-IC the different electron densities between the amorphous and the crystalline phases are considered responsible for the scattering and its evolution, induced by the stretching along the vertical tensile direction [71,75]. Renouf-Glauser et al. [79] described a characteristic peanut and lemon shape for the scattering signal of annealed PLLA. First, a peanut-shaped scattering developed in the meridian direction and with a higher deformation also a scattering developed in the equatorial direction, which had a lemon-like shape. In this present work, the signal in equatorial direction appeared close to the yield and was maybe due to scattering of initially existing crystals. It was assumed that the lemon-like, equatorial signal in PLA-IC was less developed due to the lower crystallinity compared to the literature [79].

The cavities are in general formed between different crystalline lamella since the weakest links occur between the lamella and the amorphous phase [71]. The increase of the crystalline phases from 4.6% for PLA to 28.1% for PLA-IC raised the number of lamellae and therefore the number of weak points, where cavitation can occur. Since the scattering intensities in PLA were attributed to the formation of crazes with fibrillation, it was hypothesized that in PLA-IC due to the higher initial crystallinity rather cavitation by cracks occurred than crazes with fibrillation. Even though, no fibrillation is detected, the equatorial scattering intensity could indicate an increase of the craze density [55], but since no increase of the equatorial scattering intensity was observed (Figure 4.12 a) the formation of crazes was improbable.

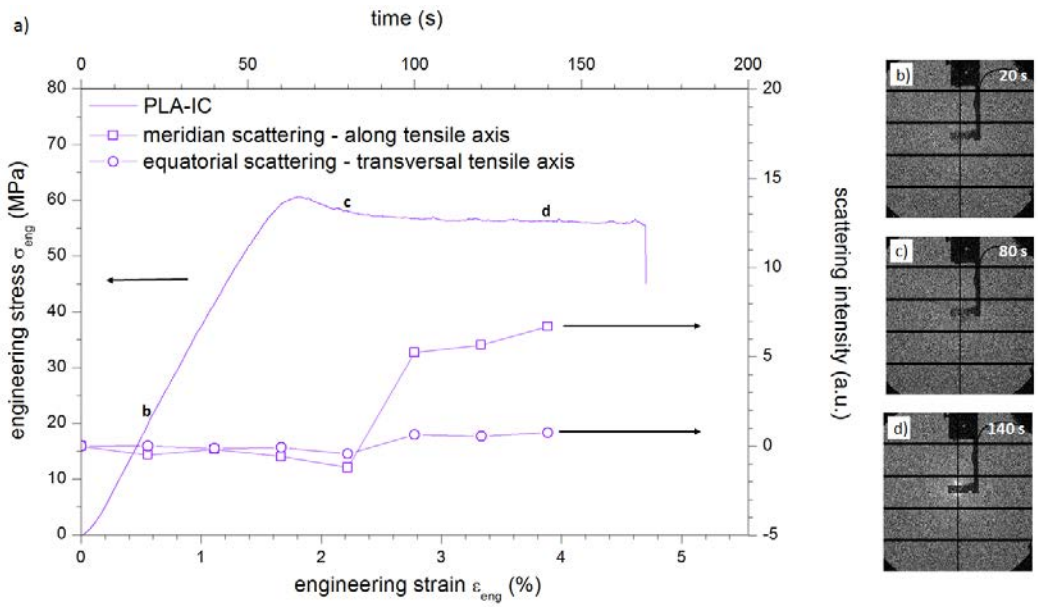

Figure 4.12 Stress-strain curve of PLA-IC with the corresponding integrated scattering intensities for the meridian and equatorial scattering signal. The letters close to the curve correspond to the scattering images at the defined time intervals. The tensile axis was vertical and the beam center was close to the center.

Compared to PLA, PLA-IC offered a different crack formation and their evolution was observed in-situ by the optical microscope. Some representative images of PLA-IC are shown Figure 4.13 b-e. While the cracks in PLA (Figure 4.10) were straight and appeared more individual, the cracks in PLA-IC offered a wave-like shape and appeared all at the same time in whole detection section. After 70 s (Figure 4.13 b) nearly no cracks were observed, but just 5 s later (Figure 4.13 c, just after the yield point) cracks appeared in the whole detected range. Different as for PLA, the cracks grew less in the equatorial direction. With increasing strain, more cracks were detected and the cracks just opened slightly in the meridian direction. The elevated crystallinity had two effects on the crack formation: On one side, more cracks were formed at once and on the other side, the growing of the cracks was

limited. Since the transition from lamellar to amorphous phase favors the crack formation [71], the increased number of crystals supported the simultaneous crack formation. The engineering stress-strain curves obtained for PLA and PLA/IC (Figure 4.13 a, LHA) are given along a quantitative estimation of the area of voids obtained from the treatment of the optical microscope images with the software ImageJ (Figure 4.13 a, RHA). Regarding the engineering stress-strain curves, as stated before, the increased initial crystallinity increases the tensile modulus as well as the yield and final stress. The comparison of all tested samples proved that the final strain for PLA-IC was in general lower than for PLA, but for both materials, the reproducibility was poor. This lack of reproducibility was related to the stochastic character of the damage process in both materials resulting in different failure points observed for various samples of the same material.

For both materials, the crack formation started after the yield point. For PLA, the first cracks were quantified after 53 s, although smaller cracks were already observed after 45 s (Figure 4.10 b), and the detected area of voids was less than 2%. For PLA-IC, the first quantification of the area of voids after 75 s led to a value of close to 7%. This result supports the assumption that in PLA-IC more cracks appeared at once, while the cracks in PLA appeared more in succession. With increasing strain, the area of voids increased for PLA and PLA-IC to 20% and 30%, respectively, and PLA-IC's area of voids increased with a higher rate. The increase of the voids' area for both PLA and PLA-IC was due to the formation of cracks that developed in the transverse direction (Figure 4.10 b-f and Figure 4.13 b-e), but for PLA-IC the cracks grew less individually, while the density of cracks increased (Figure 4.13 a). For semicrystalline polymers, it was shown that lamella created weak points from which crack can develop [71]. This may be also the case here, the higher crystallinity in PLA-IC explains the higher number of cracks due to the increased number of weak points that were induced by the lamella. At the same time, the lamella limited the growth of the cracks and the transversal direction of these cracks had a higher mechanical resistance, which led to the higher stress values compared to PLA.

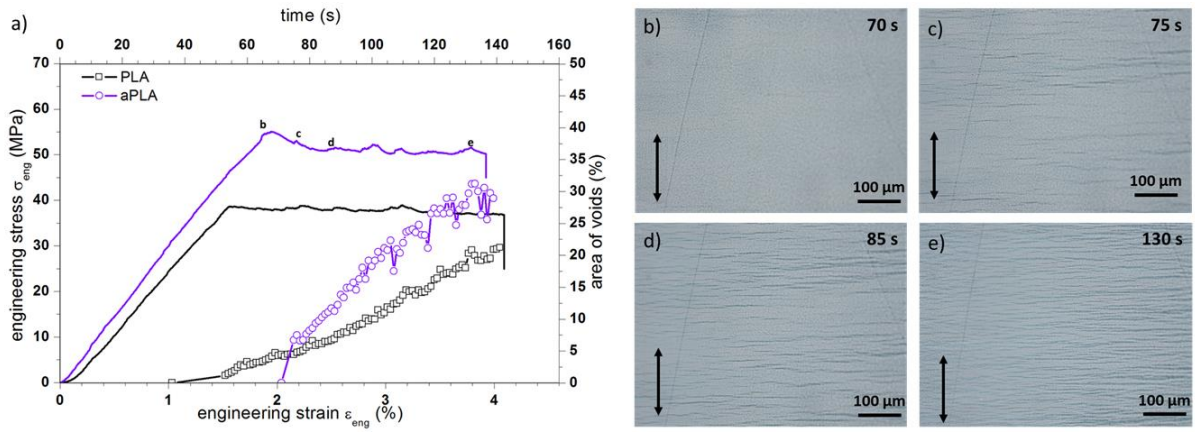

Figure 4.13 (a) Engineering stress-strain curve for a representative PLA-IC sample and PLA as a reference sample. The letters (b to e) mark the stage of the optical microscope images of PLA-IC. The right hand axis shows the area of voids compared for PLA-IC and PLA. The tensile axis was vertical.

Regarding the true stress-strain curve of PLA-IC (Figure 4.14 a), it exhibits slight differences compared to the PLA sample. The Young's modulus of PLA-IC was about 3.5 GPa, which was 21% higher than for PLA (2.9 GPa) and can be related to the higher initial crystallinity [79]. The yield point occurred for both samples at a strain about 0.02. While the engineering stress-strain measurements obtained similar elongation at break values for PLA and PLA-IC, the true strain at the break for PLA (ε_{11} = 0.18) was 2 times higher than for PLA-IC (ε_{11} = 0.08). These different elongation at break values can be reasoned by an increased strain localization, which was induced by the isothermal crystallization, as it was observed for annealed polystyrene [136]. It is not negligible, that at room temperature the irregular crack formation and deformation of PLA samples led to different defects in the samples and caused a variation of elongation at break values. Furthermore, semicrystalline polymers possess a heterogeneous distribution of the crystals and therefore, the crack formation and propagation is not homogeneous.

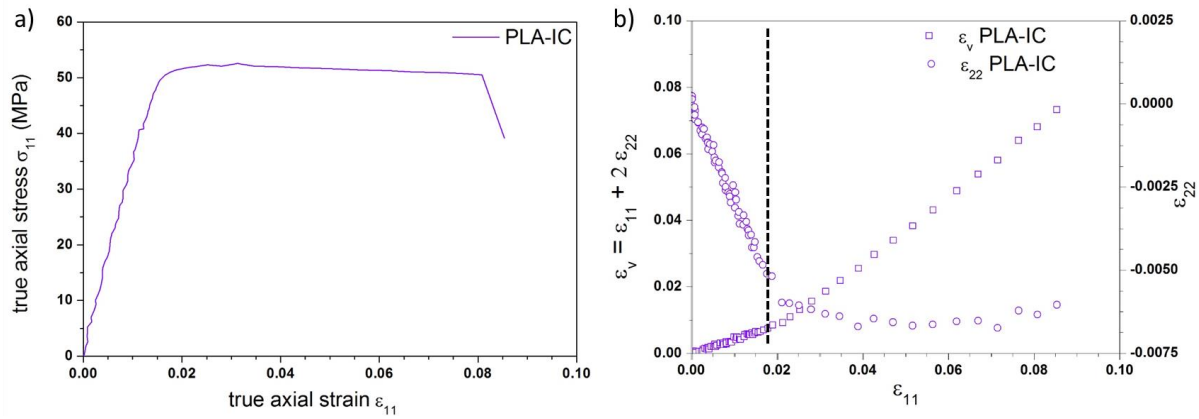

Figure 4.14 (a) true stress-strain tensile curve of PLA-IC and (b) correlated plots of volume strain and transversal strain vs the axial strain.

Regarding the behavior of the transversal strain ε_{22} or volume strain ε_v with respect to the axial strain ε_{11}, the exact same features are observed for PLA-IC as for PLA (Figure 4.11 b): The elastic regime (0 < ε_{11} < 0.018) shows a linear dependency of the transversal strain to the axial strain corresponding to the same coefficient of 0.29. In the plastic region (ε_{11} > 0.3), the transversal strain remained constant around -0.006 and the volume strain was governed by the axial strain. As for PLA, the damage was associated with the opening of the cracks and no relevant necking of the samples was observed. The initial cross-section remained at 96% of its initial size.

4.3.5 Influence of the Plasticization on Polylactides's Deformation Heterogeneities

To understand the impact of plasticization on PLA's deformation heterogeneities, the same type of characterization was carried out on the two plasticized materials: (i) pPLA plasticization performed by reactive extrusion with a slight crosslinking, as well as grafted and free inclusions of poly(acrylPEG) and (ii) PLA/acrylPEG plasticization performed by a simple blending of the PLA matrix with the same plasticizer, creating neither crosslinking nor grafting.

Both plasticized materials had a crystallinity of 13.5% (pPLA) and 14.5% (PLA/acrylPEG) just between PLA (4.6%) and PLA-IC (28.1%). They also had reduced glass transition temperatures: 62.5°C for PLA, 36.4°C for pPLA, and 11.4°C for PLA/acrylPEG. Reducing the glass transition temperature is one of the main effects of plasticization and results in a higher drawability at lower temperatures. Both samples did not reach the breaking point during the tensile deformation under the same conditions and achieved the limit of machine deformation with about 15% engineering strain.

The impact of both plasticization methods on the PLA cavitation is pointed by Figure 4.15. Neither pPLA nor PLA/acrylPEG showed an important scattering in the SAXS measurements and the integration of the intensity (Figure 4.15 g) supported this observation. For pPLA, both determined scattering intensities were close to zero and did not change during the time of deformation. Therefore, it was assumed, that no objects, which can induce a scattering, were formed during the tensile deformation of pPLA. This means that in pPLA neither crazes with fibrillation nor a further development of cracks appeared. For polystyrene, it was shown that crosslinking hinders the formation of fibrillation since fibrillation requires fast motion of molecular chains, which is reduced by the crosslinking [137]. Hence, the grafting of inclusions and the crosslinking could constrain the formation of crazes with fibrillation in pPLA. The equatorial scattering intensity of PLA/acrylPEG was over the whole measuring range close to zero, whereas the meridian signal increase between 20 s and 60 s suddenly. After the jump of intensity, the intensity stayed constant, but with high variations and

still in a very low-intensity range, up to the end of the measurement. It is probable that no scattering objects were formed and the slightly increased intensity could be just an experimental defect.

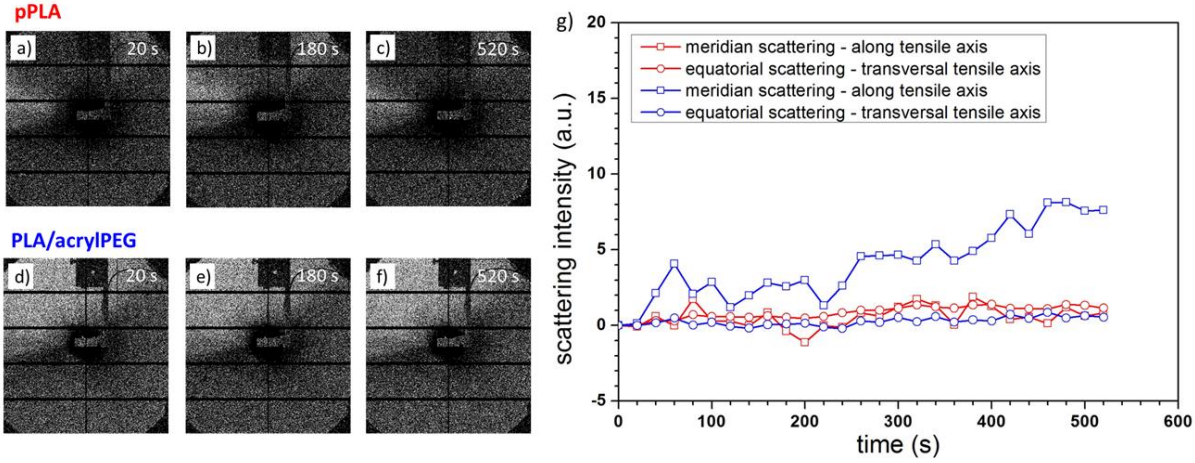

Figure 4.15 SAXS scattering images for pPLA (a-c) and PLA/acrylPEG (d to f) in the defined time intervals. The tensile axis was meridian and the beam center was close to the image center. The scattering intensities of pPLA (red) and PLA/acrylPEG (blue) for the meridian and equatorial scattering are displayed in graph (g).

The optical microscope observations for PLA/acrylPEG in Figure 4.16 show no deformation heterogeneities over the whole deformation range. These measurements support the assumption that the light increase of the scattering intensity was not induced by cavities. Even at the maximum deformation of 15% (Figure 4.16 c) PLA/acrylPEG showed no formation of cracks.

In pPLA, the observation of deformation heterogeneities by the optical microscope was complicated because of pPLA's roughness. While the other samples (PLA, PLA-IC and PLA/acrylPEG) had a smooth surface, pPLA was uneven and hence, just smaller parts of the surface images could be analyzed. The first visible defects were detected after 132 s (Figure 4.17 c). These defects were considered as submicron cracks and not crazes since no craze scattering signal was detected by SAXS. These cracks were observed for all following images, but a quantification of the area of voids, as for PLA and PLA-IC (Figure 4.13), was not possible due to the rough surface. In a different way as for both PLA samples, the cracks occurred in specific areas and were not distributed over the whole sample. The cracks opened slightly (Figure 4.17 d) but not in a uniform way, so that in the images at higher deformation again closed cracks were observed (Figure 4.17 e and f). The samples exhibited a high heterogeneity and regions with many cracks were observed in addition to crack free regions. As for PLA-IC, the cracks had a more wave-like shape, but the observed cracks were much smaller than in both PLA samples. The increased crystallinity, from 4.6% for PLA to 13.5% for pPLA, could induce weak points as already described for PLA-IC [71]. Furthermore, the heterogeneity of the material by the grafting and

crosslinking could as well create weak points where cavitation was initiated, but the crosslinked structure could also limit the growth of the cracks. In PLA/acrylPEG, the plasticization increased the mobility, so that it was possible to compensate the weak points, which were created by increased crystallinity. In pPLA, the grafting and the crosslinking reduced the chain mobility. The combination of crystal-induced weak points and reduced mobility by crosslinking and grafting provoked very local strains leading to the direct formation of small cracks. In addition, the crosslinking also prevented fibrillation [137].

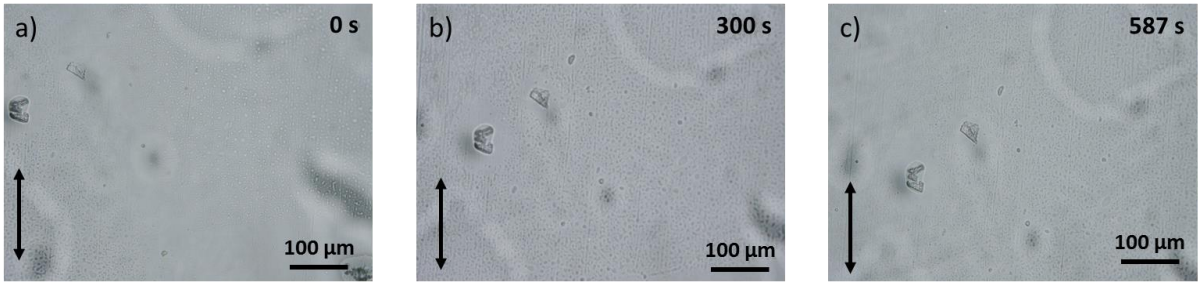

Figure 4.16 Optical microscope images during tensile deformation of PLA/acrylPEG. Images after defined time intervals. The tensile axis was vertical.

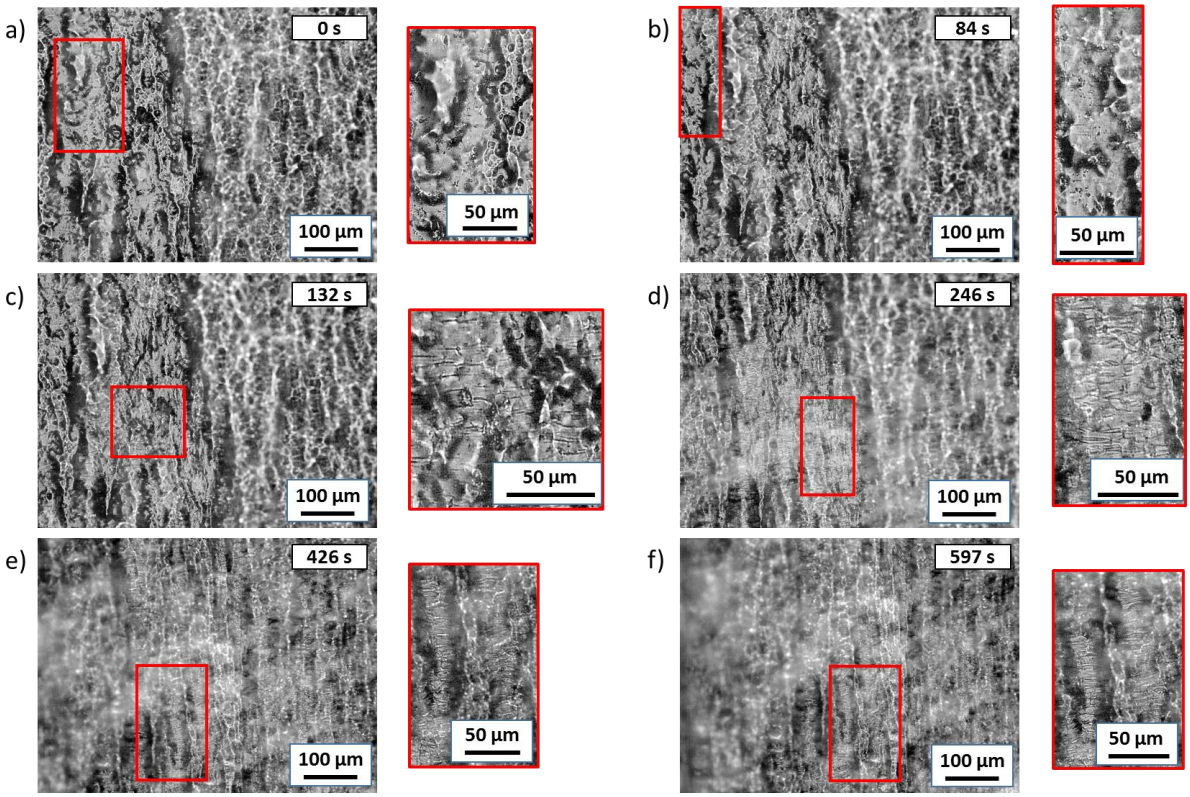

Figure 4.17 Optical microscope images during tensile deformation of pPLA. Images after defined time intervals. The tensile axis was vertical.

As already described, the tensile deformation of both plasticized PLA samples pPLA and PLA/acrylPEG reached the limits of the testing equipment (maximum engineering strain of 15%) and therefore their elongations were much higher compared to the two PLA samples (ε_{eng} < 5%). In Figure 4.18 a, the true stress-strain curves of the plasticized samples are compared and it is obvious that both plasticization methods lead to different tensile behaviors. While the PLA samples, PLA and PLA-IC, had Young's moduli of 2.9 GPa and 3.5 GPa, respectively, pPLA and PLA/acrylPEG obtained lower values of 1.1 GPa and 0.4 GPa, respectively. These lower Young's moduli indicate a decrease in stiffness for both plasticized samples compared to the PLA samples, but the reactive extrusion with a free radical initiator supports the toughness-ductility balance and allows keeping a moderate tensile modulus [52].

It is well known, that blending of PLA with acrylPEG leads to a rubber-like material with low stress values and a low initial tensile modulus [41,51]. The decrease in stiffness was also reflected by the lower stress values that were obtained by the plasticized samples. The sample with grafting and crosslinking, pPLA, showed a clear yield point with a stress level of 21.9 MPa and a stress release to 19.0 MPa, followed by a strain hardening region up to 29.8 MPa. The pPLA material behaved like PLA at temperatures close to their glass transition temperature [75,126]. In contrast, PLA/acrylPEG offered lower stress levels for the whole testing range with a stress at yield level of 7.3 MPa, no stress release and a final stress of 10.6 MPa.

Notwithstanding that crosslinking was proved to favor a brittle behavior [71], the pPLA sample was ductile and reached a true strain of 0.7. Since the plasticization reduced the glass transition temperature to 36.4°C, the drawing temperature for the plasticized materials was nearer to the glass transition temperature than for the PLA materials. The decrease of the glass transition temperature by plasticization has a similar effect just as the increase of the drawing temperature - the drawing is performed at a temperature close to the glass transition temperature - the plasticized samples behave like PLA materials at elevated temperatures [75,126]. The comparison with PLA/acrylPEG clarifies the roles of the different structural elements in pPLA. With the non-grafted plasticizer, the glass transition temperature was stronger decreased and a rubber-like material with low stiffness was obtained. It was shown, that increased chain mobility (by elevated temperature) increases the crystal unit cell size and reduces the van der Waals bond strength [71]. This results in an easier crystal shear and hence, deformation without voiding can occur. The van der Waals bond strength is related to the Young's modulus and presents the stiffness of the material [126]. The increased chain mobility by plasticization in both materials seems to reduce the van der Walls bond strength and therefore the stiffness. Although plasticization creates a tensile behavior at room temperature similar to PLA at elevated temperatures, the blending seems to prevent the formation of cracks, which were still observed in

PLA even at elevated temperatures parallel to the drawing direction [75,126]. In contrast, pPLA showed small cracks in the material during deformation. While the plasticization decreased the van der Waals bond strength and allowed a cavitation-free deformation, the grafting and crosslinking in pPLA had a contrary effect, but the ductile deformation behavior was kept. Due to the grafting of the plasticizer and the crosslinking, the plasticizing effect and therefore the crack formation was more localized.

The plots of the volume and transversal strains against the axial strain (Figure 4.18 b) illustrate a different behavior as observed for the PLA samples. While both PLA samples offered two different slopes before and after the yield, the plasticized samples show a more continuous slope. For pPLA, the initial and the final slope of the volume strain just differed slightly and led to coefficients of D^{-1} = 0.37 and D^{-1} = 0.39 for the elastic region and the plastic region, respectively. PLA/acrylPEG was classified as a nearly completely rubbery material, with apparent coefficients of D^{-1} = 0.44 and D^{-1} = 0.45 for the initial and the final volume strain, and a constant slope of the transversal strain over the whole measurement range. The classification by the coefficient confirmed the previously determined mechanical properties. While pPLA offers still a sufficient stiffness with a Young's modulus of 1.1 GPa, PLA/acrylPEG showed a more rubber-like deformation behavior as already described in previous works [41,52].

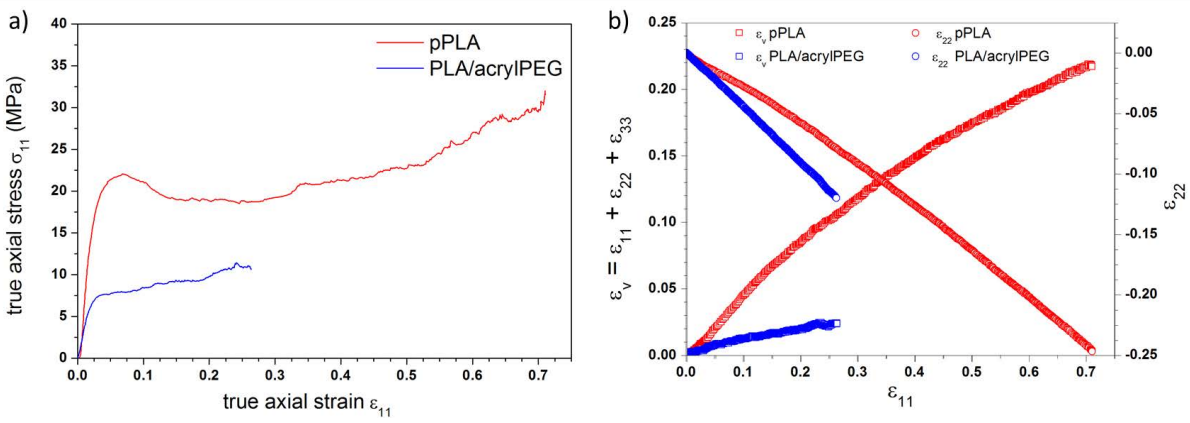

Figure 4.18 (a) true stress-strain tensile curve of pPLA and PLA/acrylPEG, and (b) correlated plots of volume strain and transversal strain vs the axial strain.

Interestingly, the final true strain values for pPLA and PLA/acrylPEG were quite different from those of engineering strain. For the engineering strain, both materials reached the limit of the testing equipment (same displacement of the grips corresponding to with ε_{eng} ≈ 15%) without breaking. The final true strain for PLA/acrylPEG of 0.26 was much lower than for pPLA (ε_{11} = 0.70) for tensile tests

performed with the same displacement of the grips. This means that the localization of strain differs for the two materials.

The true strain fields measured for both samples at the same true strain value $\varepsilon \approx 0.2$ are represented in Figure 4.19 a and b. Since the value of the true strain $\varepsilon \approx 0.2$ was determined between two points in the middle of the specimen, the overall true strain values determined by DIC can vary from this value. For pPLA, the strain was clearly localized in the middle section of the specimen, while the parts outside the cross-section were not impacted by the applied stress. In PLA/acrylPEG, the strain is less localized according to the comparison made in Figure 4.19 c of the longitudinal strain profiles taken along the central axis for both specimens and was less localized in the cross-section. This phenomenon of strain localization explains the different final true strain values. The axial true tensile strain was measured in the center of the specimen and due to the higher strain localization in pPLA, this sample reached higher true strain values. The grafting and crosslinking points in pPLA have been seen to increase significantly the yield stress, which favors the strain localization in the middle of the specimen driven by the initial specimen geometry. In contrast, PLA/acrylPEG offered a higher chain mobility induced by the plasticization, which could favor a more distributed strain appearance.

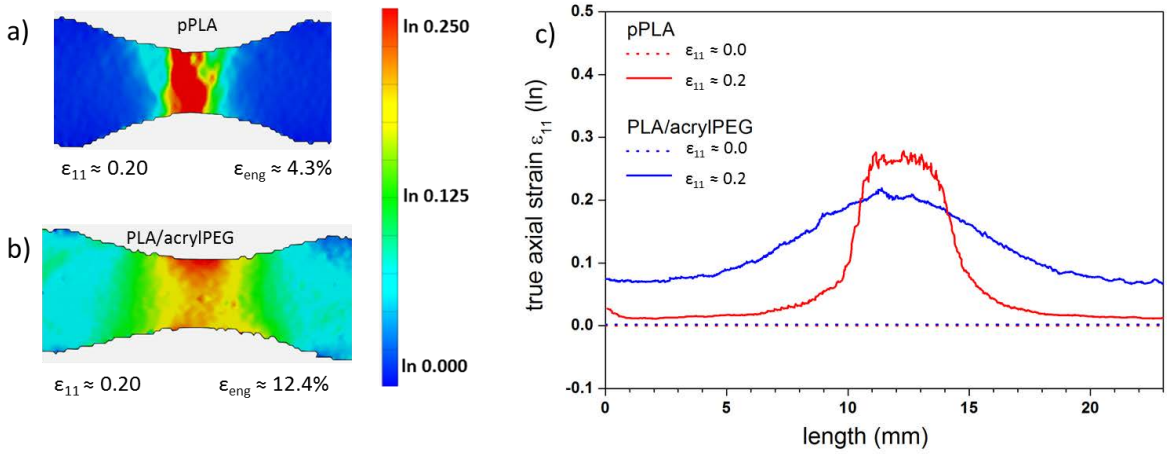

Figure 4.19 DIC true strain fields for the plasticized materials: (a) pPLA and (b) PLA/acrylPEG at the same true strain value of 0.2 and comparison of the true strain profiles along with the drawing axis at true strain values of 0 and 0.2.

4.3.6 Deformation Heterogeneities Related to the Initial Structure

It is obvious that the initial structure of the materials has a high impact on the deformation heterogeneities. The optical images in Figure 4.20 underline the difference of the four materials. The cavitation in PLA is similar to the ones described in the literature [55,71,75,79]. The applied strain induces the formation of crazes with fibrils and at a sufficient stress the fibrils break down and cracks are formed. The formation of cracks takes normally place between the crystalline lamella in the

amorphous phase [71]. In Figure 4.20 a, the cracks perpendicular to the drawing direction are observed and caused a visible whitening of the breaking zone in PLA.

For PLA-IC, the initial structure offers a higher crystallinity compared to PLA and the sample appears less transparent compared to PLA (Figure 4.20 b). The cracks had a similar appearance as for PLA and appeared in the breaking zone perpendicular to the drawing direction. It has to be mentioned, that the cracks appeared more on one side of the sample and the crack distribution was inhomogeneous. The higher initial crystallinity led to more lamellae and transitions between crystalline and amorphous were present. Since the cavitation appeared in the amorphous phase, but close to the lamella structures, an increase of the lamella structures also increases the sites for cavitation formation [71]. In SAXS no scattering of craze-like structures with fibrils was observed. The lack of crazes is assumed to correlate with the reduced amount of amorphous phase that normally forms the fibrils due to its higher mobility compared to the crystalline structures. Furthermore, a direct fibril breakdown is possible and leads to the crack formation at many places at the same time, which was observed in the optical microscope analysis. Since less growing of the cracks was observed in PLA-IC than in PLA, it is assumed that the crystals limit the expanding of cracks, which also correlates to higher stress values in the plastic region.

The plasticized PLA samples with a crystallinity index between those of PLA and PLA-IC offer higher deformation strains, which were related to a decreased glass transition temperature. Despite the higher crystallinity, PLA/acrylPEG appears completely transparent and even after deformation the optical appearance remained the same (Figure 4.20 d). In contrast, pPLA is slightly turbid before the deformation and the cavitation induces whitening of the sample (Figure 4.20 c). The white lines with an angle of about 45° to the drawing direction appear like shear bands, but the onset of shear bands could not be proved by the SAXS or optical microscope experiments.

In addition to the crystallinity, the different structural elements in pPLA have a big influence on the cavitation behavior. While the free part of plasticizer, as seen in PLA/acrylPEG, promotes a crack free deformation, the grafting and crosslinking limited the chain mobility. In SAXS, no crazes were observed as a result of the crosslinking that decreased the chain mobility, but small cracks appeared perpendicular to the drawing direction as observed by the optical microscope. These results lead to the assumption, that pPLA offers an increased chain mobility compared to the PLA-systems, but the crosslinking and grafting limit the chain motion compared to PLA/acrylPEG. Therefore, no fibrillation for crazes formation occurs and also the crack growing is limited.

The PLA/acrylPEG shows no formation of cracks in the optical microscope images. The plasticizer molecules were dispersed in the PLA matrix and allowed the material to dissipate the applied stress,

which was also supported by the strain dissipation over the whole sample (Figure 4.19). Hence, the increased chain motion prevented a formation of cracks. Compared to pPLA, which contained grafting and crosslinking, the material's higher chain mobility allows a fast reaction to the formation of cavitation and avoids the formation of crazes.

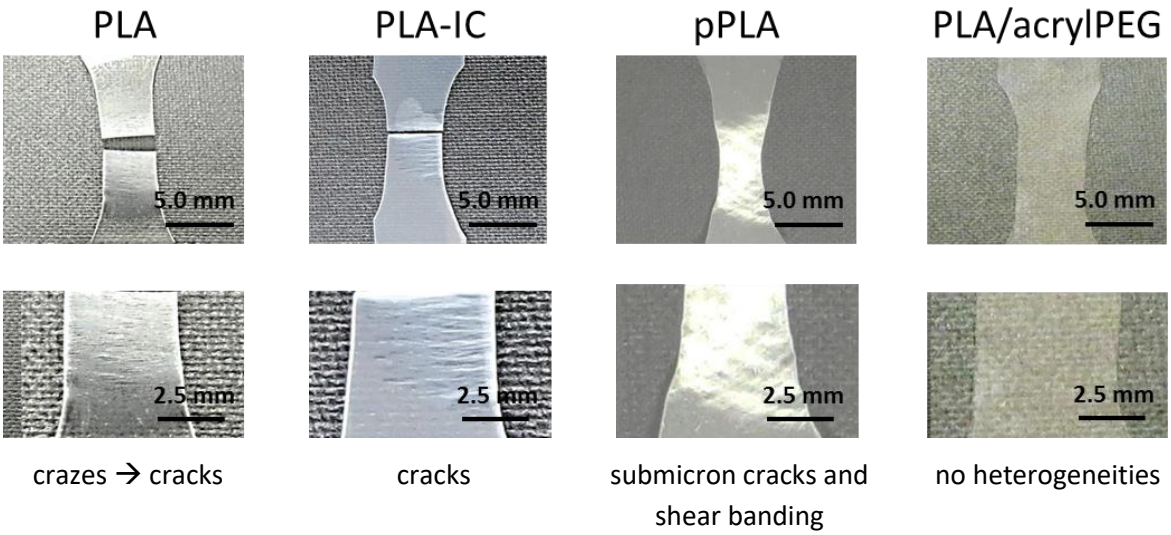

Figure 4.20 Tensile specimen of PLA-based materials with a corresponding zoomed view of the deformation section showing the deformation heterogeneities.

4.4 Impact of Deformation on the Inclusion's Structure

This subchapter is partially adapted from the publication: Resolving inclusion structure and deformation mechanisms in polylactide plasticized by reactive extrusion by B. Brüster, C. Amozoqueño, P. Grysan, I. Peral, B. Watts, J.-M. Raquez, P. Dubois, and F. Addiego. Submitted to Macromolecular Materials and Engineering in July 2017.

4.4.1 Processing

The experimental details of this section are explained in the Appendix (A.4.1 to A.4.4, and A.3.10 to A.4.9).

For this study, the same film samples of PLA, pPLA and PLA/acrylPEG were used as used in 4.3 Deformation Heterogeneities in PLA-Based Materials at Room Temperature.

4.4.2 Inclusion's Chemical Structure after Deformation

As already described in 3.5 Plasticizer Inclusion's Chemical Structure and Mechanical Behavior, the inclusions consisted of polymerized plasticizer (poly(acrylPEG)) and offered a core-shell structure. The 2D composition maps obtained from STXM micrographs of deformed pPLA recorded at 288.5 eV (PLA-rich domains) and 289.7 eV (poly(acrylPEG)-rich domains) were represented in Figure 4.21. Damage characterized by submicron defects oriented perpendicular to tensile direction was observed in the vicinity of plasticizer inclusions (Figure 4.21 a). Such defects have not been detected in pPLA with other techniques (4.2 Deformation Mechanisms of Plasticized Polylactide). From the 2D composition map in Figure 4.21 a, it was not clear whether damage was generated in the matrix or from the inclusions. In another area (Figure 4.21 c), it can be seen that damage was originated from one inclusion and propagated to a neighboring inclusion. Knowing this mechanism and coming back to Figure 4.21 a, it was clearer that the defects started from one inclusion and propagated to another inclusion, but on the overall, damage remained localized. In the case of poly(acrylPEG)-rich domain image (Figure 4.21 b), the core-shell structure of the inclusions was preserved after drawing without any particular damage, which was suitable. The observed defects were considered as submicron cracks and not submicron crazes. Indeed, in PLA, the tensile deformation induces crazes in the matrix, which can be observed by small-angle X-ray scattering (SAXS) testing as two perpendicular scattering streaks on the patterns [55,134]. However, in the case of the pPLA, no scattering streak was observed in SAXS patterns (4.3 Deformation Heterogeneities in PLA-Based Materials at Room Temperature). The presence of inclusions acted as stress concentration points upon drawing inducing damage. In PLA blended with rubber particles, the localization of stress induced crazing initiated by the rubber inclusions [80]. Crazing was in this case followed by internal cavitation of the rubber particles, these two damage mechanisms enabling further plasticity compared to neat PLA. Similar observations were

made in HIPS [138]. In the case of pPLA, the reactive blending of PLA with acrylPEG engendered crosslinking points between the plasticizer and the matrix. Such crosslinking points may locally hinder fibrillation to dissipate stress around the inclusions explaining the occurrence of cracking instead of crazing, which was a priori not suitable concerning plasticity [137]. Generally, cracks can quickly propagate and coalesce engendering material failure, while crazing may better dissipate stress than cracking due to internal fibril rearrangement enhancing plasticity. Nevertheless, the observed submicron cracks appeared localized between inclusions and did not propagate further, which was a posteriori desirable for ensuring a good plasticity.

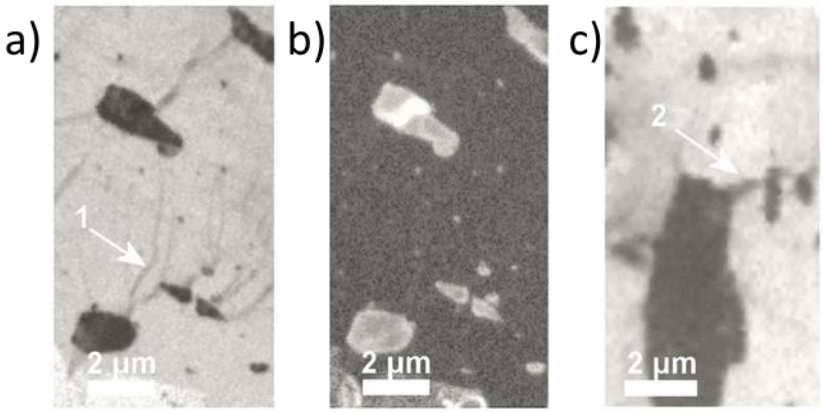

Figure 4.21 Composition maps obtained from STXM micrographs of pPLA at a strain level of 12% indicating the present amount of a) PLA at 288.5 eV, and b) poly(acrylPEG) at 289.7 eV in a first area, and c) PLA at 288.5 eV in a second area. Tensile axis is diagonal (about 45° diagonally from the upper left to lower right). 1: submicron crack at the vicinity of inclusions of plasticizer, and 2: submicron crack originated from one inclusion and propagating to a neighboring inclusion.

Complementary information about the mechanical behavior of the plasticizer inclusions was obtained by micro-computed X-ray tomography (µCT) testing performed on a drawn tensile specimen of pPLA (Figure 4.22 a). In particular, the center of the tensile specimen (the most deformed area), and an undeformed or little-deformed area were analyzed (Figure 4.22 b and c). The 2D image recorded for a little or undeformed area of pPLA exhibited a quite homogeneous contrast of X-ray absorption (Figure 4.22 b). It was not possible to distinguish the inclusions from the PLA matrix due to the lack of density contrast and/or limitation in spatial resolution (about 1 µm) of µCT that did not permit to visualize the inclusions. In the case of the most deformed area of pPLA, the 2D image recorded at the core of tensile specimen exhibited a totally different aspect compared to the previous case. Indeed, an important density of ellipsoids oriented in the tensile direction with a dark contrast was observed (Figure 4.22 c, zone labeled 1). These ellipsoids had a lower density than the matrix, and hence, appeared as voids by µCT due to the limited spatial resolution of this equipment and/or to the low

density of the inclusion core that did not absorb X-ray. The core-shell structure, which was already observed in the STXM/NEXAFS results (Figure 3.12), was also present in the µCT image of the deformed zone (Figure 4.22 c, zone labeled 2). It can be concluded that drawing caused an important decrease of the density in the poly(acrylPEG)-poor core, as well as in the poly(acrylPEG)-rich shell of the inclusions since both are clearly visible compared to the undeformed area (Figure 4.22 b and c). This finding confirmed the previous results obtained by means of a scanning transmission electron microscope in section 4.2 Deformation Mechanisms of Plasticized Polylactide. The deformation impacted both the inclusion's core and its shell resulting in a decrease of density, and no inclusion-matrix debonding was noted. The observed deformation mechanism of plasticizer inclusions is hence suitable for increasing PLA plasticity by locally dissipating stress without internal damage and inclusion-matrix debonding. It is worth to mention that the resolution of this technique restricted to observe the cracks between the inclusions as observed before by STXM (Figure 4.21). Furthermore, shear bands were observed in the most deformed area of the tensile specimen (Figure 4.22 a). These bands occurred with an angle of about 45°C to the drawing direction and were probably due to the crosslinking points in pPLA that may locally limit chain drawability. From the present studies, the exact interaction between the shear bands and the cracking could not be clarified. Nevertheless, it is expected that the millimeter shear bands contain the submicron cracks.

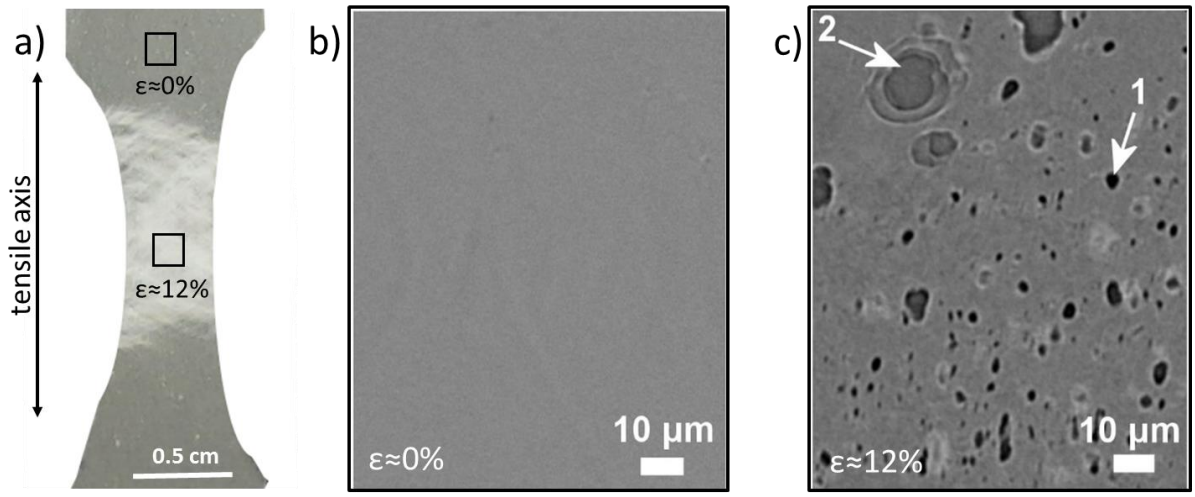

Figure 4.22 a) Picture of a drawn tensile sample of pPLA at a strain of 12% with the two areas marked for the 2D µCT images recorded in b) a undeformed or little deformed area, and c) the most deformed area (both µCT images were recorded with a spatial resolution of about 1 µm and 0.3 µm of voxel size). Tensile axis is vertical. 1: inclusion without density contrast, 2: inclusion with a density contrast indicating the presence of the shell.

4.4.3 Inclusion's Structure Model

Based on STXM/NEXAFS, AFM and µCT results, the structure of the plasticizer inclusions in pPLA was represented in Figure 4.23 before and after drawing. At the undeformed state, the inclusions had a shell structure rich in poly(acrylPEG) that was grafted/crosslinked to PLA matrix, while the core structure of the inclusions contained less poly(acrylPEG) compared to the shell (Figure 4.23 a). After drawing, the poly(acrylPEG) domains of the inclusions were stretched so that the local density became lower in the core as well as in the shell (Figure 4.23 b). These results confirm the previous assumed deformation of inclusions with a density decrease (Figure 4.8 b). Last, cracks bridging inclusions also appeared with the imposed strain probably due to the presence of crosslinking points.

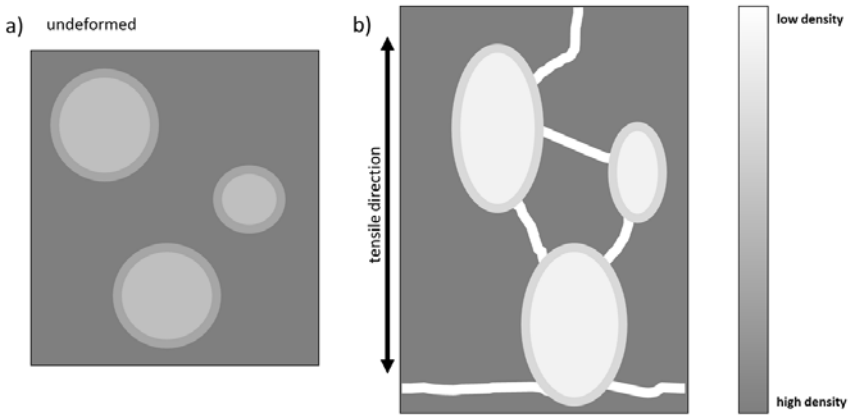

Figure 4.23 Schematic representation of pPLA inclusion structure a) prior drawing showing the core-shell morphology and b) after drawing characterized by a marked decrease of the density of the inclusion core as well as inclusion shell and by the formation of cracks bridging the inclusions.

4.5 Conclusion

This chapter highlights the different mechanisms that rule the deformation in pPLA and PLA. It was shown that depending on the deformation conditions (temperature and strain rate) the mechanisms are different. While at elevated temperature the phase transformations of the amorphous and crystalline phases were crucial, at room temperature the cavitation dominates. PLA is brittle at room temperature and pPLA is ductile due to its reduced glass transition temperature. The comparison of the phase transition mechanisms at different temperatures leads to the conclusion, that in pPLA at room temperature crystal formation due to the ordering of the amorphous chains and destruction of the initial crystals due to shearing are in competition. The same behavior was observed for PLA but just at temperatures close to its glass transition temperature. In general, it was observed that, higher crystallinity indices were reached at higher temperatures due to the increased chain mobility and that lower strain rates favor the formation of crystals while higher strain rates constrain the formation of crystals due to the time to react to the applied stress. The morphological investigation showed that the poly(acrylPEG) inclusions were deformed within the matrix to an ellipsoid shape with the major axis oriented in the tensile direction. Whitening occurred in both, PLA and pPLA, but it was correlated to different factors. In PLA, the whitening was permanent and induced by formation of crazes, developing to cracks that are expected to scatter light. Interestingly, the whitening in pPLA (bulk samples) was nonpermanent and was, hence, related to the deformation of inclusions which could indicate a partial recovery of the material. The deformation of inclusions was related to a possible nanovoid formation inside the inclusions with a decrease of density and specimen whitening.

The deformation of the film samples at room temperature highlighted the different deformation heterogeneities in PLA and pPLA and showed the impact of the initial crystallinity and the plasticization method. While PLA showed the formation of crazes that develop under higher stress to cracks, the samples with a higher initial crystallinity by isothermal crystallization (PLA-IC) showed directly the formation of cracks and no crazes with fibrillation were observed. The observed cracks in PLA developed perpendicular to the strain direction as well as grew in this direction. In PLA-IC the cracks were shaped like waves rather formatted new at the same time then grew. The area of voids was 1.5 times higher for PLA-IC than for PLA, which was related to the higher number of weak points induced by the initial crystallinity. For both PLA samples, non-isovolumetric deformation was observed. The plasticization of PLA leads to more ductile materials with a higher elongation. The determination of the coefficient D as indices about the isovolumetric deformation behavior, confirmed, that PLA/acrylPEG was more rubber-like and pPLA was more rigid than PLA/acrylPEG but more rubber-like than the PLA samples. While in PLA/acrylPEG no cracks were observed, pPLA offered a high inhomogeneity and crack-rich and crack-poor regions because of the induced crosslinking network

with a high heterogeneity. The tensile behavior of pPLA and PLA/acrylPEG was similar to PLA's deformation at elevated temperatures close to or above the glass transition temperature since the plasticization decreases the glass transition temperature. However, the crosslinking and grafting caused a higher strain localization, which was related to the network formation and the higher stiffness. In summary, isothermal crystallization or plasticization hindered the formation of fibrillated crazes in the PLA matrix.

The plasticizer inclusions in pPLA have an impact on the deformation behavior. The expected decrease of density was proved by µCT. It was shown that the inclusion deformation occurs without debonding from the matrix. These findings demonstrated that the deformation mechanisms of the pPLA inclusions may enhance the plasticity of the material since no damage occurred. In contrast, submicron cracks bridging neighboring inclusions were observed. Despite the detrimental aspect of cracking, cracks in pPLA were localized between inclusions and did not further propagate, which is believed to be suitable to ensure a good plasticity.

One critical point is the origin of the whitening in pPLA. While in PLA the formation of voids causes the permanent whitening, in pPLA, different observations were made. The whitening was less permanent and for some cases, the samples turned into transparent appearance again, but this phenomenon was not reliably reproducible, and hence a detailed analysis was impossible. The different whitening behavior can be attributed to the structure of pPLA. The chemical structure is gained by radical reactions and therefore not homogeneous and very local effects impact the properties. In summary, the grafting of plasticizer inclusions leads to a good stress management and allows to keep a moderate tensile (Young's) modulus. The material of pPLA is not completely rubber-like and combines for the deformation mechanism the advantages of the stiff PLA matrix with the improvement of ductility by plasticization. Concerning the application of pPLA, the whitening effect, if controllable, could be useful to create opaque film and/or film with porosities required for specific applications.

5 Structure Evolution with Reprocessing

5.1 Introduction

Despite many advantages over conventional plastics, the use of biopolymers is still limited. One reason for this is the vicious cycle connected to the end-of-life of these new materials. Despite the possibility of biodegradation, reuse and recycling are often more suitable for the value creation chain. While the thermomechanical recycling of common petroleum-based polymers like high-density polyethylene (HDPE) [139], polypropylene (PP) [140], and polyethylene terephthalate (PET) [141] was intensively investigated and is applied in the industry, the critical mass of used biopolymers is too low to create a profitable recycling mass for these materials. Consequently, the lack of recycling is considered as a disadvantage compared to conventional plastics and prevents bioplastics to be considered as an alternative material.

To overcome these issues, possible end-of-life scenarios for biopolymers have to be analyzed and especially the thermomechanical recycling needs special attention to obtain materials that are competitive with common plastic materials. Polylactide (PLA) offers different end-of-life scenarios (composting, incineration, and chemical recycling) that all provide a low carbon dioxide footprint [142], as well as thermomechanical recycling by further reprocessing, which could reduce energy and renewable resource consumption [143]. Different studies dealt with the suitability of thermomechanical reprocessing in relation to PLA degradation. Pillin et al. [89] reprocessed PLA by injection molding up to seven times and observed a decrease of the glass transition temperature from 66°C to 57°C. The molecular weight decreased to 50% of its initial value already after three reprocessing steps and the viscosity dropped from an initial value of 3960 Pa.s to 25 Pa.s after seven cycles. At the same time, the crystallinity increased strongly. The first processing formed a nearly amorphous PLA (X_c = 0.3%), while after the last cycle a crystallinity index of 56.3% was reached. Concerning mechanical properties, the authors showed that recycling had no impact on the tensile modulus of PLA after seven cycles, while at the same time the stress at break was drastically decreased from 65 MPa to 25 MPa. This last observation was explained by the increase in crystallinity and the molecular weight lowering induced by the reprocessing. Badia et al. [88] confirmed these results and justified the occurrence of chain scission with increasing crystallization enthalpy, while the cold crystallization temperature decreased by nearly 10°C. In contrast, in this particular study PLA remained amorphous during the recycling and by FTIR no significant change in functional groups was observed. Another study [87] dealt with the impact of multiple extrusions on PLA properties. Regarding mechanical properties, the tensile strength, the tensile stress at break and the impact strength were observed to decrease slightly by less than 10% and the Young's modulus did not vary.

The glass transition temperature remained unchanged, but the cold crystallization temperature decreased significantly. Since the crystallization and melting enthalpies increased equally, the material was considered to remain amorphous, despite the increased cold crystallization ability. All studies dealing with the recycling or reprocessing of PLA came to the same conclusion. The main degradation mechanism was proved to be chain scission resulting in a change of thermal properties and a decrease of mechanical performances. It was concluded that PLA material cannot be reused for the same applications unless virgin pellets of PLA are mixed with a maximum of 50% of recycled ones [86] or stabilizers are used in the initial formulation [89].

Compared to PET or HDPE, the low thermal stability and the low impact resistance at room temperature of PLA limit its application range. A common way to improve PLA's impact resistance is its plasticization by dispersing a plasticizer within PLA matrix [36] like it was shown with the plasticization by reactive extrusion with acrylPEG and a free radical initiator [14,34,41,49–52]. Up till now, just a few studies dealt with the thermomechanical recycling of modified or plasticized PLA. Scaffaro et al. [94] analyzed the degradation mechanisms of PLA containing 8% of a commercial impact modifier after multiple injection molding procedures and reached the same conclusions like for neat PLA: The main degradation mechanism was chain scission leading to poor mechanical properties, although the crystallinity was improved. However, little details were provided in this pioneering work that lacks microstructural and molecular characterization of the recycled modified PLA, as well as some comparison with the reference neat PLA.

The objective of this chapter is to identify the degradation mechanisms engendered by multiple reprocessing of the plasticized PLA grade (pPLA) obtained by grafting/polymerizing acrylPEG within PLA via reactive extrusion, and of a neat PLA grade as a reference. Due to the complexity of the pPLA structure, a multi-scale characterization approach was considered. In particular, the viscoelastic, tensile, and impact behaviors were first assessed as a function of the processing number. Thermal characterization of the materials by DSC was also conducted. To understand these macroscopic aspects, the microstructure of the as-(re)processed materials was analyzed by SEM and AFM. Last, attention was focused on the molecular scale in terms of (i) chemical structure by nuclear magnetic resonance spectroscopy (^{1}H NMR), (ii) chemical functions by Fourier transform infrared spectroscopy (FTIR), and (iii) molecular weight by GPC and rheology testing. To provide details about the degradation mechanisms of pPLA, some separations between the non-grafted plasticizer and the PLA matrix phase were conducted by Soxhlet extraction, and the extracted material fractions were analyzed at the molecular scale.

The second part of this chapter concentrates on different reprocessing cycles. In the literature, it was shown that reprocessing simulated by several extrusions [87] or multiple injection molding steps [89] had a similar impact on the degradation of PLA. To check this point, three different reprocessing cycles were considered, that consisted in up to five steps of (i) extrusion + compression molding, (ii) extrusion, and (iii) extrusion + injection molding. Since the chain scission mechanisms were identified as the main mechanisms during the thermomechanical reprocessing, the samples were characterized by their molecular weight.

Since the thermomechanical reprocessing increased the crystallinity, the isothermal crystallization behaviors of PLA and pPLA after several reprocessing steps were compared. The isothermal crystallization was quantified by the means of the Avrami model, as already described in Section 3.1. The Avrami equation (5.1) describes the typical S-shaped curve of the crystallinity index X_c as a function of the crystallization time with the Avrami exponent n, providing information about the nature of crystal nucleation and crystal growth geometry and the Avrami factor k, reflecting the overall rate constant associated with both nucleation and growth contributions [97]. The determination of the Avrami parameters enables the calculation of the half-time crystallization $t_{1/2}$ by Equation (5.2). The half-time crystallization defines the time when the crystallization is half finished.

$$X_c(t) = 1 - \exp(-k\, t^n) \tag{5.1}$$

$$t_{1/2} = \left(\frac{\ln(2)}{k}\right)^{\frac{1}{n}} \tag{5.2}$$

The Avrami parameters, as well as the half-time crystallization, allow the comparison of the crystallization kinetics of different materials [59,62–67]. In this way, this chapter analyzes the differences in neat PLA and pPLA during thermomechanical reprocessing and helps to understand the different degradation mechanisms in the two materials.

5.2 Thermomechanical Degradation of Plasticized Polylactide After Reprocessing

This subchapter is adapted from the publication: Thermo-mechanical degradation of plasticized poly(lactide) after multiple reprocessing to simulate recycling: Multi-scale analysis and underlying mechanisms by B. Brüster, F. Addiego, F. Hassouna, D. Ruch, J.-M. Raquez and P. Dubois in Polymer Degradation and Stability 131 (2016), 132-144. [144]

5.2.1 Processing

The details about the processing equipment are given in Appendix A.2 and the description of the characterization methods can be found in Appendix A.5.

The processing and the reprocessing of PLA and pPLA were simulated at the laboratory scale, meaning with small material quantities and specific machines under operating conditions that may only partially reflect industrial realities. Nevertheless, lab-scale simulation of recycling appeared as a fast and cost-effective procedure to get first information about recycling-induced degradation mechanisms of the materials enabling to optimize an eventual scale-up study of their recycling. Both materials, PLA (PLA/acrylPEG/L101 with weight composition 100/0/0) and plasticized pPLA (PLA/acrylPEG/L101 with weight composition 79/20/1) were extruded using a twin screw micro-compounder with a nitrogen flow. The melting temperature was set to 180°C and the screw speed was adjusted to 50 rpm with a residence time of 5 min. After shaping by compression molding, the recycling was simulated by several cutting/extrusion/cutting/compression molding procedures, as represented in Figure 5.1. Each cutting step was done by hand using a sharp tile nipper. Before each re-extrusion, pPLA pellets were dried at 30°C in a vacuum oven for 12 h, while PLA pellets were dried at 50°C under the same conditions due to the T_g difference between the two materials. All samples were named starting with their material type (PLA, pPLA) and finishing with the number of compression molding steps (CM1, CM3, CM5). It is to be noted that the characterization was systematically conducted from the shaped plates of PLA or pPLA.

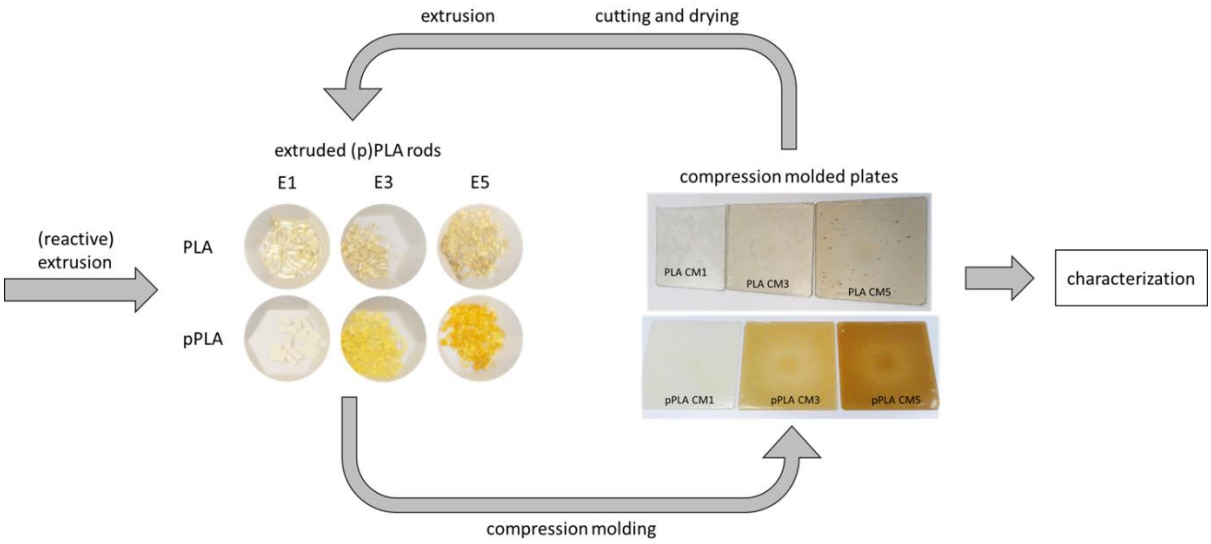

Figure 5.1 Schematic processing and reprocessing procedures of (p)PLA including images of the extruded rods and the compression molded plates for the (p)PLA materials.

5.2.2 Influence of the Reprocessing on the Macroscopic Behavior

The viscoelastic behavior of pPLA and of the neat reference PLA processed under the same conditions were studied by DMA analyses. For the case pPLA CM5, it was not possible to machine DMA specimen that systematically broke during the machining, highlighting a certain brittleness of the materials. Figure 5.2 illustrates the viscoelastic responses of pPLA and PLA in the temperature range from -100°C to 120°C at a frequency of 5Hz. Briefly, in the temperature range -30°C to 50°C, plasticizing led to a stronger decrease of pPLA storage modulus and an advanced and broaden increase of pPLA loss factor, indicating a lower ability to restore mechanical energy and a higher ability to dissipate it, in comparison with PLA. The glass transition temperature T_g was defined as the corresponding peak position in the tan δ – temperature T curves. T_g was equal to 50°C for pPLA CM1 and 65°C for PLA CM1. Consequently, the reactive extrusion of PLA with acrylPEG led to a decrease of T_g of about 15°C in comparison with neat PLA. Based on all the DMA data obtained at different frequencies, no important impact of recycling was noted on the E' - T, E'' - T and tan δ – T curves. However, recycling caused a weak shift of the cold-crystallization peak toward lower temperatures when comparing CM1 with CM3 for pPLA (Figure 5.2 a) and CM1 with CM3 or CM5 for PLA (Figure 5.2 b). Recycling also engendered a decrease of the storage modulus of PLA when comparing CM1 with CM3 or CM5, demonstrating a lower ability of PLA to restore mechanical energy after reprocessing (Figure 5.2 a).

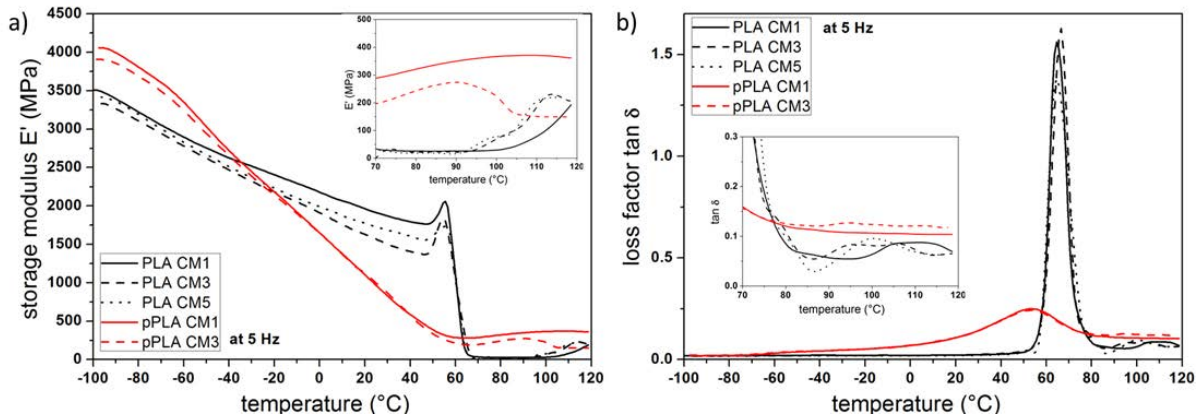

Figure 5.2 DMA analysis of PLA and pPLA after 1,3, and 5 processing cycles in the temperature range from -100°C to 120°C at 5Hz with some high temperature close-in views: a) storage modulus E', and b) loss factor tan δ.

The typical tensile behavior of PLA and pPLA assessed at 50°C was represented in Figure 5.3, while the extracted mechanical parameters at all the temperatures were reported in Table 5.1. It was decided to test all the materials at 50°C and 80°C, while at 20°C only PLA CM1, pPLA CM1, and pPLA CM3 were tested. This is due to the fact that tensile testing is material-consuming especially for repeatability, it was hence chosen to promote tensile testing at high temperatures for which PLA and pPLA may exhibit a high ductility. At 20°C, the tensile modulus of PLA CM1 was higher than that of pPLA CM1 (3062.0 MPa vs. 1134.7 MPa), as was the case in the evolution of the storage modulus E' as a function of temperature in DMA measurement (Figure 5.2 a). Moreover, plasticization improved the ductility as shown by the increase of elongation at break from 4.1% for neat PLA CM1 to 54.1% for pPLA CM1, resulting in a material having an effective wide plastic stage at 20°C. At the same time, the plasticization decreased the tensile resistance as shown by the decrease of ultimate stress σ_u from 71.9 MPa for PLA CM1 to 19.4 MPa for pPLA CM1, and the decrease of yield stress σ_y from 77.9 MPa for PLA CM1 to 26.6 MPa for pPLA CM1. For the non-recycled materials, the tensile modulus E decreased, the yield stress σ_y decreased, the ultimate strain ε_u increased and the ultimate stress σ_u decreased with increasing temperature. It is to be noted that PLA was very soft at 80°C with a tensile modulus of about 2 MPa, and hence, achieved the displacement limit of the machine corresponding to 800% of elongation with no breaking point. pPLA was more ductile than PLA only at room temperature, for the other temperatures the opposite case was noted. The tensile modulus of pPLA did not significantly vary with recycling, as noted for the storage modulus measurements by DMA (Figure 5.2 a). In contrast, pPLA ultimate strain markedly decreased with recycling at all the temperatures, demonstrating an important embrittlement of the material that exhibited no or limited plasticity (Table 5.1). For example, between CM1 and CM5, ε_u decreased from 142.3% to 5.2% at 50°C, and from 221.8% to 2.8% at 80°C. Excepted at 20°C, where the ultimate stress σ_u of pPLA was quite

constant with recycling (CM1 to CM3), σ_u of pPLA markedly decreased with the recycling number. Concerning PLA, recycling engendered a decrease of the tensile modulus when comparing CM1 with CM3 or CM5 at 50°C, as noted by DMA for the storage modulus measurements (Figure 5.2 a). Contrary to pPLA, no embrittlement was noted in the case of PLA with recycling. Only a decrease of the tensile resistance was observed through the decrease of σ_u when comparing the non-recycled material with the materials processed 3 times or 5 times at 50°C and 80°C.

The impact testing, carried out at 20°C, showed for PLA a slight decrease from the first to the third recycling cycle, but no change up to the fifth (Table 5.1). Concerning pPLA, it was again not possible to machine impact testing specimen that systematically broke during the machining of the notch, showing again a certain brittleness of the materials. pPLA CM1 exhibited a higher impact energy (4.7 kJ/m^2 compared to 3.6 kJ/m^2 for PLA CM1), but after three recycling stages the impact energy of pPLA decreased to 2.1 kJ/m^2 (pPLA CM3), which was below that of the recycled PLA samples PLA CM3 (2.4 kJ/m^2). Therefore, after 3 processing, the toughness of pPLA decreased by 55.3%, while that of PLA decreased by 33.3%. The toughness decrease was hence more marked for pPLA than for PLA. Regarding the toughness, it is important to mention that very different values were obtained under different processing conditions: 101.6 kJ/m^2 for PLA/acrylPEG/L101 79/20/1 wt% in a previous study [50] and 38.4 kJ/m^2 for the same material produced in this study (section 3.2.4 Impact Resistance). Indeed, due to a motor torque limitation of the extruder it was not possible to mix the same amount of material (12 g instead of 15 g) and use the same speed (50 rpm instead of 100 rpm) as in the previous study [50] The actual processing conditions certainly lead to a less intense elongational flow in the extruder compared to the previous study. It is thought, that decreasing elongational flow yields to a lower dispersion state of the plasticizer and free-radical initiator within PLA matrix, and hence, to a suboptimal dispersion of the inclusions limiting the toughness increase. Furthermore, the preparation of the impact testing specimen was different: injection molding for the results given in section 3.2.4 Impact Resistance and compression molding for the samples used in this analysis of the influence of the reprocessing cycles.

Table 5.1 Mechanical parameters with standard deviation obtained from tensile testing at 20°C, 50°C and 80°C, and impact testing for pPLA and PLA as reference (n.t. stands for not tested, n.m. stands for not measurable, no b.p. stands for no breaking point at the maximum cross-head displacement of the tensile machine).

	Material	Tensile modulus E (MPa)	Yield Stress σ_y(MPa)	Ultimate Strain ε_u (%)	Ultimate Stress σ_u(MPa)	Impact energy IE (kJ/m^2)
temperature 20°C	PLA CM1	3062.0 ± 17.3	77.9 ± 2.3	4.1 ± 0.3	71.9 ± 0.1	3.6 ± 0.8
	PLA CM3	n.t	n.t	n.t	n.t	2.4 ± 0.1
	PLA CM5	n.t	n.t	n.t	n.t	2.4 ±0.1
	pPLA CM1	1134.7 ± 56.1	26.6 ± 0.4	54.1 ± 9.7	19.4 ± 1.0	4.7 ± 0.7
	pPLA CM3	1212.7 ± 36.3	2.3 (-)	3.2 ± 2.3	22.5 ± 3.8	2.1 ± 0.2
	pPLA CM5	n.t.	n.t.	n.t.	n.t.	n.t.
temperature 50°C	PLA CM1	2511.5 ± 2.4	46.2 ± 1.0	272.0 ± 2.0	34.1 ± 1.3	
	PLA CM3	1930.4 ± 242.6	42.2 ± 4.5	217.5 ± 55.5	22.5 ± 4.2	
	PLA CM5	1458.0 ± 296.8	39.0 ± 1.9	233.7 ± 92.5	22.4 ± 6.8	
	pPLA CM1	297.1 ± 10.4	12.3 ± 0.1	142.3 ± 9.5	11.5 ± 0.2	
	pPLA CM3	273.4 ± 18.6	7.1 ± 0.3	6.6 ± 0.5	9.5 ± 0.4	
	pPLA CM5	285.5 ± 7.3	5.3 (-)	5.2 ± 4.7	5.3 ± 0.6	
temperature 80°C	PLA CM1	2.9 ± 0.5	1.0 ± 0.0	> 800, no b.p.	> 11.9, no b.p.	
	PLA CM3	2.7 ±0.1	0.7 ± 0.0	> 800, no b.p.	> 4.1, no b.p.	
	PLA CM5	2.5 ± 0.2	0.7 ± 0.0	> 800, no b.p.	> 1.5, no b.p.	
	pPLA CM1	131.6 ± 12.5	n.m.	221.8 ± 75.6	6.9 ± 0.1	
	pPLA CM3	147.8 ± 19.5	4.5 ± 0.4	5.8 ± 0.4	5.8 ± 0.7	
	pPLA CM5	148.8 ± 6.5	n.m.	2.8 ± 0.5	3.5 ± 0.6	

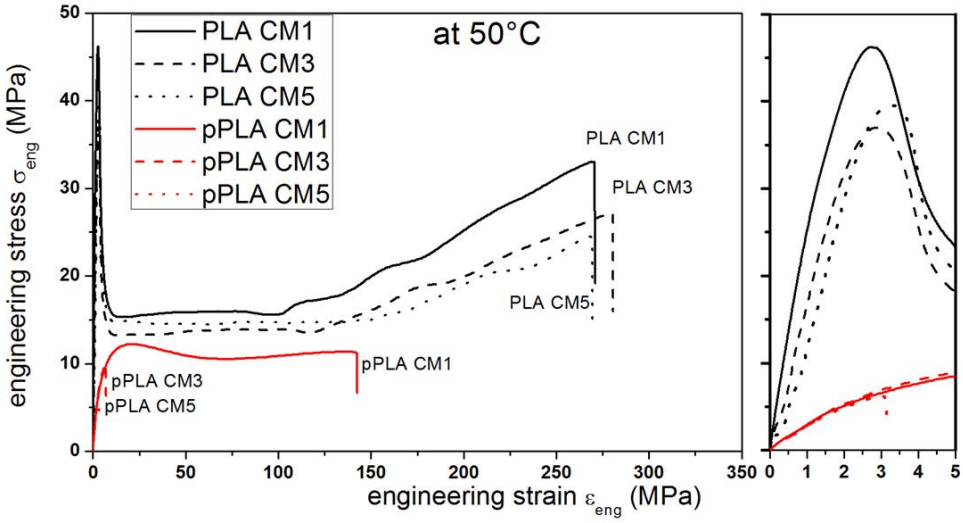

Figure 5.3 Influence of the recycling on the tensile curves of pPLA and PLA as reference obtained at 50°C - a zoom-in view is made for the initial part of the curves.

The thermal properties of PLA and pPLA were analyzed by DSC and the extracted results were summarized in Table 5.2. The pPLA exhibited a higher crystallinity compared to PLA (X_c = 31.2% vs. X_c < 1%) that was considered as being amorphous, even though cold crystallization induced crystallinity during the DSC measurements. An important finding was that pPLA crystallinity increased slightly from 31.2% to 35.6% with recycling number. At the same time, PLA remained amorphous whichever the processing number was. The determined crystallinity was confirmed by X-ray diffraction (XRD) testing based on the methodology reported in a previous work [34]. Another important finding was the presence of a double melting peak for pPLA that is transformed into a simple melting peak with recycling, while it was the opposite situation for neat PLA. Furthermore, the main melting peak was positioned at T_m = 151.0°C for pPLA and T_m = 155.8°C for PLA, indicating thinner lamellae in the case of pPLA compared to PLA during the melting stage. Based on the study of Ma et al. [107], the double melting peak in pPLA can be interpreted as the presence of thin crystals with different extent of perfection due to the grafting of the plasticizer [44,102], while for PLA, crystals may have a higher perfection and hence may be thicker [145]. Recycling caused a disappearance of the double peak for pPLA indicating a higher perfection compared to pPLA processed once. On the contrary, recycling induced crystal imperfection in the case of PLA. PLA melting temperature (T_m) increased slightly when comparing PLA CM1 with PLA CM3 or PLA CM5, while that of pPLA was quite constant. Furthermore, for PLA the cold crystallization enthalpy (ΔH_{cc}) increased with the processing number, while the cold crystallization temperature (T_{cc}) decreased. In contrast to PLA, pPLA did not exhibit any cold crystallization peak in DSC unlike in DMA. Cold crystallization results from sufficient chain mobility that

leads to chain orientations. Zhang et al. [146] demonstrated that the simple addition (without grafting) of the amorphous phase of poly(3-hydroxybutyrate-co-3-hydroxyvalerate) (PHBV) and poly(butylene succinate) (PBS) could activate the chain mobility of PLA and enhance the cold crystallization. The structure of pPLA structure was earlier described by Hassouna et al. [49] as a PLA matrix plasticized with partially grafted poly(acrylPEG) that formed partially crosslinked inclusions. The bonds between the PLA matrix and the plasticizer phase can reduce the PLA chain mobility and hinder the cold crystallization, while the crystallization from the melted state is possible. It is to be noted that cold crystallization of pPLA was observed by DMA testing that was conducted at a lower heating rate (2 K/min) compared to DSC (10 K/min). As shown in previous works [41,51], pPLA shows a lower glass transition temperature (T_g = 34°C) compared to amorphous PLA (T_g = 60°C). After recycling, pPLA glass transition is poorly visible and the exact glass transition temperature could not be determined by DSC, but DMA measurement showed already that recycling had no influence on T_g up to three processing. The glass transition temperature of PLA stayed stable with increasing the recycling number.

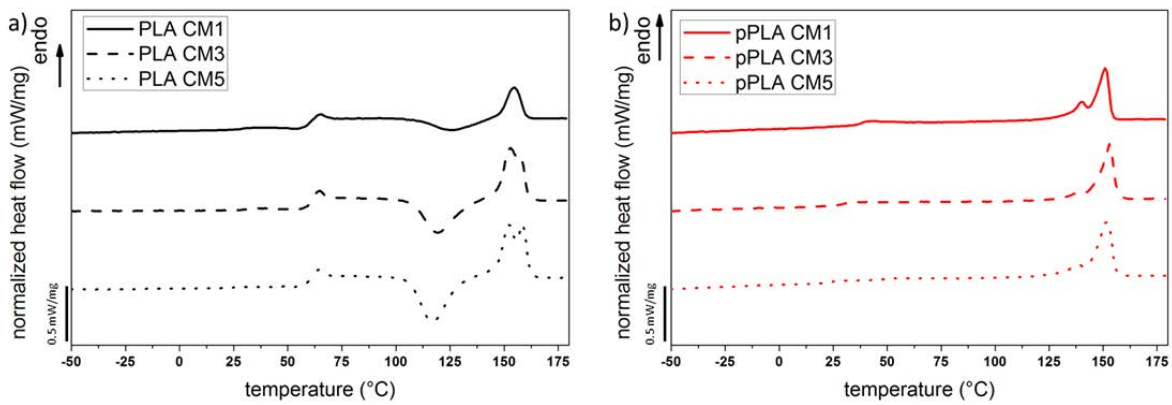

Figure 5.4 Representative DSC curves of a) PLA and b) pPLA after 1, 3, and 5 processing.

Table 5.2 Data from DSC measurements with standard deviation.

Material	T_g (°C)	T_{cc} (°C)	T_m (°C)	ΔH_{cc} (J/g)	ΔH_m (J/g)	X_c (wt%)
PLA CM1	59.8 ± 0.9	127.4 ± 1.9	155.8 ± 1.1	9.0 ± 3.6	9.6 ± 2.8	0.6 ± 1.2
PLA CM3	58.9 ± 1.1	122.0 ± 4.0	158.8 ± 1.2	24.2 ± 5.7	25.3 ± 4.6	0.7 ± 3.9
PLA CM5	61.3 ± 3.0	118.4 ± 1.5	159.6 ± 1.2	30.0 ± 3.4	32.7 ± 2.6	1.8 ± 2.2
pPLA CM1	34.0 ± 8.9	63.3 ± 5.5	151.0 ± 0.2	2.2 ± 0.8	25.1 ± 1.0	31.2 ± 1.5
pPLA CM3	hardly visible	no peak	152.4 ± 0.5	1.5 ± 0.6	26.1 ± 1.8	33.5 ± 2.7
pPLA CM5	hardly visible	no peak	151.5 ± 0.5	3.2 ± 1.7	29.4 ± 1.0	35.6 ± 1.1

Based on their macroscopic behaviors, PLA and pPLA undergo different degradation mechanisms, and hence, the plasticization has an influence on the thermomechanical degradation of PLA. Concerning molecular relaxations, DMA showed nearly no effect of the recycling for pPLA, while PLA underwent a decrease of storage modulus. A shift of cold-crystallization relaxation toward lower temperatures was however observed for PLA and pPLA with recycling. Tensile testing highlighted no change of tensile modulus for pPLA with recycling (as observed in DMA), but at the same time, this material was characterized by an important loss of ductility and hence an embrittlement. Concerning PLA, tensile testing showed a decrease of the tensile modulus (as observed by DMA for the storage modulus), and a decrease of tensile resistance. Impact testing indicated a more marked decrease of toughness for pPLA than for PLA with increasing the number of processing cycles. The variation of mechanical properties can be explained by the variation of the microstructure and molecular structure. For pPLA, the microstructure is linked to the quantity, size, and morphology of poly(acrylEPG) inclusions [41], crystal quantity and morphology, and possible defects/damage. The molecular structure is linked to molecular weight, chemical structure, and chemical functions.

DSC testing provided first information enabling to understand the effect of recycling on the microstructure and molecular structure of PLA and pPLA. The increase of the cold-crystallization enthalpy of PLA is attributed to chain scission mechanisms so that shorter chains enhance the possibility of cold crystallization [89,139–141]. However, Pillin et al. [89] recycled PLA up to seven times and reported an increase of cold crystallization enthalpy, reaching a plateau after the second recycling, and a decrease of ΔH_{cc} afterward. They explained this behavior by a decrease of the molecular weight and defined 132,000 g/mol as the critical molecular weight. Below this molecular weight, the cold crystallization enthalpy decreased again. In our study, PLA's molecular weight may be higher than this critical value, since the crystallization enthalpy increased up to the fifth processing. The assumption, that the molecular weight is higher than the critical molecular weight, will be proved in the next section. This increase of cold crystallization enthalpy was accompanied by a decrease of the corresponding cold crystallization temperature for PLA and the decrease of PLA molecular weight can explain the decrease of tensile/storage modulus, tensile resistance and toughness observed in the mechanical testing. Indeed, in the case of an amorphous matrix, elasticity, tensile strength, and toughness decreased when the entanglement density decreased or when the molecular weight between entanglements increased [35,147]. Such changes of molecular structure may be induced by chain scission mechanisms, as reported in [148]. Considering that chain scission would be active in pPLA during recycling, as indicated by the shift of cold-crystallization relaxation toward lower temperatures in the DMA study, this mechanism would be in competition with the increase of crystalline fraction and degree of perfection for the control of mechanical properties. Indeed, a higher

crystallinity and higher amount of perfect crystals would increase the storage/tensile modulus, tensile resistance, and toughness. It is believed that chain scission mechanisms and crystallization mechanisms are in equilibrium concerning their influence on the viscoelastic properties of pPLA (tensile modulus or storage modulus) that are constant with increasing the recycling number. However, other mechanisms may be active during the viscoelastic stage of pPLA that worsen the mechanical properties of pPLA. These mechanisms will be identified in the next sections dedicated to pPLA microstructure and molecular structure.

5.2.3 Influence of the Reprocessing on the Microstructure

Although the PLA matrix and the poly(acrylPEG) inclusions had a similar chemical structure and an exact differentiation in SEM of both phases was complicated, Figure 5.5 showed some topographical differences when comparing non-recycled with recycled pPLA. After the first cycle, pPLA exhibited some white areas, and hence, some peaks scattering numerous secondary electrons (Figure 5.5 a). These white areas are probably the edges of the soft inclusions that are deformed along the polishing direction. With increasing recycling the edges of poly(acrylPEG) phase seemed to be better dispersed within the PLA matrix, indicating that the inclusions may be smaller (Figure 5.5 b). For the last recycling cycle, the difference between both phases was less obvious than the previous cases (Figure 5.5 c). The dispersion of the inclusions seemed even higher since the white edges were less visible (smaller inclusions), but at the same time cracks appeared in the material. The latter is obviously detrimental to the mechanical properties of the materials.

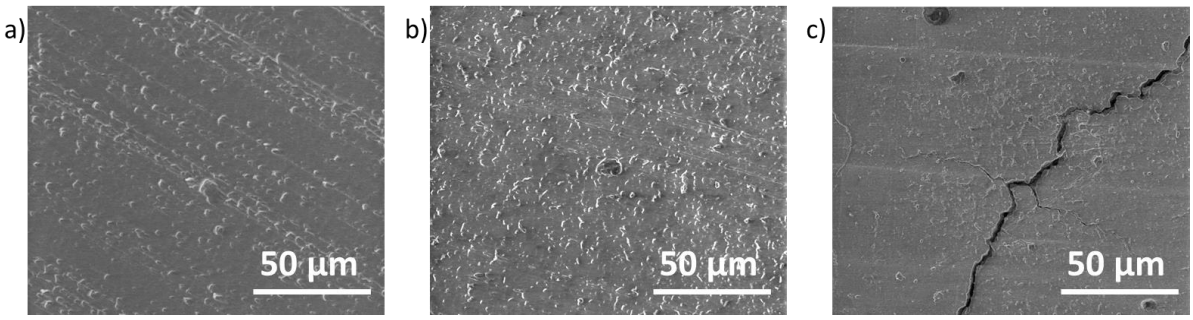

Figure 5.5 SEM images of pPLA after a) 1, b) 3, and c) 5 processing cycles.

AFM allowed a more detailed look at the evolution of the poly(acrylPEG) inclusions of pPLA with recycling. Figure 5.6 showed the inclusions in the plasticized PLA matrix after the first, third and fifth cycle. Again, the structures of PLA and poly(acrylPEG) lacked strong contrasts in AFM, but the

evolution of inclusions was visible. First, the inclusions embedded within the polymer matrix were quite round and homogeneous, while the matrix/inclusions interface seemed to be poor despite the existence of grafting. After three processing steps (Figure 5.6 b) the inclusions were hardly observable and appeared deformed and porous. Note that some of the pores were ellipsoids with the long axis oriented in the same direction indicating shearing forces. In the last image (Figure 5.6 c) a high porosity was visible in the inclusion that appeared totally fibrillated, and hence almost destroyed. This damage mechanism may explain why inclusions edges were less visible in the SEM investigation (Figure 5.6 c). Recycling causes a deformation and a damage of the inclusions that appear larger than in the non-recycled pPLA but at the same time, we can obviously suppose that the remaining fragments of poly(acrylPEG) phases within the inclusions have a reduced size. Some remaining fragments of poly(acrylPEG) phase were visible in Figure 5.6 c for pPLA CM5. Even though, AFM did not allowed any observation of the core shell structure of the inclusions, and the damage of the inclusions by possible fibrillation leads to the assumption that the initial core shell structure was destroyed. The observed transformation of the inclusions may explain the matrix cracking observed in the SEM study. Indeed, the inclusion damage/fibrillation may significantly decrease the physical interactions between the poly(acrylPEG) phases and the PLA matrix. PLA matrix is supposed to be hydrophobic, while PEG polymers are supposed to be more hydrophilic [149,150]. This mechanism may lead to local internal stress at the interface between poly(acrylPEG) and PLA and may create cracks. Another possible explanation may rely on important chain scission mechanisms within the matrix that generate local shrinkage, and finally cracking [151].

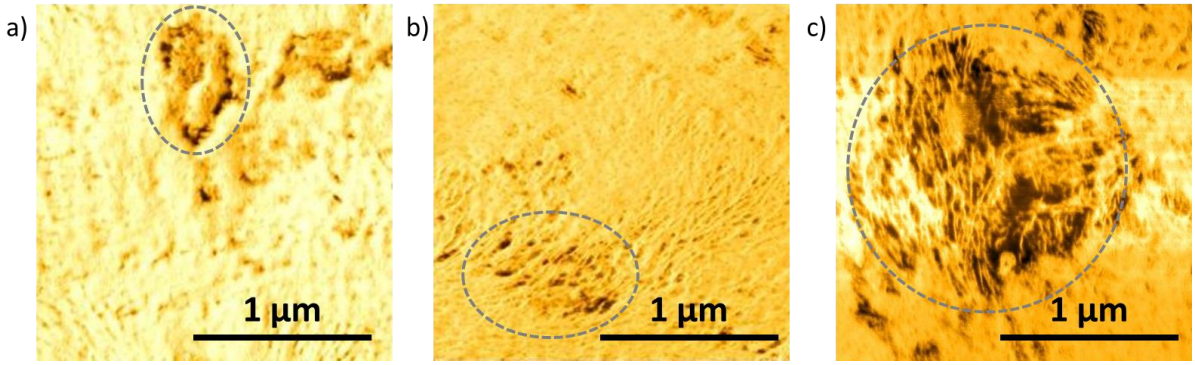

Figure 5.6 AFM phase images of pPLA inclusions: a) initial inclusions in pPLA CM1, b) slightly deformed inclusion with porosity in pPLA CM3, and c) strongly deformed inclusion with fibrillation and high porosity in pPLA CM5 (inclusions were surrounded on each image).

SEM and AFM studies reveal that poly(acrylPEG) micro-inclusions in pPLA suffer from shape deformation, intrinsic damage by the formation of porosity and finally fibrillation, which contribute to

creating weak areas in pPLA. These weak areas may localize mechanical stress and engender material breaking, explaining the reported brittleness of pPLA with recycling (Figure 5.3 and Table 5.1). The interaction between (i) the initial poor interface between the matrix and the inclusions (Figure 5.6 a), (ii) the porosity in the inclusions (Figure 5.6 b), (iii) the fibrillation of the inclusions (Figure 5.6 c), and (iv) the matrix cracking (Figure 5.5 c) was not assessed up to date, but it is hypothesized that these mechanisms may interact one to another one during the matrix cracking and sample breaking. It is to be noted that for other materials, recycling caused a decrease of the inclusion size without damaging. For example, Wang et al. [140] studied a material consisting of a polypropylene (PP) matrix with dispersed ethylene octene copolymer inclusions. Likewise PLA during recycling, PP matrix underlay mainly chain scission mechanisms, but a diminishing of the inclusion size was observed without porosity formation. Along with an increase of PP crystallinity, the decrease of inclusion size was held responsible for improvement or stabilization of the mechanical properties compared to the neat matrix material. In this previous study, the inclusions were not grafted to the polymer matrix, which may indicate that in our case the inclusion grafting may be at the origin of the severe damage of the poly(acrylPEG) micro-inclusions.

5.2.4 Influence of the Reprocessing on the Molecular Structure

First, it is important to confirm, that chain scission is the main degradation mechanism in PLA. Based on GPC measurement, the weight average molecular weight of PLA decreased from 289,000 g/mol (CM1) to 154,000 g/mol (CM5), whereas the dispersity did not vary during recycling (Table 5.3). These results confirm, that PLA's molecular weight is still above the critical molecular weight of 132,000 g/mol. After a degradation to molecular weights below this weight, a decrease of the cold crystallization enthalpy was observed [89]. The diminution of the molecular weight with stable dispersity suggest a random chain scission mechanisms through the formation of free radicals, which was described earlier and in the literature as the main mechanisms in PLA degradation [86]. Due to the absence of moisture in the materials that were systematically dried before processing and reprocessing, it is supposed that hydrolysis is not active during recycling. Furthermore, FTIR and ^{1}H NMR analyses attest a simple chain scission mechanism, since no functional group different from the original PLA structure was observed. In ^{1}H NMR, PLA possesses two signals: one doublet at 1.58 ppm and a quartet at 5.16 ppm dedicated to the CH_3 group and the CH group, respectively. PLA oligomers, with a lower molecular weight, also provide a peak at 4.37 ppm dedicated to the end-groups [152]. Even the recycled materials miss a peak dedicated to the end-groups, leading to the assumption that chain scission mechanisms suffice for a reduction of molecular weight but no formation of oligomers occurred. FTIR analysis provides as well no change after recycling. The main peaks of PLA are the

asymmetric and symmetric C-H stretching of the CH_3 group and the CH_3 deformation vibration at 2995 cm^{-1}, 2945 cm^{-1}, and 1452 cm^{-1}, respectively. The chemical structure of PLA give strong bands of oxygen functions, especially in the carbonyl band region 1700 – 1750 cm^{-1} and the observation of oxidation was not possible [153,154].

Table 5.3 Molecular weight (M_w) and dispersity (Đ) for PLA after 1, 3, and 5 processing from GPC with polystyrene standard.

	PLA CM1	PLA CM3	PLA CM5
M_w (E+05 g/mol)	2.89 ± 0.03	1.99 ± 0.04	1.54 ± 0.10
Đ (M_w/M_n)	2.21 ± 0.21	2.25 ± 0.13	2.20 ± 0.16

It is important to mention, that GPC analysis of pPLA was not possible, which was presumably due to a partial crosslinking during the reactive extrusion. The pPLA samples could not be dissolved in the GPC solvent sufficiently. Likewise PLA, no change of chemical functions was observed in ^{1}H NMR and FTIR for pPLA (Figure 5.7). However, the amount of plasticizer did not change after several recycling cycles. In ^{1}H NMR, the ratio between the PLA-protons (doublet at 1.58 ppm or quartet at 5.16 ppm at ppm) and PEG-protons (singlet at 3.59 ppm) remained stable. The calculation of the poly(acrylPEG) amount from ^{1}H NMR results, led to amounts of 14.8 wt%, 14.6 wt%, and 14.3 wt% for the samples after 1, 3, and 5 cycles, respectively. The lower detected amount of acrylPEG compared to the initially added amount of 20 wt% could confirm the assumption of a partial crosslinking. The sample was partially dissolved and not the whole sample was detected by NMR. It is to be noted that the assumption of crosslinking was approved by gel formation. PLA and pPLA pellets were swollen in chloroform for 48 h. While the PLA was dissolved completely, pPLA formed a gel. The gel was not stable enough to be separated, but the test proved the existence of crosslink bonds in pPLA even after 5 recycling cycles.

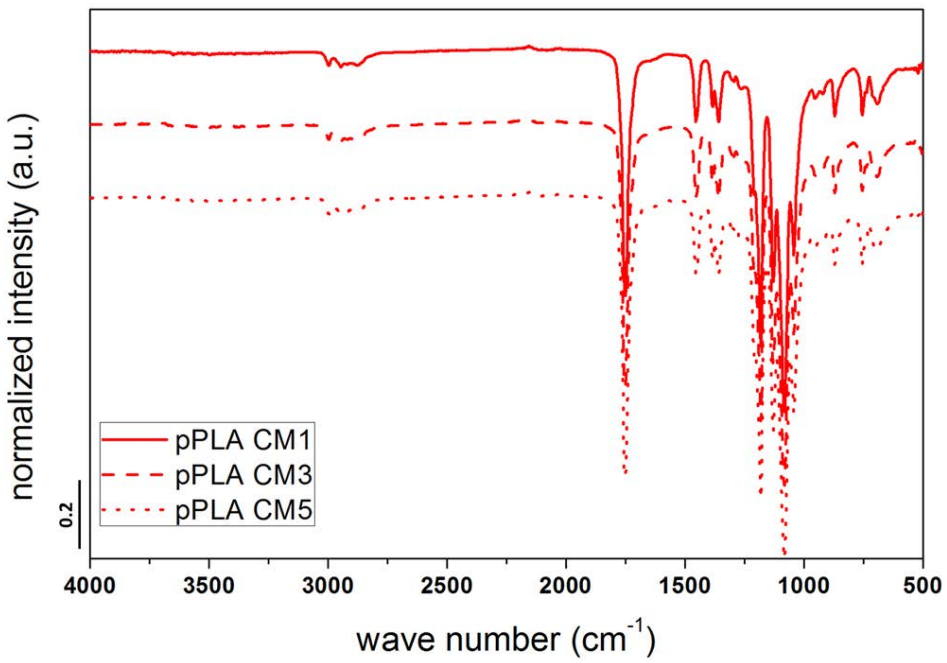

Figure 5.7 FTIR spectra of pPLA after 1, 3, and 5 processing cycles.

Figure 5.8 illustrated the frequency depending viscosity for PLA and pPLA from rheology measurements. The viscosity for pPLA CM1 was lower than for PLA CM1, which could be reasoned to a higher dispersity in pPLA due to the radical grafting reaction. It is evident, that the viscosity of both materials decreased with recycling, indicating a degradation of the material with reprocessing. The GPC results for PLA indicated a decrease of the molecular weight and at the same time an unchanged dispersity index. In general, a decrease of the molecular weight is related to a decrease in the viscosity. Assuming that the matrix in pPLA underlies the same degradation mechanisms like PLA, the dispersity index is stable and the decreasing viscosity indicates a decrease of molecular weight with recycling. For both materials, PLA and pPLA, the curves show a Newtonian plateau. Despite the crosslinking in pPLA, the plateau is visible, which leads to the assumption that the crosslinking exists in a low quantity. It is important to mention that pPLA CM3 and CM5 showed a scattering of the viscosity at low frequencies, which indicates important degradation mechanisms. In particular, this finding shows that degradation is more marked for pPLA than for PLA from the recycling number 3 since no scattering of viscosity value was noted for PLA.

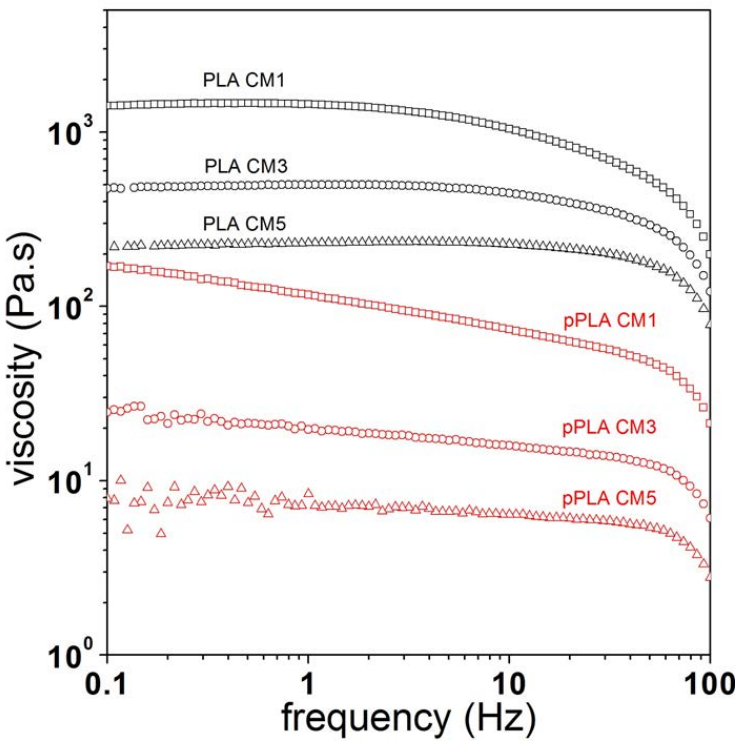

Figure 5.8 Viscosity measurements in dependency on the frequency for PLA and pPLA after 1, 3, and 5 processing cycles.

The calculation of chain scission number (*s*) gave a qualitative information about the degradation and can be calculated with the initial molecular weight (M_w^i) and the molecular weight after a recycling step (M_w) (Equation (5.3)). Accordingly, the chain scission number for PLA CM3 and CM5 was calculated with the molecular weights from GPC measurements. Since a direct determination of the molecular weight of pPLA was not possible with GPC due to insufficient solubility, the molecular weight was substituted by viscosity from the Mark-Houwink equation (Equation (5.4)). This equation gave a correlation between the viscosity η and the molecular weight M with the system depended on the parameters k and a.

$$s = \frac{M_w^i}{M_w} - 1 \tag{5.3}$$

$$\eta = kM^a \tag{5.4}$$

The parameter k was considered to be not influenced by the recycling. Therefore, the chain scission number could be described by Equation (5.5). The *a* value was determined for PLA by an optimization

to obtain the same values for the chain scission as determined with the molecular weight from GPC. The optimized *a* value was then taken to calculate the chain scission number for pPLA.

$$s = \frac{\sqrt[a]{\frac{\eta_i}{k}}}{\sqrt[a]{\frac{\eta_f}{k}}} - 1 = \sqrt[a]{\frac{\eta_i}{k} \cdot \frac{k}{\eta_f}} - 1 = \sqrt[a]{\frac{\eta_i}{\eta_f}} - 1 \tag{5.5}$$

The calculation of the *s*-values for pPLA reported in Table 5.4 was just an approach for the given assumptions, that PLA matrix in pPLA behaved like PLA and that the parameters from Mark-Houwink equation were the same. Nevertheless, the calculation supported the hypothesis that the PLA matrix was stronger damaged in pPLA than in PLA. The chain scission number for pPLA was nearly doubled (0.85 for pPLA and 0.44 for PLA) after 3 recycling steps compared to the PLA material without plasticizer and increased to 1.48 for pPLA CM5, which means that more chains are cut during the recycling process. In particular, the molecular weight of pPLA is stronger decreased and the material becomes more brittle compared to PLA with the recycling.

Table 5.4 Chain scission number for PLA calculated with molecular weight from GPC and chain scission values for PLA and pPLA calculated with the viscosity from rheology measurements at 1Hz and an optimized value a = 2.9.

		s from GPC	*s* from rheology (with a = 2.9)
PLA			
	CM3	0.45	0.44
	CM5	0.88	0.88
pPLA			
	CM3	n.m.	0.85
	CM5	n.m.	1.48

Soxhlet extraction from methanol allowed a separation of the non-grafted amount of plasticizer from the plasticized and partially crosslinked PLA matrix [41,51]. Non-grafted poly(acrylPEG) was soluble in methanol and hence was extracted, while the PLA matrix was insoluble. The amount of extracted fraction ascended from 7.3 wt% after the first cycle, to 9.0 wt% after the third cycle, and to 10.7 wt% after 5 cycles (Table 5.5). Even though in the ^{1}H NMR of the whole sample, no formation of PLA oligomers was observed, the analysis of the extracted fraction by ^{1}H NMR showed an increasing amount of PLA from 3.3 wt% after the first reprocessing to 24.7 wt% after the fifth reprocessing. The real values of extracted PEG fraction were calculated from this data (Table 5.5) and indicated just a

small increase from 7.1 wt% to 8.1 wt% after 1 and 5 processing, respectively. Contrary to the above-mentioned assumption, that the PLA matrix was not disturbed by the extraction, these results prove that PLA is partially extracted. Methanolysis of PLA was proved to occur in presence of catalysts [155,156], but the results of Soxhlet extraction create the impression, that the presence of poly(acrylPEG) enhances methanolysis as well. With increasing recycling number, the amount of extractable PLA in pPLA increased, while in the samples of neat PLA no increase of this fraction was observed (extracted fraction for PLA CM1, CM3 and CM5 ≈ 0.3 wt%). These findings lead to the assumption that the plasticizer phase increases the degradation of PLA matrix.

Table 5.5 Extracted fraction EF (in wt%) for PLA and pPLA after Soxhlet extraction from methanol.

	Soxhlet extraction EF (wt%)	Amount of PLA in the extracted fraction (wt%)	Amount of extracted PEG (wt%)
pPLA CM1	7.9	3.3	7.1
pPLA CM3	9.4	14.7	7.7
pPLA CM5	10.5	24.7	8.1

Concerning the poly(acrylPEG) inclusions, on one side, the partial crosslinking remained, which was proved by the solubility (GPC), the unchanged amount of soluble PEG (^{1}H NMR), and the possibility of gel formation after recycling. On the other side, a slightly higher amount of poly(acrylPEG) was extracted with average molecular weights between 6800 g/mol and 590 g/mol (Figure 5.9). The peak of higher molecular weight belonged to the oligomers of acrylPEG, which was not grafted and could be extracted easily. The second peak was associated to PEG oligomers, which did not graft during the reactive extrusion or were unhinged from the poly(acrylPEG) inclusions. With increasing recycling number, the peak of single units became broader and more molecules with a molecular weight between 580 g/mol and 6800 g/mol were extracted. Since the partial crosslinking endure the recycling, the extracted poly(acrylPEG) was part of the inclusions before recycling and the amount of bonded poly(acrylPEG) in inclusions seem to be diminished. Furthermore, the observed porosity in AFM (Figure 5.6) could simplify the extraction of PEG units from the poly(acrylPEG) inclusions. As mentioned above, PLA with a high molecular weight could not be extracted from methanol, but low molecular weight PLA (like lactic acid monomer) seemed to be extracted from hot methanol. The peak with the higher average molecular weight increased with recycling and became broader. The extracted PLA seemed to be in this molecular weight range (around and below 6800 g/mol). From these results, two important parts of the degradation mechanisms of pPLA were concluded. First, poly(acrylPEG) phase size in the PLA matrix is diminished confirming AFM investigation, while the crosslinking

remains, and second, PLA is degraded to low molecular weight PLA by chain scission and can be extracted from hot methanol. These findings confirm the observed higher degradation for pPLA in rheology measurements and could be reasoned by a higher hydrophilicity induced by PEG-based polymers that was already described in the literature [157].

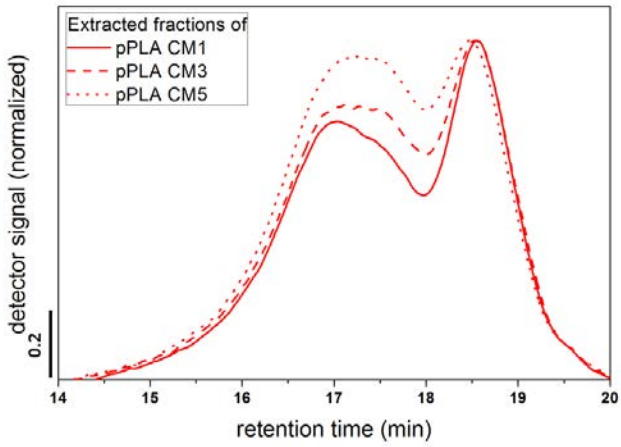

Figure 5.9 GPC of soluble fraction after Soxhlet extraction from methanol.

5.2.5 Degradation Scheme of Plasticized Polylactide

Despite the initial assumption, the PLA matrix in pPLA is differently affected by recycling than unmodified PLA matrix. Figure 5.10 illustrates the main degradation mechanisms in pPLA during multiple processing, affecting the matrix and the inclusions. The degradation of PLA matrix leads to shorter PLA chains, and at the same time its crystallinity increases. Furthermore, the initial spherical inclusions are deformed, damaged and fibrillated engendering a decrease of poly(acrylPEG) phase size and leading to a high porosity in the material. The initial core-shell structure is damaged as well and fibrillation explains the lower density of the inclusions. It is important to mention that the inclusion's grafting and crosslinking endure the recycling. For high recycling number, a crack formation occurs within the polymer matrix. Cracking may be due to the loss of physical interaction between the PLA matrix and the poly(acrylPEG) phases, and the important chain scission mechanisms of the matrix yielding to local shrinkage and then cracking. The damage of the inclusions engendering porosity and the polymer matrix cracking are believed to be responsible for the material brittleness observed during tensile and impact testing.

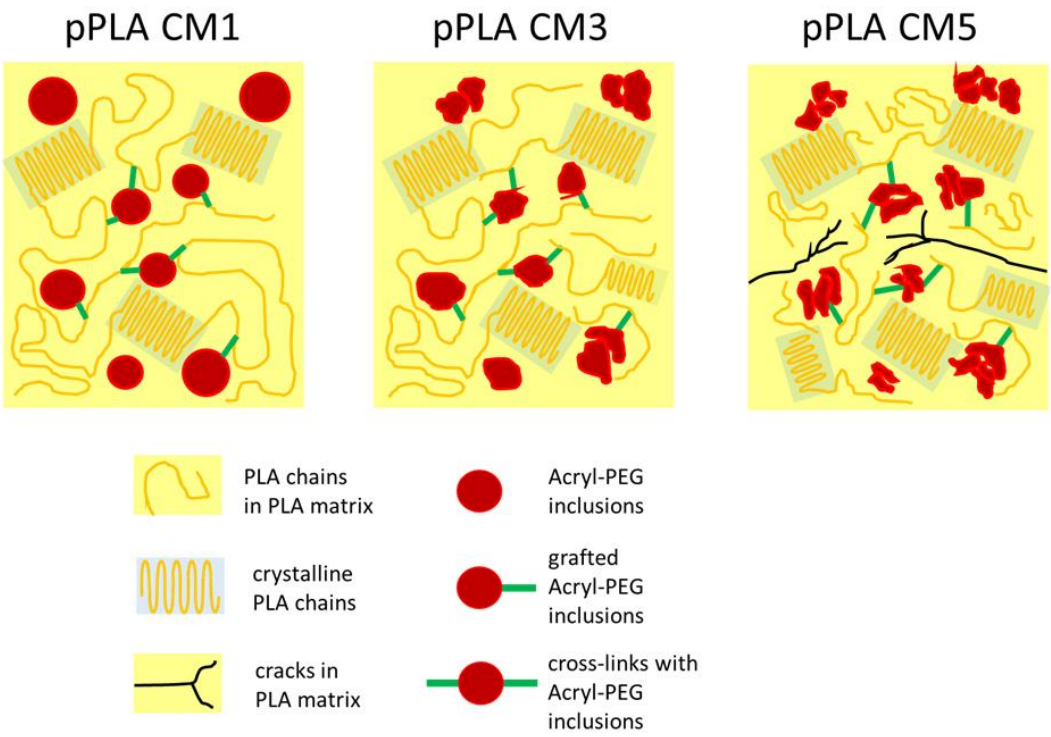

Figure 5.10 Schematic degradation scenario of pPLA after 1, 3, and 5 processing cycles.

The main difference between the recycling mechanisms of PLA and pPLA is the damage of the PLA matrix. In PLA, the matrix seems to be more stable and just simple chain scission occurs, which lowers the tensile resistance and toughness, while PLA remained ductile. In contrary, in pPLA, the PLA matrix underlies a stronger degradation in comparison with neat PLA. In particular, chain scission was accelerated and the molecular weight decreased strongly so that low molecular weight PLA was extracted from methanol in the case of pPLA. Indeed, the ^{1}H NMR analysis proved an increasing amount of PLA in the extracted fraction and GPC showed that the extracted fraction has molecular weights between 580 g/mol and 6800 g/mol, so that PLA degraded to short chains. This phenomenon could be reasoned by the different hydrophobicity of the materials. The more hydrophilic nature of pPLA compared to PLA could support the hydrolytically induced degradation of the PLA matrix [52,157].

5.3 Comparison between Different Thermomechanical Reprocessing Cycles

The thermomechanical reprocessing leads to degradation of the PLA matrix. The above studied reprocessing cycle contained two thermomechanical steps: extrusion and compression molding. In the literature, recycling was simulated by just one thermomechanical step: by multiple extrusion [87] or multiple injection molding [89]. Therefore, the thermomechanical reprocessing cycle with extrusion and compression molding was compared to two other reprocessing cycles. The first one contained up to five extrusion steps without any shaping step. The analyzed samples from this cycle were named E1, E3, and E5. The second reprocessing cycle contained instead of the compression molding step an injection molding shaping step. The samples were named with IM1, IM3, and IM5. The reprocessing procedures are schematically described in Figure 5.11.

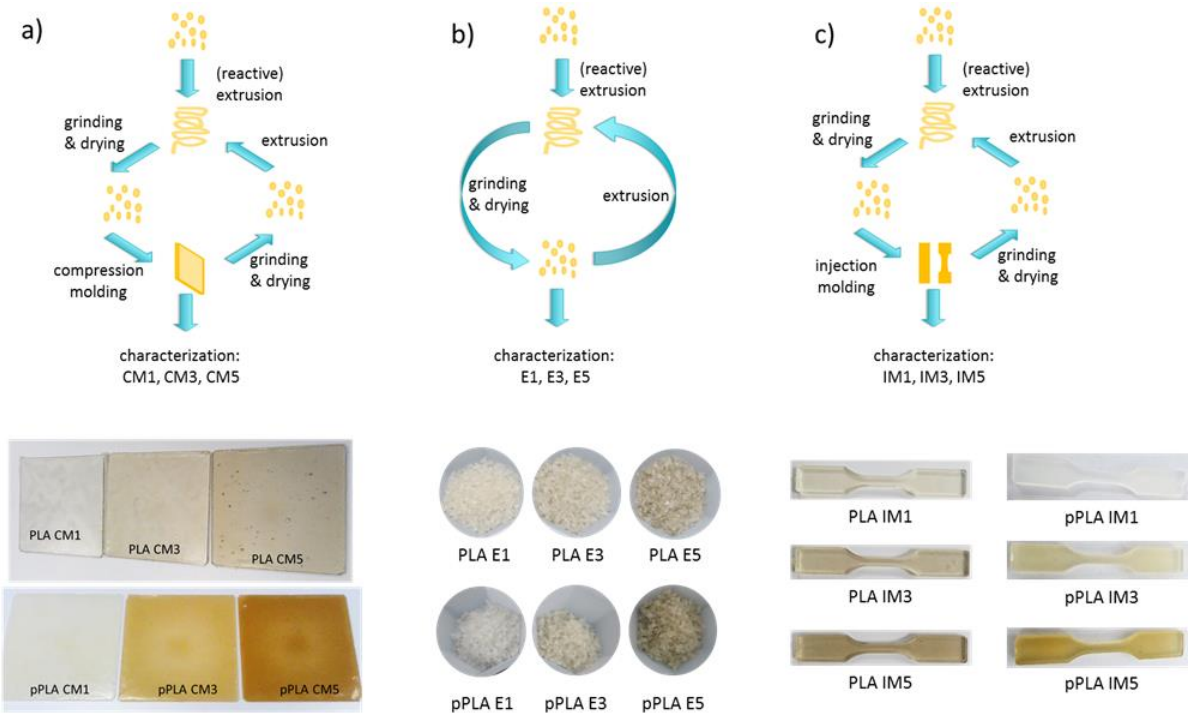

Figure 5.11 Schematic presentation of the three different reprocessing procedures: (a) extrusion and compression molding (CM), (b) just extrusion (E), and (c) extrusion and injection molding (IM).

Since the degradation of PLA was ruled by chain scission mechanisms, the molecular weight was compared for the three reprocessing cycles. Indeed, the molecular weight of the PLA fraction in pPLA was also determined, even if this gives just a partial information about the degradation. Since the filtration of the pPLA samples removes the crosslinked structures, the molecular weight of the PLA matrix in pPLA was much lower than in the non-crosslinked neat PLA. This assumption was confirmed

by the polydispersity measurements (Table 5.6). While PLA offered a polydispersity slightly higher than 2, pPLA's polydispersity was ever lower than 2. By GPC analysis, only the comparison of the neat PLA structures is possible and the crosslinked part is neglected due to the filtration. Nevertheless, the comparison between molecular weights after one, three, or five processing cycles exhibited differences. It has to be mentioned that the GPC analysis in this section was conducted on another equipment than the GPC analysis in section 5.2.4 Influence of the Reprocessing on the Molecular Structure. Therefore, the molecular weights of the PLA CM samples are different in absolute values, but the relative decrease of the molecular weight was similar. The cycle with just one thermomechanical step for each cycle (just extrusion E-cycle) shows the lowest degradation of the PLA matrix, even though a degradation is clearly visible for each step. Both cycles with an additional shaping step, CM-cycle and IM-cycle, obtained lower molecular weights compared to the E-cycle, especially for PLA. The reprocessing cycle with compression molding showed the highest degradation of the molecular weight for PLA as well as for pPLA. This could be reasoned by the procedure of compression molding. The material is exposed to temperatures higher than the melting temperature for more than 15 min, while the extrusion time was limited to 5 min and during the injection molding, the material was in the melted state for less than 5 min. It seems that the compression molding is the shaping technique with a high thermomechanical impact on the molecular weight and forces, therefore, the highest degradation.

Table 5.6 PLA Recycling of PLA-based samples: molecular weight of the main PLA peak.

Processing-cycle	extrusion + compression molding (CM)			extrusion (E)			extrusion + injection molding (IM)		
	$\bar{M}_n$ (kDa)	$\bar{M}_w$ (kDa)	Đ = $\bar{M}_w/\bar{M}_n$	$\bar{M}_n$ (kDa)	$\bar{M}_w$ (kDa)	Đ = $\bar{M}_w/\bar{M}_n$	$\bar{M}_n$ (kDa)	$\bar{M}_w$ (kDa)	Đ = $\bar{M}_w/\bar{M}_n$
PLA 1	73	161	2.2	90	181	2.0	70	147	2.1
PLA 3	60	126	2.1	81	175	2.1	70	140	2.0
PLA 5	46	97	2.1	76	172	2.3	58	119	2.1
pPLA 1	20	34	1.7	30	57	1.9	29	54	1.9
pPLA 3	11	18	1.6	29	55	1.9	29	55	1.9
pPLA 5	10	15	1.5	25	46	1.8	27	50	1.9

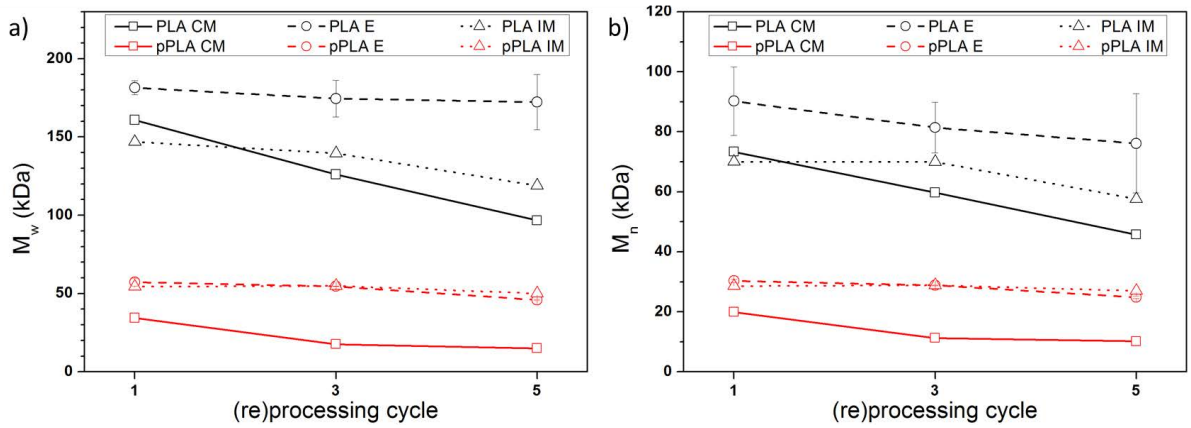

Figure 5.12 Average molecular weights for the main PLA peak in PLA and pPLA for the three different reprocessing cycles: CM, E, and IM.

The comparison of the three cycles proved, that the mode of reprocessing played an important role in the thermal degradation. While the extrusion had a weaker effect on the degradation, the compression molding showed the highest impact on the thermomechanical degradation. The period of time, when the material was exposed to temperatures above the melting temperature, seemed to have a high impact.

5.4 Isothermal Crystallization of Reprocessed Plasticized Polylactide

As already discussed for the different materials for the analysis of pPLA's structure in section 3.3, the crystallization kinetics are important for PLA-based materials and were, hence, studied for the reprocessed materials. Since the samples from the CM-cycle showed a very high degradation and obtained materials that were not reusable, the recycling combining extrusion and injection molding was chosen for this study. As already seen in the previous section 5.3 Comparison between Different Thermomechanical Reprocessing Cycles, the degradation in the reprocessing cycle was less strong regarding the molecular weight. The engineering stress-strain curves in Figure 5.13 support this observation. While for the CM-cycle completely brittle materials of pPLA were obtained after three and five reprocessing steps, the pPLA IM samples obtained a similar mechanical behavior even after five reprocessing steps. The engineering stress-strain curves for pPLA show a similar behavior for all three reprocessing steps. The flow stress of pPLA IM 1 was a little higher than for the other two pPLA samples (about 23 MPa compared to about 18 MPa). In contrast to the CM cycle, the elongation at break did not decrease and increased slightly (Table 5.7). Therefore, pPLA IM samples showed a ductile behavior even after reprocessing. These results support the assumption of less strong degradation in the IM-cycle compared to the CM-cycle. For PLA, the reprocessing caused just a few changes. The elongation at break value decreased slightly, while the other parameters stayed stable.

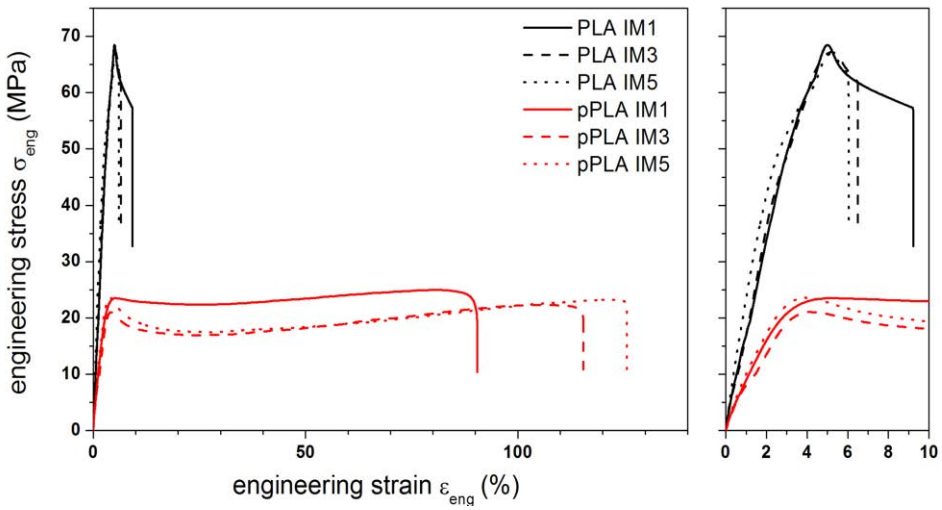

Figure 5.13 Engineering stress-strain curves of PLA and pPLA after 1,3, and 5 reprocessing cycles at 20°C.

Table 5.7 Mechanical parameters elongation at yield (ε_y), stress at yield (σ_y), elongation at break (ε_u), and stress at break (σ_u) with standard deviation obtained from tensile testing at 20°C.

	ε_y (%)	σ_y (MPa)	ε_u (%)	σ_u (MPa)
PLA IM1	5.2 ± 0.3	70.2 ± 1.5	7.4 ± 1.0	60.6 ± 3.1
PLA IM3	5.1 ± 0.1	67.9 ± 1.6	7.7 ± 1.7	59.9 ± 3.4
PLA IM5	5.4 ± 0.5	66.1 ± 0.7	6.3 ± 0.4	62.9 ± 2.0
pPLA IM1	5.3 ± 0.3	23.2 ± 0.8	91.1 ± 4.3	26.1 ± 1.0
pPLA IM3	4.0 ± 0.4	20.5 ± 1.8	114.3 ± 1.1	22.0 ± 0.2
pPLA IM5	3.9 ± 0.2	23.3 ± 1.4	127.0 ± 5.3	22.9 ± 0.2

As crystallization temperatures, values of 90°C for PLA and 55°C for pPLA were selected. At these temperatures, the crystallization occurred in a good time frame to analyze the impact of reprocessing: The crystallization was not too slow and not too fast so that a shift of the curve could be easily detected. The evolution of the crystallinity index as a function of the time was plotted in Figure 5.14, while the corresponding characteristics were reported in Table 5.8. In Figure 5.14 a, it is obvious that the reprocessing accelerated the crystallization for PLA. In particular, the crystallization half-time decreased from 143 min to 72 min and finally to 57 min after one, three, and five processing steps, respectively. While for PLA a clear shift to small crystallization times was observed, for pPLA the curves overlap for the most part (Figure 5.14 b) and the crystallization half-time increased slightly from 33 min to 42 min and 40 min for pPLA IM1, IM3, and IM5, respectively (Table 5.8). A good agreement of the Avrami calculated crystallization half-time with the graphically determined one was observed. For PLA, the Avrami parameter n increased slightly with reprocessing from 2.3 to a maximum of 2.8 in the case of PLA IM3. In the case of pPLA, reprocessing induced an increase of n from 1.1 for pPLA IM1 to 1.8 for pPLA IM5. The Avrami parameter n indicates a disk-like geometry for PLA crystal growth and a rod-like geometry for pPLA crystal growth. Nevertheless, for the two cases, reprocessing tended to increase the homogeneity of crystal growing through the increase of n. It has to be noted that no clear crystallinity index evolution with reprocessing was found for PLA and pPLA.

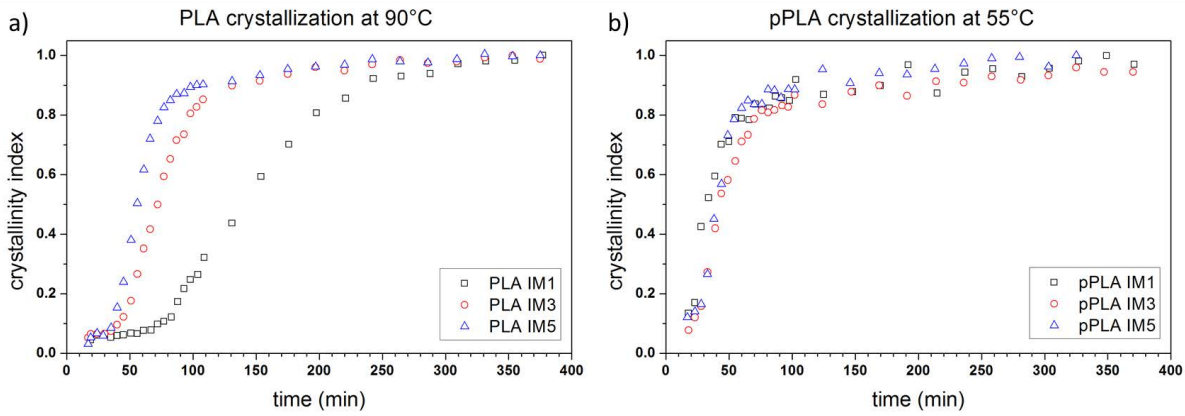

Figure 5.14 Evolution of crystallinity index as a function of time during isothermal crystallization testing a) at 90°C for PLA and b) 55°C for pPLA after 1, 3, and 5 processing cycles.

Table 5.8 Crystallization data extracted from experimental curves and Avrami modelling for PLA crystallized at 90°C and pPLA crystallized at 55°C after 1, 3, and 5 processing cycles.

			Avrami parameters		
	X_c (%)	$t_{1/2}$ (min)	n	k (min^{-n})	$t_{1/2}$ (min)
PLA IM1 T90	25.3	143	2.3	5.9 E-07	147
PLA IM3 T90	19.8	72	2.8	4.2 E-06	72
PLA IM5 T90	24.1	57	2.6	1.5 E-05	58
pPLA IM1 T90	15.5	33	1.1	1.7 E-02	32
pPLA IM3 T90	19.2	42	1.5	2.1 E-03	46
pPLA IM5 T90	16.6	40	1.8	8.3 E-04	41

The different degradation mechanisms in PLA and pPLA were already discussed previously (5.2 Thermomechanical Degradation of Plasticized Polylactide After Reprocessing), but the different thermomechanical steps induce a different impact on the degradation during the reprocessing (5.3 Comparison between Different Thermomechanical Reprocessing Cycles). It was shown that the injection molding step engenders less degradation than compression-molding, which is maybe due to the reduced time of exposure to heating of the materials. The less strong degradation was supported by the mechanical parameters of pPLA IM samples. Nevertheless, it is important to identify the degradation mechanisms in pPLA to understand the different kinetics for isothermal crystallization.

First, the analysis of the molecular weight (by GPC) was compared to the viscosity measurements from rheology. The GPC results give just an idea about the degradation in pPLA since just the soluble part of the PLA matrix can be analyzed. In addition, the complex viscosity can help to identify the degradation mechanisms. The evolution of the complex viscosity η as a function of shear rate $\dot{\gamma}$ was

represented in Figure 5.15 and the values of viscosity at zero shear rate η_o (determined by the Carreau-Yasuda model) are compared in Table 5.9 to the molecular weights of the PLA fraction of the materials. All materials exhibited a non-Newtonian behavior characterized by a Newtonian plateau at low shear rate and a shear thinning at high shear rate. When increasing the number of reprocessing, η_o decreased from 4521.9 Pa for PLA IM1 to 1213.6 Pa for PLA IM5 and from 4025.4 Pa for pPLA IM1 to 1206.1 Pa for pPLA IM5. This finding suggests a degradation of PLA and pPLA during recycling with respect to the molecular weight. These results were just partially supported by the GPC analysis. For PLA, the molecular weight decreased slightly to the third processing step and strongly to the fifth. In the case of pPLA, the molecular weight remained quite stable with a small decrease to the fifth processing step, but it was in all cases much lower than for PLA (about one-third for the materials after processing). These results explain the crystallization kinetics just partially. On one hand, for PLA the decreased molecular weight and the decreased viscosity explain the reduced crystallization half-time. On the other hand, for pPLA, where a decrease in the viscosity and a slightly stable molecular weight of soluble PLA fraction was observed with reprocessing, the crystallization half-time remained stable or increased slightly. Since the thermal properties were also impacted by the recycling, the samples were analyzed by DSC.

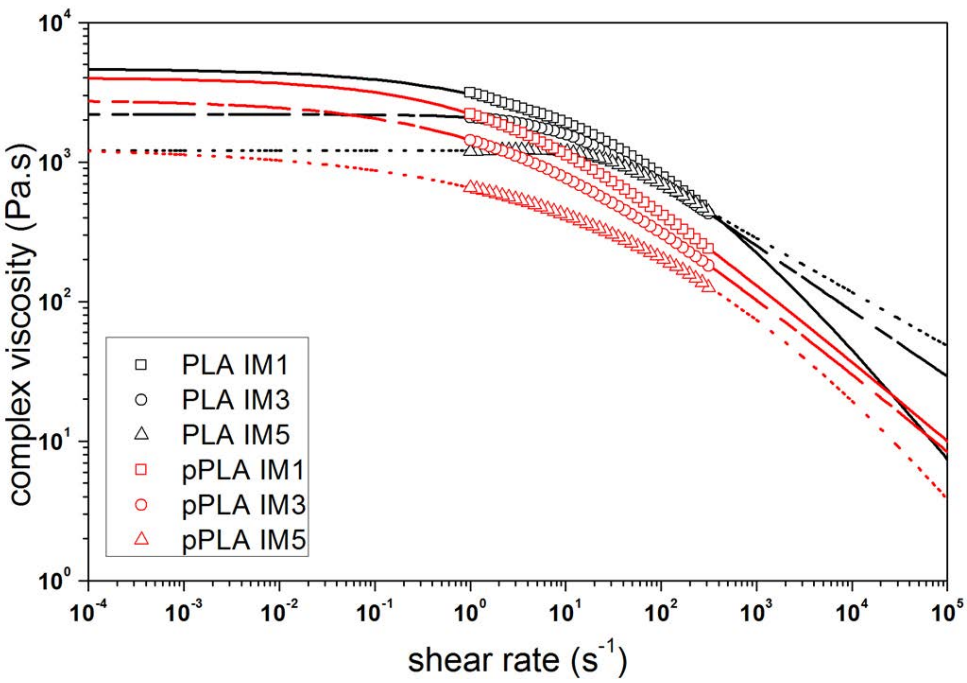

Figure 5.15 Experimental (dots) and Carreau-Yasuada theoretical (lines) plots of the complex viscosity vs. the shear rate in the case of PLA and pPLA.

Table 5.9 Molecular weights determined by GPC and zero shear viscosity by rheology for PLA and pPLA of the IM-cycle after 1,3, and 5 processing steps.

	GPC			rheology
	$\bar{M}_n$ (kDa)	$\bar{M}_w$ (kDa)	Đ = $\bar{M}_w/\bar{M}_n$	η_0 (Pa s)
PLA IM1	70	147	2.1	4521.9
PLA IM3	70	140	2.0	2191.5
PLA IM5	58	119	2.1	1213.6
pPLA IM1	29	54	1.9	4025.4
pPLA IM3	29	55	1.9	3062.9
pPLA IM5	27	50	1.9	1206.1

The mechanism of simple random chain scission for PLA was supported by the DSC analysis (Figure 5.16 and Table 5.10). While the glass transition temperature and the melting temperature remained nearly constant during the reprocessing, the cold crystallization enthalpy increased with ongoing reprocessing. Different as in reprocessing cycle with the compression molding step, the cold crystallization temperature decreased less, as well as the cold crystallization enthalpies, were lower for the IM-cycle (Table 5.2). These results were in good accordance with the less reduced molecular weight in the IM-cycle. Nevertheless, in all cases, PLA was nearly amorphous (X_c < 3%). The DSC results support the previous assumption that the decrease of the molecular weight leads to a faster crystallization.

The pPLA samples of the IM-cycle showed a slightly different behavior than the samples of the CM-cycle. For any of the pPLA IM samples, a glass transition was observed and no cold crystallization occurred. For all samples, a double melting peak was observed, which was due to the grafting of the plasticizer that caused crystals having a different extent of perfection [107]. During the reprocessing, the peak located at the lower temperature moved to lower temperatures whereas the peak at higher temperature moved to higher temperatures. This leads to the hypothesis, that with ongoing reprocessing, the crystalline structure of pPLA changed and the number of crystals with a higher extent of perfection increased. The higher perfection of crystals was also assumed by the increase of the Avrami parameter n, but the DSC results give no information to explain the crystallization half-times of pPLA.

Table 5.10 DSC results (from the second heating stage) for the samples of PLA and pPLA from the IM-cycle with standard deviation.

	Tg (°C)	Tcc (°C)	Tm (°C)	ΔH_{cc} (J/g)	ΔH_m (J/g)	X_c (%)
PLA IM1	60.7 ± 0.1	127.9 ± 0.1	154.5 ± 0.1	1.7 ± 0.1	2.6 ± 0.5	1.0 ± 0.6
PLA IM3	60.8 ± 0.1	128.0 ± 0.1	155.1 ± 0.1	16.0 ± 0.7	18.4 ± 0.4	2.7 ± 0.2
PLA IM5	60.1 ± 0.6	124.6 ± 0.2	153.9 ± 0.8	26.4 ± 1.5	28.4 ± 0.8	2.1 ± 0.7
pPLA IM1	-	-	146.7 ± 1.2 & 151.4 ± 0.4	-	23.3 ± 0.1	27.4 ± 0.2
pPLA IM3	-	-	145.6 ± 1.1 & 152.2 ± 0.6	-	22.7 ± 0.1	26.7 ± 0.1
pPLA IM5	-	-	144.5 ± 0.1 & 152.6 ± 0.2	-	24.6 ± 1.0	29.0 ± 1.2

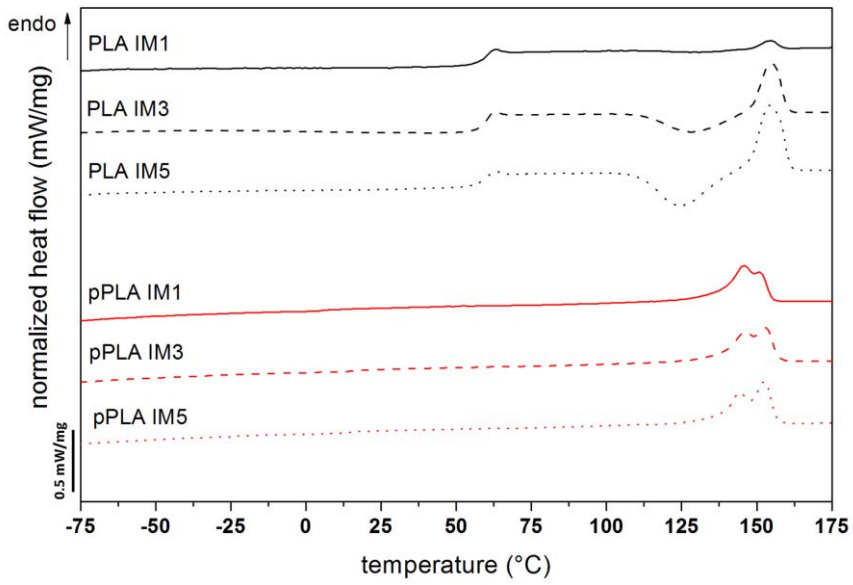

Figure 5.16 DSC curves (from the second heating stage) of PLA and pPLA from the IM-cycle after 1,3, and 5 reprocessing steps.

Since the analysis of the molecular weight and the thermal properties give a very limited view on the pPLA material, the material was further analyzed to understand the impact on the crystallization mechanisms. The amount of plasticizer was determined by proton NMR and the amount of free plasticizer was calculated after Soxhlet extraction. Proton NMR proved, that the amount of plasticizer

did not change during the reprocessing (Table 5.11). It is worth to mention, that the reprocessed samples show a smaller amount (about 14 wt% instead of the added 20 wt%). This was due to the fact that pPLA was not completely soluble in the solvent, and the grafted part could just partially be detected. Since the amount of detected PEG did not increase, it was assumed that the crosslinked insoluble part remains after the reprocessing. The Soxhlet extraction supports this assumption because the extracted amount just slightly increased (Table 5.11).

Table 5.11 Amount of PEG in the pPLA samples from the IM-cycle (by proton NMR) and non-grafted amount of PEG (by Soxhlet).

	PEG content from NMR (wt%)	non-grafted amount of PEG from Soxhlet (wt%)
pPLA IM1	14.5	5.8 ± 0.1
pPLA IM3	14.3	6.4 ± 0.6
pPLA IM5	14.2	6.4 ± 0.1

The results of the proton NMR and the Soxhlet extraction show that the PEG amount in the samples remains similar with recycling. In addition, the molecular weight of the soluble PLA amount was not changed (GPC). These results could give a consideration about the isothermal crystallization kinetics of pPLA. The isothermal crystallization of pPLA is already quite fast at 55°C and, in addition, the molecular weight of the soluble part of PLA (GPC) and the amount of grafted and free plasticizer seemed to be unchanged. Therefore, it was assumed that the isothermal crystallization kinetics, as well as the mechanical performance, were less impacted by the reprocessing.

Indeed, these results give an idea about the isothermal crystallization kinetics. The isothermal crystallization kinetics of pPLA seem to depend more on the PLA matrix. For PLA, where a decrease of the molecular weight of the matrix was observed, the crystallization half-time decreased and for pPLA, where the molecular weight of the PLA matrix remained, the crystallization half-time remains stable. However, a strong decrease in the viscosity indicating a degradation of pPLA was observed, but not represented in the isothermal crystallization time or in the mechanical performance. In conclusion, the PLA matrix seems to have a higher impact on the crystallization kinetics, but a more detailed study on the crystallization behavior is missing with respect to the degradation mechanisms in pPLA, which are different depending on the thermomechanical reprocessing steps.

5.5 Conclusion

Thermomechanical reprocessing of both PLA and pPLA materials has been studied to understand and compare the resulting degradation mechanisms. The pPLA consisted of a plasticized PLA matrix with dispersed inclusions of poly(acrylPEG) that were partially grafted onto the PLA backbone, yielding a partial crosslinking of the PLA matrix. It was shown that the degradation during thermomechanical reprocessing strongly depends on the type of the thermomechanical step. In the first part, compression molding was used as a thermomechanical reprocessing step and the pPLA's mechanical properties worsened strongly. For this study, both PLA and pPLA materials were characterized at the macroscopic, microstructural, and microstructure scales after 1, 3, and 5 processing cycles.

For PLA, where neither grafting nor crosslinking was present, the main degradation mechanisms were identified as a simple random chain scission. This mechanism was proved by a decrease of the molecular weight to 69% and 53% after the third and fifth processing respectively. The increased ability of cold crystallization was also attributed to the lower molecular weight due to a higher chain mobility, but PLA materials remained amorphous. The analysis of chemical structure indicated no additional chemical function (end groups of PLA) compared to the non-recycled PLA. In conclusion, for PLA only a random chain scission mechanism was active during the reprocessing and was believed to be responsible for the decrease in mechanical performance.

In pPLA, the clarification of the degradation mechanisms needed a different look, focusing on all components that interact with each other. On one hand, the mechanical properties got worsened from the first processing to the third processing. The material became brittle with a markedly loss of tensile ductility and drop of the toughness. On the other hand, the viscoelastic properties such as storage modulus and tensile modulus of pPLA were unaffected by the reprocessing. The morphology of pPLA changed strongly with reprocessing. The inclusions of poly(acrylPEG) were damaged by deformation of their shape, reducing their size, and the occurrence of porosity and fibrillation. In accordance with the loss of mechanical properties, cracks were observed in the material after the fifth processing, but the origin of these cracks could not be clarified completely. It was assumed that the decrease of inclusion size in combination with the increasing porosity reduces the physical interaction between the matrix and the inclusions resulting in cracks. A second possibility is that the chain scission mechanism induces a chain shrinking resulting in cracks. Like for PLA, no change of the chemical end-functions of the polymer chains was observed but the strong decrease in the viscosity leads to the assumption that in pPLA the same chain scission mechanisms occur as in PLA, even if the thermal properties showed differences between both materials. For pPLA, the crystallinity increased with recycling, but no cold crystallization was observed. It was assumed that the crosslinking and grafting endures the reprocessing. Also, pPLA was not filterable for after dissolving for the GPC after

reprocessing, so that crosslinking was still present. The chain scission number calculated from the rheological measurements was double for pPLA compared to PLA, which leads to the assumption that the PLA matrix in pPLA underlies stronger degradation than in PLA. Soxhlet extraction allowed the separate analysis of the PLA matrix and the plasticizer phase. Hereby, it was shown that the PLA matrix is stronger degraded in pPLA since PLA was partially extracted with the plasticizer phase. The slight increasing amount of plasticizer in the extracted fraction indicated a partial destruction of the inclusions and the increasing amount of PLA in the extracted fraction indicated the degradation of PLA polymer chains to short PLA oligomer chains. The chain scission mechanism seemed to be in balance with the increasing crystallization since the viscoplastic properties of pPLA were not influenced by recycling. In contrast, the cracks in the matrix and the damage of the inclusions were believed to be responsible for the decrease in the elasto- and viscoplastic properties and therefore the high brittleness of the material after reprocessing. In summary, this recycling methodology was not suitable for pPLA and led to a very brittle material. The degradation resulted in a stronger decrease of pPLA's mechanical properties than for PLA.

In the second part, the impact of three different thermomechanical procedures for the reprocessing was briefly studied: (i) extrusion and compression molding (CM), (ii) extrusion (E), and (iii) extrusion and injection molding (IM). The different reprocessing methods obtained different levels of degradation. It was shown that the compression molding step as used for the first part of this chapter has the highest impact on the decrease of the molecular weight and the other two procedures had a less strong impact. The higher degradation was related to the more detrimental step of compression molding, where the material is in the melted state for a longer time than for all other thermomechanical steps.

The isothermal crystallization study was conducted on the materials from the IM-cycle and proved again the different degradation mechanisms in PLA and pPLA. Even though the chain scission mechanism for PLA was less strong as for the other study, the crystallization half-time decreased to the half after three processing cycles and to one-third after the fifth reprocessing. This indicated a high correlation between the isothermal crystallization ability with the molecular weight of PLA. In contrast, pPLA's crystallization half-time did not decrease with reprocessing and rather increased slightly. It was shown that the free, non-crosslinked part of PLA was not changed during the reprocessing. At the same time, it was assumed that when the grafting and crosslinking endures the stronger reprocessing conditions (with compression molding as a thermomechanical step) then it also endures this reprocessing. Nevertheless, the rheological results proved a degradation of pPLA after each processing cycle. On one hand, no cold crystallization was observed which was related to the grafting and crosslinking that decreased the chain motions. On the other hand, plasticization

decreased the glass transition temperature and increased, therefore, the chain mobility. So in pPLA, two contradictory effects are present. The degradation mechanisms in pPLA seem to be different from the ones in PLA and the exact impact on the isothermal crystallization behavior needs further analysis.

The different studies on the degradation mechanisms of pPLA highlighted the differences compared to PLA and the importance of the type of thermomechanical reprocessing steps. Therefore, pPLA can just be used in applications where a limited number of reprocessing steps is considered or the thermomechanical reprocessing step is not as detrimental as the compression molding. Nevertheless, the grafting/crosslinking endured the reprocessing procedures and could, therefore, be suitable for plasticization of other materials, which are more suitable for thermomechanical reprocessing.

6 General Conclusions and Perspectives

As mentioned along with the manuscript, the development of novel bioplastics requires an understanding of their structure formation and thermomechanical formations to boost their possibilities to replace common plastic materials. Polylactide (PLA) is one of these forward-looking bioplastics but cannot be used in many applications without modification due to its brittle behavior at room temperature. The first point, which was addressed by this thesis, was the multi-scale structure characterization of a plasticized PLA by reactive extrusion. This method was already described to create a PLA-based material with a suitable flexibility-stiffness balance. The reactive extrusion of PLA with acrylPEG as a plasticizer and L101 as a free radical initiator forms a PLA-based material with inclusions of the polymerized plasticizer that are partially grafted onto the PLA matrix. In addition, the radical recombination reactions induce a slight crosslinking. The analysis of the inclusions, which consist in polymerized acrylPEG, showed the formation of core-shell structure inclusions with a poly(acrylPEG)-rich shell and a less poly(acrylPEG)-rich core. The scale up indicated that pPLA can be produced in a semi-continuous process suitable for application related processing, but the formation of the materials' structures differed, depending on the process. The radical reactions during this process were not controllable due to lack of possibility to quantify the grafting/crosslinking, but the structure formation was profitable for the mechanical performance of this material. In addition, it was shown, that the reactive plasticization increased the crystallization ability, but the final crystallinity index in isothermal crystallization was limited.

On one side, the plasticization effect of acrylPEG improved the ductility of the material and, on the other side, the grafting and crosslinking received partially the initial stiffness of PLA materials, which is lost by blending plasticization. Due to the reduced glass transition temperature, pPLA exhibited a tensile behavior similar to PLA at a temperature close to its glass transition temperature, but with different deformation mechanisms. In PLA, the deformation leads to the formation of crazes that develop to cracks and create a failure at a low elongation at break. In pPLA, on one side, the grafting and crosslinking avoid the formation of crazes and leads to the direct formation of cracks, but on the other side, the inclusions limited the growth of the cracks. During the deformation, the inclusions were deformed within the matrix and gained an ellipsoidal shape. No debonding was observed and the crosslinking and grafting was still present after deformation. Another point that underlined the complex structure of pPLA was the whitening. Whitening occurred in all samples but was nonpermanent in some cases. The whitening was related to two phenomena: First, the deformation of the inclusions inside the matrix and void formation inside the inclusions with a decrease of density and second, the formation of shear bands. In the case of whitening disappearance with time, it was assumed that the material offered a damage recovery, but this could not be proved and was not

reproducible. Since it was impossible to control the exact structure of pPLA due to the radical reactions, this different behavior was associated with the heterogeneous formation of inclusions during the processing.

In addition to the mechanical performance, the degradation mechanisms during recycling were considered to be essential for bioplastics. The thermomechanical reprocessing, simulating a recycling process, indicates the importance of the thermomechanical steps for the degradation mechanisms. In PLA the main degradation mechanism is chain scission. In pPLA, chain scission occurred as well, but the PLA matrix was stronger damaged and cracking occurred. In addition, the initial inclusion structure was damaged, but the grafting/crosslinking endured the thermomechanical reprocessing. The longer the material was exposed to temperatures above the melting temperature, the more detrimental was the degradation. The samples of pPLA, which were reprocessed by compression molding, lost completely the mechanical performance and were not reusable. In contrast, the reprocessing with injection molding was less harmful and, furthermore, improved the elongation at break in the tested range. This increase of mechanical properties could be related to a higher homogeneity after another processing step that overcame the disadvantages of degradation. A similar behavior was observed for the samples which were produced with the mini-extruder: A second processing step allowed the production of film samples and increased the homogeneity of the material. Despite the strong degradation in the first mentioned process, the grafting and crosslinking endured this thermomechanical reprocessing and just a stronger degradation of the PLA matrix was observed.

In conclusion, it was shown that the reactive extrusion of PLA with a reactive plasticizer and free radical initiator forms a material with improved mechanical performance and crystallization ability. The use of this process is suitable for industrial studies. Despite the formation of the structure was not controllable, the properties of the material could be adapted to the industrial needs and allow broadening the application range for bioplastics. The Figure below summarizes the main research goals, which were achieved in this thesis.

For further studies, it could be interesting to study the aging and biodegradation of the materials plasticized by reactive extrusion. The grafting of the plasticizer seems to be stable during deformation and reprocessing and this technique could help to improve the problems of plasticizer leaching also for other polymer plasticizer combinations. The main problem of the process is the controllability of the reactions. It was not completely clarified if the crosslinking along with the grafting had also a positive impact on the mechanical performance and the resistance of the material to plasticizer leaching during deformation and reprocessing. A material with a higher or lower degree of crosslinking

could help to identify the role of crosslinking, but only if the crosslinking could be quantified, what was not possible in the present studies.

It was shown that the recycling procedure has a high impact on the materials after reprocessing. Therefore, additional studies of the reprocessing with the mini-extruder could help to identify the degradation mechanisms in an industrial simulated processes to make PLA-based materials more suitable for applications.

As the last perspective, this process of durable plasticization by reactive extrusion could be conducted with natural plasticizers. The usefulness of natural plasticizers for PLA was already studied but due to their often small size, the leaching is often detrimental to the properties and this problem could be solved by reactive grafting of these plasticizers.

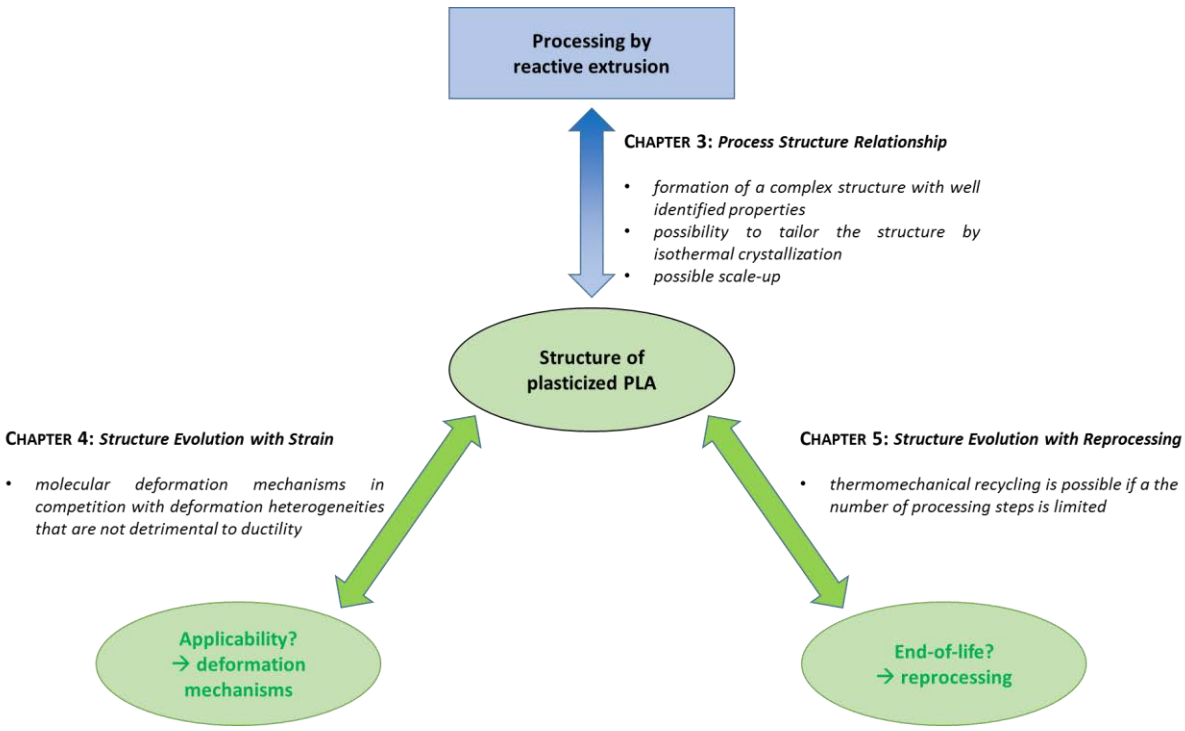

7 List of References

[1] Oxford University Press. Definition of “plastic.” Oxford Dictionary (British & World English) n.d. https://en.oxforddictionaries.com/definition/plastic.

[2] "PC/BPA-group P. Bisphenol A - European Information Center on Bisphenol A n.d. http://www.bisphenol-a-europe.org/en_GB/safety (accessed May 11, 2017).

[3] British Plastics Federation. BPF - Oil Consumption 2017. http://www.bpf.co.uk/press/oil_consumption.aspx (accessed February 13, 2017).

[4] Jamshidian M, Tehrany EA, Imran M, Jacquot M, Desobry S. Poly-Lactic Acid: Production, Applications, Nanocomposites, and Release Studies. Comprehensive Reviews in Food Science and Food Safety 2010;9:552–71. doi:10.1111/j.1541-4337.2010.00126.x.

[5] European Environment Agency (EEA). Municipal waste recycling rates in 32 European countries, 2001 and 2010 — European Environment Agency (EEA) n.d. http://www.eea.europa.eu/ (accessed February 15, 2017).

[6] Castro-Aguirre E, Iñiguez-Franco F, Samsudin H, Fang X, Auras R. Poly(lactic acid)-Mass production, processing, industrial applications, and end of life. Advanced Drug Delivery Reviews 2016;107:333–66. doi:10.1016/j.addr.2016.03.010.

[7] Lancaster M, Royal Society of Chemistry (Great Britain). Green chemistry: an introductory text. 2nd ed. Cambridge: Royal Society of Chemistry; 2010.

[8] European Bioplastics e.V. european bioplastics - Publications - 2016. http://www.european-bioplastics.org/news/publications/ (accessed February 15, 2017).

[9] Jawaid M, Salit MS. Green Biocomposites - Design and Applications. 1st ed. Springer International Publishing; 2017. doi:10.1007/978-3-319-49382-4.

[10] Gotro J. Polymer Innovation Blog - Practical tips and advices for polymer, innovation and product developement professionals 2012. https://polymerinnovationblog.com/poly-lactic-acid-pla-is-gaining-traction-in-the-market/ (accessed July 21, 2017).

[11] Carothers WH, Hill JW. Studies of polymerization and ring formation. XII. Linear superpolyesters. Journal of the American Chemical Society 1932;54:1559–66. doi:10.1021/ja01343a051.

[12] Hartmann MH. High MolecularWeight Polylactic Acid Polymers. In: Kaplan DL, editor. Biopolymers from Renewable Resources. 1st ed., Springer-Verlag Berlin Heidelberg; 1998, p. 367–411.

[13] Lasprilla AJR, Martinez G a R, Lunelli BH, Jardini AL, Filho RM. Poly-lactic acid synthesis for application in biomedical devices - A review. Biotechnology Advances 2012;30:321–8. doi:10.1016/j.biotechadv.2011.06.019.

[14] Raquez J-M, Narayan R, Dubois P. Recent Advances in Reactive Extrusion Processing of Biodegradable Polymer-Based Compositions. Macromolecular Materials and Engineering 2008;293:447–70. doi:10.1002/mame.200700395.

[15] Pillin I, Montrelay N, Grohens Y. Thermo-mechanical characterization of plasticized PLA: Is the miscibility the only significant factor? Polymer 2006;47:4676–82. doi:10.1016/j.polymer.2006.04.013.

[16] Auras R, Harte B, Selke S. An overview of polylactides as packaging materials. Macromolecular

Bioscience 2004;4:835–64. doi:10.1002/mabi.200400043.

[17] Yates MR, Barlow CY. Life cycle assessments of biodegradable, commercial biopolymers - A critical review. Resources, Conservation and Recycling 2013;78:54–66. doi:10.1016/j.resconrec.2013.06.010 Review.

[18] Ebewele RO. Polymer Science and Technology. CRC Press; 2000.

[19] Vollmert B, Immergut EH. Polymer Chemistry. Heidelberg: Springer Berlin Heidelberg; 2012.

[20] Tieke B. Makromolekulare Chemie: Eine Einführung. 2nd ed. Weinheim: Wiley-VCH; 2005.

[21] Stoclet G, Seguela R, Vanmansart C, Rochas C, Lefebvre J-M. WAXS study of the structural reorganization of semi-crystalline polylactide under tensile drawing. Polymer 2012;53:519–28. doi:10.1016/j.polymer.2011.11.063.

[22] Niaounakis M. Biopolymers reuse, recycling, and disposal. Oxford, UK; Waltham, MA: William Andrew; 2013.

[23] Mama Mundo Inc. Life Without Plastic 2012. https://www.lifewithoutplastic.com/store/common_plastics_no_1_to_no_7#.WOsXu3q2DeQ (accessed April 10, 2017).

[24] Siracusa V. Food packaging permeability behaviour: A report. International Journal of Polymer Science 2012;2012. doi:10.1155/2012/302029.

[25] Ishihara N. Syntheses and properties of syndiotactic polystyrene. Macromolecular Symposia 1995;89:553–62. doi:10.1002/masy.19950890151.

[26] Bartolome L, Imran M, Cho BG, Al-Masry W a., Kim DH. Recent Developments in the Chemical Recycling of PET. In: Achilias DD, editor. Materials Recycling - Trends and Perspectives, INTECH; 2012, p. 65–84. doi:10.5772/33800.

[27] Kim KH, Cho JC, Kim WS. Highly pure polystyrene, method for preparing the same and disposable food container using the same. WO Patent App. PCT/KR1999/000,536, 2000.

[28] Carrasco F, Pagès P, Gémez-Pérez J, Santana OO, Maspoch ML. Processing of poly(lactic acid): Characterization of chemical structure, thermal stability and mechanical properties. Polymer Degradation and Stability 2010;95:116–25. doi:10.1016/j.polymdegradstab.2009.11.045.

[29] Joziasse CAP, Veenstra H, Grijpma DW, Pennings AJ. On the chain stiffness of poly(lactide)s. Macromolecular Chemistry and Physics 1996;197:2219–29. doi:10.1002/macp.1996.021970713.

[30] Grijpma DW, Penning JP, Pennings a. J. Chain entanglement, mechanical properties and drawability of poly(lactide). Colloid & Polymer Science 1994;272:1068–81. doi:10.1007/BF00652375.

[31] Wu S. Predicting chain conformation and entanglement of polymers from chemical structure. Polymer Engineering & Science 1992;32:823–30. doi:10.1002/pen.760321209.

[32] Garlotta D. A Literature Review of Poly (Lactic Acid). Journal of Polymers and the Environment 2002;9:63–84.

[33] Lim L-T, Auras R, Rubino M. Processing technologies for poly(lactic acid). Progress in Polymer Science 2008;33:820–52. doi:10.1016/j.progpolymsci.2008.05.004.

[34] Hassouna F, Raquez J-M, Addiego F, Toniazzo V, Dubois P, Ruch D. New development on plasticized poly(lactide): Chemical grafting of citrate on PLA by reactive extrusion. European

Polymer Journal 2012;48:404–15. doi:10.1016/j.eurpolymj.2011.12.001.

[35] Grijpma DW, Pennings AJ. (Co)polymers of L-lactide, 2. Mechanical properties. Macromolecular Chemistry and Physics 1994;195:1649–63. doi:10.1002/macp.1994.021950516.

[36] Martin O, Avérous L. Poly (lactic acid): plasticization and properties of biodegradable multiphase systems. Polymer 2001;42:6209–19. doi:10.1016/S0032-3861(01)00086-6.

[37] Hu Y, Hu YS, Topolkaraev V, Hiltner A, Baer E. Crystallization and phase separation in blends of high stereoregular poly(lactide) with poly(ethylene glycol). Polymer 2003;44:5681–9. doi:10.1016/S0032-3861(03)00609-8.

[38] Wang L, Jing X, Cheng H, Hu X, Yang L, Huang Y. Blends of Linear and Long-Chain Branched Poly(L-lactide)s with High Melt Strength and Fast Crystallization Rate. Industrial & Engineering Chemistry Research 2012;51:10088–99. doi:10.1021/ie300526u.

[39] Simões CL, Viana JC, Cunha AM. Mechanical properties of poly(ε-caprolactone) and poly(lactic acid) blends. Journal of Applied Polymer Science 2009;112:345–52. doi:10.1002/app.29425.

[40] Liu H, Zhang J. Research progress in toughening modification of poly(lactic acid). Journal of Polymer Science Part B: Polymer Physics 2011;49:1051–83. doi:10.1002/polb.22283.

[41] Kfoury G, Hassouna F, Raquez J-M, Toniazzo V, Ruch D, Dubois P. Tunable and Durable Toughening of Polylactide Materials Via Reactive Extrusion. Macromolecular Materials and Engineering 2014;299:583–95. doi:10.1002/mame.201300265.

[42] Ljungberg N, Wesslén B. Tributyl citrate oligomers as plasticizers for poly(lactic acid): thermo-mechanical film properties and aging. Polymer 2003;44:7679–88. doi:10.1016/j.polymer.2003.09.055.

[43] Ambrosio-Martín J, Fabra MJ, Lopez-Rubio a., Lagaron JM. An effect of lactic acid oligomers on the barrier properties of polylactide. Journal of Materials Science 2014;49:2975–86. doi:10.1007/s10853-013-7929-x.

[44] Piorkowska E, Kulinski Z, Galeski A, Masirek R. Plasticization of semicrystalline poly(l-lactide) with poly(propylene glycol). Polymer 2006;47:7178–88. doi:10.1016/j.polymer.2006.03.115.

[45] Baiardo M, Frisoni G, Scandola M, Rimelen M, Lips D, Ruffieux K, et al. Thermal and Mechanical Properties of Plasticized Poly(L-lactic acid). J Appl Polym Sci 2003;90:1731–8. doi:10.1002/app.12549.

[46] Jacobsen S, Fritz HG. Plasticizing polylactide - The effect of different plasticizers on the mechanical properties. Polymer Engineering & Science 1999;39:1303–10. doi:10.1002/pen.11517.

[47] Carlson D, Nie L, Narayan R, Dubois P. Maleation of polylactide (PLA) by reactive extrusion. Journal Of Applied Polymer Science 1999;72:477–85. doi:papers://590F92D9-0B76-4B88-8729-9AF064BE5AC8/Paper/p2628.

[48] Pan J, Wang Y, Qin S, Zhang B, Luo Y. Grafting reaction of poly(D,L)lactic acid with maleic anhydride and hexanediamine to introduce more reactive groups in its bulk. Journal of Biomedical Materials Research - Part B Applied Biomaterials 2005;74:476–80. doi:10.1002/jbm.b.30208.

[49] Hassouna F, Raquez JM, Addiego F, Dubois P, Toniazzo V, Ruch D. New approach on the development of plasticized polylactide (PLA): Grafting of poly(ethylene glycol) (PEG) via reactive extrusion. European Polymer Journal 2011;47:2134–44. doi:10.1016/j.eurpolymj.2011.08.001.

[50] Kfoury G, Raquez J-M, Hassouna F, Leclère P, Toniazzo V, Ruch D, et al. Toughening of Poly(lactide) Using Polyethylene Glycol Methyl Ether Acrylate: Reactive Versus Physical Blending. Polymer Engineering & Science 2015;55:1408–19. doi:10.1002/pen.

[51] Choi K, Choi M-C, Han D-H, Park T-S, Ha C-S. Plasticization of poly(lactic acid) (PLA) through chemical grafting of poly(ethylene glycol) (PEG) via in situ reactive blending. European Polymer Journal 2013;49:2356–64. doi:10.1016/j.eurpolymj.2013.05.027.

[52] Choi K-M, Lim S-W, Choi M-C, Kim Y-M, Han D-H, Ha C-S. Thermal and mechanical properties of poly(lactic acid) modified by poly(ethylene glycol) acrylate through reactive blending. Polymer Bulletin 2014;71:3305–21. doi:10.1007/s00289-014-1251-x.

[53] Zhang J, Tashiro K, Tsuji H, Domb AJ. Disorder-to-Order Phase Transition and Multiple Melting Behavior of Poly (L-lactide) Investigated by Simultaneous Measurements of WAXD and DSC. Macromolecules 2008;41:1352–7. doi:10.1021/ma0706071.

[54] Zhang J, Duan Y, Domb AJ, Ozaki Y. PLLA Mesophase and Its Phase Transition Behavior in the PLLA−PEG−PLLA Copolymer As Revealed by Infrared Spectroscopy. Macromolecules 2010;43:4240–6. doi:10.1021/ma100301h.

[55] Stoclet G, Lefebvre JM, Séguéla R, Vanmansart C. In-situ SAXS study of the plastic deformation behavior of polylactide upon cold-drawing. Polymer 2014;55:1817–28. doi:10.1016/j.polymer.2014.02.010.

[56] Kulinski Z, Piorkowska E. Crystallization, structure and properties of plasticized poly(l-lactide). Polymer 2005;46:10290–300. doi:10.1016/j.polymer.2005.07.101.

[57] Müller AJ, Àvila M, Saenz G, Salazar J. Crystallization of PLA-based materials. In: Jiménez A, Peltzer M, Ruseckaiter R, editors. Poly(lactic acid) Science and Technology: Processing, Properties, Additives and Applications, The Royal Society of Chemistry; 2015.

[58] Saeidlou S, Huneault M a., Li H, Park CB. Poly(lactic acid) crystallization. Progress in Polymer Science 2012;37:1657–77. doi:10.1016/j.progpolymsci.2012.07.005.

[59] Lai WC, Liau WB, Lin TT. The effect of end groups of PEG on the crystallization behaviors of binary crystalline polymer blends PEG/PLLA. Polymer 2004;45:3073–80. doi:10.1016/j.polymer.2004.03.003.

[60] Li H, Huneault MA. Effect of nucleation and plasticization on the crystallization of poly(lactic acid). Polymer 2007;48:6855–66. doi:10.1016/j.polymer.2007.09.020.

[61] Urayama H, Moon S Il, Kimura Y. Microstructure and thermal properties of polylactides with different L- and D-unit sequences: Importance of the helical nature of the L-sequenced segments. Macromolecular Materials and Engineering 2003;288:137–43. doi:10.1002/mame.200390006.

[62] Avrami M. Kinetics of Phase Change. II - Transformation-Time Relations for Random Distribution of Nuclei. Journal of Chemical Physics 1940;8:212–24. doi:10.1063/1.1750631.

[63] Dhanvijay PU, Shertukde V V. Review: Crystallization of Biodegradable Polymers. Polymer-Plastics Technology and Engineering 2011;50:1289–304. doi:10.1080/03602559.2010.543744.

[64] Miyata T, Masuko T. Crystallization behaviour of poly (L-lactide). Polymer 1998;39:5515–21.

[65] Zhou WY, Duan B, Wang M, Cheung WL. Crytsallization Kinetics of Poly(L-lactide)Carbonated Hydroxyapatite Nanocomposite Microspheres. Journal of Applied Polymer Science 2009;113:4100–15. doi:10.1002/app.

[66] You J, Yu W, Zhou C. Accelerated Crystallization of Poly(lactic acid): Synergistic Effect of Poly(ethylene glycol), Dibenzylidene Sorbitol, and Long-Chain Branching. Industrial & Engineering Chemistry Research 2014;53:1097–107.

[67] Xiao L, Wang B, Yang G, Gauthier M. Poly(Lactic Acid)-Based Biomaterials: Synthesis, Modification and Applications. Biomedical Science, Engineering and Technology, 2006, p. 247–82. doi:10.5772/23927.

[68] Hoekstra A, Schennink GGJ, De VS. An essentially biobased, thermoformable composition and containers formed thereof. WO 2013131649 A1, 2013.

[69] Wei L, Tedford RA, Thoman BJ. Thermoformed articles made from reactive extrusion products of biobased materials. US 8231954 B2, 2010.

[70] Schischko J, Busch D, Rosenbaum S. Verfahren zur herstellung von biologisch abbaubaren verpackungen aus biaxial verstreckten folien. WO 2002072335 A1, 2002.

[71] Zhang XC, Butler MF, Cameron RE. The ductile-brittle transition of irradiated isotactic polypropylene studied using simultaneous small angle X-ray scattering and tensile deformation. Polymer 2000;41:3797–807. doi:10.1016/S0032-3861(99)00594-7.

[72] Zhang X, Schneider K, Liu G, Chen J, Brüning K, Wang D, et al. Structure variation of tensile-deformed amorphous poly(L-lactic acid): Effects of deformation rate and strain. Polymer 2011;52:4141–9. doi:10.1016/j.polymer.2011.07.003.

[73] Stoclet G, Seguela R, Lefebvre JM, Elkoun S, Vanmansart C. Strain-Induced Molecular Ordering in Polylactide upon Uniaxial Stretching. Macromolecules 2010;43:1488–98. doi:10.1021/ma9024366.

[74] Stoclet G, Seguela R, Lefebvre J-M, Rochas C. New Insights on the Strain-Induced Mesophase of Poly(D,L-lactide): In Situ WAXS and DSC Study of the Thermo-Mechanical Stability. Macromolecules 2010;43:7228–37. doi:10.1021/ma101430c.

[75] Zhang X, Schneider K, Liu G, Chen J, Brüning K, Wang D, et al. Deformation-mediated superstructures and cavitation of poly(L-lactide): In-situ small-angle X-ray scattering study. Polymer 2012;53:648–56. doi:10.1016/j.polymer.2011.12.002.

[76] Stoclet G, Séguéla R, Lefebvre JM, Li S, Vert M. Thermal and Strain-Induced Chain Ordering in Lactic Acid Stereocopolymers: Influence of the Composition in Stereomers. Macromolecules 2011;44:4961–9. doi:10.1021/ma200469t.

[77] Krenz HG, Kramer EJ, Ast DG. The structure of solvent crazes in polystyrene. Journal of Materials Science 1976;11:2211–21. doi:10.1007/BF00752084.

[78] Kramer EJ. Craze fibril formation and breakdown. Polymer Engineering & Science 1984;24:761–9. doi:10.1002/pen.760241006.

[79] Renouf-Glauser AC, Rose J, Farrar DF, Cameron RE. The effect of crystallinity on the deformation mechanism and bulk mechanical properties of PLLA. Biomaterials 2005;26:5771–82. doi:10.1016/j.biomaterials.2005.03.002.

[80] Kowalczyk M, Piorkowska E. Mechanisms of Plastic Deformation in Biodegradable Polylactide / Poly (1,4- cis -isoprene) Blends. Journal of Applied Polymer Science 2011;124:4579–89. doi:10.1002/app.

[81] Kowalczyk M, Piorkowska E, Dutkiewicz S, Sowinski P. Toughening of polylactide by blending with a novel random aliphatic–aromatic copolyester. European Polymer Journal 2014;59:59–68. doi:10.1016/j.eurpolymj.2014.07.002.

[82] McNeill IC, Leiper H a. Degradation studies of some polyesters and polycarbonates—2. Polylactide: Degradation under isothermal conditions, thermal degradation mechanism and photolysis of the polymer. Polymer Degradation and Stability 1985;11:309–26. doi:10.1016/0141-3910(85)90035-7.

[83] Rudnik E. Compostable Polymer Materials. First Edit. Amsterdam: Elsevier; 2008.

[84] Ramirez M. Sustainable Packaging: PLA Polylactide n.d. http://sustpkgg.blogspot.lu/2009/07/pla-polylactide.html (accessed April 16, 2017).

[85] LOOPLA by Galactic SA 2009. http://www.loopla.org/cradle/cradle.htm.

[86] Soroudi A, Jakubowicz I. Recycling of bioplastics, their blends and biocomposites: A review. European Polymer Journal 2013;49:2839–58. doi:10.1016/j.eurpolymj.2013.07.025.

[87] Żenkiewicz M, Richert J, Rytlewski P, Moraczewski K, Stepczyńska M, Karasiewicz T, et al. Characterisation of multi-extruded poly(lactic acid). Polymer Testing 2009;28:412–8. doi:10.1016/j.polymertesting.2009.01.012.

[88] Badia JD, Strömberg E, Karlsson S, Ribes-Greus A. Material valorisation of amorphous polylactide. Influence of thermo-mechanical degradation on the morphology, segmental dynamics, thermal and mechanical performance. Polymer Degradation and Stability 2012;97:670–8. doi:10.1016/j.polymdegradstab.2011.12.019.

[89] Pillin I, Montrelay N, Bourmaud A, Grohens Y. Effect of thermo-mechanical cycles on the physico-chemical properties of poly(lactic acid). Polymer Degradation and Stability 2008;93:321–8. doi:10.1016/j.polymdegradstab.2007.12.005.

[90] Jamshidi K, Hyon S-H, Ikada Y, Hyon S-H, Ikada Y, Hyon S-H, et al. Thermal characterization of polylactides. Polymer 1988;29:2229–34. doi:10.1016/0032-3861(88)90116-4.

[91] Kopinke F, Remmler M, Mackenzie K, Milder M. Thermal decomposition of biodegradable polyesters -11. Poly(lactic acid). Polymer Degradation and Stability 1996;53:329–42.

[92] Badia JD, Strömberg E, Ribes-Greus A, Karlsson S. Assessing the MALDI-TOF MS sample preparation procedure to analyze the influence of thermo-oxidative ageing and thermo-mechanical degradation on poly (Lactide). European Polymer Journal 2011;47:1416–28. doi:10.1016/j.eurpolymj.2011.05.001.

[93] Hamad K, Kaseem M, Deri F. Effect of recycling on rheological and mechanical properties of poly(lactic acid)/polystyrene polymer blend. Journal of Materials Science 2010;46:3013–9. doi:10.1007/s10853-010-5179-8.

[94] Scaffaro R, Morreale M, Mirabella F, La Mantia FP. Preparation and Recycling of Plasticized PLA. Macromolecular Materials and Engineering 2011;296:141–50. doi:10.1002/mame.201000221.

[95] Wu D, Hakkarainen M. Recycling PLA to multifunctional oligomeric compatibilizers for PLA/starch composites. European Polymer Journal 2015;64:126–37. doi:10.1016/j.eurpolymj.2015.01.004.

[96] Fischer EW, Sterzel HJ, Wegner G. Investigation of the structure of solution grown crystals of lactide copolymers by means of chemical reactions. Kolloid-Z uZ Polymere 1973;251:980–90. doi:10.1007/BF01498927.

[97] Nanthananon P, Seadan M, Pivsa-Art S, Suttiruengwong S. Enhanced crystallization of poly(lactic acid) through reactive aliphatic bisamide. IOP Conference Series: Materials Science and Engineering 2015;87. doi:10.1088/1757-899X/87/1/012067.

[98] "U.S. Department of Health & Human Service." U.S. Food & Drug Administration. CFR - Code of Federal Regulations Title 21 2016. https://www.accessdata.fda.gov/scripts/cdrh/cfdocs/cfcfr/CFRSearch.cfm?CFRPart=170&showFR=1 (accessed May 10, 2017).

[99] Debaud F, Defrancisci A, Palys LH. SP and CST Technologies – A new generation of cost saving curatives in rubber processing. 2004.

[100] Carlson D, Dubois P, Nie L, Narayan R. Free radical branching of polylactide by reactive extrusion. Polymer Engineering & Science 1998;38:311–21. doi:10.1002/pen.10192.

[101] Oyama HT. Super-tough poly(lactic acid) materials: Reactive blending with ethylene copolymer. Polymer 2009;50:747–51. doi:10.1016/j.polymer.2008.12.025.

[102] Ku Marsilla KI, Verbeek CJR. Modification of poly(lactic acid) using itaconic anhydride by reactive extrusion. European Polymer Journal 2015;67:213–23. doi:10.1016/j.eurpolymj.2015.03.054.

[103] Phillips PJ. Chapter 18: Spherulite Crystallization in Macromolecules. In: Hurle DTJ, editor. Handbook of Crystall Growth, Elsevier; 1994, p. 1168–216.

[104] Mano JF, Wang Y, Viana JC, Denchev Z, Oliveira MJ. Cold Crystallization of PLLA Studied by Simultaneous SAXS and WAXS. Macromolecular Materials and Engineering 2004;289:910–5. doi:10.1002/mame.200400097.

[105] Nofar M, Zhu W, Park CB, Randall J. Crystallization Kinetics of Linear and Long-Chain-Branched Polylactide. Industrial & Engineering Chemistry Research 2011;50:13789–98. doi:10.1021/ie2011966.

[106] Hutter JL, Bechhoefer J. Banded spherulitic growth in a liquid crystal. Journal of Crystal Growth 2000;217:332–43. doi:10.1016/S0022-0248(00)00479-6.

[107] Ma P, Jiang L, Ye T, Dong W, Chen M. Melt Free-Radical Grafting of Maleic Anhydride onto Biodegradable Poly(lactic acid) by Using Styrene as A Comonomer. Polymers 2014;6:1528–43. doi:10.3390/polym6051528.

[108] Cai S, Zeng C, Zhang N, Li J, Meyer M, Fink RH, et al. Enhanced mechanical properties of PLA/PLAE blends via well-dispersed and compatilized nanostructures in the matrix. RSC Adv 2016. doi:10.1039/C6RA01367H.

[109] Leung BO, Hitchcock AP, Cornelius R, Brash JL, Scholl A, Doran A. X-ray spectromicroscopy study of protein adsorption to a polystyrene-polylactide blend. Biomacromolecules 2009;10:1838–45. doi:10.1021/bm900264w.

[110] Schöll A, Fink R, Umbach E, Mitchell GE, Urquhart SG, Ade H. Towards a detailed understanding of the NEXAFS spectra of bulk polyethylene copolymers and related alkanes. Chemical Physics Letters 2003;370:834–41. doi:10.1016/S0009-2614(03)00215-X.

[111] Dhez O, Ade H, Urquhart SG. Calibrated NEXAFS spectra of some common polymers. Journal of Electron Spectroscopy and Related Phenomena 2003;128:85–96. doi:10.1016/S0368-2048(02)00237-2.

[112] Zwahlen M, Herrwerth S, Eck W, Grunze M, Hähner G. Conformational Order in Oligo(ethylene glycol)-Terminated Self-Assembled Monolayers on Gold Determined by Soft X-ray Absorption. Langmuir 2003;19:9305–10. doi:10.1021/la0350610.

[113] Menzies DJ, Cowie B, Fong C, Forsythe JS, Gengenbach TR, McLean KM, et al. One-step method for generating PEG-like plasma polymer gradients: Chemical characterization and analysis of

protein interactions. Langmuir 2010;26:13987–94. doi:10.1021/la102033d.

[114] Stöhr J. NEXAFS Spectroscopy. Heidelberg: Springer; 1992.

[115] Díez-Pascual AM, Naffakh M. Mechanical and thermal behaviour of isotactic polypropylene reinforced with inorganic fullerene-like WS2 nanoparticles: Effect of filler loading and temperature. Materials Chemistry and Physics 2013;141:979–89. doi:10.1016/j.matchemphys.2013.06.039.

[116] McCrum NG, Buckley CP, Bucknall CB. Principles of Polymer Engineering. Oxford University Press; 1988.

[117] Addiego F, Dahoun A, G'Sell C, Hiver J-M. Characterization of volume strain at large deformation under uniaxial tension in high-density polyethylene. Polymer 2006;47:4387–99. doi:10.1016/j.polymer.2006.03.093.

[118] Eddoumy F, Addiego F, Dhieb H, Célis J-P, Muller R, Toniazzo V, et al. Sliding wear behaviour of oriented ultrahigh molecular weight polyethylene. Polymer International 2013;62:867–77. doi:10.1002/pi.4404.

[119] Farge L, André S, Meneau F, Dillet J, Cunat C. A common multiscale feature of the deformation mechanisms of a semicrystalline polymer. Macromolecules 2013;46:9659–68. doi:10.1021/ma4019747.

[120] Rinde JA. Poisson's ratio for rigid plastic foams. Journal of Applied Polymer Science 1970;14:1913–26. doi:10.1002/app.1970.070140801.

[121] Wang K, Brüster B, Addiego F, Kfoury G, Hassouna F, Ruch D, et al. Strain-induced deformation mechanisms of polylactide plasticized with acrylated poly(ethylene glycol) obtained by reactive extrusion. Polymer International 2015;64:1544–54. doi:10.1002/pi.4927.

[122] Castellani L, Maestrini C. Rubber-like tensile behaviour of yielded high-impact polystyrene. Polymer 1990;31:2278–86. doi:10.1016/0032-3861(90)90313-N.

[123] Choi JH, Ahn KH, Kim SY. Effects of the degree of graft on the tensile and dynamic behavior of high impact polystyrene. Polymer 2000;41:5229–35. doi:10.1016/S0032-3861(99)00726-0.

[124] Brooks NW, Ghazali M, Duckett RA, Unwin AP, Ward IM. Effects of morphology on the yield stress of polyethylene. Polymer 1999;40:821–5. doi:10.1016/S0032-3861(98)00324-3.

[125] Lazzeri A, Bucknall CB. Applications of dilatational yielding model to rubber-toughened polymers. Polymer 1995;36:2895–902.

[126] Rezgui F, Swistek M, Hiver JM, G'Sell C, Sadoun T. Deformation and damage upon stretching of degradable polymers (PLA and PCL). Polymer 2005;46:7370–85. doi:10.1016/j.polymer.2005.03.116.

[127] Cherry BW, Hin TS. Polymer communications Stress whitening in polyethylene. Polymer 1981;22:1610–2.

[128] Farge L, Andre S, Pawlak A, Baravian C, Irvine SC, Philippe AM. A study of the deformation-induced whitening phenomenon for cavitating and non-cavitating semicrystalline polymers. Journal of Polymer Science, Part B: Polymer Physics 2013;51:826–41. doi:10.1002/polb.23267.

[129] Blaise A, Baravian C, Dillet J, Michot LJ, André S. Characterization of the mesostructure of HDPE under "In situ" uniaxial tensile test by incoherent polarized steady-light transport. Journal of Polymer Science, Part B: Polymer Physics 2012;50:328–37. doi:10.1002/polb.23020.

[130] Halary JL, Laupretre F, Monnerie L. Polymer Materials: Macroscopic Properties and Molecular Interpretations. New Jersey: John Wiley & Sons Inc., Hoboken; 2011.

[131] Dong H, Jacob KI. Effect of molecular orientation on polymer free volume distribution: An atomistic approach. Macromolecules 2003;36:8881–5. doi:10.1021/ma034758p.

[132] Rozanski A, Galeski A. Controlling cavitation of semicrystalline polymers during tensile drawing. Macromolecules 2011;44:7273–87. doi:10.1021/ma201090z.

[133] Lauterwasser BD, Kramer EJ. Microscopic mechanisms and mechanics of craze growth and fracture. Philosophical Magazine A 1979;39:469–95. doi:10.1080/01418617908239285.

[134] Salomons GJ, Singh MA, Bardouille T, Foran WA, Capel MS. Small-angle X-ray scattering analysis of craze-fibril structures. Journal of Applied Crystallography 1999;32:71–81. doi:10.1107/S0021889898010486.

[135] Gámez-Pérez J, Velazquez-Infante JC, Franco-Urquiza E, Pages P, Carrasco F, Santana OO, et al. Fracture behavior of quenched poly(lactic acid). Express Polymer Letters 2011;5:82–91. doi:10.3144/expresspolymlett.2011.9.

[136] Brady TE, Yeh GSY. Similarity between craze morphology and shear-band morphology in polystyrene. Journal of Materials Science 1973;8:1083–94. doi:10.1007/BF00632758.

[137] Berger LL, Kramer EJ. The effect of temperature on the transition from crazing to shear deformation in crosslinked polystyrene. Journal of Materials Science 1988;23:3536–43. doi:10.1007/BF00540492.

[138] Donald AM, Kramer EJ. Internal structure of rubber particles and craze break-down in high-impact polystyrene (HIPS). Journal of Materials Science 1982;17:2351–8. doi:10.1007/BF00543744.

[139] Kealy T. Rheological Analysis of the Degradation of HDPE During Consecutive Processing Steps and for Different Processing Conditions. Journal of Applied Polymer Science 2009;112:639–48.

[140] Wang K, Addiego F, Bahlouli N, Ahzi S, Rémond Y, Toniazzo V, et al. Analysis of thermomechanical reprocessing effects on polypropylene/ethylene octene copolymer blends. Polymer Degradation and Stability 2012;97:1475–84. doi:10.1016/j.polymdegradstab.2012.05.005.

[141] Badía JD, Vilaplana F, Karlsson S, Ribes-Greus a. Thermal analysis as a quality tool for assessing the influence of thermo-mechanical degradation on recycled poly(ethylene terephthalate). Polymer Testing 2009;28:169–75. doi:10.1016/j.polymertesting.2008.11.010.

[142] Papong S, Malakul P, Trungkavashirakun R, Wenunun P, Chom-In T, Nithitanakul M, et al. Comparative assessment of the environmental profile of PLA and PET drinking water bottles from a life cycle perspective. Journal of Cleaner Production 2014;65:539–50. doi:10.1016/j.jclepro.2013.09.030.

[143] Piemonte V. Bioplastic Wastes: The Best Final Disposition for Energy Saving. Journal of Polymers and the Environment 2011;19:988–94. doi:10.1007/s10924-011-0343-z.

[144] Brüster B, Addiego F, Hassouna F, Ruch D, Raquez J-M, Dubois P. Thermo-mechanical degradation of plasticized poly(lactide) after multiple reprocessing to simulate recycling: multi-scale analysis and underlying mechanisms. Polymer Degradation and Stability 2016;131:132–44.

[145] Wei Z, Song P, Zhou C, Chen G, Chang Y, Li J, et al. Insight into the annealing peak and microstructural changes of poly(l-lactic acid) by annealing at elevated temperatures. Polymer

(United Kingdom) 2013;54:3377–84. doi:10.1016/j.polymer.2013.04.027.

[146] Zhang K, Mohanty AK, Misra M. Fully biodegradable and biorenewable ternary blends from polylactide, poly(3-hydroxybutyrate-co-hydroxyvalerate) and poly(butylene succinate) with balanced properties. ACS Applied Materials & Interfaces 2012;4:3091–101. doi:10.1021/am3004522.

[147] Monnerie L, Halary JL, Kausch HH. Deformation, yield and fracture of amorphous polymers: Relation to the secondary transitions. Advances in Polymer Science 2005;187:215–364. doi:10.1007/b136957.

[148] Fayolle B, Richaud E, Colin X, Verdu J. Review: Degradation-induced embrittlement in semi-crystalline polymers having their amorphous phase in rubbery state. Journal of Materials Science 2008;43:6999–7012. doi:10.1007/s10853-008-3005-3.

[149] Israelachvili J. The different faces of poly(ethylene glycol). Proceedings of the National Academy of Sciences of the United States of America 1997;94:8378–9. doi:10.1073/pnas.94.16.8378.

[150] Siparsky GL, Voorhees KJ, Dorgan JR, Schilling K. Water transport in polylactic acid (PLA), PLA/polycaprolactone copolymers, and PLA/polyethylene glycol blends. Journal of Environmental Polymer Degradation 1997;5:125–36. doi:10.1007/BF02763656.

[151] Fayolle B, Audouin L, George GA, Verdu J. Macroscopic heterogeneity in stabilized polypropylene thermal oxidation. Polymer Degradation and Stability 2002;77:515–22. doi:10.1016/S0141-3910(02)00110-6.

[152] Gratia A, Merlet D, Ducruet V, Lyathaud C. A comprehensive NMR methodology to assess the composition of biobased and biodegradable polymers in contact with food. Analytica Chimica Acta 2015;853:477–85. doi:10.1016/j.aca.2014.09.046.

[153] Badia JD, Monreal L, Sáenz de Juano-Arbona V, Ribes-Greus A. Dielectric spectroscopy of recycled polylactide. Polymer Degradation and Stability 2014;107:21–7. doi:10.1016/j.polymdegradstab.2014.04.023.

[154] Rasselet D, Ruellan A, Guinault A, Miquelard-Garnier G, Sollogoub C, Fayolle B. Oxidative degradation of polylactide (PLA) and its effects on physical and mechanical properties. European Polymer Journal 2014;50:109–16. doi:10.1016/j.eurpolymj.2013.10.011.

[155] Song X, Zhang X, Wang H, Liu F, Yu S, Liu S. Methanolysis of poly(lactic acid) (PLA) catalyzed by ionic liquids. Polymer Degradation and Stability 2013;98:2760–4. doi:10.1016/j.polymdegradstab.2013.10.012.

[156] Carné Sánchez A, Collinson SR. The selective recycling of mixed plastic waste of polylactic acid and polyethylene terephthalate by control of process conditions. European Polymer Journal 2011;47:1970–6. doi:10.1016/j.eurpolymj.2011.07.013.

[157] Li SM, Rashkov I, Espartero JL, Manolova N, Vert M, Li SM, et al. Synthesis, Characterization, and Hydrolytic Degradation of PLA / PEO / PLA Triblock Copolymers with Short Poly (L -lactic acid) Chains. Macromolecules 1996;29:50–6.

[158] Raabe J, Tzvetkov G, Flechsig U, Böge M, Jaggi A, Sarafimov B, et al. PolLux: A new facility for soft x-ray spectromicroscopy at the swiss light source. Review of Scientific Instruments 2008;79. doi:10.1063/1.3021472.

[159] Watts B, McNeill CR, Raabe J. Imaging nanostructures in organic semiconductor films with scanning transmission X-ray spectro-microscopy. Synthetic Metals 2012;161:2516–20.

doi:10.1016/j.synthmet.2011.09.016.

[160] G'Sell C, Aly-Helal NA, Semiatin SL, Jonas JJ. Influence of deformation defects on the development of strain gradients during the tensile deformation of polyethylene. Polymer 1992;33:1244–54. doi:10.1016/0032-3861(92)90770-W.

[161] Prince E. International Tables for Crystallography, Mathematical, Physical and Chemical Tables. 3rd ed. Dordrecht (NL): Kluwer Academic Publishers; 2004.

[162] Ahmed J, Varshney SK. Polylactides—Chemistry, Properties and Green Packaging Technology: A Review. International Journal of Food Properties 2011;14:37–58. doi:10.1080/10942910903125284.

[163] Roberto A, Rachele C, Gennaro G, Veronica A. Plasticization of poly(lactic acid) through blending with oligomers of lactic acid: effect of the physical aging on properties. EUROPEAN POLYMER JOURNAL 2015. doi:10.1016/j.eurpolymj.2015.02.040.

[164] López-Rodríguez N, Sarasua JR. Plasticization of Poly- L -lactide with L -Lactide , D -Lactide , and D , L -Lactide Monomers. Polymer Engineering & Science 2013. doi:10.1002/pen.

[165] Martino VP, Jiménez A, Ruseckaite RA. Processing and Characterization of Poly(lactic acid) Films Plasticized with Commercial Adipates. Journal of Applied Polymer Science 2009;112:2010–8. doi:10.1002/app.29784.

[166] Labrecque L V, Kumar R a, Dave V, Gross R a, McCarthy SP. Citrate esters as plasticizers for poly(lactic acid). Journal of Applied Polymer Science 1997;66:1507–13. doi:10.1002/(sici)1097-4628(19971121)66:8<1507::aid-app11>3.0.co;2-0.

[167] Arrieta MP, López J, Ferrándiz S, Peltzer MA. Characterization of PLA-limonene blends for food packaging applications. Polymer Testing 2013;32:760–8. doi:10.1016/j.polymertesting.2013.03.016.

[168] Hilschmann J, Kali G. Bio-based polymyrcene with highly ordered structure via solvent free controlled radical polymerization. European Polymer Journal 2015;73:363–73. doi:10.1016/j.eurpolymj.2015.10.021.

Appendix

A Experimental Section

A.1 Materials

Polylactide (PLA, 4042D, 4.2% D-lactide content) was purchased from NatureWorks LLC (Minnetonka, MN, USA). PLA of this grade was used for the studies with the micro-compounder. For studies with the mini-extruder, the same PLA (4.2% D-lactide), but named 4043D was supplied by NatureWorks LLC. The name was replaced by the supplier, but the grade was the same. These grades of PLA contained neither stabilizer nor antioxidant. PLA was dried before use in the vacuum oven (Heraeus, Thermo Scientific, Langenselbold, Germany) at 50°C for at least 6 h to remove humidity before processing. The plasticizer poly(ethylene glycol) methyl ether acrylate (acrylPEG, Mn 480 g/mol) and the free-radical initiator 2,5-Bis(*tert*-butylperoxy)-2,5-dimethylhexane (Luperox101 or L101) were ordered at Sigma-Aldrich (Steinheim, Germany).

A.2 Processing Equipment

A.2.1 Micro-Compounder

Extrusions were conducted with a Micro 15cc Twin Screw Compounder from DSM Xplore (Sittard, The Netherlands). In total 6 g of material were introduced into the extruder per batch. For plasticized PLA samples, PLA was first melted in the extruder. The liquid plasticizer and initiator were mixed in a small glass vial and added to PLA in the extruder by a syringe. The force during the extrusion was recorded by the Software DSM Xplore Data Acquisition and Control v1.8 during the residence time. The samples were extruded in a rod shape with a diameter of 2 to 3 mm and cut to strands of 3 to 5 mm or ground to flakes/powder by a grinder (reference Baby-Line-B08.10f) from Wanner Technik GmbH (Wertheim, Germany) equipped with a mesh with 4 mm holes.

A.2.2 Mini-Extruder

The extrusions in pre-industrial scale were conducted with a mini-extruder HAAK RHEOMEX PTW 16-40 from Thermo Fischer Scientific (Karlsruhe, Germany). The screw diameter was 16 mm, L/D ratio was 40 and the mini-extruder operates in co-rotating mode. The 10 heating zones could be set to different temperatures (between room temperature and 350°C). For PLA extrusion, the PLA pellets were added to the extruder by a feeder (DSR20-10, Brabender Technology, Duisburg, Germany). The feeder could be set to values between 0.1 kg/h and 1.6kg/h. The mini-extruder could be used with

two different dies: a sheet die to obtain films and a cylindrical die. The feeding of the PLA/plasticizer/initiator-blend was done manually for the processing of plasticized PLA. PLA, the plasticizer, and the initiator were mixed in a glass beaker and introduced into the extruder. The feeding rate, the temperature of the different zones and the rotation speed of the screws could be controlled by the software PolySoft Monitor. Furthermore, the software allowed recording all parameters during the extrusion, e.g. the torque and temperatures. The extruded samples were ground by a grinder (Wanner Technik GmbH (Wertheim Germany), reference Baby-Line-B08.10f) or a pelletizer (Thermo Fischer Scientific (Waltham, MA, USA)).

A.2.3 Compression Molding

Compression molding was conducted on a Carver manual press (Wabash, IN, USA) and plates with a size 10 cm x 10 cm and a thickness of 0.2 mm were obtained. The polymer material (pellets, flakes, or powder) was melted at 180°C for 10 min in the mold without pressure. After several degassing steps by compression and decompressing procedures with a pressure of 70 bar, the materials were compressed at 180°C for 10 min. The plates were cooled down under 70 bar within 5 min by water cooling. Aluminum foil was used to obtain a flat surface on both sides of the plates during compression molding and was removed after the compression molding step.

A.2.4 Injection Molding

Injection molding was conducted with a Thermo Scientific HAAKE MiniJet II (Waltham, MA, USA). The cylinder temperature was set to 180°C and the mold temperature to 65°C. After melting the polymer in the cylinder for 2 min the machine injected the sample with a pressure of 700 bar for 5 sec followed by a post pressure of 100 bar for 3 sec. Three different molds (Thermo Scientific, Waltham, MA, USA) were used according to the followed characterization. For tensile testing, the mold Zugprüfstab ASTM 0638-V (reference 557-2299), for impact testing Mold MiniJet 63.5x12.7x3.2 mm (reference 557-2285), and for DMA Mold HAAKE MiniJet 60x11x3 mm (reference 557-2296) were used.

A.3 Characterization Methods for Chapter 3: Process-Structure Relationship

A.3.1 Processing in the Micro-Compounder

The samples for the pPLA structural analysis were processed in the micro-compounder at 180°C with a screw speed of 50 rpm and a residence time of 5 min under nitrogen purge. The materials' compositions are listed in Table A. 1. For PLA/poly(acrylPEG), first acrylPEG and L101 were blended in the extruder to obtain poly(acrylPEG), and afterward, PLA was blended with poly(acrylPEG).

Table A. 1 Composition of materials for pPLA structural analysis.

sample's name	PLA (wt%)	acrylPEG (wt%)	L101 (wt%)	poly(acrylPEG) (wt%)
pPLA	79	20	1	0
PLA/L101	99	0	1	0
PLA/acrylPEG	80	20	0	0
poly(acrylPEG)	0	95	5	0
PLA/(poly(acrylPEG)	79	0	0	21
PLA	100	0	0	0

A.3.2 Processing in the Mini-Extruder

The scale-up process was conducted in a mini-extruder. The impact of the processing conditions was analyzed by variation of the screw speed (10, 50, or 100 rpm) and the temperature (180°C or 200°C for all temperature zones) for the processing of plasticized PLA. Since no liquid feeding system was not available, PLA, acrylPEG, and L101 were mixed in a glass beaker in a weight composition of 79/20/1 and fed manually to the extruder. The samples were produced with the cylindrical die and named with the label -ME for the mini-extruder followed by the screw speed and the extrusion temperature.

The film samples were produced with the sheet die, but for pPLA it was not possible to obtain directly films. Therefore, pPLA was produced in two steps. In the first step, rods of pPLA were produce, which were in a second extrusion step reshaped to films. PLA and PLA/acrylPEG films were produced in one step with the weight compositions PLA/acrylPEG/L101 100/0/0 and 80/20/0, respectively. All films had a thickness of about 2 mm. The samples were named with the ending -film. All samples produced with the mini-extruder for the first chapter are listed in Table A. 2.

Table A. 2 Processing parameters of plasticized PLA samples and film samples produced with the mini-extruder.

		screw speed (rpm)	temperature for all zones (°C)	die shape	feeding rate
pPLA-ME-50-180		50	180	rod	manually
pPLA-ME-10-180		10	180	rod	manually
pPLA-ME-100-180		100	180	rod	manually
pPLA-ME-50-200		50	200	rod	manually
pPLA-film	1st step	100	200	rod	manually
	2nd step	100	200	sheet	0.5 kg/h
PLA/acrylPEG-film		100	200	sheet	manually
PLA-film		100	200	sheet	0.5 kg/h

A.3.3 Soxhlet Extraction

The Soxhlet extraction technique allows the separation of materials regarding their difference in solubility. Figure A. 1 shows the experimental set-up for a Soxhlet extraction. The solvent is continuously heated, evaporates and condenses at the reflux condenser. The solvent drops down to the extraction chamber on the source material in an extraction thimble. When the solvent level in the chamber rises above the siphon arm, the solvent flows back in the solvent flask. In this way the solvent circulates and extracts the soluble part from the material in the extraction chamber.

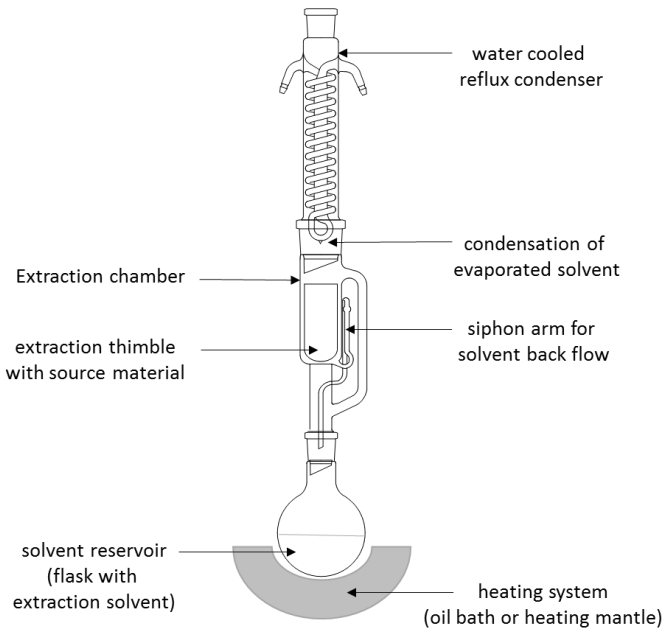

Figure A. 1 Experimental set-up for the Soxhlet extrusion.

The technique of Soxhlet extraction was used to determine the non-grafted part of the plasticizer on the PLA matrix [41,51]. While the matrix of PLA and therefore the grafted part of the acrylPEG plasticizer are not soluble in methanol, the non-grafted part can be extracted. A cellulose extraction thimble was filled with about 1-2 g sample (m_{sample}) and put in a 100 ml Soxhlet extractor. The extractor was set between a 500 ml round-bottom flask filled with about 350 ml methanol and a reflux condenser. The soluble fraction was extracted for 24 h under reflux. Afterwards, the solid fraction was dried at 50°C in a vacuum oven over night and the amount of extracted fraction (EF_{solid}) was calculated by Equation (**Fehler! Verwenden Sie die Registerkarte 'Start', um Heading 6 dem Text zuzuweisen, der hier angezeigt werden soll.**.1). The methanol was evaporated and the soluble fraction was dried at 50°C in a vacuum oven over night and the amount of extracted fraction was calculated by Equation (**Fehler! Verwenden Sie die Registerkarte 'Start', um Heading 6 dem Text zuzuweisen, der hier angezeigt werden soll.**.2). For the pPLA, the extracted fraction EF_{liquid} was about 7%. The calculation from the solid fraction was not that exact since the hot methanol could induce methanolysis and increased the crystallinity.

$$EF_{solid}\ (\%) = \frac{m_{sample} - m_{solid\ fraction}}{m_{sample}} \cdot 100\%$$

(**Fehler! Verwenden Sie die Registerkarte 'Start', um Heading 6 dem Text zuzuweisen, der hier angezeigt werden soll.**.1)

$$EF_{liquid}\ (\%) = \frac{m_{liquid\ fraction}}{m_{sample}} \cdot 100\%$$

(**Fehler! Verwenden Sie die Registerkarte 'Start', um**

Heading 6 dem Text zuzuweisen, der hier angezeigt werden soll..2)

A.3.4 Gel Permeation Chromatography

The solid samples were dissolved in tetrahydrofuran (THF) to a concentration of 1mg/ml and stirred overnight. Before the analysis, the samples were filtered with Agilent PTFE 0.2 µm filters. The gel permeation chromatography (GPC) characterizations were performed on an Agilent Technologies 1200 Series apparatus combined to a Viscotek 270 Dual detector (laser 262 nm wavelength). Separation was performed on an unique mixed bed column (PLgel Mixed-C 300 x 7.5 mm, size 5 µm, Agilent) with a precolumn (PLgel, 50 x 7.5 mm, size 5 µm, Agilent) at 35°C. THF was used as eluent at a flow rate of 1 ml/min, while 100 µL of the 1mg/ml sample solution was injected. Polystyrene standards (EasiVial) from Agilent were used as calibrants to estimate the molecular weights MW of the samples.

A.3.5 Swelling Tests in Chloroform

Small pieces of the solid samples of about 0.5 g - 1 g were covered with about 3 ml of chloroform and left over night. Although, some samples formed a gel, a separation of the gel and the solvent was not possible since the gels were not stable enough. The swelling tests were just used as qualitative analysis.

A.3.6 Differential Scanning Calorimetry

The differential Scanning Calorimetry (DSC) allows the determination of the glass transition temperature T_g as a shallow endothermic increase, the melting temperature T^m as an endothermic peak with the melting enthalpy ΔH_m, and the cold crystallization temperature T_{cc} as an exothermic peak with the cold crystallization enthalpy ΔH_{cc} for semicrystalline polymers. The DSC measurements were conducted on a Netzsch DSC 204 F1 (Selb, Germany), and the data were analyzed with the Software Netzsch Proteus Thermal Analysis. 3-6 mg of a sample were placed in an aluminum pan with

a fixed cap with a hole. The samples were cooled to -100°C, heated to 180°C and again cooled to -100°C and heated to 180°C. All tests were conducted under nitrogen gas flow and the cooling and heating rates were -10 K/min and 10 K/min, respectively. The glass transition temperature (T_g), the melting temperature (T_m), the melting enthalpy (ΔH_m), and the cold crystallization enthalpy (ΔH_{cc}) were determined from the heating stage: From the first heating cycle for samples with a pretreatment (e.g. tensile testing) and from the second heating cycle to compare the samples with a similar thermal history. In the case of the semicrystalline polymer PLA, the crystallinity was calculated based on Equation (**Fehler! Verwenden Sie die Registerkarte 'Start', um Heading 6 dem Text zuzuweisen, der hier angezeigt werden soll.**.3), where $\Delta H_{m,0}$ was the melting enthalpy of a 100% crystalline PLA determined to be $H_{m,0} = 93 J/g$ [96]. Since the plasticizing of PLA forms a composite, just the effective amount of PLA x_{PLA} is considered for the calculation of the crystallinity.

$$X_c = \frac{\Delta H_m - \Delta H_{cc}}{x_{PLA} \cdot \Delta H_{m,0}} \cdot 100\%$$

(**Fehler! Verwenden Sie die Registerkarte 'Start', um Heading 6 dem Text zuzuweisen, der hier angezeigt werden soll.**.3)

A.3.7 Atomic Force Microscope

Height and Stiffness Analysis of Micro-compounder samples

The samples of pPLA, PLA/acrylPEG, and pPLA aS were melted on a glass surface at 180°C. After air cooling, these very smooth, melted sides of the samples were studied by atomic force microscope, while special attention was paid on the topography and stiffness of the samples. AFM PeakForce QNM measurement mode was performed using a Dimension ICON AFM (Bruker, Santa Clara) with a RTESPA probe (40 N/m spring constant, 10 nm tip radius) to map the topography and mechanical properties

of the bioplastic blend samples. The cantilever stiffness was calibrated prior to measurements by applying a force distance curve on sapphire substrate to get the cantilever deflection sensitivity and then the thermal tune module was used to finally determined the spring constant.

Topography Analysis after Isothermal Crystallization

The topography images to analyze the crystalline structures were recorded after surface smoothing at low temperatures. The samples were prepared with a cryo-ultramicrotome Leica EM UC6/UF6 (Vienna, Austria) at -50°C by cutting small surfaces first with a glass knife and polishing the surface subsequently with a diamond blade (Diatome Cryo 35°, Hatfield, PA, USA). The AFM height images were recorded on a BRUKER Dimension Icon (Bellerice, MA, USA).

A.3.8 Impact testing

Impact testing allowed analyzing the impact energy and leads to a specification of toughness. The specimen were produced by injection molding 63.5 x 12.7 x 3.2 mm (mold reference 557-2285). The specimen were notched with an Instron Ceast Motorized Notchvis machine (Norwood, MA, USA). The radius of the notch was 25 mm, while its angle was 45°. The samples were tested on an impact pendulum Instron Ceast 9050 (Norwood, MA, USA) equipped with a hammer 2.75J N.127 (reference CODE 7600.202) at room temperature according to ISO 180-4A standard and an angle of the hammer of 150°. The exact specimen dimensions were measured and the impact energy was calculated by the integrated software of the pendulum machine.

A.3.9 Isothermal Crystallization Measured by Wide-Angle X-ray Scattering

X-ray diffraction (XRD) with controlled sample temperature was used to determine the isothermal crystallization kinetics of the materials. The XRD machine was a Panalytical X'Pert Pro MPD (Almelo, The Netherlands) configured with its classical diffraction mode (θ-2θ) and generating X-ray with the K_α radiation of copper (wavelength λ = 1.54 Å). As sample holder, a heating chamber Anton Paar TTK 450 (Graz, Austria) was utilized. The analyzed samples were small plates of approximate dimensions 12 mm × 10 mm × 1.5 mm. Irradiation was conducted on the main face of the sample with an irradiated surface of about 12 mm × 8 mm. Prior XRD analyses, samples were heated at 200°C for 3 minutes and quickly cooled in liquid nitrogen to erase their thermal history and to obtain an amorphous structure. Due to surface buckling during the heating procedure, samples were polished to a thickness of 1.5mm. As primary optics, a programmable divergent slit was used, while as secondary optics a Panalytical

PIXcel detector was chosen. The thermal procedure consisted of heating samples from 25°C to the imposed crystallization temperature at 5°C/min, and then keeping samples at this temperature until the maximum crystallization was reached, but at most 10h. The imposed crystallization temperatures T_c were 80°C, 85°C, 90°C, 100°C, and 110°C for PLA, and 50°C, 55°C, 60°C, 65°C, 70°C, 80°C and 90°C for pPLA. The intensity I – 2θ diffractograms were recorded between 15.5° and 20° enabling to observe the two main crystalline peaks of PLA (reflections (110/200) at 16.4° and (203) at 18.7° of orthorhombic units α and α' [73]), with an acquisition time of 2 min. Such an acquisition time represented the best compromise between the diffractogram resolution and the acquisition speed. The intensity of the diffractograms was first corrected to get a constant irradiated volume in the 2θ range of acquisition by means of the software HighScore Plus (Panalytical, Almelo, The Netherlands). Then, the diffractograms were analyzed by means of the software PeakFit (Systat Software, Framingham, MA, USA) enabling to conduct the amorphous and crystalline peaks deconvolution. Accordingly, Gaussian function were considered to simulate two crystalline peaks ((110/200) positioned at 16.4° and (203) at 18.7°). The crystallinity index (CI) was determined by Equation (**Fehler! Verwenden Sie die Registerkarte 'Start', um Heading 6 dem Text zuzuweisen, der hier angezeigt werden soll.**.4), where $(A_{16.4°} + A_{18.7°})$ was the sum of the area of the two crystalline peaks at the time t and $(A_{16.4°} + A_{18.7°})_\infty$ was the maximum area of the two peaks after the isothermal crystallization.

$$CI = \frac{(A_{16.4°} + A_{18.7°})}{(A_{16.4°} + A_{18.7°})_\infty}$$

(**Fehler! Verwenden Sie die Registerkarte 'Start', um Heading 6 dem Text zuzuweisen, der hier angezeigt werden soll.**.4)

From the plots of CI as a function of time t, the crystallization half-time $t_{1/2}$ was determined at the point where the CI reached 0.5. After the isothermal crystallization, the overall crystallinity $X_c(\infty)$ was determined by recording a diffractogram between 5° and 40°. The intensity was corrected and the diffractograms were treated with the software PeakFit. The background was subtracted and three amorphous halos around 15.0°, 21.2° and 31.0°, as well as the four crystalline peaks at 14.6°, 16.4°, 18.7°, and 22.2° were fitted by Gaussian functions. The overall crystallinity was finally calculated by Equation (**Fehler! Verwenden Sie die Registerkarte 'Start', um Heading 6 dem Text zuzuweisen, der hier angezeigt werden soll.**.5), where A_{amorph} was the area of all amorphous peaks and $A_{crystalline}$ was the area of all crystalline peaks.

$$X_c = \frac{A_{crystalline}}{A_{crystalline} + A_{amorph}}$$

(**Fehler! Verwenden Sie die Registerkarte 'Start', um Heading 6 dem Text zuzuweisen, der hier angezeigt werden soll.**.5)

Finally, Avrami model (Equation (**Fehler! Verwenden Sie die Registerkarte 'Start', um Heading 6 dem Text zuzuweisen, der hier angezeigt werden soll.**.6)) was used to further analyze the crystallization kinetics of the materials during isothermal crystallization testing, whereas n reflected the nature of the crystal nucleation and crystal growth geometry, while k corresponded to the overall rate constant associated to nucleation and growth contributions. The fitting of experimental curves with Avrami model was conducted by means of Matlab software (MathWorks, Natick, MA, USA) enabling to calculate n and k. Based on Equation (**Fehler! Verwenden Sie die Registerkarte 'Start', um Heading 6 dem Text zuzuweisen, der hier angezeigt werden soll.**.7), the theoretical crystallization half-time $t_{1/2}$ was calculated.

$$X(t) = 1 - \exp(-k\, t^n)$$

(**Fehler! Verwenden Sie die Registerkarte 'Start', um Heading 6 dem Text zuzuweisen, der hier angezeigt werden soll.**.6)

$$t_{1/2} = \left(\frac{\ln(2)}{k}\right)^{\frac{1}{n}}$$

(**Fehler! Verwenden Sie die Registerkarte 'Start', um Heading 6 dem Text zuzuweisen, der hier angezeigt werden soll.**.7)

A.3.10 Atomic Force Microscope Analysis of Film samples

Atomic force microscope (AFM) measurements were done by means of an Asylum MFP3D Infinity (Santa Clara, California) in fast force mapping, which allowed the recording of topography and a force curve at each pixel of the 256 pixels × 256 pixels images at a line speed from 0.5 Hz to 1 Hz. For this characterization, the samples cut from the extruded films were melted against a glass slide at 180°C and then were slowly cooled to room temperature in air. This procedure enabled to obtain a reasonable flat surface for the AFM measurements. Prior to measurements, tips' cantilever force constant was calibrated with a Sadler noncontact method. The calibration was further checked by the

analysis of a known polycarbonate reference sample (from Asylum) with an elastic modulus of 2.5 GPa. Different cantilever stiffnesses were chosen in function of the elastic moduli of the inclusion. Accordingly, PLA, pPLA, and PLA/acrylPEG were analyzed with ACT160TS (37 N/m), ACT240TS (2 N/m) and TR800PSA (0.7 N/m), respectively. On each image, at least five zones were picked up within the matrix and the inclusions, the choice being made in function of the local topography with a preference for flat surfaces. For the inclusion, the force curves were extracted by Asylum retreatment software and fitted with Hertz punch model for pPLA and with Oliver-Pharr model for PLA/acrylPEG to extract the elastic modulus.

A.3.11 Scanning Transmission X-ray Microscope

The scanning transmission X-ray microscopy (STXM) experiments coupled with near-edge X-ray absorption fine structure (NEXAFS) nano-spectroscopy were performed at the PolLux beamline at the Swiss Light Source (Paul Scherrer Institute, Villigen, Switzerland) [158]. Details about the technique used can be found in the literature [159]. Briefly, a Fresnel zone plate focused the monochromatic synchrotron X-ray beam onto a small spot (less than 30 nm) on the sample, while the transmitted X-rays were measured by a photomultiplier tube coupled with a scintillator screen. The relative position of the zone plate (hence the focused spot of the X-ray beam) and the sample was measured by an interferometer and coupled to the piezo-driven scanning stage to ensure positioning stability and reproducibility. The experiments were conducted under high vacuum (about 10^{-6} mbar). All STXM samples, excepted poly(acrylPEG), were cut into 100 nm-thick lamellae by means of a cryo-ultramicrotome Leica EM UC6/UF6 (Wien, Austria) that was operated at -30°C. Samples were cut into thin lamellae by wet sectioning with a diamond knife using a dimethyl sulfoxide/water mixture (60/40 vol%) before being transferred onto copper grids. In the case of poly(acrylPEG), it was not possible to prepare thin lamellae by wet-sectioning due to the high solubility/swellability of this material in water. Hence, poly(acrylPEG) was directly dissolved in water, dropped on the copper grid and dried at room temperature. The copper grids carrying samples were mounted on an earthed metal sample plate and positioned to be in the focal position of the monochromatic X-ray beam. Composition maps were calculated from transmission images taken at photon energies of 280 eV (pre-edge), 288.5 eV (PLA resonance), 289.7 eV (acrylPEG resonance) and 320 eV (chemically insensitive). The aXis2000 software package (McMaster University, Hamilton, ON, Canada) was used for the data analysis.

A.4 Characterization Methods for Chapter 4: Structure Evolution with Strain

A.4.1 Processing of the Materials

The materials PLA and pPLA for the tensile testing at different temperatures and strain rates (4.2 Deformation Mechanisms of Plasticized Polylactide) were produced in a similar procedure as described in A.2.1 Micro-Compounder. The compounding was conducted at 180°C with a screw speed of 100 rpm and a residence time of 5 min. A nitrogen purge was used and 15 g in total per batch were introduced into the micro-compounder. Prior to the extrusion PLA was dried for 12 hours at 60°C in a vacuum oven (Thermo Scientific reference Heraeus). PLA was first introduced and melted in the micro-compounder. The plasticizer acrylPEG and the initiator L101 were then mixed in a small glass vial and injected into the extruder by using a syringe. The two PLA/acrylPEG/L101 systems with the compositions 79/20/1 and 100/0/0 (in wt%) were chosen and denoted as pPLA and PLA, respectively. The extruded rods of pPLA and PLA were ground and hot-pressed with a manual press Carver to obtain tensile specimens based on ASTM D638-10 with sample type V. The specimen had an overall length of 63.5 mm and a thickness of 3 mm. The gauge section of the specimen had a length of 25 mm and a minimum width of 3 mm. The hot-pressing procedure consisted in (i) heating the material at 180°C for 3 min without any pressure to ensure its complete melting and inter-pellets chain diffusion, (ii) degassing the material by several successive compression and decompression procedures during 2 min, (iii) compressing the material at 180°C with progressively increasing the pressure from 0.3 to 1.5 MPa during 5 min to ensure a good consolidation, and (iv) cooling down the material with a water circulation within the press plates (water temperature of about 15°C) under 1.5 MPa.

For the studies in 4.3 Deformation Heterogeneities in PLA-Based Materials at Room Temperature and 4.4 Impact of Deformation on the Inclusion's Structure the film samples pPLA-film, PLA/acrylPEG-film, and PLA-film, as produced for 3.2 Analysis of the Structure were used and processing procedure is described in A.2.2 Mini-Extruder. For the isothermal crystallization, the PLA film samples were placed between two metal plates and heated to 100°C for 2 h in an oven (Thermo-Scientific Heraeus, Waltham, MA, USA) under vacuum. After 2h, the heating was stopped and the samples were slowly cooled to room temperature under vacuum. The samples were called PLA-IC (PLA after isothermal crystallization). All samples that were used in this chapter are listed in Table A. 3.

Table A. 3 List of the materials that were used in chapter 4 with the reference to section where the processing was described.

	material is used in section	processing equipment	processing is described in section
pPLA	4.2	micro-compounder	A.3.1

PLA	4.2	micro-compounder	A.3.1
pPLA-film	4.3	mini-extruder	A.4.1
PLA/acrylPEG-film	4.3	mini-extruder	A.4.1
PLA-film	4.3	mini-extruder	A.4.1
PLA-IC-film	4.3	mini-extruder	A.4.1
pPLA-film	4.4	mini-extruder	A.4.1
PLA-film	4.4	mini-extruder	A.4.1
PLA/acrylPEG-film	4.4	mini-extruder	A.4.1

A.4.2 Tensile Testing

For compression molded samples

The quasi-static uniaxial tensile testing of the compression molded samples in section 4.2 Deformation Mechanisms of Plasticized Polylactide was done with a universal testing machine Instron model 5967 (Norwood, MA, USA) equipped with an environmental chamber. To get the same experimental condition for each testing, at each change of temperature the chamber was first heated without specimen for 30 min to obtain the temperature uniform. Then, the specimen was set into the chamber for 15 min to allow thermal equilibration, and finally was tested. The engineering axial stress σ– axial strain ε curves were recorded at the constant crosshead rates of 0.6, 6 and 60 mm/min. Based on the tensile specimen gauge length of 25 mm, the corresponding initial strain rates were 4×10^{-4} s^{-1}, 4×10^{-3} s^{-1} and 4×10^{-2} s^{-1}, respectively. For each strain rate, tensile testing was carried out at the temperatures T of 20°C, 50°C and 80°C. As usually noted for polymers, PLA and pPLA samples underwent a nonuniform deformation process inducing a necking that generally initiated at geometrical, structural, and/or mechanical defects [160]. Due to technical limitations, it was not possible to measure the local mechanical variables at the necking level. A special attention was paid on the influence of the experimental conditions (T and $\dot{\varepsilon}$) on the tensile modulus E, the yield stress σ_y, the ultimate strain ε_u and the ultimate stress σ_u of the materials. The characterization of the specimens was conducted ex-situ at different strain levels. Each considered strain corresponded to the maximum strain reached at the end of the loading stage. Then, the specimen strain was kept constant during 30 min by a stress relaxation stage (at the same time the specimen was rapidly cooled down to 20°C for testing conducted at 50°C and 80°C), and finally the specimen was quickly analyzed by the different techniques.

For film samples

A miniature tensile/compression module Kammrath & Weiss (Dortmund, Germany) was utilized to get the deformation mechanisms of the materials. This machine was equipped with a 5 kN load cell (1 N of resolution within all the load range), and a linear variable differential transformer (LVDT) enabling to measure sample displacement. The dumbbell-shaped specimen were cut from the extruded film with their axis oriented parallel to the extrusion direction. Their initial gauge length L_o was about 37 mm and their width in the gauge section W_o was about 5 mm (exact values were measured for each sample). Drawing of the samples was conducted at 20°C with a crosshead displacement speed $\Delta L/\Delta t$ of 10 µm/s. The engineering strain ε_{eng} (in %) was calculated as $100 \cdot \Delta L/\Delta \mathrm{L}_0$ and the corresponding strain rate $\Delta\varepsilon\ /\Delta t = 1/L_0 \cdot \Delta L/\Delta t$ was evaluated to be 2.7×10^{-4} s^{-1}. The engineering stress σ_{eng} was calculated from the measured load divided by the initial cross-section S_0. The samples were drawn to a maximum engineering strain of 15%, which was the limitation of the machine.

A.4.3 Wide-Angle X-ray Scattering

Wide-angle X-ray scattering (WAXS) technique was selected to reveal the structural features of PLA and pPLA as a function of strain. Testing was made with a Panalytical X'Pert Pro MPD equipment configured with the transmission mode and using the Copper K_α radiation (wavelength λ = 1.54 Å) generated at 40 kV and 40 mA. The samples were cut from the center of the drawn tensile specimen. The diffractograms were recorded at room temperature in the 2Theta (2θ) range 5°- 40°. As primary optics, a focusing mirror was used with specific slits to allow a high resolution in the 2θ range of interest. As secondary optics, the PIXcel detector (Panalytical) was utilized to record the scattering intensity. The specimen was positioned onto a spinner that enabled to analyze different azimuthal angles Φ. When the angle Φ was equal to 0°, the detection was performed perpendicular to the tensile axis, and when the angle Φ was equal to 90°, the detection was performed parallel to the tensile axis. The analyzed volume corresponded to an irradiated surface of 0.6 mm x 2 mm multiplied by the specimen thickness, which depended on the deformation state. Note that the final thickness of each specimen was systematically measured by means of a digital calipers. The scattering intensity I (2θ) was first corrected by means of the Beer-Lambert relationship by considering an absorption coefficient of 9.23 cm^{-1} for PLA and pPLA, and the sample thickness. The absorption coefficient for PLA repeating unit $-(C_3H_4O_2)_n-$ was calculated as the sum of the atom mass coefficients considering their weight fraction in the repeating unit. The used atom mass coefficients for a Cu K_α radiation of C, H, and O were 4.51 cm^2/g, 0.391 cm^2/g, and 11.5 cm^2/g, respectively [161]. Then, the WAXS curves were treated with the software PeakFit (Systat Software) to perform the background subtraction by means of an exponential function and the peak deconvolution by means of Gaussian functions (Figure A. 2). To this end, we considered three amorphous halos located at a 2θ angle of around 15.0°, 21.2°, and 31.0° (Figure A. 2). The two first scattering halos were attributed to interchain periodicities, while the last scattering halo was attributed to an intrachain periodicity (distance between methyl groups) [73]. Concerning crystalline phases, we considered the peaks centered at the 2θ angles of 14.6°, 16.5°, 18.8° and 22.2° (Figure A. 2 b) attributed to the (010), (110/200), (203) and (210) reflections, respectively [51,73]. Since it is generally not possible to unambitiously distinguish between the crystalline phases α and α', we only considered one crystalline phase for all the WAXS analyses [21]. In the case of PLA, an amorphous to mesomorphic phase transformation can occur when drawing the material resulting in the formation of a board peak centered at 16.5° [76]. For a given azimuthal Φ direction, the weight fraction of crystallinity X_c was calculated as the ratio between the total crystalline peak area to the overall peak area. The average crystallinity $<X_c>$ was calculated based on the following equation [117,118]:

$$< X_c > = \frac{\int_0^{\pi/2} X_c(\Phi) \cdot \sum A(\Phi) \cdot \sin(\Phi) \cdot d(\Phi)}{\int_0^{\pi/2} \sum A(\Phi) \cdot \sin(\Phi) \cdot d(\Phi)}$$

(**Fehler! Verwenden Sie die Registerkarte 'Start', um Heading 6 dem Text zuzuweisen, der hier angezeigt werden soll.**.8)

where <$X_c(\Phi)$>was the crystallinity obtained for a given azimuthal angle Φ, while $\sum A(\Phi)$ was the sum of the area of all the peaks (amorphous, crystalline, and mesomorphic phases) for a given azimuthal angle Φ. The same methodology was used to calculate the weight fraction of the mesophase <X_{meso}>. The Herman's orientation function was calculated based on Equation (Fehler! Verwenden **Sie die Registerkarte 'Start', um Heading 6 dem Text zuzuweisen, der hier angezeigt werden soll.**.9) for the three amorphous halos, the two main crystalline peaks (110/200) and (203), and the mesomorphic peak:

$$f_{i,z} = \frac{3 < \cos^2 \Phi_{i,z} > -1}{2}$$

(**Fehler! Verwenden Sie die Registerkarte 'Start', um Heading 6 dem Text zuzuweisen, der hier angezeigt werden soll.**.9)

where *i* is the considered case, and $< \cos^2 \Phi_{i,z} >$ was the average of cosine squared angle between the normal of the considered scattering planes *i* (evolved by the crystalline diffractions or by the amorphous molecular scatterings) and the drawing direction *z*. In the following, $f_{1,z}$ corresponded to the amorphous halo positioned at 15.0°, $f_{2,z}$ corresponded to the amorphous halo positioned at 21.2°, $f_{3,z}$ corresponded to the amorphous halo positioned at 31.0°, $f_{(110/200),z}$ corresponded to the crystalline peak (110/200), $f_{(203),z}$ corresponded to the crystalline peak (203), and $f_{meso,z}$ corresponded to the mesophase. $< \cos^2 \Phi_{i,z} >$ was calculated from Equation (Fehler! Verwenden **Sie die Registerkarte 'Start', um Heading 6 dem Text zuzuweisen, der hier angezeigt werden soll.**.10):

$$< \cos^2 \Phi_{i,z} > = \frac{\int_0^{\pi/2} I_i(\Phi) \cdot \sin(\Phi) \cdot \cos^2(\Phi) \cdot d(\Phi)}{\int_0^{\pi/2} I_i(\Phi) \cdot \sin(\Phi) \cdot d(\Phi)}$$

(**Fehler! Verwenden Sie die Registerkarte 'Start', um Heading 6 dem Text zuzuweisen, der hier angezeigt werden soll.**.10)

where $I_i(\Phi)$ corresponded to the scattering intensity of the considered i objects (crystalline peaks or amorphous halos) for a given azimuthal Φ direction.

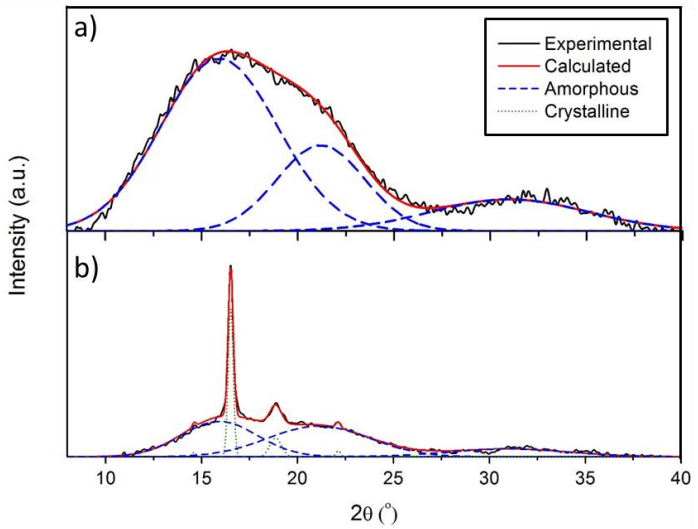

Figure A. 2 WAXS diagram deconvolution of a) PLA and b) pPLA at the undeformed state exhibiting in the two cases three amorphous halos at 2θ = 15.0°, 21.2°, and 31.0° and in the case of pPLA four crystalline peaks at 2 θ = 14.6°, 16.5°, 18.8°, and 22.2° engendered by the (010), (110/200), (203) and (210) reflections, respectively.

A.4.4 Differential Scanning Calorimetry

Differential scanning calorimetry (DSC) testing was carried out in the same way as described in A.3.6 and the thermal paramaters were determined similarly. In addition, the mesophase content in neat PLA was determined by using the mesophase enthalpy (ΔH_{meso}) based on the following equation, where $\Delta H_{meso,0}$ was the heat of fusion for a 100% mesophase PLA taken equal to 70 J/g [74].

$$X_{meso} = \frac{\Delta H_{meso}}{\Delta H_{meso,0}} \cdot 100\% \quad (11)$$

(Fehler! Verwenden Sie die Registerkarte 'Start', um Heading 6 dem Text zuzuweisen, der hier angezeigt werden soll..

A.4.5 Scanning Electron Microscopy

The microstructure of PLA and pPLA induced by drawing was studied by means of a pressure-controlled scanning electron microscope (SEM) model Quanta FEG 200 from FEI. The materials were first observed with the large field detector (LFD) at a water pressure of 150 Pa from polished samples in the case of PLA and cryo-surfaced samples in the case of pPLA. Cryo-surfacing consisted in removing very thin specimen sections at -30°C with a cryo-ultramicrotome Leica EM UC6/UF6 equipped with a glass knife. Observations were ever conducted at the center of the specimen necking characterized by the highest deformation level. The pPLA sample was also investigated with the transmission mode of the SEM called STEM mode from 80 nm-thick specimens prepared with the cryo-ultramicrotome. To this end, a small specimen volume was first extracted and grossly trimmed with a razor blade from the center of the tensile specimen. The specimen was afterward sectioned at -30°C parallel to the tensile direction with a glass knife and subsequently with a diamond blade (reference Diatome Cryo 35°). STEM images were recorded with the bright field detector enabling phase contrast imaging.

A.4.6 Time-Resolved Small-Angle X-ray Scattering

The time-resolved SAXS experiments were carried out at the Elettra synchrotron (Trieste, Italy) with a photon energy of 8 keV that corresponded to the Cu k_α wavelength radiation of 0.154 nm. The incident X-ray beam hitting the specimen had the dimensions of about 2000 µm × 400 µm (rectangle with the vertical axis parallel to tensile direction). The scattering signal was recorded by means of a 2D detector Pilatus 100K from Dectris (Baden, Switzerland), using an acquisition time of 20 s. The detector was positioned at about 1.80 m from the samples, which allowed to measure periodicities ranging from 4 nm to 60 nm. Before the measurement, a background image was recorded without specimen and the background signal was subtracted from all images by means of the software ImageJ (National Institutes of Health, USA).

The calibration was established with silver behenate sample supplied by the synchrotron beamline. The calibration parameters (beam center, detector distance, tilt plane rotation angle, tilt angle, and proportional D-spacing) were determined by means of the software Fit2D (ESRF, Grenoble, France) and used to determine the scattering intensity as a function of the q-range for all samples.

The intensity vs q-range plots were generated for two zones of interest. The first zone included the equatorial region, which was perpendicular to the drawing direction, and the second zone included the meridian region, which was parallel to the drawing axis. To this aim, two masks with an angle of 45° were generated (Figure A. 3), which also allowed excluding the dead pixels from the beam stop for the integration. The created intensity vs q-range plots allowed an integration for the equatorial mask in the q-range of 9.86×10^{-2} – 2.31 nm^{-1}, and for the meridian mask in the q-range 2.44×10^{-1} –

2.12 nm^{-1}. The scattering intensities over the q-ranges were integrated by means of the software OriginPro8 and due to the exposure time of 20 s, a scattering intensity value was obtained every 20 s for both, the equatorial and the meridian scattering. To get impact of the deformation on the scattering intensity, the equatorial and meridian intensity values for the first image (undeformed, at 0 s) were subtracted of all following scattering intensity values of the samples for the equatorial and meridian direction, respectively. The measurement of scattering intensity is considered as a semi-quantitative information enabling to characterize the possible formation of craze in PLA-based materials. In this case, the scattering in the equatorial zone was related to the fibrillation inside crazes, while the meridian scattering was related to the scattering by craze walls [55,126]. As previously show the scattering intensity in the meridian zone was proportional to the volume fraction of craze forming in semicrystalline polymers [117].

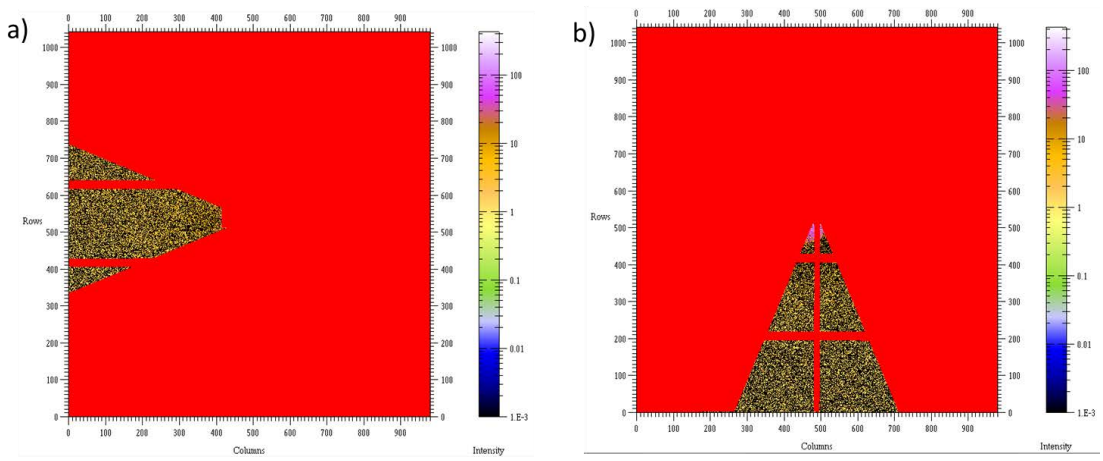

Figure A. 3 Equatorial (transverse the tensile axis) and (b) meridian (along the tensile axis) masks on a SAXS pattern for the integration of the scattering intensity. Both masks have an angle of 45°. The tensile axis was vertical.

A.4.7 Optical Microscope Analysis

To observe the deformation heterogeneities of the samples under optical probing, the miniature tensile module was placed under a stereomicroscope Leica MZ 125 (Heerbrugg, Switzerland) with a x20 objective. The central section of the samples was observed during the tension and images were recorded. For PLA 1 image per second was recorded, while for pPLA and PLA/acrylPEG, 1 image per 5 seconds was recorded due to the higher possible elongation.

The determination of the surface defect density was done by means of the software ImageJ (National Institutes of Health, Bethesda, MD, USA). The images were converted to black-white images, where the voids were determined as black areas and the ratio of the black part was determined.

A.4.8 Digital Image Correlation

Digital Image Correlation (DIC) was conducted with an Aramis 6M system from Gom Optical Measuring Techniques (Braunschweig, Germany). The system was equipped with two cameras to allow a 3D analysis of the material's strain field. The samples were first painted with white color and afterward speckled with a spray of black color creating a pattern that allowed the DIC process by the software AramisProfessional. The images were recorded with a fixed frame rate of 1Hz during the tensile testing with the miniature tensile testing machine. Only the main tensile specimen face was visualized by DIC. To obtain the axial and transversal strains of the samples, in the center of the specimen, two 2-Point distances ($l_{t,axial}$ and $l_{t,transversal}$) were created with an gauge length of about 1.5 mm, that defined the distance of these 2 points at a given time t. With the initial distances ($l_{0,axial}$ and $l_{0,transversal}$) the axial (ε_{11}) and transversal strain (ε_{22}) were calculated with the Equations (**Fehler! Verwenden Sie die Registerkarte 'Start', um Heading 6 dem Text zuzuweisen, der hier angezeigt werden soll.**.12) and (**Fehler! Verwenden Sie die Registerkarte 'Start', um Heading 6 dem Text zuzuweisen, der hier angezeigt werden soll.**.13), respectively. Due to the low thickness of the samples, the second transversal strain (ε_{33}) was not measured, but it was assumed that $\varepsilon_{33} \approx \varepsilon_{22}$. A rough estimation of the volume strain (ε_v) can be obtained as the sum of the strains in the three directions as described by Equation (Fehler! Verwenden **Sie die Registerkarte 'Start', um Heading 6 dem Text zuzuweisen, der hier angezeigt werden soll.**.14).

$$\varepsilon_{11} = \ln \frac{\mathrm{l}_{\mathrm{t,axial}}}{l_{0,axial}}$$

(**Fehler! Verwenden Sie die Registerkarte 'Start', um Heading 6 dem Text zuzuweisen, der hier angezeigt werden soll.**.12)

$$\varepsilon_{22} = \ln \frac{\mathrm{l_{t,transversal}}}{l_{0,transversal}}$$

(**Fehler! Verwenden Sie die Registerkarte 'Start', um Heading 6 dem Text zuzuweisen, der hier angezeigt werden soll.**.13)

$$\begin{aligned} \varepsilon_v &= \varepsilon_{11} + \varepsilon_{22} + \varepsilon_{33} \\ &= \end{aligned}$$

$$\varepsilon_{11} + 2 \cdot \varepsilon_{22}$$

(**Fehler! Verwenden Sie die Registerkarte 'Start', um Heading 6 dem Text zuzuweisen, der hier angezeigt werden soll.**.14)

The ratio of the axial deformation (ε_{11}) to the average absolute value of the transversal deformation ($|\varepsilon_t|$) was defined as the coefficient $D = \varepsilon_{11}/|\varepsilon_t|$, whereas $\varepsilon_t = (\varepsilon_{22} + \varepsilon_{33})/2$. With the assumption $\varepsilon_{33} \approx \varepsilon_{22,}$ D can be determined as $D = \varepsilon_{11}/|\varepsilon_{22}|$ or from the volume strain measurement as described by Equation (**Fehler! Verwenden Sie die Registerkarte 'Start', um Heading 6 dem Text zuzuweisen, der hier angezeigt werden soll.**.15). In the elastic regime, the factor D can be related to the Poisson coefficient ν ($D^{-1} = \nu$).

$$\varepsilon_v = (1 - 2D^{-1}) \cdot \varepsilon_{11}$$

(**Fehler! Verwenden Sie die Registerkarte 'Start', um Heading 6 dem Text zuzuweisen, der hier angezeigt werden soll.**.15)

In the case that the deformation heterogeneities are crazes an increase of the volume strain was expected [117]. The true stress (σ_{true}) was calculated by Equation (**Fehler! Verwenden Sie die Registerkarte 'Start', um Heading 6 dem Text zuzuweisen, der hier angezeigt werden soll.**.16) taking into account the variation of the cross-section with the above mentioned assumption that the two transversal strains are equal.

$$\sigma_{true}(MPa) = \frac{F(N)}{S_0(mm^2)} \cdot \exp(-\epsilon_{22} + \epsilon_{33})$$

$$= \frac{F(N)}{S_0(mm^2)} \cdot \exp(-2 \cdot \epsilon_{22})$$

(**Fehler! Verwenden Sie die Registerkarte 'Start', um Heading 6 dem Text zuzuweisen, der hier angezeigt werden soll.**.16)

A.4.9 Micro-Compounded X-ray Tomography

Micro-computed X-ray tomography (µCT) testing was conducted on a drawn pPLA tensile sample to investigate the structure of the material. The equipment used was an Xradia 510 Versa 3D X-ray Microscope from Zeiss (Pleasanton, CA, USA). The µCT images were recorded during 19.5 h at 40 kV, 3 W, and with a 40× objective. One area at the center of tensile specimen at the most deformed zone (where intense whitening was observed), and one area at a not or little deformed zone of tensile specimen (transparent area) were scanned. The two volumes were reconstructed with a 0.3 µm voxel size. Note that only 2D images were extracted from the reconstructed volume corresponding to a slice taken at the center of each volume.

A.5 Characterization Methods for Chapter 5: Structure Evolution with Reprocessing

A.5.1 Processing and Reprocessing

Processing and reprocessing of PLA and pPLA were simulated with laboratory equipment, meaning with small material quantities and specific machines with operating conditions that may only partially reflect industrial realities. Nevertheless, lab-scale simulation of recycling appeared as a fast and cost-effective procedure to get first information about recycling-induced degradation mechanisms of the materials enabling to optimize an eventual scale-up study of their recycling.

PLA and pPLA were produced as described in A.2.1 Micro-Compounder. Before the first extrusion, neat PLA was dried in a vacuum at 50°C for 12h. The two materials, PLA (PLA/acrylPEG/L101 with weight composition 100/0/0) and plasticized pPLA (PLA/acrylPEG/L101 with weight composition 79/20/1) were extruded using a twin screw micro-compounder with a nitrogen purge. The melting temperature was set to 180°C and the screw speed was adjusted to 50 rpm. In total 12 g per batch were introduced within the micro-compounder for a total extrusion time of 5 min (with recirculation) to produce strands of diameter 3 to 5 mm. For pPLA reactive extrusion, acrylPEG and L101 were first mixed in a glass vial and then injected within the micro-compounder by means of a syringe after the PLA was melted in the extruder.

Before shaping by compression molding, the extruded strands were cut by hand into 5 mm-long pellets. Compression molding was conducted on a Carver manual press (Wabash, IN, USA) equipped with heating plates. The PLA or pPLA pellets were placed in a tile mold Carver (Wabash, IN, USA) enabling to produce plates of 10 cm x 10 cm x 0.2 cm and then were melted at 180°C for 10 min without applying any pressure. After several degassing steps by successive compressing/ decompressing procedures with a maximum applied load of 7 metric tons, the materials were compressed with a constant applied load of 7 metric tons at 180°C for 10 min. The plates were cooled

down under the same pressure during 10 min by a room temperature water circulation within the press plates.

After the shaping by compression molding, the recycling was simulated by several cutting/extrusion/cutting/compression-molding procedures, as represented in Figure A. 4. Each cutting step was done by hand using a sharp tile nipper. Before each re-extrusion, pPLA pellets were dried at 30°C in a vacuum oven for 12 h, while PLA pellets were dried at 50°C under the same conditions due to the T_g difference between the two materials. All samples were named starting with their material type (PLA, pPLA) and finishing with the number of compression molding steps (CM1, CM3, CM5). It is to be noted that the characterization was systematically conducted from the shaped plates of (p)PLA.

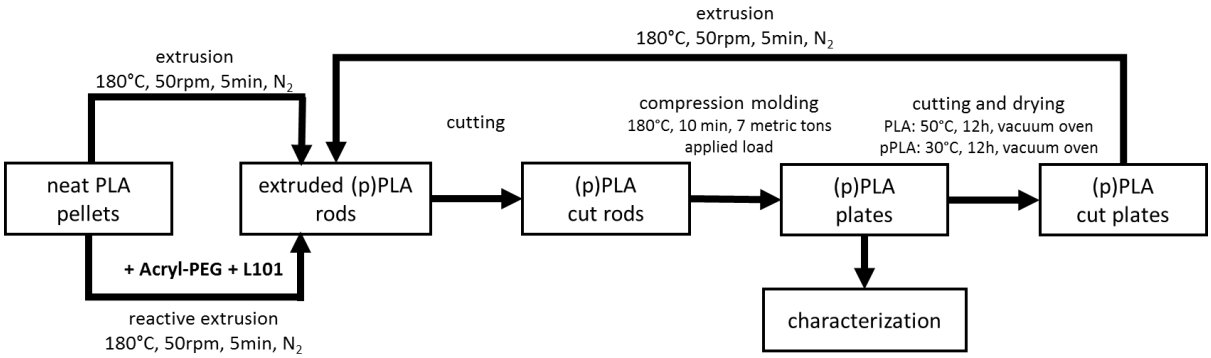

Figure A. 4 Processing and reprocessing procedures of (p)PLA including the main experimental conditions.

As a comparison samples with different reprocessing cycles were processed. The first reprocessing cycle contained as a thermomechanical step just extrusion and the second comparison cycle contained instead of compression molding injection molding as a shaping step. The samples were named with their material type (PLA or pPLA) followed by the reprocessing cycle (E for extrusion and IM for extrusion and injection molding) with the respective number of extrusion or shaping steps.

A.5.2 Dynamic Mechanical Analysis

The viscoelastic response of (p)PLA was assessed by dynamic mechanical analysis (DMA) using a Netzsch DMA 42 C equipment (Selb, Germany). For this measurement, samples with dimensions 10 mm x 60 mm x 2 mm were machined from compression-molded plates. DMA testing was conducted with the double cantilever mode of flexural loading in the temperature range from -100°C to 120°C with a heating rate of 2 K/min. The specimen were subjected to a loading amplitude of 20 µm and frequencies of 1, 5, 10, 50 and 100 Hz. Attention was focused on the evolution of storage modulus E',

and loss factor tan δ = E''/E' (E'' was the loss modulus) as a function of the temperature. All the materials were tested twice.

A.5.3 Tensile Testing

The elasto- and viscoplastic response of (p)PLA at different temperatures was obtained by tensile testing. Dumbbell specimens were machined from the 2mm-thick compression-molded plates to obtain ASTM D638-10 sample type V specimens. The quasi-static uniaxial tensile testing was measured with a universal testing machine Instron model 5967 (Norwood, MA, USA) equipped with an environmental chamber at the temperatures 20°C, 50°C and 80°C. First, the environmental chamber was heated to the targeted testing temperature and then was left to this temperature for temperature homogenization during 30 min. The specimen was mounted and left 15 min at the chamber temperature for thermal equilibration before being tested. The engineering axial stress σ– axial strain ε curves were recorded at the constant crosshead speed of 60 mm/min. Based on the tensile specimen gauge length of 25 mm, the corresponding initial strain rate $\dot{\varepsilon}$ was 4×10^{-2} s^{-1}. It is important to note that the deformation of (p)PLA was nonuniform and led to necking due to geometrical, structural, and/or mechanical defects [160]. Our reported engineering axial stress σ – axial strain ε tensile curves did not take into account localization of strain because of technical limitations. The tensile modulus E, the yield stress σ_y, the ultimate strain $\varepsilon_u$and the ultimate stress σ_u of the materials were calculated as a function of the number of recycling cycles and the temperature. For every condition at least three specimens were tested.

A.5.4 Impact Testing

For impact testing, specimen of dimensions 62 mm x 8 mm x 2 mm were machined from compression molded plates. The specimen were notched with an Instron Ceast Motorized Notchvis machine (Norwood, MA, USA). The radius of the notch was 25 mm, while its angle was 45°. The samples were tested on an impact pendulum Instron Ceast 9050 (Norwood, MA, USA) at room temperature according to ISO 180 standard. The exact specimen dimensions were measured and the impact energy was calculated by the integrated software of the pendulum machine. At least 5 specimens were tested per material.

A.5.5 Differential Scanning Calorimetry

The DSC was conducted as described in A.3.6 Differential Scanning Calorimetry.

A.5.6 Scanning Electron Microscope

The microstructure of pPLA was studied by means of a pressure-controlled scanning electron microscope (SEM) model Quanta FEG 200 from FEI (Eindhoven, The Netherlands). The samples were cut from compression molded plates and prepared by polishing the surface with a manual polishing machine. SEM observations were done at a water pressure of 150 Pa, with an accelerating voltage ≤ 7 kV to limit the pPLA surface degradation and with the large field detector for topographical contrast imaging.

A.5.7 Atomic Force Microscope

The morphology of the samples was characterized by means of an atomic force microscope (AFM) in acoustic mode on an Agilent 5100 from Agilent Technologies (Santa Clara, CA, USA). The scanned pictures consisted of 512 pixels x 512 pixels images obtained at a scanning speed comprised between 0.9 and 1.1 lines per second. As operating parameters, a cantilever free amplitude of 2 µm and a resonance frequency of 285.8 kHz were selected. The samples were prepared with a cryo-ultramicrotome Leica EM UC6/UF6 (Vienna, Austria) at -50°C by cutting small surfaces first with a glass knife and polishing the surface subsequently with a diamond blade (Diatome Cryo 35°, Hatfield, PA, USA).

A.5.8 Gel Permeation Chromatography

Thermomechanical Reprocessing with Compression Molding

The molecular weight and molecular weight distribution of PLA were assessed by gel permeation chromatography (GPC). To this end, samples were dissolved in chloroform to a concentration of 1.5 mg/ml and filtered with a nylon acrodisc syringe filter (pore size 0.45 µm). GPC was performed on an Agilent Technologies series 1200 (Santa Clara, CA, USA) working with a differential refractive index detection and two linear columns (PLgel 5µm Mixed-D, 200 Da < MW < 400 kDa) in addition to a protection column. The number average (M_n) and weight average molecular (M_w) weights standardized to polystyrene and the dispersity index ($Đ = M_w/M_n$) were determined for all the samples. At least 3 samples were tested for each material and the average with standard deviation was calculated from these 3 values. Note that pPLA samples were not totally soluble in chloroform, so that no GPC measurement on this material could be performed.

Comparison of the Three Reprocessing Cycles

The GPC for the comparison of the three reprocessing cycles was conducted as described in A.3.4 Gel Permeation Chromatography.

A.5.9 Fourier Transform Infrared Spectroscopy

The chemical functions of (p)PLA were characterized by Fourier transform infrared spectroscopy (FTIR). Such analyses were conducted on a Bruker Tensor 27 (Ettlingen, Germany) in attenuated total reflection (ATR) mode. First, a background spectrum was recorded and subtracted from the sample spectrum in the area from 4000 cm^{-1} to 400 cm^{-1}.

A.5.10 Nuclear Magnetic Resonance Spectroscopy

The chemical structure of (p)PLA was analyzed by nuclear magnetic resonance spectroscopy (NMR). In particular, the samples were dissolved in deuterated chloroform ($CDCl_3$, containing 0.03% of tetramethylsilane (TMS)) to obtain a concentration of about 50 mg/ml. ^1H NMR spectra were recorded with a Bruker AMX-500 (Karlsruhe, Germany) at a frequency of 500 MHz and in a magnetic field of 11.6 Tesla. Peak positions and integrals (PLA: CH_3 doublet at 1.58 ppm and CH at 5.16 ppm; poly(acrylPEG): CH_2 singlet at 3.59 ppm) were determined with the software MestReNova (Mestrelab Research S.L., Santiago de Compostela, Spain) and the acrylPEG weight content was determined by the Equation (Fehler! Verwenden **Sie die Registerkarte 'Start', um Heading 6 dem Text zuzuweisen, der hier angezeigt werden soll.**.17):

$$wt\%(PEG) = \frac{\frac{area_{PEG}}{N_{H,PEG}} \cdot M_{PEG}}{\frac{area_{PLA}}{N_{H,PLA}} \cdot M_{PLA} + \frac{area_{PEG}}{N_{H,PEG}} \cdot M_{PEG}}$$

(**Fehler! Verwenden Sie die Registerkarte 'Start', um Heading 6 dem Text zuzuweisen, der hier angezeigt**

werden

soll..17)

A.5.11 Rheology Measurements

Compression molding cycle

The rheology measurements were conducted to obtain from the viscosity values qualitative information about the molecular weight of crosslinked pPLA samples. To this end, testing was conducted on an ARES Rheometer from Rheometrics (Piscataway, NJ, USA) at 180°C. The gap for the sample was 0.5 mm and the diameter of the plates was 25 mm. The measurements were conducted on the same samples in two modes. Strain sweep mode at a frequency of 1 Hz was conducted in the strain range 100% to 0.01%, while frequency sweep mode at a strain of 1% (if 1% contained in the linear area of strain sweep) was conducted from 100 Hz to 0.01 Hz. For both measurement modes, 30 points per decade were recorded.

Injection molding cycle

Rheological properties of PLA and pPLA were determined on a Modular Compact Rheometer MCR302 WESP from Anton Paar equipped with a heating system (Peltier System H-PTD 200), that heats the top and the bottom of the samples. All rheology measurements were performed on PLA (IM1, IM3, and IM5) and pPLA (IM1, IM3, and IM5) at 180°C. The flakes of pPLA were molten for 2 min, and a 3 min pre-shear at a shear rate of 5 s^{-1} was used for homogenization. The frequency sweep in the frequency range from 314 s^{-1} to 0.1 s^{-1} with an amplitude of 5% strain allowed the determination of the storage modulus G', the loss modulus G'', and the loss factor $\sigma = G''/G'$ as a function of frequency. Subsequent to the frequency sweep measurement, flow curves were detected with the same sample, even if a slight degradation between two measurements with the same sample was observed.

A.5.12 Soxhlet Extraction

The Soxhlet extraction was conducted as described in A.3.3 Soxhlet Extraction.

A.5.13 Isothermal Crystallization Process

The isothermal crystallization was conducted by the same methodology as described in A.3.9 Isothermal Crystallization Measured by Wide-Angle X-ray Scattering.

B Limonene and Myrcene as New Plasticizers for Polylactide

B.1 Introduction

Polylactide (PLA) is a bio-based and (bio)degradable polymer that raised hope to be substitute common plastic materials [17,32,86,162]. PLA, such as other biopolymers, allow producing plastic materials without the disadvantages of common plastic materials like production from non-renewable resources. The common plastics are petrol-based and create a high pollution due to their high consummation and resistance to degradation. However, PLA has some drawbacks compared to the common plastic materials, especially its brittleness at room temperature limits the application range. Plasticization with different molecules or polymers was investigated to improve the brittle behavior at room temperature [15,40,163,164], but migration and phase separation limit the plasticizing effect or the durability of plasticization [40,165,166]. Reactive plasticization allows grafting of a plasticizer onto the PLA matrix and while plasticization by blending often causes a strong decrease in stiffness and gains rubber-like materials, the reactive plasticization creates materials with a good stiffness-ductility balance [14,34,41,51]. This reactive extrusion was used for PEG derivatives [41,51] but never used for natural plasticizers. For the reactive plasticization, the plasticizer requires a functional group that is able to react with a free radical initiator to create a grafting onto the PLA chains. Limonene is already known as a plasticizer for PLA [167] and offers with double bonds possible reactive functions for the reactive plasticization. In addition, myrcene, which is like limonene a terpene, offers also reactive functions and could be used for the plasticization of PLA. The chemical structures of both natural possible plasticizers are shown in Figure B. 1.

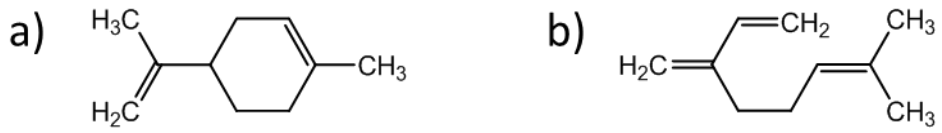

Figure B. 1 Chemical structures of the two plasticizers a) limonene and b) myrcene.

As described in the previous chapters of this manuscript and in the literature [41,50–52], the reactive plasticization of PLA with acrylPEG as plasticizer forms inclusions of poly(acrylPEG). This same technique was applied to create PLA-based materials with limonene or myrcene as a plasticizer. For both materials, the reactive plasticization was compared to the simple blending. In this chapter, the mechanical and thermal properties of four materials were analyzed: PLA/limonene (80/20),

PLA/limonene/L101 (79/20/1), PLA/myrcene (80/20) and PLA/myrcene/L101 (79/20/1), whereas the numbers give the weight percent of the components.

B.2 Plasticization by (Reactive) Extrusion

As already seen before (3.2.1 Processing of Plasticized Polylactide in a Batch-Compounder), the extrusion force can indicate the reactions during the extrusion and lead to information about the formed chemical structures. Both cases of plasticization with limonene, the simple blending (orange curve) and the reactive compounding (pink curve) exhibited a similar extrusion force curve (Figure B. 2 a). After the injection of the liquid plasticizer or plasticizer-initiator mixture, the force decreased and reached with slight variation a stable value that remained to the end of the extrusion. The final force was for both materials slightly lower than the starting force for neat PLA. In contrast, for the plasticization with myrcene (Figure B. 2 b), the simple blending (green curve) showed the decrease of the force after the liquid plasticizer injection followed by a curve with higher up- and down turns, reaching at the end of the extrusion time a similar force as the neat PLA. For the reactive compounding with myrcene and the initiator (blue curve), the force decreased slightly after the injection of the plasticizer-initiator mixture but increased up to the end of the extrusion time continuously, reaching a force value higher than for the neat PLA.

These extrusion force curves can lead to the assumption that no grafting or polymerization reactions happened in the samples plasticized with limonene. Even the addition of the initiator seemed to have no impact and no reactions with increasing or decreasing the viscosity were observed. For PLA/myrcene, a similar behavior with no clear force increase was observed and no conclusion about reactions could be made. The only sample with a clearly increasing force was PLA/myrcene/L101. This behavior could indicate that this reactive blend undergoes reactions during the reactive blending and polymerization of myrcene and/or grafting of myrcene onto the PLA matrix could occur. In the literature, it was shown that myrcene is able to be polymerized by a radical initiator [168] and due to the three functional groups, different microstructures of the polymerized myrcene could occur. It was assumed that these reactions can also arise during the reactive compounding.

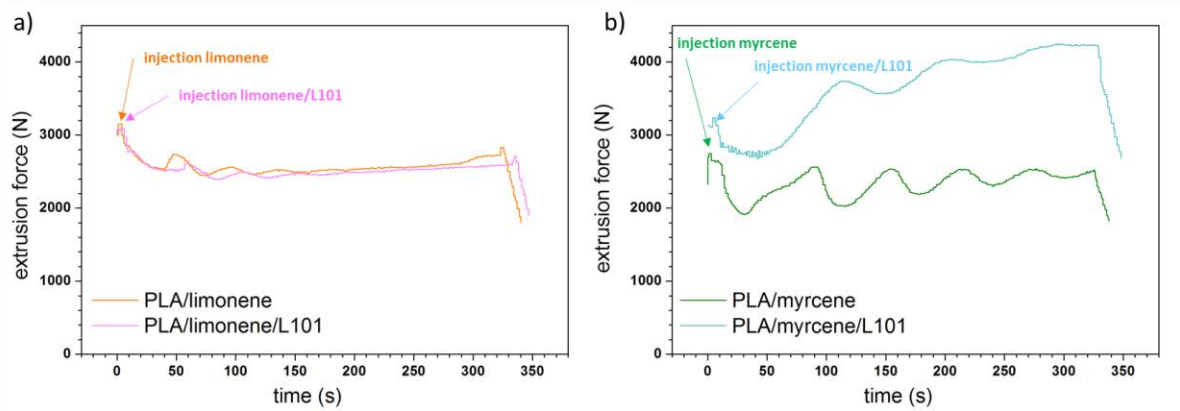

Figure B. 2 Extrusion force curves for the non-reactive and reactive blending with a) limonene and b) myrcene.

B.3 Mechanical Investigation

The main goal of plasticization is to improve the mechanical performances of PLA-based materials. The engineering stress-strain curves in Figure B. 3 and the parameters in Table B. 1 indicate that limonene and myrcene are effective plasticizers for PLA. In the normal case plasticization of PLA induces both effects on the mechanical behavior: On one side, the elongation at break is increased and the material becomes more ductile, and, on the other side, the initial stiffness of PLA is lost and a decreased tensile modulus, as well as lower stress values, are obtained. Both plasticizers and both plasticization methods showed these two effects but with different intensities. All four samples exhibited a higher elongation at break than observed for brittle PLA. The differences between limonene and myrcene were quite obvious – the limonene-plasticized samples reach nearly double of the elongation of break of the myrcene samples – but the impact of the initiator is less clear. For limonene, the elongation at break is similar for both plasticization methods (ε_{eng} ≈ 120%), and for myrcene, the elongation at break is about one quarter lower for the reactive blending (ε_{eng} = 45.0%) compared to the non-reactive blending (ε_{eng} = 62.7%). The tensile modulus for limonene-plasticized samples (E = 1.0 GPa and E = 1.2 GPa for PLA/limonene and PLA/limonene/L101, respectively) was clearly reduced compared to PLA (E = 2.3 GPa) and as shown in earlier studies with acrylPEG [41,50], the tensile modulus is slightly higher for the sample from reactive plasticization. In contrast, for the two myrcene samples (E = 1.9 GPa and E = 1.7 GPa for PLA/myrcene and PLA/myrcene/L101, respectively), the tensile modulus was for both plasticization methods between the tensile modulus of the limonene-plasticized samples and the PLA comparison sample. Surprisingly, the tensile modulus for PLA/myrcene was slightly higher than for the non-reactive blending.

In addition to an increase of the ductility, plasticization can improve the toughness. The reactive and non-reactive blending with acrylPEG as plasticizer increased the impact energy to 38.4 kJ/m^2 and 84.2

kJ/m^2, respectively (3.2.4 Impact Resistance). Compared the plasticization with acrylPEG, the impact energy is less increased for both limonene- and myrcene-plasticized materials. The maximum value was reached for PLA/myrcene IE = 12.5 kJ/m^2, while the other samples obtained values below 6 kJ/m^2. Nevertheless, all plasticized materials offered an improved impact energy compared to neat PLA with IE = 2.7 kJ/m^2.

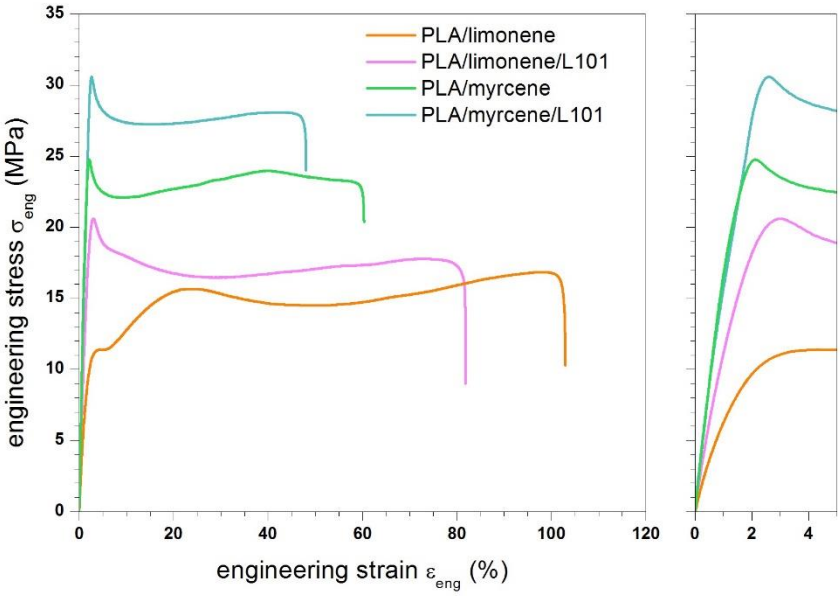

Figure B. 3 Engineering stress-strain curves for limonene- and myrcene-plasticized materials.

Table B. 1 Mechanical parameters for limonene- and myrcene plasticized materials compared to PLA.

	tensile modulus E (GPa)	stress at yield σ_y(MPa)	ultimate strain ε_u (%)	ultimate stress σ_u (MPa)	impact energy IE (kJ/m^2)
PLA/limonene	1.0 ± 0.2	12.6 ± 2.8	117.5 ± 21.5	15.8 ± 2.6	5.5 ± 0.5
PLA/limonene/L101	1.2 ± 0.2	20.1 ± 1.6	120.2 ± 23.5	17.2 ± 1.9	5.8 ± 0.6
PLA/myrcene	1.9 ± 0.1	25.8 ± 1.3	62.7 ± 13.2	18.7 ± 0.8	12.5 ± 0.9
PLA/myrcene/L101	1.7 ± 0.2	30.2 ± 0.8	45.0 ± 8.4	24.8 ± 0.9	4.9 ± 0.1
PLA	2.3 ± 0.3	70.2 ± 1.5	7.4 ± 1.0	60.6 ± 31.1	2.7 ± 0.1

B.4 Thermal Properties

Plasticization, independent if by reactive or non-reactive blending, influences the thermal properties. In general, the plasticization increases the free volume of the material and decreases, therefore, the glass transition temperature. Figure B. 4 a compared the first (dashed line) and the second (continuous line) heating for the four materials and the cooling stages are plotted in Figure B. 4 b. During the cooling stage, none of the materials crystallized and just slight glass transitions were observed. The glass transition temperatures of all materials stage were slightly lower than for PLA (54.4°C). For both limonene-plasticized samples, the glass transitions temperatures were 46.5°C and 48.1°C for the non-reactive and the reactive blending, respectively. The samples with myrcene had higher glass transition temperature of 50.5°C and 52.6°C for the nonreactive and the reactive blending, respectively. For both plasticizers, the glass transition temperature was a few degrees higher for the reactive blending compared to the nonreactive blending. This could indicate that grafting or crosslinking occurred which lowers the free volume in the samples compared to the simple blending method. However, the decrease was very low, so that the grafting or crosslinking density would be low as well or this increase was just a measurement artifact.

In the heating stages (Figure B. 4 a), differences between both plasticizers became apparent. Both limonene-plasticized samples show a strong decrease of the glass transition temperature to a value below 30°C for the first heating stage. Interestingly, the glass transition temperature was in the cooling state observed at over 40°C and finally in the second heating state around 50°C, which is just 10°C lower than for PLA with 60.9°C. The same behavior was observed for the cold crystallization temperature. First, a low cold crystallization temperature was observed at about 70°C and in the second heating stage, the cold crystallization temperature was higher than 100°C for both materials. The melting temperature raised just by a few degrees from the first to the second heating stage. It is obvious that the cold crystallization appears as a narrow peak in the first heating stage and with a broad peak in the second heating stage. However, it was observed, that the effect of the reactive blending is very low for the plasticization with limonene since all thermal properties were quite similar for both samples (Table B. 2). This supports the previous interpretation of the extrusion force, where no differences between the nonreactive and the reactive blending were observed, too. Just the crystallinity indices were slightly higher for the reactive blending.

For both myrcene-plasticized materials, higher glass transition temperatures were observed for the first heating compared to the limonene-plasticized samples and just an increase by a few degrees was recognized in the second heating stage. In the second heating stage, the glass transition temperatures of PLA/myrcene (Tg = 54.3°C) and PLA/myrcene/L101 (Tg = 57.1°C) were just a few degrees lower than for PLA (Tg = 60.9°C). In the first heating stage, the glass transition was accompanied by a small

endothermal peak, which was not present in the second heating stage. This endothermal peak was also observed in neat PLA and was attributed to the melting of the mesophase or aging of the samples [54,55]. For PLA/myrcene, the cold crystallization temperature was more than 13°C higher comparing the first and second heating stage. In contrast, for PLA/myrcene/L101 just a minor difference of about 3°C was observed. This stable cold crystallization temperature was the only obvious difference between the reactive and non-reactive blends with myrcene. In the first heating stage, both samples showed a double melting peak, which disappeared in the second heating stage. This could lead to the assumption, that the material is more homogeneous in the second heating stage or at least the crystal formation during the cold crystallization is more homogeneous. Again the crystallinity was slightly higher for the non-reactive blending and lower for the second heating stage compared to the first heating stage.

Table B. 2 DSC parameters for limonene- and myrcene-plasticized materials compared to PLA.

		T_g (°C)	T_{cc} (°C)	T_m (°C)	ΔH_{cc} (J/g)	ΔH_m (J/g)	X_c (%)
PLA/limonene	1	27.1 ± 0.2	70.5 ± 4.6	144.8 ± 0.5	12.5 ± 5.5	22.0 ± 1.1	10.2 ± 4.8
	2	46.5 ± 1.3					
	3	50.6 ± 0.3	105.1 ± 0.6	148.9 ± 0.1	16.5 ± 0.5	19.9 ± 0.5	3.6 ± 0.1
PLA/limonene/ L101	1	27.5 ± 0.8	71.9 ± 1.2	143.4 ± 1.1	7.3 ± 2.2	21.3 ± 0.3	15.0 ± 2.0
	2	48.1 ± 1.1					
	3	50.7 ± 0.6	109.2 ± 0.3	147.2 ± 0.4	11.8 ± 1.4	18.2 ± 0.6	6.9 ± 0.9
PLA/myrcene	1	49.9 ± 1.7	97.1 ± 3.1	142.4 ± 1.8 & 150.8 ± 0.4	13.3 ± 1.6	21.1 ± 1.0	8.4 ± 0.7
	2	50.5 ± 0.5					
	3	54.3 ± 0.4	110.5 ± 2.3	148.4 ± 0.3	18.1 ± 0.8	21.5 ± 1.1	3.6 ± 0.2
PLA/myrcene/ L101	1	54.3 ± 0.4	102.0 ± 0.7	145.2 ± 0.2 150.5 ± 0.3	11.4 ± 0.5	17.5 ± 1.5	6.5 ± 2.3
	2	52.6 ± 0.5					
	3	57.1 ± 0.5	105.8 ± 2.3	147.9 ± 0.6	13.1 ± 1.8	18.0 ± 0.4	5.2 ± 1.5
PLA	1	60.8 ± 0.6	126.9 ± 0.0	155.4 ± 0.5	4.7 ± 0.1	8.3 ± 1.4	3.9 ± 1.4
	2	54.4 ± 0.4	-	-	-	-	-
	3	60.9 ±0.1	127.9 ± 0.1	154.5 ± 0.1	2.1 ± 0.8	2.8 ± 0.5	0.8 ± 0.3

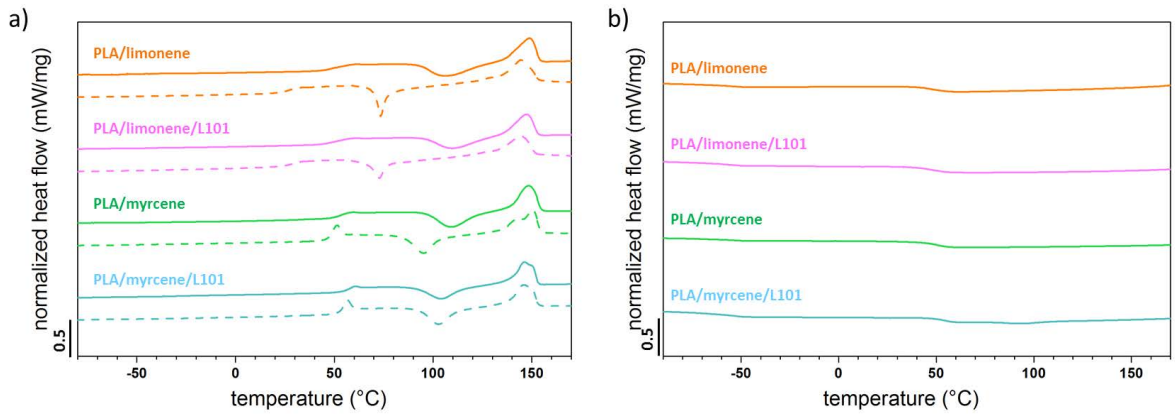

Figure B. 4 DSC curves of limonene- and myrcene-plasticized materials for a) the first (dashed line) and second (continuous line) heating and b) the cooling stages.

The comparison between the first and the second heating stage allows the comparison for the as-processed materials and materials with a similar thermal history and for the plasticized materials the differences are obvious. This behavior could indicate, that the materials' properties are changed by further thermal steps and maybe more homogeny materials are formed. It is important to mention that despite the higher glass transition temperatures (which were close to PLA's glass transition temperature) the mechanical properties indicated a good plasticization effect of both plasticizers.

B.5 Conclusion & Outlook

The comparison of the reactive and the non-reactive blending of PLA with the two natural plasticizers limonene and myrcene showed promising mechanical performances. Both plasticizers were melt-blended with PLA in the absence or presence of a free radical initiator. The composition for the materials was 80/20 wt% (PLA/plasticizer) for the non-reactive blends and 79/20/1 wt% (PLA/plasticizer/initiator) for the reactive blends. The elongation at break was increased for the four studied materials and ductile materials were obtained. The tensile modulus was lower compared to PLA, but still in the range for a non-rubberlike stiff material. Impact testing indicated a higher toughness for all plasticized materials, whereas PLA/myrcene showed the strongest increase. The thermal properties indicated that the glass transition temperature is decreased for the four materials, but not as strong as observed for other plasticizers by this two plasticization methods. In general, the materials' thermal properties were close to PLA's thermal properties. The lower glass transition temperatures in the limonene-plasticized samples compared to the myrcene plasticized samples were in good agreement with the higher observed elongation at break for these samples. In conclusion, the plasticization by limonene and myrcene leads to materials a high ductility and thermal properties like

PLA. The less decreased glass transition temperature compared to other plasticization methods could broaden the application range of plasticized PLA materials.

The plasticization with limonene and myrcene by reactive and non-reactive melt-blending in a micro-compounder leads to materials with interesting mechanical and thermal properties and the further study of these materials could be interesting. Especially, the different effects of reactive and non-reactive blending have to be studied. For both limonene samples, just slight differences were observed, which leads to the assumption, that the initiator play a minor role and maybe no reaction occurred between limonene and the initiator. For myrcene, differences were observed for the reactive and the non-reactive blending, but the ongoing reactions were not clarified. It is important to know the occurring chemical reactions between the plasticizer, the initiator, and the matrix to understand the impact of the chemical structure on the materials properties. It was not clarified if the initiator induces a grafting of the plasticizer onto the matrix and reduces the problems of small plasticizers like migration. For this purpose, the chemical reactions during the compounding have to be analyzed and aging studies could be conducted to study the permanence of plasticization. In addition, limonene and myrcene are natural plasticizers and therefore a (bio)degradation of these materials could be more interesting compared to, for example, recycling and could be suitable for further studies.

Structure of polylactide-based materials obtained by reactive extrusion: formation and thermomechanical transformations

Polylactide (PLA), a biodegradable and bio-based polymer, raised researchers' attention to replace conventional plastics. At room temperature, PLA is brittle and requires physical plasticization that increases its ductility but at the same time drastically decreases its stiffness. As an alternative, plasticization by reactive extrusion was recently developed. The reactive extrusion of PLA with acrylated poly(ethylene glycol) (acrylPEG) as plasticizer yields a plasticized PLA named pPLA. This thesis aims at identifying the structure of this pPLA and studying its evolution engendered by thermomechanical transformations as drawing and recycling. First, pPLA's structural features are analyzed by a multi-scale and multi-disciplinary approach. pPLA is characterized by partially grafted and partially free inclusions of the polymerized plasticizer and a slightly crosslinked PLA matrix. These plasticizer inclusions lead to a material with a good stiffness-ductility balance. Second, the deformation mechanisms of pPLA upon drawing indicate that chain orientation mechanisms are predominant compared to damage, the latter dominating deformation in PLA. Third, the thermomechanical recycling of pPLA shows that degradation is dependent on the type of processing step. Compression-molding is detrimental to pPLA inducing after recycling a higher degradation compared to PLA. This thesis releases new characterization methodologies enabling a better identification of biopolymer structural features.

Keywords: polylactide, plasticization, recycling, deformation

Structure de matériaux à base de polylactide obtenus par extrusion réactive : formation et transformation thermomécaniques

Le polylactide (PLA) est un polymère à la fois biodégradable et biosourcé focalisant l'attention des chercheurs pour le remplacement des plastiques conventionnels. A la température ambiante, le PLA est fragile et nécessite d'être modifié par plastification physique afin d'augmenter sa ductilité, mais dans le même temps sa rigidité chute fortement. Une alternative à cette plastification physique est la plastification par extrusion réactive. L'extrusion réactive du PLA avec l'acrylate de poly(éthylène glycol) (acrylPEG) donne lieu à un PLA plastifié nommé pPLA. Cette thèse a pour objectifs l'identification de la structure du pPLA et l'étude de son évolution lors de transformations thermomécaniques d'étirage et de recyclage. La structure du pPLA a été analysée par une approche multi-échelles et multi-disciplinaire. L'acrylPEG polymérisant et formant des inclusions, est partiellement greffé au PLA et partiellement libre. De plus, les réactions conduisent à une légère réticulation de la matrice. La présence de plastifiant conduit à un bon équilibre entre rigidité et ductilité. Les mécanismes de déformation du pPLA sous étirage ont montré que les mécanismes d'orientation moléculaire sont prépondérants par à l'endommagement, qui lui prédomine dans le PLA. L'analyse du recyclage thermomécanique du pPLA a mis en évidence une dégradation du matériau dépendant du type de procédé utilisé. L'utilisation de la compression à chaud est le procédé le plus défavorable, conduisant à une dégradation plus importante du pPLA par rapport au PLA. Ces travaux ont permis de développer des méthodologies de caractérisation permettant une meilleure identification structurale des biopolymères.

Mots de clé : polylactide, plastification, recyclage, déformation